A Numerical Model for Multicomponent Reactive Transport in Variably Saturated Porous Media

by Klaus Ulrich Mayer

A thesis
presented to the University of Waterloo
in fulfilment of the
thesis requirement for the degree of
Doctor of Philosophy
in
Earth Sciences

Waterloo, Ontario, Canada, 1999

The University of Waterloo requires the signatures of all persons using or photocopying this thesis. Please sign below, and give address and date.

Abstract

A general multicomponent reactive transport model (MIN3P) for variably-saturated porous media was developed. The model includes a simulator for geochemical batch problems as well as a variably-saturated flow module, and it solves the coupled reactive transport equations. The governing equations are discretized using a locally mass conservative finite volume method and linearized by a global implicit solution technique. Advective-diffusive transport of dissolved species and diffusive gas transport are included. The model is based on a partial equilibrium formulation. Reaction processes included are aqueous complexation, oxidation-reduction, ion-exchange, gas dissolution-exsolution and mineral dissolution-precipitation reactions. General rate expressions for kinetically-controlled intra-aqueous and dissolution-precipitation reactions were developed and allow the consideration of a large number of rate expressions reported in the literature. All reaction and rate parameters can be specified from a database, which allows utilization of the model for a wide range of reactive transport scenarios involving inorganic and organic chemicals. Several numerical techniques have been implemented and tailored towards reactive transport applications to increase the efficiency and robustness of the model. Verification examples involving the generation of acid mine drainage, reactive transport affected by ion exchange reactions and the mining of copper from a five-spot well pattern by acid leaching were conducted to prove the functionality and versatility of the model. Batch and one-dimensional simulations were conducted to demonstrate the model's capabilities for the investigation of the generation and fate of acid mine drainage. A final set of simulations demonstrates the versatility of the model as an analysis tool for the investigation of field data. The remediation of groundwater contaminated by hexavalent chromium and chlorinated organic chemicals by a reactive barrier composed of zero-valent iron is simulated and the results are compared to field observations. One and two-dimensional simulations were conducted to semi-quantitatively describe the processes defined in the conceptual model and to assess the possible effect of preferential flow and secondary mineral formation and on the treatment quality.

Acknowledgements

I would like to thank my supervisor Dr. Emil Frind for his continuous support throughout this research. I would also like to thank the members of my advisory committee Dr. R. B. Simpson, Dr. E. A. Sudicky and Dr. J. F. Sykes for their advice, and especially Dr. D. W. Blowes for his support and helpful comments regarding the geochemical aspects of my thesis. I am also grateful to Joel VanderKwaak for providing the iterative matrix solver, which constitutes an important part of the model developed during this research. Furthermore, I would like to thank André Unger for sharing his insight into spatial discretization of PDE's using the finite volume method and for providing the subroutines for calculating influence coefficients for diffusive-dispersive transport. I would like to thank Dr. P. C. Lichtner for providing the data that contributed significantly to the verification of the present model. I am also grateful to my external examiner Dr. C. I. Steefel and to my examiners Dr. P. A. Forsyth and Dr. W. C. Lennox for their critical comments. Thanks also to the Modelling- and GRIME-Groups at the University of Waterloo for their support. In particular I would like to thank Jeff Bain for introducing me to field-work and for dealing with my geochemical questions. The technical support provided by John Molson and Rob McLaren is much appreciated. I would like to express special thanks to Kerry MacQuarrie and Shawn Benner for many helpful discussions and suggestions during the course of this research.

Financial support for this research was provided by a scholarship from the Government of Canada Awards program, which proved to be essential for the completion of this work. Additional financial support was provided by an NSERC (Natural Sciences and Engineering Research Council of Canada) operating grant awarded to Dr. Emil Frind and by the Waterloo Centre for Groundwater Research (WCGR, now CresTech). Funding for the modelling study of the treatment of contaminated groundwater by a reactive barrier was provided by the US Environmental Protection Agency (Robert S. Kerr Lab).

I would like to thank my friends for spending time with me during my extended stay at the University of Waterloo. Thanks to everybody who contributed to replace my stolen bike. This allowed me to continue riding and to stay in shape. Special thanks to Jos, Lavinia, Kelly, Ruth, Sebastian, Mario, Kristin, Steve, Julie, Antonia, Pascale, Sonia, Martin, Che, Cheryl, Cory, Jean and Mary for their companionship during various social, sports and leisure activities. I also would like to thank Oldsmobile for building great cars back in the early 1980's, and providing efficient transportation throughout most of this study and minimizing my down-time.

I would like to express special thanks to my parents, who supported and encouraged me in pursuing my career throughout my studies in Germany and in Canada and who kept me up-to-date with occurrences in Germany.

Foremost, I would like to thank Connie for her love, support and patience during hard times and for sharing the good times with me. It was her love and care which kept me on track during the completion of this work. I also would like to thank her for critically reading my thesis and for attempting to introduce me to the intricacies of the English language.

Contents

List of Tables

List of Figures

Chapter 1

Introduction

Reactive transport modelling of groundwater systems has become an important field of research during recent years. The transport of reactive chemicals through aquifers is characterized by a high degree of complexity, which is primarily caused by the simultaneous occurrence of physical transport and chemical reactions and the interactions of chemical species among each other. The primary goal of this research is to develop a generally applicable reactive transport model, which can be used to describe a broad range of coupled reaction-transport problems in variably-saturated porous media.

Applications for multicomponent reactive transport in partially-saturated and fully-saturated porous media address many problems of interest in the fields of geology and engineering. Possible applications include the generation and fate of acid mine drainage from tailings impoundments or waste rock dumps [*Jaynes et al.*, 1984b, *Narasimhan et al.*, 1986, *Liu and Narasimhan*, 1989b, *Walter et al.*, 1994b, *Wunderly et al.*, 1996], radioactive waste disposal [*Lichtner and Seth*, 1996, *Steefel and Lichtner*, 1998, *Viswanathan et al.*, 1998], infiltration and subsequent reactive transport of landfill leachate into aquifers [*Hunter et al.*, 1998], the effect of chemical weathering on the global CO_2-cycle [*Lasaga et al.*, 1994], hydrothermal systems [*Steefel and Lasaga*, 1994], groundwater contamination due to septic systems [*MacQuarrie*, 1997], passive remediation schemes such as reactive barrier or "Funnel-and-Gate" systems [Chapter 7 of this thesis] and applications in agriculture [*Suarez and Šimůnek*, 1993, *Šimůnek and Suarez*, 1994]. Reactive transport models can be used to better understand the evolutionary processes, which control the quality of groundwater, soil gas and the mineralogical composition of aquifer systems. The models can also be applied to test conceptual models or as a design tool for labora-

tory experiments and field installations of passive remediation technologies, radioactive waste disposal facilities [*Viswanathan et al.*, 1998] or septic systems [*MacQuarrie*, 1997].

1.1 Previous Model Developments

A number of geochemical equilibrium models have been developed for the evaluation of geochemical batch data [*I and Nancollas*, 1972, *Parkhurst et al.*, 1980, *Perkins et al.*, 1990, *Wolery et al.*, 1990, *Allison et al.*, 1991, *Ball and Nordstrom*, 1991, *Claesson and Andersson*, 1996]. These models have been proven powerful tools for the interpretation of geochemical data and have arrived at a high degree of maturity. Geochemical equilibrium models such as PHREEQE [*Parkhurst et al.*, 1980], EQ3/6 [*Wolery et al.*, 1990] and MINTEQA2 [*Allison et al.*, 1991] provide a great degree of flexibility for the evaluation of geochemical data, but have only limited or no capabilities for considering the influence of physical transport on geochemical reaction processes.

The need to investigate dynamic groundwater systems involving geochemical reactions and physical transport has triggered the development of solution methods for reactive transport problems [*Nguyen et al.*, 1982, *Rubin*, 1983, *Lichtner*, 1985, *Bahr and Rubin*, 1987, *Ortoleva et al.*, 1987a, *Willis and Rubin*, 1987, *Kirkner and Reeves*, 1988, *Lichtner*, 1988, *Herzer and Kinzelbach*, 1989, *Kinzelbach and Schäfer*, 1989, *Knapp*, 1989, *Friedly and Rubin*, 1992, *Rubin*, 1992, *Sevougian et al.*, 1993]. Several reactive transport models of varying complexity have been developed in conjunction with these investigations [*Helgeson et al.*, 1970, *Jennings et al.*, 1982, *Miller and Benson*, 1983, *Jaynes et al.*, 1984a, *Lichtner*, 1985, *Cederberg et al.*, 1985, *Bryant et al.*, 1986, *Förster*, 1986, *Liu and Narasimhan*, 1989a, *MacQuarrie et al.*, 1990, *Engesgaard and Kipp*, 1992, *Sevougian et al.*, 1993, *Zysset et al.*, 1994, *Walter et al.*, 1994a, *Steefel and Lasaga*, 1994, *Marzal et al.*, 1994, *McNab Jr. and Narasimhan*, 1994, *Lichtner*, 1996a, *Shen and Nikolaidis*, 1997, *Hunter et al.*, 1998]. Many of these models incorporate one of the above mentioned geochemical equilibrium models in order to describe the reaction processes. This approach provides the versatility of the existing batch models. Most of the reactive transport models developed to date are limited to fully-saturated conditions.

The development of multicomponent reactive transport models applicable under variably-saturated conditions is a fairly new area of research. *Yeh and Tripathi* [1991] have coupled a reactive transport model to a variably-saturated flow model, but neglected gas

transport processes. Gas transport in the unsaturated zone has been considered previously in reactive transport models by *Prein* [1994], *Šimůnek and Suarez* [1994], *Wunderly et al.* [1996], and *MacQuarrie* [1997]. However, these reactive transport models are limited to specific applications or significantly simplify transport or reaction processes. *Lichtner* [1996a] developed a multicomponent-multiphase reactive transport model, which includes gas transport processes and is capable of considering general geochemical systems.

1.2 Objectives and Scope

The objective of this thesis is to develop a general multicomponent-reactive transport model suitable for the simulation of physical and geochemical processes that control the evolution of pore water, pore gas and the mineralogical composition in variably-saturated porous media in one, two or three spatial dimensions. To achieve this goal it is necessary to consider a large number of species and various geochemical reaction processes. The model must also be numerically robust and efficient to ensure its applicability to problems of varying complexity and difficulty.

The present model (MIN3P) considers advective-dispersive transport in the aqueous phase, as well as diffusive gas transport. Darcy velocities are calculated internally using a variably-saturated flow module. The model formulation is based on the global implicit solution approach [*Steefel and Lasaga*, 1994], which considers reaction and transport processes simultaneously. This formulation enforces a global mass balance between solid, surface, dissolved and gaseous species and thus facilitates the investigation of the interactions of reaction and transport processes.

MIN3P is characterized by a high degree of flexibility with respect to the definition of the geochemical reaction network to facilitate the model application to a wide range of hydrogeological and geochemical problems. Chemical processes included are homogeneous reactions in the aqueous phase, such as complexation and oxidation-reduction reactions, as well as heterogeneous reactions, such as ion exchange, mineral dissolution-precipitation and gas exchange reactions. Reactions within the aqueous phase and dissolution-precipitation reactions can be considered as equilibrium or kinetically-controlled processes. The present formulation is conceptually similar to the reactive transport models developed by *Steefel and Lasaga* [1994] and *Lichtner* [1996a].

A new, general framework for kinetically-controlled intra-aqueous and mineral dissolution-precipitation reactions is developed. All kinetically-controlled reactions can be described as reversible or irreversible reaction processes. Different reaction mechanisms for dissolution-precipitation reactions are considered, which can be subdivided into surface- and diffusion-controlled reactions [*Berner*, 1978, *Steefel and Lasaga*, 1994]. This approach allows the consideration of a large number of rate expressions reported in the literature. Related reaction and rate parameters can be incorporated into the model through an accompanying database. The model is primarily designed for problems involving inorganic chemistry, but reactions involving organic chemicals can also be accommodated.

To allow the practical application of the model, various existing numerical techniques are implemented and adjusted to the requirements of reactive transport modelling. The methods are tested for their effect on efficiency and robustness when solving the governing equations and also for their impact on the accuracy of the solution. Among the methods included are different spatial weighting schemes for advective transport [*Unger et al.*, 1996] in the aqueous phase and an adaptive time stepping and update modification algorithm. The model also allows the use of different master variables for oxidation-reduction reactions.

A series of simulations are conducted to evaluate the functionality and versatility of the model formulation. The applications include reactive transport scenarios involving ion-exchange reactions [*Valocchi et al.*, 1981], applications in acid mine drainage [*Wunderly et al.*, 1996, *Lichtner*, 1997a], the mining of copper by an *in-situ* leaching operation [*Lichtner*, 1997b] and a modelling analysis of a reactive barrier system for the remediation of contaminated groundwater based on the conceptual model and data from *Bennett* [1997].

1.3 Organization of Thesis

Chapter 2 presents the conceptual framework and common solution approaches for reactive transport modelling. Important physical transport and geochemical reaction processes are described. A general conceptual model based on the REV approach [*Bear*, 1972, *Lichtner*, 1996a], which incorporates the most relevant reaction and transport processes is presented. The fundamental equations describing the governing physical and chemical processes are defined in conjunction with the most important terminology for

reactive transport models. Physical and temporal scales and scaling relationships involving numerical parameters are summarized from previous studies [*Bahr and Rubin*, 1987, *Knapp*, 1989, *Luckner and Schestakow*, 1991, *Lichtner*, 1993, *Lichtner*, 1996a, *Steefel and MacQuarrie*, 1996] and presented in a general framework. Temporal and spatial scales of physical and chemical processes are discussed in conjunction with the temporal and spatial parameters of the discretized equations. The solvability of the equations and the resolution of the transport and reaction processes using the discretized equations are evaluated. Solution approaches such as the mixing-cell method, the global-implicit solution approach [*Steefel and Lasaga*, 1994], and various operator-splitting approaches [e.g.: *Yeh and Tripathi*, 1989, *Zysset et al.*, 1994, *MacQuarrie*, 1997] are reviewed and the advantages and disadvantages of the methods are discussed.

Chapter 3 presents the theoretical development behind the current multicomponent reactive transport model. Simplifying assumptions affecting the global model formulation are stated followed by the governing equations for variably-saturated flow and the derivation of the multicomponent reactive transport equations based on the fundamental equations given in Chapter 2. The mathematical formulation of geochemical reactions considered in the current model is also presented in this chapter. The focus is primarily on the formulation of homogeneous and heterogeneous kinetically-controlled reactions.

The governing equations presented in Chapter 3 are discretized in Chapter 4. An outline of the comprehensive mass-balance calculations implemented in the present model is provided. Numerical techniques employed to increase the efficiency and robustness of the present model are presented along with an example application to investigate the influence of the numerical parameters on the model performance and accuracy.

Chapter 5 presents the verification of the newly developed model MIN3P based on four test problems. The test problems include a comparison with PYROX [*Wunderly et al.*, 1996], an investigation of reactive transport involving ion-exchange reactions [*Valocchi et al.*, 1981] and two comparisons with the model MULTIFLO developed by *Lichtner* [1996a]. The comparison with PYROX involves the simulation of pyrite oxidation in unsaturated porous media. The first comparison with MULTIFLO addresses acid mine drainage generation due to pyrite oxidation in an unsaturated soil column with subsequent reactive transport of the reaction products [*Lichtner*, 1997a]. The second problem describes the *in-situ* leaching of copper from a five-spot well pattern [*Lichtner*, 1997b].

The next two chapters demonstrate the applicability of MIN3P for sensitivity analyses and the simulation of reactive transport under field conditions. Chapter 6 consists

of example applications for the investigation of the generation and the fate of acid mine drainage. Sensitivity analyses were conducted to illustrate the applicability of MIN3P for kinetic batch simulations and one-dimensional reactive transport simulations. Chapter 7 presents a modelling study of a reactive barrier installed at the U.S. Coast Guard Support Center near Elizabeth City, NC [*Bennett*, 1997] including one- and two-dimensional simulations. The remediation of groundwater contaminated with hexavalent chromium, trichloroethylene and its degradation products was simulated.

The final chapter of this study summarizes the findings of the previous chapters concentrating on the present model development. The limitations of reactive transport modelling are addressed in this context. Recommendations for future model developments and improvements are made based on these findings.

Chapter 2

Conceptual Framework and Solution Approaches

This chapter defines transport and reaction processes, which are of importance for the description of reactive transport in aquifer systems. A general conceptual model based on the REV-approach [*Bear*, 1972, *Lichtner*, 1996a] which serves as a basis for the formulation of reactive transport models is presented. The fundamental mathematical relationships that are used to describe the relevant processes are introduced along with the essential terminology. These mathematical relationships facilitate the implementation of the conceptual model into a numerical model that is capable of describing the transient evolution of mineral-water-gas systems and the compositional changes within each phase. The implementation of the model equations into a numerical model requires spatial and temporal discretization of the governing equations. Spatial and temporal scales of the governing processes have a significant influence on the formulation, performance and accuracy of reactive transport models [*Bahr and Rubin*, 1987, *Willis and Rubin*, 1987, *Lichtner*, 1988, *Knapp*, 1989, *Lichtner*, 1993, *Zysset et al.*, 1994, *Lichtner*, 1996a, *Steefel and MacQuarrie*, 1996] and are discussed in conjunction with the discretization parameters of the model equations. Special topics such as the local equilibrium approximation [*Lichtner*, 1985, *Knapp*, 1989], the development of moving dissolution-precipitation fronts [*Lichtner*, 1985, *Willis and Rubin*, 1987 and quasi-steady state conditions [*Lichtner*, 1985, *Lichtner*, 1988], *Sevougian et al.*, 1993] are addressed in this context. Common solution approaches for the reactive transport equations are discussed along with the evaluation of their advantages and disadvantages.

2.1 Physical Transport and Geochemical Reaction Processes

This section provides a brief summary of the physical and chemical processes taking place in fully- and partially-saturated groundwater systems. Transport processes of interest are advective, diffusive and dispersive transport. Advective transport in the aqueous phase is caused by the bulk displacement of dissolved species with the flowing groundwater. The driving force for this transport mechanism is the hydraulic gradient. Pressure gradients in the gaseous phase displace the soil gas. Other transport processes of importance are mechanical dispersion and molecular diffusion, which also take place in both phases. Mechanical dispersion is caused by a hydraulic mixing process due to pore-to-pore variations in flow velocity. Molecular diffusion describes the transport of dissolved species or gaseous species due to concentration gradients.

Chemical reactions of interest in groundwater systems include homogeneous reactions, which take place in a single phase or heterogeneous reactions which involve mass exchange between two or more phases [*Lasaga*, 1981, *Rubin*, 1983, *Lichtner*, 1985, *Lasaga*, 1998]. Homogeneous reactions between dissolved constituents include aqueous complexation, i.e. the interactions among the dissolved species, which undergo hydrolysis and ion-pairing, and oxidation-reduction reactions. The most important heterogeneous reactions are dissolution and precipitation of minerals, adsorption and ion exchange reactions, and gas dissolution-exsolution reactions.

Geochemical reactions can be described by equilibrium or kinetic relationships. Equilibrium reactions provide only information about the final composition of a geochemical system. Kinetically-controlled reaction rates describe the transient chemical evolution towards an equilibrium state. For complex systems, the description of reaction kinetics is inherently more difficult than that of thermodynamics, because kinetically-controlled processes are dependent on the reaction path [*Lasaga*, 1981]. Equilibrium reactions are uniquely defined by the law of mass action. There are, on the other hand, often many possibilities to express the progress of a kinetic reaction.

If all species contained in a groundwater system are in a state of equilibrium and both water and gas phases are immobile, reactions will not take place as long as the equilibrium state of the system is not disturbed by a change in the state variables such as temperature or pressure or by external processes. An external process can be the injection or infiltration of water with a different chemical composition than the ambient

groundwater or the ingress of atmospheric gases into a partially-saturated porous medium. These external processes can be described by the transport processes defined above, which cause the movement of dissolved species and gases through a porous medium. The resulting state of disequilibrium provides the driving force for geochemical reactions to occur and force the groundwater system towards a new and often different equilibrium state that may involve compositional changes within the phases. In practical terms, these compositional changes result in geochemical weathering of the solid phase. The rates of geochemical weathering may, for example, depend on the following factors [based on *Sparks*, 1989]:

- temperature
- hydraulic conductivity
- phase saturations
- porosity
- mineralogy
- surface area of minerals
- ligand concentration of recharge water
- O_2 and CO_2 concentration of soil gas
- pH of recharge water

The composition of the infiltrating water and pore gas, as well as the mineralogical composition and structure of the porous medium will, however, predominantly determine the geochemical evolution of the system. If the flowing groundwater is in contact with a reactive porous medium, heterogeneous reactions between the aqueous and the solid phase will likely contribute significantly to the system's composition.

It can be concluded that transport processes will tend to offset the equilibrium-state of a particular mineral-water-gas system, while geochemical reactions will tend to reestablish an equilibrium condition. This new equilibrium composition will likely be different from the original equilibrium composition (if equilibrium existed previously). Reactive transport models are designed to keep track of these compositional changes within the

gas, water and solid phase. In a natural system many of these processes occur simultaneously and influence each other. The purpose of a reactive transport model is to describe these complex, nonlinear interactions. In the following sections the conceptual framework for reactive transport models is discussed.

2.2 Conceptualization of Physico-Chemical System

Groundwater flow and reactive transport models are a conceptualization of a natural system, which is based on the REV-approach [*Bear*, 1972, *Lichtner*, 1996a]. *Lichtner* [1996a] defines this conceptualization for reactive transport models as the replacement of a discrete physical system consisting of mineral particles, adsorbed species and pore spaces filled with water and/or gases by a continuum in which physico-chemical variables vary continuously in space. One advantage of this conceptualization is that physico-chemical parameters, which vary on the microscale, can be expressed in terms of their average values on the REV-scale [*Bear*, 1972, *Lichtner*, 1996a]. Example parameters are phase saturations and pressures, partial gas pressures, species concentrations, mineral volume fractions and mineral reactive surface areas [*Lichtner*, 1996a]. The REV description allows any number of continua to occupy the same physical space at the same time [*Bear*, 1972, *Lichtner*, 1996a] and permits the coexistence of any number of species within each phase [*Bear*, 1972].

A REV for a reactive transport model (excluding non-aqueous phase liquids) includes three phases:

- aqueous phase,
- gaseous phase,
- solid phase,

where the solid phase includes mineral and adsorbed species. Figure 2.1 presents the conceptualization of a groundwater system for reactive transport in variably-saturated porous media. The conceptualized system includes source and sink terms, which can be subdivided into external and internal sources and sinks. External sources and sinks are due to physical transport processes of the mobile species into or out of the REV. Sources and sinks for dissolved species and gases due to transport processes are defined in Figure

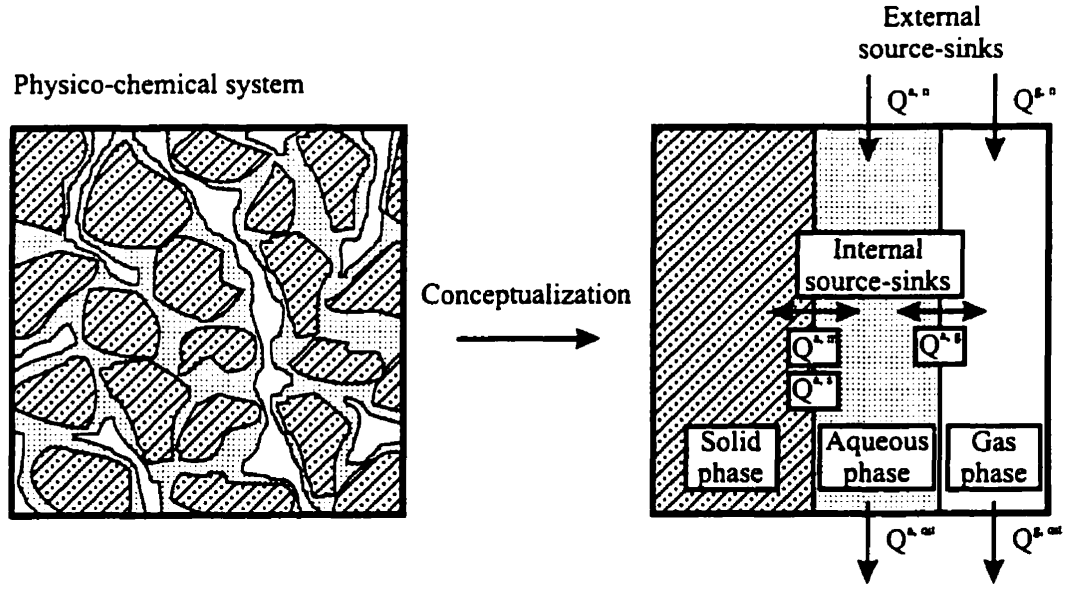

Figure 2.1: Conceptualization of physico-chemical system

2.1 as $Q^{a,in}$, $Q^{g,in}$, $Q^{a,out}$ and $Q^{g,out}$, where the superscript a defines the aqueous phase and g identifies the gaseous phase. Internal sources and sinks on the other hand are due to reaction processes and describe the mass transfer due to heterogeneous reactions between the phases, here defined as $Q^{a,s}$, $Q^{a,m}$ and $Q^{a,g}$, where the superscript s defines surface species and m identifies the mineral phases. The various phases are composed of a number of constituents, which are summarized in Table 2.1. The solid phase is made up of minerals, amorphous solid phases, sorbed and ion-exchanged species and possibly organic matter, while the aqueous phase consists primarily of the solvent water itself and the dissolved species. The gaseous phase is composed of gases common in the atmosphere, but may also include other gases such as methane, hydrogen sulfide and hydrogen gas. Internal sources and sinks are due to heterogeneous reactions (see also Table 2.1) such as dissolution-precipitation reactions, ion exchange and adsorption as well as gas exchange between the gaseous and the aqueous phase. Homogeneous reactions within the phases include hydrolysis, complexation, oxidation-reduction and mineral alteration reactions. This REV-conceptualization assumes that water is fully wetting, and that no direct contact between the gaseous phase and the solid phase exists. The transport of colloidal particles is also neglected.

phase	solid	aqueous	gaseous
constituents	*Minerals* aluminosilicates carbonates sulfides oxides hydroxides sulfates halides phosphates elements *Ion-exchanged and adsorbed species* *Organic matter*	H_2O *Major constituents* H^+, Na^+, Cl^-, SO_4^{2-}, Mg^{2+}, Ca^{2+}, K^+, CO_3^{2-}, H_4SiO_4, Al^{3+}, Fe *Dissolved gases* CO_2(aq), O_2(aq), N_2(aq), H_2S(aq), CH_4(aq), H_2(aq), etc. *Trace metals* Cd, Cr, Cu, Pb, Zn, etc. *Radionuclides* Ra, U, Th, etc.	*Gases* O_2(g), CO_2(g), N_2(g), H_2S(g), CH_4(g), H_2(g), etc.
homogeneous reactions	alteration	hydrolysis complexation oxidation-reduction	
heterogeneous reactions	dissolution-precipitation ion-exchange sorption oxidation-reduction	dissolution-exsolution	

Table 2.1: Important chemical species and reactions in a solid-water-gas system

2.3 Fundamental Equations and Modelling Terminology

The basic equations for reactive transport models and the accompanying terminology including numerical parameters important for the understanding of the modelling issues are introduced. Reactive transport models can be formulated based on the following fundamental equations:

- a system of partial differential equations describing physical transport,
- a system of algebraic equations describing geochemical equilibrium reactions,

- a system of ordinary differential equations, which define kinetically-controlled geochemical reactions.

A mass conservation equation including physical transport can be written for each mobile species in the aqueous and gaseous phase. The number of mobile species in the aqueous phase is given by $N_d = N_c + N_x$ and is equivalent to the number of dissolved species. N_c corresponds to the number of components and N_x to the number of aqueous complexes, which can be expressed in terms of the components based on equilibrium relationships. N_g defines the number of gases present in the gaseous phase. The corresponding mass conservation equations which consider the processes of advection and dispersion can be written as:

$$\frac{\partial}{\partial t}[S_a\phi C_j^c] - \nabla\cdot[\mathbf{v}_a C_j^c] + \nabla\cdot[S_a\phi\mathbf{D}_a\nabla C_j^c] - Q_j^c = 0 \qquad j = 1, N_c \qquad (2.1)$$

$$\frac{\partial}{\partial t}[S_a\phi C_i^x] - \nabla\cdot[\mathbf{v}_a C_i^x] + \nabla\cdot[S_a\phi\mathbf{D}_a\nabla C_i^x] - Q_i^x = 0 \qquad i = 1, N_x \qquad (2.2)$$

$$\frac{\partial}{\partial t}[S_g\phi C_i^g] - \nabla\cdot[\mathbf{v}_g C_i^g] + \nabla\cdot[S_g\phi\mathbf{D}_g\nabla C_i^g] - Q_i^g = 0 \qquad i = 1, N_g \qquad (2.3)$$

where S_a is the saturation of the aqueous phase [m^3 water m^{-3} void], S_g is the saturation of the gaseous phase [m^3 gas m^{-3} void], ϕ is the porosity [m^3 void m^{-3} bulk], C_j^c is the concentration of the j^{th} component as species in solution [mol l^{-1} water], C_i^x is the concentration of i^{th} aqueous complex [mol l^{-1} water], and C_i^g is the concentration of the i^{th} gaseous species present in the gaseous phase [mol l^{-1} gas]. The vectors $\mathbf{v}_a$ and $\mathbf{v}_g$ represent the Darcy flux for the aqueous phase and gaseous phase respectively [m bulk s^{-1}]. $\mathbf{D}_a$ defines the dispersion tensor in the aqueous phase [m^2 bulk s^{-1}] and $\mathbf{D}_g$ represents the dispersion tensor in the gaseous phase, respectively. For simplicity the dispersion tensor is assumed to be equivalent for all species within each of the mobile phases. Q_j^c, Q_i^x and Q_i^g represent the source/sink terms for the consumption or production of a particular mobile species due to geochemical reactions or boundary fluxes [mol l^{-1} bulk s^{-1}] (i.e. internal and external sources and sinks). A positive quantity defines a source for the species of concern.

Mass conservation equations are formulated for all immobile species, which can be defined by N_s species sorbed to the mineral surfaces and N_m mineral phases:

$$\frac{dC_i^s}{dt} - Q_i^s = 0 \qquad i = 1, N_s \tag{2.4}$$

$$\frac{dC_i^m}{dt} - Q_i^m = 0 \qquad i = 1, N_m \tag{2.5}$$

C_i^s is the concentration of the i^{th} sorbed species [mol l^{-1} bulk], and C_i^m is the concentration of the i^{th} mineral [mol l^{-1} bulk]. Q_i^s and Q_i^m represent the source/sink terms for the consumption or production of a particular immobile species due to geochemical reactions [mol l^{-1} bulk s^{-1}] (i.e. internal sources and sinks).

Relationships describing the reaction stoichiometry of geochemical reactions can be expressed in terms of components. The dissociation and association of aqueous complexes, gas dissolution-exsolution reactions, ion exchange and mineral dissolution-precipitation reactions are considered in this context. A stoichiometric relationship for the dissociation of the aqueous complex A_i^x into the components as species in solution A_j^c can be written as [*Steefel and Lasaga*, 1994]:

$$A_i^x \rightleftharpoons \sum_{j=1}^{N_c} \nu_{ij}^x A_j^c \qquad i = 1, N_x \tag{2.6}$$

where ν_{ij}^x is the stoichiometric coefficient of the j^{th} component in the i^{th} aqueous complex. The partitioning of a gas A_i^g from the gaseous phase into the aqueous phase and subsequent dissociation into components as species in solution can be expressed as:

$$A_i^g \rightleftharpoons \sum_{j=1}^{N_c} \nu_{ij}^g A_j^c \qquad i = 1, N_g \tag{2.7}$$

where ν_{ij}^g is the stoichiometric coefficient of the j^{th} component in the i^{th} gas. Ion-exchange reactions can be expressed in a similar fashion:

$$A_i^s \rightleftharpoons \nu_{ij}^s A_j^s + A_i^s - \nu_{ij}^s A_j^c \qquad i = 1, N_s \tag{2.8}$$

where equation 2.8 describes ion-exchange reactions based on the Gaines-Thomas convention [*Appelo and Postma*, 1993]. A_i^s is the i^{th} ion-exchanged species competing for surface-sites with the ion-exchanged species A_j^s, which in return affects the concentrations

of the dissolved species A_i^c and A_j^c. ν_{ij}^s is the stoichiometric coefficient for the ion-exchange reaction defined by the ratio of the charge of the reacting species. An appropriate reaction equation for the dissolution of mineral A_i^m can be written as:

$$A_i^m \rightleftharpoons \sum_{j=1}^{N_c} \nu_{ij}^m A_j^c \qquad i = 1, N_m \tag{2.9}$$

where ν_{ij}^m is the stoichiometric coefficient of the j^{th} component in the i^{th} mineral.

Geochemical reactions can be described by algebraic equations, if they are "sufficiently fast" and reversible, or have to be described by kinetic relationships, if they are "insufficiently fast" and/or irreversible [*Rubin*, 1983, *Mangold and Tsang*, 1991, see also Sections 2.4.1 and 2.4.3]. If the reactions are "sufficiently fast", the law of mass action can be used to generate a system of algebraic equations, which define the equilibrium relationships for reaction equations 2.6-2.9. Equilibrium relationships for aqueous complexes can be written as:

$$C_i^x = (K_i^x \gamma_i^x)^{-1} \prod_{j=1}^{N_c} \left(\gamma_j^c C_j^c\right)^{\nu_{ij}^x} \qquad i = 1, N_x \tag{2.10}$$

where K_i^x is the dissociation constant for the i^{th} aqueous complex, γ_i^x is the activity coefficient of the i^{th} aqueous complex and γ_j^c is the activity coefficient of the j^{th} component as species in solution. The corresponding relationships for gas dissolution-exsolution can be defined as:

$$C_i^g = (RTK_i^g \gamma_i^g)^{-1} \prod_{j=1}^{N_c} \left(\gamma_j^c C_j^c\right)^{\nu_{ij}^g} \qquad i = 1, N_g \tag{2.11}$$

where R is the ideal gas constant [1 atm K^{-1} mol^{-1}], T is temperature [K], K_i^g is the equilibrium constant for the dissolution of the i^{th} gas, γ_i^g is the fugacity coefficient of the i^{th} gas. Gas concentrations can alternatively be expressed as partial gas pressures. The partial gas pressures are defined as:

$$p_i^g = (K_i^g \gamma_i^g)^{-1} \prod_{j=1}^{N_c} \left(\gamma_j^c C_j^c\right)^{\nu_{ij}^g} = RTC_i^g \qquad i = 1, N_g \tag{2.12}$$

where p_i^g is the partial pressure of the i^{th} gas [atm].

An equilibrium relationship for ion-exchange reactions based on the Gaines-Thomas convention [*Appelo and Postma*, 1993] for the i^{th} and j^{th} ion-exchanged species can be written as:

$$\beta_i = (K_i^s)^{-1}(\beta_j)^{\nu_{ij}^s}(\gamma_i^c C_i^c)(\gamma_j^c C_j^c)^{-\nu_{ij}^s} \qquad i = 1, N_s \tag{2.13}$$

where β_i and β_j are the activities of the ion-exchanged species expressed as equivalent fractions [meq meq^{-1}] and K_i^s is the selectivity coefficient for the ion exchange reaction involving the dissolved species A_i^c and A_j^c. The actual concentrations of the ion-exchanged species in relation to the cation exchange capacity of the soil can be calculated according to [*Appelo and Postma*, 1993]:

$$C_i^s = \frac{\rho_b}{100} CEC (Z_i^s)^{-1} \beta_i \tag{2.14}$$

where ρ_b is the dry bulk density of the porous medium [g solid cm^{-3} bulk], CEC is the cation exchange capacity [meq (100g)$^{-1}$ solid] and Z_i^s is the charge of the ion-exchanged species [mmol meq^{-1}]. The factor 100 is a scaling factor [g (100g)$^{-1}$]. The concentration of the ion-exchanged species A_i^s is given in units [mol l^{-1} bulk]. An equilibrium relationship for mineral dissolution-precipitation reactions is defined by:

$$1 \geq (K_i^m)^{-1} \prod_{j=1}^{N_c} \left(\gamma_j^c C_j^c\right)^{\nu_{ij}^m} \qquad i = 1, N_m \tag{2.15}$$

where K_i^m defines the equilibrium constant for the dissolution of the mineral A_i^m.

If reactions 2.6 - 2.9 cannot be described by equilibrium relationships, kinetic rate expressions have to be defined to describe the transient evolution of the geochemical conditions. The occurrence of kinetically-controlled homogeneous reactions within the aqueous phase requires the definition of an additional stoichiometric relationship to define the consumption and production of components within the aqueous phase [*Lichtner*, 1996b]:

$$\emptyset \rightleftharpoons \sum_{j=1}^{N_c} \nu_{ij}^a A_j^c \qquad i = 1, N_a \tag{2.16}$$

where ν_{ij}^a are the stoichiometric coefficients of the components involved in the i^{th} kinetically-controlled homogeneous reaction. N_a is the number of kinetically-controlled homo-

geneous reactions in the aqueous phase. For simplicity it is assumed that all kinetically-controlled reactions are elementary reactions, reversible and take place along a single reaction path. A reaction expression for the production and consumption of components in the aqueous phase can then be defined as:

$$R_i^a = -k_i^a \left[\prod_{\nu_{ij}^a<0} \left(\gamma_j^c C_j^c\right)^{-\nu_{ij}^a} - (K_i^a)^{-1} \prod_{\nu_{ij}^a>0} \left(\gamma_j^c C_j^c\right)^{\nu_{ij}^a} \right] \qquad i = 1, N_a \tag{2.17}$$

where R_i^a is the absolute reaction rate for the i^{th} kinetically-controlled homogeneous reaction in the aqueous phase [mol l^{-1} water s$-$1] and k_i^a is the rate constant for the forward reaction. In this case, the forward reaction is defined by the direction of the reaction and results in the consumption of the components with negative stoichiometric coefficients. The production or consumption rate of a particular component can be calculated based on:

$$\frac{dC_j^c}{dt} = -\nu_{ij}^a R_i^a \tag{2.18}$$

Kinetic expressions for gas dissolution-exsolution and ion-exchange reactions can also be derived, but are not considered in this work. Kinetically-controlled mineral dissolution-precipitation reactions can be described by:

$$R_i^m = -S_i k_i^m \left[1 - (K_i^m)^{-1} \prod_{j=1}^{N_c} \left(\gamma_j^c C_j^c\right)^{\nu_{ij}^m} \right] \qquad i = 1, N_m \tag{2.19}$$

where R_i^m is the absolute dissolution-precipitation rate of the i^{th} mineral [mol l^{-1} bulk s^{-1}], k_i^m is the dissolution rate constant for the i^{th} mineral and S_i is the reactive surface area of the i^{th} mineral [m^2 mineral l^{-1} bulk]. Equation 2.19 is based on the assumption that the dissolution and precipitation of the mineral A_i^m can be described as an elementary, reversible reaction.

In this context it was assumed that the reaction progress of all kinetically-controlled reactions depends exclusively on the activities of the components as species in solution. It can also be envisaged that other species, such as aqueous complexes, influence the reaction progress. In Chapter 3 a more general formulation for kinetically-controlled reactions is presented.

Equations 2.1-2.5, 2.10-2.15 and 2.17-2.19 define the fundamental equations for reactive transport models including homogeneous and heterogeneous reactions. The source-sink terms Q_j^c, Q_i^x, Q_i^g, Q_i^s and Q_i^m allow the coupling of transport and reaction processes. The basic equations can be combined in various ways to yield the different formulations used in reactive transport modelling. Section 2.5 presents the different approaches and qualitatively discusses their advantages and limitations. This discussion will depend to a large extent on how rapid the processes are taking place in relation to each other, and how well the processes can be resolved by the numerical model. It is therefore necessary to define the time scales of physical and geochemical processes and relate these time scales to the spatial and temporal discretization parameters of the numerical model. The following section will address these issues as a prerequisite for the discussion of the model formulations and will present some special cases, which have an impact on the performance and efficiency of reactive transport models.

2.4 Temporal and Spatial Scales

One of the major difficulties of coupling physical transport and geochemical reactions is the wide range of spatial and temporal scales characterizing the various transport and reaction processes. A rapid process is characterized by a short time scale, while long time scales identify slow processes. For example, the formation of outer-sphere complexes or hydration reactions are very fast. *Lasaga* [1984] and *Stumm and Morgan* [1996] report equilibration times in the order of 10^{-10} to 10^{0} seconds for most of these reactions. Dissolution-precipitation reactions, on the other hand, may be very slow with equilibration times on the order of days to years or even decades. The time scales of advective transport processes directly depend on the groundwater flow rates and therefore directly on the physical properties of the porous medium. Diffusive transport time scales are strongly influenced by the porosity, the phase saturations and the free-phase diffusion coefficients [*Millington*, 1959]. Gaseous diffusion coefficients for example are on the order of four magnitudes larger than aqueous diffusion coefficients and the time scale for diffusive transport of gaseous species will therefore be orders of magnitudes smaller. The time scales of the physico-chemical processes have a pronounced influence on the formulation of the geochemical reactions in a reactive transport model and also on the formulation of the overall governing equations [*Lichtner*, 1985, *Bahr and Rubin*, 1987, *Willis and Rubin*, 1987, *Lichtner*, 1988, *Sevougian et al.*, 1993] and require further consideration. The time

scales of physical transport and geochemical reactions are discussed below based on earlier studies by *Damköhler* [1936], *Bahr and Rubin* [1987], *Lichtner* [1988], *Knapp* [1989], *Zysset* [1993], *Zysset et al.* [1994] and *Steefel and MacQuarrie* [1996]. Their relation to each other is assessed and their relationship to spatial and temporal discretization parameters in a numerical model is evaluated.

2.4.1 Characteristic Time Scales

Macroscopic transport time scales can be defined for each phase independently. The time scale for advective mass transport in phase p is given by:

$$t_{a,p} = \frac{l_{a,p}}{v_p} \tag{2.20}$$

where v_p [m s^{-1}] is the transport velocity in phase p and $l_{a,p}$ [m] is a representative advection length in phase p. The corresponding time scale for diffusive mass transport in phase p can be expressed as:

$$t_{D,p} = \frac{l_{D,p}^2}{D_p} \tag{2.21}$$

where D_p [m^2 s^{-1}] is the effective phase diffusion coefficient and $l_{D,p}$ [m] is a characteristic diffusion length in phase p.

The reaction time scales have to be defined separately for each reaction process. The time scale for a diffusion-controlled reaction with the reaction index i, for example, is defined by:

$$t_{r,i} = \frac{l_{r,i}^2}{D_{r,i}} \tag{2.22}$$

where $D_{r,i}$ [m^2 s^{-1}] is the effective diffusion coefficient for the transport of a reacting species in the i^{th} reaction through the medium of concern and $l_{r,i}$ [m] is some characteristic length for microscale-diffusive transport from the bulk solution to the reaction site for the i^{th} reaction. This relationship defines, for example, the time scale for a dissolution reaction, in which case the reaction progress is controlled by the diffusion of a reactant through a surface coating or a stagnant water film. For reactions that do not depend on the transport of reactants or reaction products, the reaction time scale for the i^{th} reaction

simply depends on the effective rate constant $k_{\text{eff},i}$ expressed in units [s^{-1}]:

$$t_{r,i} = \frac{1}{k_{\text{eff},i}} \tag{2.23}$$

The relation between the time scales of macroscale transport processes and geochemical reactions can be estimated from advective and diffusive Damköhler numbers [*Damköhler*, 1936]. The Damköhler number, which relates the time scale of the i^{th} reaction to the time scale of advective transport in phase p, for example, can be defined as [*Damköhler*, 1936, *Bahr and Rubin*, 1987]:

$$Da_{r,i}^{a,p} = \frac{t_{a,p}}{t_{r,i}} \tag{2.24}$$

The corresponding Damköhler number for diffusive transport can be obtained by replacing the time scale for advective transport by the one for diffusive transport [*Damköhler*, 1936]:

$$Da_{r,i}^{D,p} = \frac{t_{D,p}}{t_{r,i}} \tag{2.25}$$

A general Damköhler number comparing representative time scales of transport and reactions with each other can simply be defined as:

$$Da = \frac{t_t}{t_r} \tag{2.26}$$

where t_r is the time scale representative for all reactions and t_t is the time scale representative for all transport processes. The time scales used to represent t_r and t_t are dependent on the case being considered and also depend on the questions asked. It is often problematic, however, to determine t_r, because reaction rates are often not constant in time and space and are commonly dependent on concentrations, activity coefficients, mineral volume fractions and reactive surface areas. t_r is based on the time scales of the individual reactions taking place in the system, which may vary significantly for different reactions. The Damköhler number can therefore only be used to estimate whether the time scale of macroscopic physical transport or the time scale of geochemical reactions will dominate a particular problem. The relationship between reaction and transport time scales has a significant impact on the solvability of reactive transport problems and on the efficiency and accuracy of the different formulations.

2.4.2 Temporal and Spatial Discretization

A numerical model requires the transformation of the partial differential equations, which provide a continuous description of physico-chemical parameters in space and time, into a discrete approximation. A representative spatial discretization increment Δx and a representative time increment Δt are introduced for the following discussion. Temporal and spatial discretization parameters affect the resolution of the governing equations and the accuracy of the model results. It is practical to describe the representative length scale for macroscale transport processes in terms of the spatial discretization interval Δx. A control on the space and time discretization is given by the Peclet and Courant criteria [*Daus et al.*, 1985, *Steefel and MacQuarrie*, 1996, *Unger et al.*, 1996]. The specific constraints will depend on the temporal and spatial discretization method used [*Unger et al.*, 1996]. The Peclet number compares the time scale for dispersion and diffusion with the time scale for advection [*Steefel and MacQuarrie*, 1996]. Defining $l_{a,p} = l_{D,p} = \Delta x$, the Peclet number for phase p can be written as:

$$Pe_p = \frac{v_p \Delta x}{D_p} \tag{2.27}$$

The Courant number (also defined as CFL- or Courant-Friedrichs-Lewy criterion), here defined as the "advective Courant number", determines the fractional distance traveled relative to the grid spacing due to advection in a single time step [*Steefel and MacQuarrie*, 1996]. The advective Courant number can also be defined as the ratio of the time increment Δt, which characterizes the temporal resolution of a numerical model, to the time scale for advective transport. The advective Courant number for phase p is given by:

$$Cr_{a,p} = \frac{v_p \Delta t}{\Delta x} \tag{2.28}$$

where the characteristic length for advection is defined by the spatial discretization interval Δx. A similar expression to the Courant number may be derived for purely diffusive transport, here defined as the "diffusive Courant number" [*Hall and Porsching*, 1990, *Steefel and MacQuarrie*, 1996]. The diffusive Courant number for phase p can be expressed as

$$Cr_{D,p} = \frac{2 D_p \Delta t}{\Delta x^2}, \tag{2.29}$$

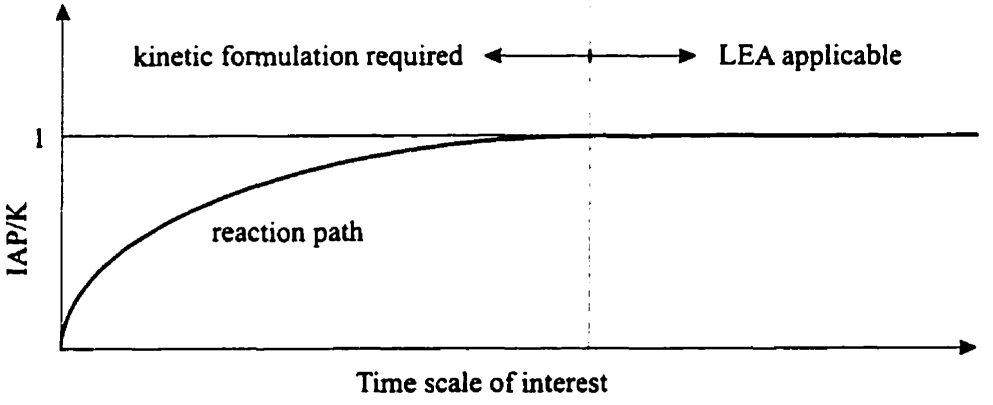

Figure 2.2: Applicability of local equilibrium approximation

and relates the time increment Δt to the time scale of macroscale diffusive transport. A constraint equivalent to the Courant number can be developed to relate the time scale for geochemical reactions to the time increment Δt [e.g. *Valocchi and Malmsted*, 1992, *Kaluarachichi and Morshed*, 1995].

$$Cr_r = \frac{\Delta t}{t_r} \tag{2.30}$$

For a zero-order kinetically-controlled and irreversible reaction, this constraint states for $Cr_r = 1$, that the mass contained in a certain control volume becomes completely depleted during the time interval Δt, provided the reaction rate remains constant [e.g. *Luckner and Schestakow*, 1991].

2.4.3 The Local Equilibrium Approximation

All geochemical reactions are from a theoretical point of view kinetically-controlled processes. A forward reaction is accompanied by a backward reaction assuming that the principle of detailed balancing is valid [*Lasaga*, 1981, 1998]. In this case, the rate constants k_f and k_b for the forward and backward reactions, respectively, are related to each other by [*Lasaga*, 1981, *Stumm and Morgan*, 1996]:

$$K_{eq} = \frac{k_f}{k_b} \tag{2.31}$$

where K_{eq} is the equilibrium constant of the reaction. *Lasaga* [1981] interprets equilibrium as a dynamic balance, rather than a cessation of all contributing reaction processes, where all rates in a given direction have counterbalancing rates in the opposite direction. Figure 2.2 depicts the progress of a reaction from an arbitrary initial state of disequilibrium towards an equilibrium state. The time scale of a particular reaction process defines loosely how fast equilibration is occurring. For reactive transport modelling, the time scale of interest is often defined by the time scales of the transport processes and might furthermore be limited by the spatial and temporal discretization constraints. If the reaction processes are fast in comparison to the transport processes, equilibrium relationships may be used to describe the reactions [*Bahr and Rubin*, 1987, *Knapp*, 1989, *Lichtner*, 1993, *Steefel and MacQuarrie*, 1996]. This is, however, only possible if forward and backward reactions can be specified, i.e. only in the case of reversible reactions. This approach is known as the local equilibrium approximation (LEA) [*Lichtner*, 1985, *Bahr and Rubin*, 1987, *Knapp*, 1989, *Lichtner*, 1993]. The characteristic transport lengths $l_{a,p}$ and $l_{D,p}$ are in this case approximated by the discretization interval Δx. The Damköhler number can be used to determine whether the local equilibrium assumption is valid. If $Da \gg 1$, the time scales of geochemical reactions are much shorter than the time scales for physical transport, and geochemical reactions can therefore be expressed as equilibrium reactions [*Damköhler*, 1936, *Bahr and Rubin*, 1987]. If $Da \ll 1$, transport processes are fast in comparison to geochemical reactions and kinetic rate expressions are needed to describe the reactions [*Bahr and Rubin*, 1987].

2.4.4 Moving Dissolution Boundaries and Quasi-Steady State

Another important aspect of reactive transport modelling is that "moving dissolution boundaries" may develop during a simulation [*Lichtner*, 1985, *Willis and Rubin*, 1987, *Lichtner*, 1988]. Moving dissolution boundaries exist, if mineral phases become completely depleted during the course of a simulation and the mineral dissolution fronts move through the solution domain with a front velocity smaller or equal to the advective transport velocity of the pore water. Moving dissolution boundaries lead to numerical difficulties for the solution of reactive transport problems, because the disappearance of a mineral phase introduces a discontinuity into the governing equations [*Lichtner*, 1985, 1988]. The depletion of a mineral phase usually results in a rapid change in aqueous and gaseous concentrations at a specific spatial location. The advancement of mineral dissolution boundaries can also be described as the "propagation of dissolution-precipitation

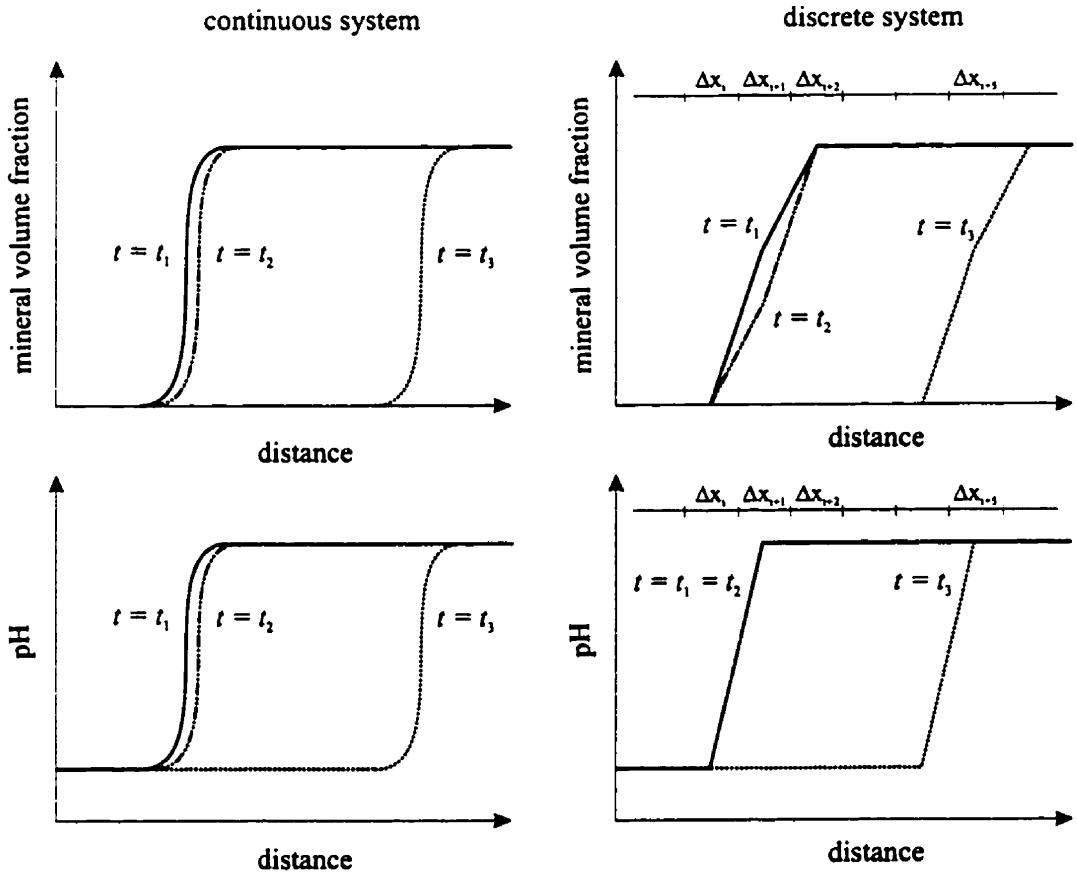

Figure 2.3: Effect of spatial discretization on moving dissolution boundaries

waves" [*Sevougian et al.*, 1993]. Several solution methods have been developed to solve this problem [*Willis and Rubin*, 1987, *Lichtner*, 1988, Chapter 4 of this work].

Figure 2.3 shows a schematic description of a moving dissolution boundary for a continuous description of the governing equations and for the discretized system. A mineral phase is dissolving and leads to pH-buffering of the pore water. The pH remains high in the zone where the mineral phase is present and drops where the mineral phase is completely depleted. The concentrations of other dissolved species (not shown), which comprise the mineral phase, are affected in a similar way. Between the times t_1 and t_3, the mineral dissolution front has advanced over several grid cells. Whenever the mineral phase became completely depleted in a particular control volume, significant

concentration changes also occurred in the aqueous phase in this control volume.

Figure 2.3 also includes the conditions at t_2, where $t_1 < t_2 \ll t_3$. In this case, the continuous description shows a slight advancement of the mineral dissolution front. However, this advancement cannot be resolved by the discretized equations, and the mineral is present in grid cell Δx_{i+1} at t_1 and t_2. Assuming that the mineral reactivity is not a function of the mineral volume fraction present, a "quasi-steady state condition" may exist between t_1 and t_2 in the aqueous phase. A quasi-steady state prevails, if the concentrations in the aqueous phase and/or gaseous phase remain constant in time and space, even though heterogeneous reactions between the phases are taking place [*Lichtner*, 1985, 1988]. This is indicated in Figure 2.3 by the pH-profiles, which are equal or at least similar to each other at t_1 and t_2.

In general, it can be stated that a series of quasi-steady state conditions develops, if the mineral dissolution fronts move through the solution domain with a front velocity much smaller than the advective transport velocity of the pore water. This is possible, since the minerals present in the aquifer provide a significant "storage capacity" for chemical species [*Lichtner*, 1988, 1996a] and may therefore support dissolution reactions for long time periods. A quasi-steady state condition may develop under equilibrium or kinetically-controlled conditions. The only requirement for a quasi-steady state condition is mass balance between external and internal source and sink terms (see Figure 2.1), characterized by a dynamic equilibrium between heterogeneous reaction processes and physical transport or other heterogeneous reaction processes. Production, consumption, and transport into and away from a specific spatial location are leading to a zero net change in the concentrations of aqueous and gaseous species. Possible examples are:

- Production of a certain species due to dissolution of a mineral, which is offset by the transport of the same quantity of this species away from the zone of dissolution (e.g.: dissolution of gypsum and removal of calcium and sulfate by transport processes).
- Production of a certain species due to the dissolution of a mineral, which is offset by the precipitation of the same amount of this species in form of a secondary mineral (e.g.: dissolution of kaolinite combined with the precipitation of gibbsite and amorphous silica in conjunction with pH-buffering).
- Production of a dissolved gas due to the dissolution of a mineral, which is offset by the exsolution of the gas and the subsequent transport of the gas to the atmosphere (e.g. dissolution of carbonate minerals and exsolution of carbon dioxide).

- Infiltration of a gas into the porous medium, partitioning of the gas to the aqueous phase and reaction of the dissolved gas with a mineral phase; produced dissolved species are transported downstream in the aqueous phase (e.g. infiltration of gaseous oxygen and subsequent pyrite oxidation).

A quasi-steady state condition can be maintained until a mineral phase becomes completely depleted, or until significant changes in porosity or reactive surface area occur. A quasi-steady state is also characterized by slowly changing mineral parameters such as mineral volume fractions and mineral reactive surface areas in case of a kinetic formulation [*Lichtner*, 1988]. Slowly changing mineral parameters have a number of advantages for reactive transport formulations:

- Parameters such as mineral volume fractions and reactive surface areas may be updated explicitly after completion of a time step without introducing a significant error [e.g.: *Steefel and Lasaga*, 1994].
- Changing mineral parameters define the overall time scale of interest in the physico-chemical system; given an appropriate reactive transport formulation, large time steps may be possible.

How long a quasi-steady state condition lasts depends primarily on the mineral quantities actively participating in the heterogeneous reactions. A typical example for a problem dominated by long-lasting quasi-steady states is the geochemical weathering of a rock formation consisting of aluminosilicate minerals [*Lichtner*, 1988]. A problem characterized by rapidly moving mineral dissolution boundaries is often encountered in mine tailings simulations, which involve the dissolution of mineral phases present in trace quantities and the formation and dissolution of secondary mineral phases [e.g. *Walter et al.*, 1994a and 1994b].

2.5 Solution Approaches

The common approaches for the coupled solution of physical transport and geochemical reactions are presented in this section and the advantages and limitations of each method are discussed. The present review is largely based on the comprehensive discussion on this topic by *Steefel and MacQuarrie* [1996]. For simplicity, this review only considers

methods for steady-state flow and constant porosity. The findings should nevertheless be generally applicable. The following topics will be addressed:

- Continuum and mixing cell approaches
- Kinetic, equilibrium and partial equilibrium formulations
- Global implicit and operator-splitting techniques

The efficiency of the various formulations and methods will be addressed in a qualitative sense, based on Peclet, Courant, and Damköhler constraints.

2.5.1 Continuum and Mixing-Cell Approaches

The continuum approach is directly dependent on the REV-concept. Physico-chemical variables are described by functions, which are continuous at the macroscale in space and time [*Bear*, 1972, *Lichtner*, 1996a]. These functions can adequately be expressed in terms of partial differential equations, which take into account transport and reaction processes. The continuum approach therefore allows the description of the interactions of transport and reaction processes in multiple dimensions for a multiphase, multi-species system on a physical basis. Many numerical models of varying complexity and capability have been developed based on this approach [e.g.: *Jennings et al.*, 1982, *Walsh et al.*, 1984, *Cederberg et al.*, 1985, *Lichtner*, 1985, *Förster*, 1986, *Bryant et al.*, 1986, *Reeves and Kirkner*, 1988, *Yeh and Tripathi*, 1991, *Šimůnek and Suarez*, 1994, *Steefel and Lasaga*, 1994, *Walter et al.*, 1994a, *Zysset et al.*, 1994, *Lichtner*, 1996a, *Wunderly et al.*, 1996, *MacQuarrie*, 1997, *Shen and Nikolaidis*, 1997].

The mixing cell approach also makes use of the REV-conceptualization in the sense that each cell is represented by a REV. This method is usually only applied, but not restricted to, one spatial dimension and is explicit in time with respect to the transport processes. Transport and reaction processes are considered sequentially. Therefore, the solution requires small timesteps to obtain a physically correct solution. It should be noted, however, that reactive transport problems can be described adequately with the mixing cell approach [see for example *Morin and Cherry*, 1988, *Appelo and Postma*, 1993, *Prein*, 1994, *van Breukelen et al.*, 1998]. The mixing cell method is in practical terms equivalent to a continuum approach based on a non-iterative operator-splitting method (see Section 2.5.3) and an explicit time integration scheme for transport processes.

2.5.2 Equilibrium, Fully Kinetic and Partial Equilibrium Formulations

A fully-kinetic formulation for reactive transport can be developed based on equations 2.1-2.5 and 2.17-2.19. The advantage of this approach is that it provides the most general description for reactive transport problems, because the fully-kinetic formulation can also be used to describe geochemical equilibrium conditions [*Steefel and MacQuarrie*, 1996]. A model based on a fully-kinetic description with forward and backward reactions will automatically determine if a particular reaction is at equilibrium or not at equilibrium, and information on the relation between transport and reaction time scales is not needed *a priori*. However, a disadvantage of this method is that very rapid kinetically-controlled reactions may significantly increase the stiffness of the system of equations and will therefore increase the difficulty of solving the problem. A stiff system of equations is defined by the simultaneous occurrence of long and short time scales [*Hindmarsh and Petzold*, 1995a]. Very rapid reversible reactions may also lead to numerical inaccuracies due to round-off errors, because a small overall reaction rate is expressed as the difference of large forward and backward reaction rates. A third problem is that each species remains as a primary unknown and the system of equations to be solved might become very large. In the most general case the number of primary unknowns would be : $N_p = N_c + N_x + N_g + N_s + N_m$ at each spatial discretization point. The solution of the resulting large and possibly stiff system of equations might be computationally extremely expensive. Its application is therefore limited to operator-splitting solutions (see Section 2.5.3).

Alternatively, all geochemical reactions may be expressed in terms of equilibrium reactions [*Kirkner and Reeves*, 1988, *Sevougian et al.*, 1993, *Steefel and MacQuarrie*, 1996]. A reactive transport formulation can then be based on equations 2.1-2.5 and 2.10-2.15. This, however, is strictly only possible if the local equilibrium approximation is applicable for all reactions, meaning that the time scale for the slowest reaction is still much shorter than the time scale for the fastest transport process. If an equilibrium formulation is used inappropriately, inaccuracies or even errors are introduced. An equilibrium formulation may provide a more efficient solution algorithm than a kinetic description, because the replacement of kinetic rate expressions by equilibrium relationships decreases the stiffness of the system of equations. On the other hand, this approach increases the nonlinearity of the system of equations, which may adversely affect its convergence properties. A positive side effect is that the number of unknowns describing a reaction network can be greatly reduced using an equilibrium formulation [*van Zeggeren and Storey*, 1970, *Steefel and Lasaga*, 1994, *Steefel and MacQuarrie*, 1996], since each equilibrium relationship,

which replaces a kinetic relationship, can be utilized to eliminate one primary unknown. The number of primary unknowns per spatial discretization point can be decreased to $N_p = N_c$, or even less, if mineral phases are in equilibrium with the solution.

A formulation containing both equilibrium and kinetically-controlled reactions is termed a partial equilibrium approach [*Lichtner*, 1985, *Sevougian et al.*, 1993, *Steefel and Lasaga*, 1994]. A partial equilibrium approach ideally treats fast geochemical processes as equilibrium reactions, while slow processes are described by kinetically-controlled reactions. This formulation can also be based on equations 2.1-2.5; geochemical reactions can be described by equations 2.10-2.15 and 2.17-2.19, depending on the time scales of the reactions in comparison to the transport time scales. This approach requires an *a priori* knowledge of the applicability of the local equilibrium approximation for each reaction. It is practical to group reactions based on their expected Damköhler numbers. For example, it is likely that the local equilibrium assumption is valid for all hydrolysis reactions, which facilitates the use of an equilibrium formulation for these reactions. Time scales characterizing dissolution-precipitation reactions on the other hand may vary widely. Dissolution-precipitation reactions may therefore be described globally as kinetically-controlled reactions [e.g.: *Steefel and Lasaga*, 1994]. This approach benefits from utilizing the advantages of the fully kinetic and the equilibrium formulations. The system of equations can be simplified without affecting the adequacy of the solution. The number of unknowns will range from $N_p = N_c$ to $N_p = N_c + N_x + N_g + N_s + N_m$ dependent on the formulation.

Irreversible reactions can only be handled by fully-kinetic or partial equilibrium formulations. Table 2.2 summarizes the Damköhler constraints for the various reactive transport formulations discussed and define their applicability. Two different Damköhler numbers have to be specified in this context:

- Da_1 is determined by the time scale of the slowest reaction and the time scale of the most rapid transport process.
- Da_2 is determined by the time scale of the fastest reaction and the time scale of the slowest transport process.

Da_2 has to be obeyed only if it is anticipated to resolve the progress of all reactions or if an explicit or partly explicit time discretization is chosen for the computation of the reaction rates.

Method	Damköhler constraints
Equilibrium	$Da_1 \gg 1$ for all reactions
Fully kinetic	$Da_2 < 1$ for all reactions
Partial equilibrium	$Da_1 \gg 1$ for all equilibrium reactions
	$Da_2 < 1$ for all kinetically-controlled reactions

Table 2.2: Comparison of Damköhler constraints for various reactive transport formulations

2.5.3 Coupling Techniques

Two distinct formulations are commonly used for coupling physical transport and geochemical reactions [*Yeh and Tripathi*, 1989, *Steefel and Lasaga*, 1994]: These are the global implicit method or the one-step approach [*Steefel and Lasaga*, 1994], and the operator-splitting formulation, or the two-step approach [*Engesgaard and Christensen*, 1988, *Yeh and Tripathi*, 1989]. The major difference between these methods is that physical transport and geochemical reactions are solved simultaneously using the global implicit method, while the operator-splitting technique considers transport and reactions sequentially. Various methods have been used to solve the system of equations resulting from both formulations. They can be distinguished based on how the fundamental equations for reactive transport problems are combined, how the governing equations are formulated and which variables are chosen as the primary dependent variables [*Yeh and Tripathi*, 1989].

A solution of the global implicit method can be obtained using either the DAE (mixed differential-algebraic equation) approach or the DSA (direct substitution approach) [*Yeh and Tripathi*, 1989]. Chemical reaction expressions are not substituted into the transport equations in case of the DAE approach, but are nevertheless solved simultaneously with the transport equations. This implies that all chemical species are retained as primary unknowns. Alternatively, equilibrium expressions can be substituted directly into the transport equations (DSA approach). This leads to a set of nonlinear partial differential equations, which is solved simultaneously. The latter method can reduce the number of primary dependent variables (primary unknowns) greatly and has become the standard method for the solution of reactive transport problems using the global-implicit method. The resulting system of equations is nonlinear for both methods and is commonly linearized by Newton's method. Examples for the DAE approach are the models by *Miller*

and Benson [1983] and *Lichtner* [1985], while models utilizing the DSA approach have been developed by *Jennings et al.* [1982], *Kirkner and Reeves* [1988], *Steefel and Lasaga* [1994] and *Lichtner* [1996a] among others. The solution procedure for the global implicit method can be expressed symbolically as:

$$\mathbf{c}^{t+\Delta t} = L_G \Delta t + \mathbf{c}^t \tag{2.32}$$

where L_G defines the global operator taking into account both physical transport and geochemical reactions, $\mathbf{c}^{t+\Delta t}$ is the vector of concentrations at the new time level, Δt is the time increment and $\mathbf{c}^t$ is the vector containing the known concentrations at the old time level.

The operator-splitting technique on the other hand solves chemical reactions isolated from the transport equations. The overall problem is divided into two sub-problems which can be described as a physical step and a chemical step [*Walter et al.*, 1994a]. *Walter et al.* [1994a] visualize the solution space as having three degrees of freedom: spatial, chemical and temporal. In the physical step it is assumed that all species are non-reactive or that the reaction rates are constant during a time step. Physical transport can therefore be described by a set of linear partial differential equations, which are only connected in the spatial and temporal domain. Geochemical reactions on the other hand are assumed to be unaffected by transport processes during the time step. The chemical step can be solved using a chemistry operator, which consists of a system of nonlinear algebraic equations in the case of equilibrium reactions or a set of nonlinear ordinary differential equations in the case of a fully-kinetic solution method [*Herzer and Kinzelbach*, 1989]. A partial equilibrium formulation leads to a system of nonlinear mixed differential-algebraic equations. The algebraic and/or kinetic relationships are also solved using an iterative procedure such as Newton's method.

Yeh and Tripathi [1989] discuss various methods for the solution of the two-step problem, which are all based on the SIA (sequential iteration approach). The sequential iteration approach obtains the solution for the physical step and the chemical step sequentially. The two steps are connected by a source and sink term. Iterations between the two steps take place until no further changes are observed in the source and sink terms within a specified tolerance. An alternative method commonly used is the sequential non-iterative approach (SNIA), whereby iteration between the physical and chemical steps does not take place [e.g. *Walter et al.*, 1994a].

The operators can be coupled in different ways when employing the two-step method [*Zysset et al.*, 1994, *Barry et al.*, 1996, *Kaluarachichi and Morshed*, 1995, *Steefel and MacQuarrie*, 1996, *MacQuarrie*, 1997]. Defining L_T as the transport operator and L_C as the chemistry operator allows the symbolic representation of the coupling schemes. The non-iterative coupling scheme is presented here. The concentrations at the new time level $t + \Delta t$ can be obtained using the sequence [e.g.: *Miller and Rabideau*, 1993, *Barry et al.*, 1996, *Kaluarachichi and Morshed*, 1995]:

$$\mathbf{c}^{t+\Delta t} = L_C \Delta t + L_t \Delta t + \mathbf{c}^t \tag{2.33}$$

The chemical step, which is defined by $L_C \Delta t$, can be replaced by the operator $L_C^{eq} \delta t + \Delta t$ [*Walter et al.*, 1994a] if all geochemical reactions are described by equilibrium relationships, because the solution of an equilibrium system is by definition independent of the time interval Δt. An alternative coupling method is the so-called Strang-splitting [e.g.: *Zysset et al.*, 1994, *MacQuarrie*, 1997]:

$$\mathbf{c}^{t+\Delta t} = L_C \frac{\Delta t}{2} + L_t \Delta t + L_C \frac{\Delta t}{2} + \mathbf{c}^t \tag{2.34}$$

The coupling of the operators according to equations 2.33 and 2.34 can also be applied for SIA methods [*Yeh and Tripathi*, 1989, *Walter et al.*, 1994a, *Zysset et al.*, 1994]. Examples for models based on the two-step method are the models developed by *Walsh et al.* [1984], *Cederberg et al.* [1985], *Cederberg et al.* [1985], *Bryant et al.* [1986], *Brand et al.* [1994], *Walter et al.* [1994a] and *Zysset et al.* [1994].

For complex systems the splitting of operators is often not restricted to the classical sequence of transport and chemistry, but may include several operators [e.g. *Narasimhan et al.*, 1986, *Liu and Narasimhan*, 1989a, *Wunderly et al.*, 1996, *Gerke et al.*, 1998].

2.5.4 Advantages and Disadvantages of Coupling Methods

Several authors have discussed the advantages and limitations of the common coupling methods [*Engesgaard and Christensen*, 1988, *Yeh and Tripathi*, 1989, *Mangold and Tsang*, 1991, *Steefel and Lasaga*, 1994, *Walter et al.*, 1994a]. Advantages of the two-step method are primarily that individual routines are exchangeable and that it is possible to use existing transport programs and geochemical equilibrium models [*Steefel and Lasaga*, 1994, *Walter et al.*, 1994a]. The memory and computational requirements are usually less than

those for the global implicit method, since the large Jacobian matrix which is generated by the global implicit method is replaced by several smaller systems of equations, which can be solved sequentially [*Yeh and Tripathi*, 1989, *Steefel and Lasaga*, 1994]. Additional advantages are that rapid local geochemical changes affect the convergence properties of the system of equations only locally and that the time integration scheme and the time increments for the transport and the chemistry operator can be chosen independently.

On the other hand, advantages of the one-step method are that all processes are treated simultaneously in time, physical space and chemical reaction space and that the method is mass-conservative. Errors introduced due the splitting of the operators do not occur. The existing framework allows the consideration of additional reaction processes in an implicit manner. The global implicit method may allow large time steps [*Steefel and Lasaga*, 1994], while operator-splitting methods are limited to small Courant numbers to ensure a physically meaningful solution and to control the splitting error.

Advantages and disadvantages of either method are still being debated in the literature, *Yeh and Tripathi* [1989], for example, strongly favor the two-step method and state that global implicit approaches (DSA or DAE), even using modern iterative solvers for sparse matrices, are only applicable for one-dimensional simulations as a research tool. The primary limitation is caused by the large Jacobian matrix arising from the global implicit approach, requiring excessive storage requirements and computational effort [*Yeh and Tripathi*, 1989]. These statements, on the other hand, lose their relevance in times of increasing computational power and memory capacity. The choice of the solution algorithm should rather be determined by accuracy considerations. In this case, both methods have advantages, i.e. the operator-splitting method allows a more accurate transport solution [*Steefel and Lasaga*, 1994], while the one-step method avoids numerical dispersion or mass balance errors introduced by the splitting of the operators.

Several comparisons between the different operator-splitting techniques have been carried out previously [*Zysset et al.*, 1994, *Miller and Rabideau*, 1993, *MacQuarrie*, 1997] with the result that Strang-splitting leads to more accurate results than the ordinary operator-splitting defined in equation 2.33. Theoretical studies to estimate the error of various operator-splitting techniques have been conducted by *Barry et al.* [1996], *Kaluarachichi and Morshed* [1995], *Morshed and Kaluarachichi*, 1995, *Valocchi and Malmsted* [1992] and *Hundsdorfer and Verwer* [1991]. These studies show that operator-splitting introduces an inherent error which influences the mass balance and the concentration distributions in the solution domain. The operators can be coupled sequentially, in which

case each operator is applied to the concentrations obtained from the previous operator, or in a parallel mode, in which case each operator is applied to the concentrations from the previous time level. The sequential coupling tends to introduce mass balance errors, while the parallel coupling commonly leads to additional numerical dispersion [*Barry et al.*, 1996]. *Wheeler and Dawson* [1987] provided a mathematical proof for the convergence of operator-splitting methods. Direct comparisons between the global implicit or one-step approach and operator-splitting techniques are rather rare [e.g. *Hundsdorfer and Verwer*, 1991, *Leeming et al.*, 1998] and are restricted to simple systems. All these studies essentially agree that operator-splitting methods, with or without iteration, can be used to describe reactive transport adequately, if the temporal discretization is kept within certain constraints.

In general, the performance and applicability of the various solution methods can be estimated based on Peclet, Courant and Damköhler criteria: Whether a Peclet constraint has to be obeyed depends essentially on the spatial weighting for the advective term [*Unger et al.*, 1996]. Common spatial weighting methods are centered spatial weighting, upstream weighting and a number of flux limiter schemes [*Unger et al.*, 1996, *Cirpka*, 1997]. Centered spatial weighting requires that $Pe < 2$ [e.g. *Daus et al.*, 1985, *Unger et al.*, 1996]. Peclet constraints are not required for upstream weighting or flux limiter schemes. Upstream weighting has the disadvantage that it introduces additional numerical dispersion and therefore decreases the accuracy of the solution. Flux limiter schemes, on the other hand, provide the same or even better accuracy than central spatial weighting, but have the disadvantage of introducing additional nonlinearity into the system of equations. These findings are valid independent of the coupling method and affect both the global implicit and the operator-splitting formulations.

Temporal discretization, on the other hand, affects the various solution methods in different ways. For example, an advective Courant number of $Cr < 2Pe/(2 + Pe)$ is required regardless of the coupling method, if Crank-Nicolson time weighting is employed in combination with upstream weighting for the advective terms [*Unger et al.*, 1996]. Fully implicit time weighting, on the other hand, is not subject to this constraint and allows the use of large time steps for physical transport at the cost of decreased accuracy. For the sake of efficiency, it is nevertheless often practical to use implicit time weighting. A necessary requirement for non-iterative operator-splitting methods using implicit time-weighting is to restrict advective and diffusive Courant numbers (equations 2.28 and 2.29) to values $Cr < 1$. If this constraint is not obeyed, dissolved or gaseous species are

Method	Pe	Cr	Preferred applications
Global implicit Fully implicit time weighting, centered spatial weighting for advective term	< 2	-	Slowly moving dissolution-precipitation fronts, Quasi-steady state problems
Global implicit Fully implicit time weighting, upstream weighting for advective term [1)]	-	-	
Operator splitting - SIA Crank-Nicolson time weighting, centered spatial weighting for advective term	< 2	< 1	Rapid changes in geochemical composition, e.g.: Heterogeneous reactions between aqueous and solid phase, resolution limited by spatial discretization, rapidly moving, multiple dissolution-precipitation fronts
Operator splitting - SIA Fully implicit time weighting, upstream weighting for advective term[1)]	-	-[2)]	
Operator splitting - SNIA Crank-Nicolson time weighting, centered spatial weighting for advective term	< 2	$\ll 1$	
Operator splitting - SNIA Fully implicit time weighting, upstream weighting for advective term[1)]	-	$\ll 1$[3)]	

1) also valid for high resolution flux limiter schemes
2) No Courant constraint from a theoretical point of view, practical applications will likely exhibit poor convergence properties
3) Courant constraint imposed by interactions between transport and reactions.

Table 2.3: Comparison of Peclet and Courant constraints for various coupling schemes under consideration of variable spatial and time weighting and preferred applications

transported farther than one grid interval within a single time step without accounting for the reaction processes that may consume or produce the transported species. In this case, the use of a non-iterative operator-splitting method may introduce significant errors. The time increment for non-iterative operator-splitting solutions is therefore in practical applications limited to values which yield advective and diffusive Courant numbers $Cr \ll 1$. If an iterative operator splitting method is used, it is from a theoretical point of view not necessary to obey advective or diffusive Courant criteria of $Cr < 1$. However, it can be envisaged that the convergence behavior of iterative operator-splitting techniques may be strongly impaired under such conditions. Time step sizes for these methods are therefore also limited.

Global implicit solution methods are not affected by a Courant constraint as long as

fully implicit time weighting is used, because physical transport and geochemical reactions are considered simultaneously. A Courant constraint is only imposed on a global implicit method if the time weighting contains an explicit term (e.g. Crank-Nicolson time weighting). This, however, is not practical for global implicit methods, because reactions characterized by short time scales cannot be handled by a time discretization other than fully implicit. An explicit or partly explicit time weighting would require satisfying an additional constraint based on the "geochemical reaction number" defined by equation 2.30. $Cr_r < 1$ can be defined as a stringent requirement for time discretizations that include an explicit term.

The global implicit method allows a coarse temporal discretization if the transport time scale is much shorter than the time scale for mineralogical changes. This condition allows the development of a quasi-steady state, as was previously discussed. The change in mineralogical parameters controls the geochemical evolution of the system during periods of quasi-steady state rather than changes in aqueous concentrations or gaseous concentrations. From a theoretical point of view a coarse temporal discretization is possible, even if a quasi-steady state does not prevail. However, time step sizes are often limited in practical applications by the inherent nonlinearity of the system of equations. Table 2.3 summarizes the Peclet and Courant constraints for the different solution methods and outlines applications that suit each method best.

Chapter 3

Theoretical Development

This chapter introduces the governing equations of the MIN3P model. The global implicit approach [*Steefel and Lasaga*, 1994] has been chosen for the solution of the reactive transport equations in variably-saturated media. This approach allows the most appropriate description of the interactions of physical transport and geochemical reactions, because all processes are considered simultaneously. The method also ensures a locally and globally mass-conservative solution. Firstly, the fundamental assumptions regarding the present development are discussed and the governing equations for variably-saturated flow are reviewed briefly. The governing equations for multicomponent reactive transport in variably-saturated media are derived from the fundamental equations presented in Chapter 2. The formulation of the geochemical reactions included in the model is presented. Reactions include aqueous complexation and oxidation-reduction reactions, which can be described as equilibrium or kinetically-controlled reactions, equilibrium gas dissolution-exsolution, ion exchange reactions, and kinetically-controlled dissolution-precipitation reactions. A new, general formulation for homogeneous and heterogeneous kinetically-controlled reactions has been developed and is discussed in more detail.

3.1 Simplifying Assumptions

In its most general formulation, a multiphase-multicomponent reactive transport model should be based on a compositional approach that considers the movement of groundwater and soil gas and the transport of dissolved and gaseous constituents within these

phases simultaneously with geochemical reactions. Compositional models for the simulation of groundwater contamination involving non-aqueous phase liquids have been developed by *Corapcioglu and Baehr* [1987], *Forsyth and Shao* [1991], *Sleep and Sykes* [1993] and *Unger et al.* [1995]. To date, the compositional approach has not been applied to multicomponent-multiphase reactive transport problems. The solution approach commonly used for multicomponent reactive transport is based on the decoupling of groundwater flow and reaction-transport processes and is also adopted in the present research. This simplification can be justified easily for saturated problems, where the movement of groundwater is not affected by the presence of a gas phase. This decoupling has, however, much more pronounced effects on multicomponent reactive transport in variably-saturated media, where both the aqueous and the gaseous phase are mobile.

The transport of gases in the unsaturated zone is in the most general case governed by equations that consider the combined effect of Knudsen diffusion, molecular and non-equimolar diffusion and advective gas transport [*Massmann and Farrier*, 1992, *Thorstenson and Pollock*, 1989]. The examples of *Thorstenson and Pollock* [1989] and *Massmann and Farrier* [1992] show that advective and diffusive transport are the most important transport processes, while Knudsen diffusion and non-equimolar diffusion do not contribute significantly in most applications. Advective gas transport is, unlike groundwater flow, directly influenced by diffusive gas transport and geochemical reaction processes. Geochemical reactions and diffusive gas transport are, in turn, directly affected by advective gas transport. Advective gas transport processes have been neglected in the present research, because an appropriate description of this inherent coupling is seemingly impossible with the chosen approach. A reactive transport model, which explicitly couples multiphase flow and multicomponent reactive transport can be useful for problems where the effect of geochemical reactions on advective gas transport can be neglected [*Lichtner*, 1996a]. The formulation of the present model is based on the assumption that the transport of pore gas can be described as a Fickian diffusion process. *Thorstenson and Pollock* [1989] showed that the description of gas transport as a Fickian process is usually a good approximation for reactive gases such as oxygen and carbon dioxide, if the concentration gradients of non-reactive gases contained in the soil atmosphere, e.g. nitrogen remain primarily unaffected. However, reaction-induced advective fluxes may become important whenever a large amount of gas is produced or consumed in the subsurface [*Thorstenson and Pollock*, 1989].

The omission of advective gas transport also implies that the effect of the gas phase

on groundwater movement must be negligible. This means, in practical terms, that the pressure in the gaseous phase will not affect the pressure distribution in the aqueous phase. *Forsyth* [1988] has conducted a comparison between two-phase and single-phase models for unsaturated groundwater flow and has shown that a two-phase approach is not needed to describe the movement of pore water adequately for many cases. It should be possible to apply the single phase formulation, as long as the gaseous phase does not become entrapped and the gas pressures are not influenced significantly by an internal pressure source.

The present model formulation allows for transient groundwater flow conditions, which leads to changes in phase saturations and may subsequently induce significant advective gas transport. The effect of the saturation changes have been taken into account in the present model formulation to yield a mass-conservative solution. Non-physical results may nevertheless be obtained, since advective gas transport processes have been neglected. The application of the model to transient flow conditions should be possible regardless, if the time scales for geochemical reactions involving the gases and the time scale of diffusive gas transport are much shorter than the time scale for the saturation changes.

Furthermore, it was assumed that geochemical reaction processes do not cause significant porosity changes, which could affect the medium's permeability. The model formulation also neglects density effects and assumes that isothermal conditions prevail. However, the exclusion of these processes is not a necessary requirement. For example, the feed-back of geochemical reactions on the flow regime can be included, if an appropriate permeability-porosity relationship is provided [*Ortoleva et al.*, 1987a and 1987b, *Steefel and Lasaga*, 1994, *Lichtner*, 1996a].

Based on these assumptions, the governing equations for multicomponent reactive transport in variably-saturated media consist of a mass conservation equation for water under variably-saturated conditions (Richard's equation), and a set of nonlinear transport equations coupled with geochemical reactions.

3.2 Variably-Saturated Flow

Using hydraulic head as the primary dependent variable and adopting the assumptions defined by *Neuman* [1973] and *Huyakorn et al.* [1984] (incompressible fluid, no hysterysis, passive air phase), the mass conservation equation for the aqueous phase can be written

as [*Neuman*, 1973, *Panday et al.*, 1993]

$$S_a S_s \frac{\partial h}{\partial t} + \phi \frac{\partial S_a}{\partial t} - \nabla \cdot [k_{ra} \mathbf{K} \nabla h] - Q_a = 0, \tag{3.1}$$

where a identifies the aqueous phase, t [s] is time, ϕ stands for porosity [m^3 void m^{-3} bulk], S_a is the saturation of the aqueous phase [m^3 water m^{-3} void], S_s defines the specific storage coefficient [m^{-1}] and k_{ra} is the relative permeability of the porous medium with respect to the aqueous phase [-]. h [m] is the hydraulic head, and Q_a is a source-sink term for the aqueous phase [s^{-1}], where a positive quantity defines the injection of water. $\mathbf{K}$ is the hydraulic conductivity tensor [m s^{-1}], which is defined by

$$\mathbf{K} = \frac{\rho_a g}{\mu_a} \mathbf{k}, \tag{3.2}$$

where ρ_a is the density of the aqueous phase [kg m^{-3}], g [m s^{-2}] is the gravitational acceleration vector, μ_a [kg m^{-1} s^{-1}] is the viscosity of the aqueous phase and $\mathbf{k}$ is the intrinsic permeability tensor [m^2]. The pressure head of the aqueous phase ψ_a [m] can be obtained using

$$\psi_a = h - z,$$

where z [m] defines the elevation with respect to a given datum.

Equation 3.1 is nonlinear, since the saturation and the relative permeability are a function of the aqueous phase pressure. Relationships given by *Wösten and van Genuchten* [1988] are used to describe these dependencies:

$$S_a = S_{ra} + \frac{1 - S_{ra}}{(1 + \alpha \psi_a^n)^m} \tag{3.3}$$

$$k_{ra} = S_{ea}^l \left[1 - \left(1 - S_{ea}^{1/m} \right)^m \right]^2 \tag{3.4}$$

The relative permeability k_{ra} is here conveniently expressed as a function of saturation S_a. S_{ra} [-] defines the residual saturation of the aqueous phase, α, n, m and l are the soil hydraulic function parameters, and m is defined by:

$$m = 1 - \frac{1}{n}$$

S_{ea} is the effective saturation of the aqueous phase and is given by:

$$S_{ea} = \frac{S_a - S_{ra}}{1 - S_{ra}}$$

3.3 Multicomponent Reactive Transport

The mass conservation equations for reactive transport in variably-saturated media consist of relationships describing the transport of aqueous and gaseous species under the influence of homogeneous and heterogeneous geochemical reactions. The formulation of the present model is based on a partial equilibrium approach [*Lichtner*, 1985, *Sevougian et al.*, 1993, *Steefel and Lasaga*, 1994], which contains geochemical equilibrium reactions as well as homogeneous and heterogeneous kinetic reactions. The global mass conservation equations can be derived based on the fundamental equations for reactive transport, which have been introduced in Chapter 2, Section 2.3. The mass conservation equations for N_c aqueous species, which are also components, are defined by equations 2.1. These equations are here restated as a starting point for the derivation of the present model formulation

$$\frac{\partial}{\partial t}[S_a\phi C_j^c] - \nabla\cdot[\mathbf{v}_a C_j^c] + \nabla\cdot[S_a\phi\mathbf{D}_a\nabla C_j^c] - Q_j^c = 0 \qquad j = 1, N_c,$$

where C_j^c defines the concentration of the j^{th} component as species in solution [mol l^{-1} water]. The Darcy flux vector $\mathbf{v}_a$ [m s^{-1}] can be obtained from the solution of equation [3.1] and is given by

$$\mathbf{v}_a = \frac{\mathbf{K}k_{ra}\rho_a g}{\mu_a}\nabla h. \tag{3.5}$$

The hydrodynamic dispersion tensor $\mathbf{D_a}$ is given by [*Bear*, 1972, *Bugner*, personal communication, 1985, *Burnett and Frind*, 1987, *Forsyth et al.*, 1998]

$$S_a\phi D_{a,xx} = \alpha_l\frac{v_{a,x}}{\bar{v}} + \alpha_{th}\frac{v_{a,y}}{\bar{v}} + \alpha_{tv}\frac{v_{a,z}}{\bar{v}} + S_a\phi\tau_a D_a^* \tag{3.6}$$

$$S_a\phi D_{a,yy} = \alpha_{th}\frac{v_{a,x}}{\bar{v}} + \alpha_l\frac{v_{a,y}}{\bar{v}} + \alpha_{tv}\frac{v_{a,z}}{\bar{v}} + S_a\phi\tau_a D_a^* \tag{3.7}$$

$$S_a\phi D_{a,zz} = \alpha_{tv}\frac{v_{a,x}}{\bar{v}} + \alpha_{tv}\frac{v_{a,y}}{\bar{v}} + \alpha_l\frac{v_{a,z}}{\bar{v}} + S_a\phi\tau_a D_a^* \tag{3.8}$$

$$S_a\phi D_{a,yx} = S_a\phi D_{a,xy} = (\alpha_l - \alpha_{th})\frac{v_{a,x}v_{a,y}}{\bar{v}} \tag{3.9}$$

$$S_a\phi D_{a,zx} = S_a\phi D_{a,xz} = (\alpha_l - \alpha_{tv})\frac{v_{a,x}v_{a,z}}{\bar{v}} \tag{3.10}$$

$$S_a\phi D_{a,zy} = S_a\phi D_{a,yz} = (\alpha_l - \alpha_{tv})\frac{v_{a,y}v_{a,z}}{\bar{v}}, \tag{3.11}$$

where $v_{a,x}$, $v_{a,y}$ and $v_{a,z}$ define the components of the aqueous phase velocity in x, y and z-direction, respectively. $\bar{v}$ is the magnitude of the aquoeus phase velocity, α_l is the longitudinal dispersivity, while α_{th} and α_{tv} define the transverse horizontal and transverse vertical dispersivities in of the porous medium. D_a^* is an averaged free liquid diffusion coefficient used for all dissolved species [m^2 s^{-1}] and τ_a is the tortuosity of the medium [-]. The tortuosity τ_a is given by the semi-empirical expression [*Millington*, 1959],

$$\tau = S_a^{7/3}\phi^{1/3}, \tag{3.12}$$

and describes the dependency of the effective diffusion coefficient on the phase saturation and the porosity of the porous medium.

The source-sink term Q_j^c can be subdivided into contributions originating from internal and external sources and sinks:

$$Q_j^c = Q_j^{c,int} + Q_j^{c,ext} \qquad j = 1, N_c \tag{3.13}$$

External sources and sinks are caused by mass fluxes across the domain boundary while internal sources and sinks are caused by geochemical reactions and can be attributed to equilibrium or kinetically-controlled reactions:

$$Q_j^{c,in} = Q_j^{c,int,eq} + Q_j^{c,int,kin} \qquad j = 1, N_c \tag{3.14}$$

The equilibrium source-sink term contains contributions from homogeneous and heterogeneous reactions:

$$Q_j^{c,in,eq} = Q_j^{c,int,eq,hom} + Q_j^{c,int,eq,het} \qquad j = 1, N_c \tag{3.15}$$

Homogeneous reactions include equilibrium-controlled aqueous complexation and oxidation-reduction reactions according to equations 2.6, while heterogeneous reactions encompass gas dissolution-exsolution reactions according to equations 2.7 as well as reactions at the solid-solution interface. Reactions at the solid-solution interface are here limited to ion exchange reactions according to equations 2.8. Mass conservation equations for the complexed species A_i^x, the gaseous species A_i^g, and the adsorbed species A_i^s are given by equations 2.2, 2.3 and 2.4. The internal contributions to the source and sink terms of equations 2.2-2.4 can be related to the equilibrium source sink term $Q_j^{c,int,eq}$ based on

the reaction stoichiometry defined in equations 2.6-2.8:

$$Q_j^{c,int,eq} = -\sum_{i=1}^{N_x} \nu_{ij}^x Q_i^{x,int} - \sum_{i=1}^{N_g} \nu_{ij}^g Q_i^{g,int} - \sum_{i=1}^{N_s} \nu_{ij}^s Q_i^{s,int} \qquad j = 1, N_c \tag{3.16}$$

Equation 3.16 can be used to substitute the mass conservation equations 2.2-2.4 into the mass conservation equations for the components as species in solution. This substitution leads to the elimination of $N_x + N_g + N_s$ primary unknowns from the system of equations. A global mass conservation equation for the components A_j^c can then be written as:

$$\begin{aligned}
&\frac{\partial}{\partial t}[S_a \phi C_j^c] + \sum_{i=1}^{N_x} \nu_{ij}^x \frac{\partial}{\partial t}[S_a \phi C_i^x] + \sum_{i=1}^{N_g} \nu_{ij}^g \frac{\partial}{\partial t}[S_g \phi C_i^g] + \sum_{i=1}^{N_s} \nu_{ij}^s \frac{\partial C_i^s}{\partial t} \\
&+\nabla \cdot [\mathbf{v_a} C_j^c] - \nabla \cdot [S_a \phi \mathbf{D}_a \nabla C_j^c] \\
&+\sum_{i=1}^{N_x} \nu_{ij}^x \nabla \cdot [\mathbf{v}_a C_i^x] - \sum_{i=1}^{N_x} \nu_{ij}^x \nabla \cdot [S_a \phi \mathbf{D}_a \nabla C_i^x] \\
&-\sum_{i=1}^{N_g} \nu_{ij}^g \nabla \cdot [S_g \phi \mathbf{D}_g \nabla C_i^g] \\
&-Q_j^{a,int,kin} - Q_j^{ext} = 0 \qquad j = 1, N_c
\end{aligned} \tag{3.17}$$

The advective transport term for the gaseous species has been omitted when substituting equation 2.3 into the mass conservation equation for the components as species in solution based on the assumptions made in Section 3.1. The external source and sink term in equation 3.17 contains now the contributions of all mobile species and is defined by:

$$Q_j^{ext} = Q_j^{c,ext} + \sum_{i=1}^{N_x} \nu_{ij}^x Q_i^{x,ext} + \sum_{i=1}^{N_g} \nu_{ij}^g Q_i^{g,ext} \qquad j = 1, N_c \tag{3.18}$$

Because the gas phase is assumed to be passive, the relationship

$$S_g = 1 - S_a \tag{3.19}$$

can be used to obtain the gas phase saturations S_g. The dispersion tensor for the gaseous

phase includes only contributions from diffusion, since advective transport is neglected:

$$S_g\phi D_{g,xx} = S_g\phi\tau_g D_g^\star \tag{3.20}$$

$$S_g\phi D_{g,yy} = S_g\phi\tau_g D_g^\star \tag{3.21}$$

$$S_g\phi D_{g,zz} = S_g\phi\tau_g D_g^\star \tag{3.22}$$

$D_g^\star$ defines an average free phase diffusion coefficient in air, which is applied to all gaseous species. The tortuosity of the gas filled pore space is defined analogous to the aqueous phase according to equation 3.12.

The governing equations 3.17 for reactive transport can be simplified by expressing the concentrations of all aqueous species in terms of total aqueous component concentrations T_j^a [mol l^{-1} water] [*Kirkner and Reeves*, 1988, *Steefel and Lasaga*, 1994, *Lichtner*, 1996a]:

$$T_j^a = C_j^c + \sum_{i=1}^{N_x} \nu_{ij}^x C_i^x \tag{3.23}$$

The gas concentrations can be related to the components by defining the total gaseous component concentrations T_j^g [mol l^{-1} gas] [*Lichtner*, 1996a]:

$$T_j^g = \sum_{i=1}^{N_g} \nu_{ij}^g C_i^g \tag{3.24}$$

A corresponding relationship can be defined for the adsorbed species in terms of total sorbed component concentrations T_j^s [mol l^{-1} bulk]:

$$T_j^s = \sum_{i=1}^{N_s} \nu_{ij}^s C_i^s \tag{3.25}$$

Equation 3.17 can then be written as:

$$\begin{aligned}&\frac{\partial}{\partial t}[S_a\phi T_j^a] + \frac{\partial}{\partial t}[S_g\phi T_j^g] + \frac{\partial T_j^s}{\partial t} \\ &\quad +\nabla\cdot[v_a T_j^a] - \nabla\cdot\left[S_a\phi\mathbf{D}_a\nabla T_j^a\right] - \nabla\cdot\left[S_g\phi\mathbf{D}_{gi}\nabla T_j^g\right] \\ &\quad -Q_j^{a,int,kin} - Q_j^{ext} = 0 \qquad j = 1, N_c\end{aligned} \tag{3.26}$$

All internal source and sink terms due to equilibrium reactions have been elimi-

nated from the system of equations, $Q_j^{a,int,kin}$, which defines the production or consumption of a component due to homogeneous and heterogeneous kinetically-controlled reactions, remains as the last internal source-sink term. The consumption or production of components due to intra-aqueous reactions can be defined based on the reaction rates given by equation 2.17 for the simple case of reversible, elementary reactions. Heterogeneous reactions are here limited to kinetically-controlled dissolution-precipitation reactions. When dissolution-precipitation reactions can be considered elementary reversible reactions, equations 2.19 can be used to define the source and sink terms. Kinetically-controlled gas dissolution-exsolution and adsorption reactions are not considered here. The internal source and sink term due to kinetically-controlled reactions can be expressed as

$$Q_j^{a,int,kin} = Q_j^{a,a} + Q_j^{a,m} \qquad j = 1, N_c, \tag{3.27}$$

where $Q_j^{a,a}$ is the source-sink term due to kinetically-controlled intra-aqueous reactions and $Q_j^{a,m}$ is the source-sink term due to kinetically-controlled mineral dissolution-precipitation reactions. It should be pointed out that the form of the kinetic relationships may vary and is not restricted to the simple relationships defined by equations 2.17 and 2.19. A detailed discussion of the homogeneous and heterogeneous rate expressions considered in the present model development is given in Section 3.4. The source-sink terms $Q_j^{a,a}$ and $Q_j^{a,m}$ are also defined in this context. Substituting equation 3.27 into equation 3.26 leads to a system of global mass conservation equations for reactive transport in variably-saturated media, which contains the contributions from all mobile, adsorbed and mineral species:

$$\begin{aligned} &\frac{\partial}{\partial t}[S_a \phi T_j^a] + \frac{\partial}{\partial t}[S_g \phi T_j^g] + \frac{T_j^s}{\partial t} \\ &\quad + \nabla \cdot [v_a T_j^a] - \nabla \cdot \left[S_a \phi \mathbf{D}_a \nabla T_j^a\right] - \nabla \cdot \left[S_g \phi \mathbf{D}_i \nabla T_j^g\right] \\ &\quad - Q_j^{a,a} - Q_j^{a,m} - Q_j^{ext} = 0 \qquad j = 1, N_c \end{aligned} \tag{3.28}$$

To complete the system of governing equations, an additional set of mass conservation equations has to be defined, which describes the change of mineral quantities over time [*Steefel and Lasaga*, 1994]:

$$\frac{d\varphi_i}{dt} = 10^{-3} V_i^m R_i^m \qquad i = 1, N_m \tag{3.29}$$

where φ_i is the volume fraction of the i^{th} mineral [m^3 mineral m^{-3} bulk], V_i^m is the molar volume of the i^{th} mineral [cm^3 mol^{-1}], R_i^m is the overall dissolution-precipitation rate for the i^{th} mineral [mol l^{-1} bulk s^{-1}] and 10^{-3} is a unit conversion factor [l cm^{-3}].

The nonlinear mass conservation equations 3.28 have a form similar to those given by *Kirkner and Reeves* [1988], *Steefel and Lasaga* [1994] and *Lichtner* [1996a] and are written in terms of total aqueous, gaseous and sorbed component concentrations with the components as species in solution as primary unknowns, the units of each term in equations 3.28 are [mol l^{-1} bulk s^{-1}]. Equations 3.29 have the units [m^3 mineral m^{-3} bulk s^{-1}]. Functional relationships describing the secondary variables C_i^x, C_i^g, C_i^s, as well as the source-sink terms $Q_j^{a,a}$ and $Q_j^{a,m}$ are defined in Section 3.4.

3.4 Geochemical Reactions

3.4.1 Master Variables

The master variables pH, ionic strength, E_H and pe can be used to characterize the geochemical conditions in the aqueous phase. Appropriate relationships defining these master variables are given in the following paragraphs. The computation of pH and the ionic strength are straightforward, while the computation of E_H and pe are dependent on the solution approach for oxidation-reduction reactions. For a discussion on the common solution approaches, it is referred to the recent reviews of *Liu and Narasimhan* [1989a] and *Engesgaard and Kipp* [1992].

pH The pH is defined as the negative value of the logarithm of the proton activity and can be calculated according to:

$$\mathrm{pH} = -\log\{\mathrm{H}^+\} \tag{3.30}$$

Ionic Strength The relationship for ionic strength is given by

$$I = 1/2 \sum_{Z_i \neq 0} Z_i^2 C_i^d, \tag{3.31}$$

where C_i^d is the concentration of the dissolved species A_i^d and Z_i [meq $mmol^{-1}$] defines the charge of the dissolved species A_i^d.

pe and Eh The following solution approaches are implemented into the present model:

- external approach
- dissolved oxygen gas approach
- dissolved hydrogen gas approach
- redox couples approach
- kinetic approach

The external approach, using the electron activity as the redox master variable [*Liu and Narasimhan*, 1989a], is implemented because it is the most convenient method when dealing with oxidation-reduction reactions for equilibrium systems and because it performs well under most conditions (see also Chapter 4). At this point it should be pointed out that this method is only applicable if redox-active species are not influenced by kinetically-controlled reaction processes. Also, this approach cannot be applied to unsaturated conditions in the presence of mobile, redox-active gases.

The dissolved oxygen gas approach is essentially equivalent to the oxygen fugacity approach as reported by *Liu and Narasimhan* [1989a] and used by *Wolery et al.* [1990] with the only difference that dissolved oxygen is used as the redox master variable instead of gaseous oxygen. Dissolved oxygen was selected as a possible redox master variable because it is a useful parameter to represent geochemical conditions in variably-saturated media when atmospheric oxygen is able to enter the subsurface.

Dissolved hydrogen gas on the other hand has been included as an optional redox master variable because it can be a useful parameter in anaerobic environments to delineate zones of bacterial activity [*Lovley and Goodwin*, 1988].

Equilibrium exists between the various redox couples for all three methods discussed, and the system is characterized by a unique oxidation-reduction potential. Values for E_H and pe can be calculated by applying the Nernst equation. The computation of the pe is straightforward if the electron is chosen as the redox master variable. In this case the pe is defined as the negative value of the logarithm of the electron activity:

$$\mathrm{pe} = -\log\{\mathrm{e}^-\} \tag{3.32}$$

If dissolved oxygen or dissolved hydrogen gas are chosen as the redox master variables, it is most intuitive to express the oxidation-reduction potential in terms of the corresponding half-reactions. The half-reactions for the reduction of dissolved oxygen and the oxidation of dissolved hydrogen gas are given by:

$$\tfrac{1}{4}O_2(aq) + H^+ + e^- \rightleftharpoons \tfrac{1}{2}H_2O \tag{3.33}$$

$$H^+ + e^- \rightleftharpoons \tfrac{1}{2}H_2(aq) \tag{3.34}$$

The equilibrium-pe for the dissolved oxygen gas approach and the dissolved hydrogen gas approach can be calculated based on:

$$pe = logK_{O_2(aq)} - pH + \tfrac{1}{4}log\{O_2(aq)\} - \tfrac{1}{2}log\{H_2O\} \tag{3.35}$$

$$pe = logK_{H_2(aq)} - pH - \tfrac{1}{2}log\{H_2(aq)\} \tag{3.36}$$

The E_H can simply be calculated based on the pe according to:

$$E_H = ln10\frac{RT}{F}pe \tag{3.37}$$

The redox couples approach treats each member of a redox couple as a component [*Liu and Narasimhan*, 1989a], giving rise to a mass conservation equation for each member of the redox couple. This approach does not enforce equilibrium between the redox couples [*Allison et al.*, 1991]. The kinetic approach allows, by definition, for disequilibrium between the various redox couples. A unique oxidation-reduction potential cannot be defined for both approaches.

3.4.2 Activity Corrections

The formulation for activity corrections for all dissolved species has been adopted from the thermodynamic equilibrium model MINTEQA2 [*Allison et al.*, 1991]. Activity coefficients γ_i^d for the charged dissolved species A_i^d, where A_i^d can be either a component as species in solution or an aqueous complex, are calculated based on the modified Debye-Hückel equation, given by

$$\log \gamma_i^d = \frac{-A_d Z_i^2 I^{1/2}}{1 + B_d a_i I^{1/2}} + b_i I, \tag{3.38}$$

where A_d and B_d are constants, a_i is the ion size parameter, b_i is an ion specific parameter that accounts for the decrease in solvent concentration in concentrated solutions. If a_i is available, but not b_i, equation 3.38 is used with $b_i = 0$. The Davies equation is used as an approximation when the parameter a_i cannot be provided:

$$\log \gamma_i^d = -A_d Z_i^2 \left[\frac{I^{1/2}}{1 + I^{1/2}} - 0.24I \right] \tag{3.39}$$

The activity coefficients for all neutral species excluding water are calculated according to:

$$\log \gamma_i^d = 0.1I \tag{3.40}$$

while the activity correction for water is defined by:

$$\gamma_{H_2O} = 1 - 0.017 \sum_{i=1}^{N_d} C_i^d \tag{3.41}$$

Fugacity corrections for gaseous species have not been considered in this work because partial gas pressures encountered in shallow groundwater systems do not require these corrections [*Lewis and Randall*, 1961, *Stumm and Morgan*, 1996].

3.4.3 Aqueous Complexation and Oxidation-Reduction

Interactions between dissolved species in solution can take place in form of complexation reactions or oxidation-reduction reactions. In this context, complexation reactions encompass hydrolysis reactions and ion pairing, because these reactions can be described using the same mathematical relationships. Complexation reactions are usually characterized by very rapid equilibration times and can, in most cases, be described in terms of equilibrium reactions. An example for an extremely rapid complexation reaction is the dissociation of carbonic acid into bicarbonate and a proton

$$H_2CO_3 \rightleftharpoons HCO_3^- + H^+ \qquad K_1, \tag{3.42}$$

where K_1 defines the equilibrium constant for the reaction. In this case, equilibrium conditions are achieved within 10^{-10} seconds [*Lasaga*, 1981, *Stumm and Morgan*, 1996]. Some complexation reactions may require a kinetic treatment under certain circumstances. For

example, the dissociation of hexamine cobalt(III) in acid solution

$$Co(NH_3)_6^{3+} + 6H^+ \rightleftharpoons Co^{3+} + 6NH_4^+ \qquad K_2, \tag{3.43}$$

requires several days to attain equilibrium [*Stumm and Morgan*, 1996].

Homogeneous oxidation-reduction reactions can also be treated in the same framework as complexation reactions. However, they differ from aqueous complexation reactions in many aspects. A major difference is that the average reaction speed is generally slower for oxidation-reduction reactions. An example is the oxidation of ferrous iron by dissolved oxygen to ferric iron defined by the following reaction stoichiometry

$$Fe^{2+} + \tfrac{1}{4}O_2(aq) + H^+ \rightleftharpoons Fe^{3+} + \tfrac{1}{2}H_2O \qquad K_3, \tag{3.44}$$

where K_3 can be defined as the equilibrium constant under the assumption that the reaction is reversible.

Equilibrium Formulation

A stoichiometric relationship for the dissociation of the aqueous complex A_i^x into components as species in solution can be formulated as:

$$A_i^x \rightleftharpoons \sum_{i=1}^{N_c} \nu_{ij}^x A_i^c \qquad i = 1, N_x \tag{3.45}$$

where ν_{ij}^x is the stoichiometric coefficient of the j^{th} component as species in solution in the i^{th} aqueous complex. Equilibrium complexation reactions can be described by the law of mass action. The set of algebraic equations, describing the dissociation of aqueous complex A_i^x into components as species in solution can be written as:

$$C_i^x = (K_i^x \gamma_i^x)^{-1} \prod_{j=1}^{N_c} (\gamma_j^c C_j^c)^{\nu_{ij}^x} \qquad i = 1, N_x \tag{3.46}$$

where K_i^x is the equilibrium constant for the dissociation of the i^{th} aqueous complex into components as species in solution, γ_i^x is the activity coefficient for the i^{th} aqueous complex and γ_j^c is the the activity coefficient for the j^{th} component as species in solution. The activity coefficients can be calculated according to the relationships given in Section

3.4.2.

Equation 3.46 can also be used for equilibrium-controlled homogeneous oxidation-reduction reactions. The approach is equally applicable if the electron is chosen as the redox master variable. The law of mass action is, in this case, directly applied to the half reaction.

Kinetic Formulation

A general kinetic formulation has been developed to describe the consumption and production of components due to kinetically-controlled homogeneous reactions within the aqueous phase. Reactions that can be described by these kinetic rate expressions encompass aqueous complexation and oxidation-reduction reactions. The reaction stoichiometry for a kinetically-controlled intra-aqueous reaction can be expressed in terms of components as species in solution [*Lichtner*, 1996b]

$$\emptyset \underset{k_i^{ab}}{\overset{k_i^{af}}{\rightleftharpoons}} \sum_{j=1}^{N_c} \nu_{ij}^a A_j^c \quad i = 1, N_a, \tag{3.47}$$

where ν_{ij}^a are the stoichiometric coefficients of the species participating in the reaction and k_i^{af} and k_i^{ab} are the rate constants for the forward and backward reactions respectively. The forward reaction is here defined as the reaction proceeding from the left to the right. Stoichiometric coefficients of species consumed in the forward reaction are in this case negative, while the stoichiometric coefficients of the species produced in the forward reaction are positive. N_a defines the number of kinetically-controlled intra-aqueous reactions. The stoichiometric relationship 3.47 describes a reversible reaction, which is strictly only valid under the assumption that the reaction is elementary [*Lasaga*, 1981, *Stumm and Morgan*, 1996]. In this case, the reaction progress from the left to the right depends on the activities of the species consumed in the forward reaction. The reaction order is determined by the stoichiometric coefficients of these species, because the order of the reaction is the same as the molecularity for elementary reactions [*Lasaga*, 1981, *Stumm and Morgan*, 1996]. A rate expression describing the forward reaction for the i^{th} kinetically-controlled intra-aqueous reaction can be expressed as

$$R_i^{af} = -k_i^{af} \prod_{\nu_{ij}^a < 0} (\gamma_j^c C_j^c)^{-\nu_{ij}^a}, \tag{3.48}$$

where R_i^{af} is the reaction rate of the forward reaction [mol l^{-1} water s^{-1}]. A rate expression for the corresponding backward reaction can be defined as

$$R_i^{ab} = k_i^{ab} \prod_{\nu_{ij}^a > 0} (\gamma_j^c C_j^c)^{\nu_{ij}^a}, \tag{3.49}$$

where R_i^{ab} is the reaction rate of the backward reaction [mol l^{-1} water s^{-1}]. A rate expression which takes into account both forward and backward reaction rates can be written as the sum of rate expressions 3.48 and 3.49:

$$R_i^a = -k_i^{af} \prod_{\nu_{ij}^a < 0} (\gamma_j^c C_j^c)^{-\nu_{ij}^a} + k_i^{ab} \prod_{\nu_{ij}^a > 0} (\gamma_j^c C_j^c)^{\nu_{ij}^a} \tag{3.50}$$

Rate expression 3.50 can be simplified for elementary reactions, because use can be made of the relationship between the rate constants for the forward and backward reactions and the equilibrium constant defined as K_i^a [*Lasaga*, 1981, *Steefel and MacQuarrie*, 1996, see also Chapter 2, Section 2.4.3]:

$$K_i^a = \frac{k_i^{af}}{k_i^{ab}} \tag{3.51}$$

Substituting equation 3.51 into equation 3.50 allows the expression of the reaction rate in terms of the forward rate constant and the equilibrium constant:

$$R_i^a = -k_i^{af} \left[\prod_{\nu_{ij}^a < 0} (\gamma_j^c C_j^c)^{-\nu_{ij}^a} - (K_i^a)^{-1} \prod_{\nu_{ij}^a > 0} (\gamma_j^c C_j^c)^{\nu_{ij}^a} \right] \tag{3.52}$$

This rate expression allows a convenient description of reversible kinetically-controlled elementary reactions. Rate expression 3.52 can alternatively be expressed as [e.g.: *Steefel and MacQuarrie*, 1996]:

$$R_i^a = -k_i^{af} \prod_{\nu_{ij}^a < 0} (\gamma_j^c C_j^c)^{-\nu_{ij}^a} \left[1 - (K_i^a)^{-1} \prod_{j=1}^{N_c} (\gamma_i^c C_i^c)^{\nu_{ij}^a} \right] \tag{3.53}$$

Noting that the ion activity product for reaction 3.47 is defined as:

$$IAP_i^a = \prod_{j=1}^{N_c} (\gamma_j^c C_j^c)^{\nu_{ij}^a} \tag{3.54}$$

allows the simplification of rate expression 3.53:

$$R_i^a = -k_i^{af} \prod_{\nu_{ij}^a<0} (\gamma_j^c C_j^c)^{-\nu_{ij}^a} \left[1 - \frac{IAP_i^a}{K_i^a}\right] \tag{3.55}$$

Rate expression 3.55 allows the computation of consumption and production rates for the participating species in elementary reversible reactions under far-from-equilibrium and near-equilibrium conditions.

Many reactions are, however, complex and are expressed in terms of an overall reaction which replace a sequence of elementary reactions. For example, the actual reaction mechanism for the oxidation of ferrous iron under mildly acidic conditions according to equation 3.44 consists of the following reaction steps [*Benson*, 1968, *Stumm and Morgan*, 1996]:

$$\begin{aligned}
Fe^{2+} + H_2O &\rightleftharpoons FeOH^+ + H^+ \\
FeOH^+ + O_2 &\rightleftharpoons Fe(OH)O_2^+ \\
Fe(OH)O_2^+ &\rightarrow FeOH^{2+} + O_2^{\cdot-} \\
O_2^{\cdot-} + H^+ &\rightleftharpoons HO_2^{\cdot} \\
HO_2^{\cdot} + Fe^{2+} + H_2O &\rightarrow FeOH^{2+} + H_2O_2 \\
H_2O_2 + Fe^{2+} &\rightarrow FeOH^{2+} + OH^{\cdot} \\
OH^{\cdot} + Fe^{2+} &\rightarrow FeOH^{2+}
\end{aligned}$$

If all elementary reactions occur sequentially, the progress of the overall reaction depends on the slowest elementary reaction, which can be defined as the rate-determining step [*Lasaga*, 1981]. The reaction progress of the overall reaction may, however, depend on intermediate reactant or product species, which are not part of the reaction stoichiometry of the overall reaction [*Stumm and Morgan*, 1996]. The order of the reaction rate has no mechanistic significance, but reflects the joining of the elementary steps [*Lasaga*, 1981, *Stumm and Morgan*, 1996]. In practice, laboratory experiments are conducted to determine which species control the reaction progress and what order the reaction has with respect to each of these species. The overall reaction rate for the abiotic oxidation of ferrous iron under mildly acidic conditions according to equation 3.44, for example, can be expressed as [*Singer and Stumm*, 1970, *Sung and Morgan*, 1980]

$$R_3^{af} = -k_3^{af}[\text{Fe(II)}]\{O_2(aq)\}\{OH^-\}^2 \qquad 4.5 \leq \text{pH} \leq 8.0. \tag{3.56}$$

Equation 3.56 indicates that the laboratory-determined oxidation rate of ferrous iron does not only depend on the activities of the components as species in solution as prescribed by rate expression 3.48, but may also depend on the activities of aqueous complexes (OH^-) and on total aqueous component concentrations (Fe(II)). The rate expression 3.48 can be generalized to describe irreversible overall reactions under far-from-equilibrium conditions. The generalized rate expression can be written as

$$R_i^{af} = -k_i^{af} \prod_{j=1}^{N_c} (T_j^a)^{o_{ij}^{at}} \prod_{j=1}^{N_c} (\gamma_j^c C_j^c)^{o_{ij}^{ac}} \prod_{j=1}^{N_x} (\gamma_j^x C_j^x)^{o_{ij}^{ax}}, \tag{3.57}$$

where the order of the reaction with respect to the species that control the reaction progress are no longer represented by the stoichiometric coefficients of reaction equation 3.47. This approach requires the explicit specification of the reaction orders with respect to the species, which control the reaction progress. o_{ij}^{at} is the order of the i^{th} kinetically-controlled intra-aqueous reaction with respect to the total aqueous component concentration of the j^{th} component, o_{ij}^{ac} is the order of the i^{th} kinetically-controlled intra-aqueous reaction with respect to the activity of the j^{th} component as species in solution and o_{ij}^{ax} is the order of the i^{th} kinetically-controlled intra-aqueous reaction with respect to the activity of the j^{th} aqueous complex.

The abiotic oxidation rate of ferrous iron by oxygen under acidic conditions follows a different rate expression than defined by equation 3.56 [*Singer and Stumm*, 1970, *Lowson*, 1982, *Millero*, 1985]. The appropriate rate expression is given by:

$$R_3^{af} = -k_3^{af}[\text{Fe(II)}]\{O_2(aq)\} \qquad 1.0 \leq \text{pH} \leq 3.5 \tag{3.58}$$

The reaction paths defined by equations 3.56 and 3.58 represent parallel reaction pathways. In the case of parallel reaction pathways the contributions of the different reaction processes can be assumed additive [*Lasaga*, 1981]. An appropriate rate expression describing the abiotic oxidation of ferrous iron valid for a pH-range from approximately 1 to 8 can therefore be expressed as:

$$R_3^{af} = -k_{31}^{af}[\text{Fe(II)}]\{O_2(aq)\}\{H^+\}^{-2} - k_{32}^{af}[\text{Fe(II)}]\{O_2(aq)\} \tag{3.59}$$

The general rate expression given by equation 3.57 can be expanded to facilitate the

consideration of parallel reaction pathways:

$$R_i^{af} = -\sum_{k=1}^{N_i^{ap}} k_{ik}^{af} \prod_{j=1}^{N_c} (T_j^a)^{o_{ijk}^{at}} \prod_{j=1}^{N_c} (\gamma_j^c C_j^c)^{o_{ijk}^{ac}} \prod_{j=1}^{N_x} (\gamma_j^x C_j^x)^{o_{ijk}^{ax}} \tag{3.60}$$

N_i^{ap} is here defined as the number of parallel reaction pathways for the i^{th} kinetically-controlled intra-aqueous reaction. Each parallel reaction pathway k requires the definition of its own rate constant k_{ik}^{af} and reaction orders with respect to the species, which control the reaction progress. o_{ijk}^{at}, o_{ijk}^{ac} and o_{ijk}^{ax} define the reaction orders for the k^{th} reaction pathway with respect to the total aqueous component concentrations, the activities of the components as species in solution, and the activities of the aqueous complexes, respectively. The use of rate expression 3.60 is more convenient than defining a rate expression according to equation 3.57 for each reaction pathway.

Equation 3.55 can be used to expand the rate expression for irreversible kinetically-controlled intra-aqueous reactions to reversible reactions. A general rate expression for a reversible overall reaction can be based on equations 3.55 and 3.61 and can be written as:

$$R_i^a = -\left[\sum_{k=1}^{N_i^{ap}} k_{ik}^{af} \prod_{j=1}^{N_c} (T_j^a)^{o_{ijk}^{at}} \prod_{j=1}^{N_c} (\gamma_j^c C_j^c)^{o_{ijk}^{ac}} \prod_{j=1}^{N_x} (\gamma_j^x C_j^x)^{o_{ijl}^{ax}}\right] \left[1 - \left(\frac{IAP_i^a}{K_i^a}\right)^{(\bar{\sigma}_{ik}^a)^{-1}}\right] \tag{3.61}$$

IAP_i^a defines here the ion-activity product of the overall reaction, K_i^a defines the equilibrium constant for the overall reaction and $\bar{\sigma}_{ik}^a$ defines the Tempkin-number for the reaction path considered [*Lichtner*, 1996b]. The Tempkin-number was introduced to account for the effect of the various elementary steps on the overall reaction [*Helgeson et al.*, 1984, *Lichtner*, 1996b]. The Tempkin-number can be set to unity as an approximation. This formulation is based on the assumption that the rate of the overall reaction is related to the rates of the elementary reactions comprising the overall reaction mechanism [*Lasaga*, 1981]. Whether rate expression 3.61 can be applied to extend the applicability of laboratory determined far-from-equilibrium rate expressions to near-equilibrium conditions or to describe reversible reactions has to be decided on a case-dependent basis.

For some reactions an equilibrium constant is available but equation 3.61 can still not be applied because the modelled reaction pathway is truly irreversible. Rate expression 3.60 is, on the other hand, often only applicable if the accumulation of product species is insignificant. For example, the oxidation of ferrous iron by oxygen (equation 3.44)

has to be considered an irreversible reaction, since the reduction of ferric iron leading to the production of oxygen and ferrous iron is thermodynamically not favorable. Such a reaction can be approximated by a rate expression which considers the reaction as an irreversible process, but also accounts for the build-up of reaction products in solution. An appropriate rate expression is given by:

$$R_i^{af} = -\max\left[\left[\left[\sum_{k=1}^{N_i^{ap}} k_{ik}^{af} \prod_{j=1}^{N_c} (T_j^a)^{o_{ijk}^{at}} \prod_{j=1}^{N_c} (\gamma_j^c C_j^c)^{o_{ijk}^{ac}} \prod_{j=1}^{N_x} (\gamma_j^x C_j^x)^{o_{ijk}^{ax}}\right]\left[1 - \frac{IAP_i^a}{K_i^a}\right]\right], 0\right] \quad (3.62)$$

The reaction product of the total concentrations and species activities, that control the reaction progress under far-from-equilibrium conditions can be defined as:

$$RP_{ik}^a = \prod_{j=1}^{N_c} (T_j^a)^{o_{ijk}^{at}} \prod_{j=1}^{N_c} (\gamma_j^c C_j^c)^{o_{ijk}^{ac}} \prod_{j=1}^{N_x} (\gamma_j^x C_j^x)^{o_{ijk}^{ax}} \quad (3.63)$$

Equation 3.63 can be substituted to simplify rate expressions 3.57, 3.61 and 3.62. The resulting rate expressions and their applicability are summarized in Table 3.1.

irreversible far-from-equilibrium forward rate	R_i^{af}	$=$	$-\left[\sum_{k=1}^{N_i^{ap}} k_{ik}^{af} RP_{ik}^a\right]$
reversible far-from/close-to-equilibrium forward rate constant	R_i^a	$=$	$-\left[\sum_{k=1}^{N_i^{ap}} k_{ik}^{af} RP_{ik}^a\right]\left[1 - \frac{IAP_i^a}{K_i^a}\right]$
irreversible far-from/close-to-equilibrium forward rate constant	R_i^{af}	$=$	$-\max\left[\left[\left[\sum_{k=1}^{N_i^{ap}} k_{ik}^{af} RP_{ik}^a\right]\left[1 - \frac{IAP_i^a}{K_i^a}\right]\right], 0\right]$

Table 3.1: Rate expressions for intra-aqueous reactions

The general rate expressions presented in Table 3.1 can be expressed in symbolic form as a function of the forward and backward rate constants, the activities of the components as species in solution and aqueous complexes (a_j^c and a_i^x), total aqueous component concentrations and the equilibrium constant of the reaction. The symbolic representation of the rate expressions can be written as:

$$R_i^a = f(k_{ik}^{af}, k_{ik}^{ab}, a_j^c, a_i^x, T_j^a, K_i^a) \quad i = 1, N_a,\ k = 1, N_i^{ap} \quad (3.64)$$

Rate expressions 3.57, 3.61 and 3.62 can be used to describe the reaction progress for elementary and overall reactions for intra-aqueous kinetics. The reaction progress may depend on total aqueous component concentrations, on the activities of components as species in solution and on the activities of aqueous complexes. The rate expressions can accommodate any reaction order with respect to these species and allows the consideration of parallel reaction pathways. Reactions may be reversible or irreversible and the rate expressions are applicable under far-from-equilibrium and near-equilibrium conditions.

The source-sink term defining the consumption or production of aqueous components due to the sum of all kinetically-controlled intra-aqueous reactions can be defined as

$$Q_j^{a,a} = S_a \phi \sum_{i=1}^{N_a} \nu_{ij}^a R_i^a \qquad j = 1, N_c, \tag{3.65}$$

where the contributions of the various reactions rates were scaled to express the source-sink term in the units of the global mass conservation equations [mol l^{-1} bulk s^{-1}].

3.4.4 Gas Dissolution-Exsolution

A stoichiometric relationship for the dissolution and subsequent dissociation of the gas A_i^g can be formulated as

$$A_i^g \rightleftharpoons \sum_{i=1}^{N_c} \nu_{ij}^g A_i^c \qquad i = 1, N_g, \tag{3.66}$$

where ν_{ij}^g are the stoichiometric coefficients of the components as species in solution comprising the i^{th} gaseous species. Equilibrium dissolution-exsolution reactions according to reaction equation 3.66 can also be described by the law of mass action:

$$C_i^g = (RTK_i^g)^{-1} \prod_{j=1}^{N_c} (\gamma_j^c C_j^c)^{\nu_{ij}^g} \qquad i = 1, N_g \tag{3.67}$$

The gas concentrations C_i^g are defined in units of [mol l^{-1} gas] and K_i^g is the equilibrium constant for the dissolution of i^{th} gaseous species.

3.4.5 Ion Exchange

Various formulations are available to describe ion exchange reactions [*Appelo and Postma*, 1993]. The most common approaches are the Gaines-Thomas, the Gapon, and the Vanselow conventions [*Appelo and Postma*, 1993]. All solution approaches are limited to the description of cation-exchange reactions on negatively charged mineral surfaces and assume that the reactions can be described by equilibrium relationships based on the law of mass action. The various conventions differ with respect to the definition of the activities of the adsorbed species. This is because a unified theory to compute activity corrections for adsorbed species is not available. The Gapon-convention assumes that the activity of the adsorbed ions are proportional to the number of exchange sites, while the Gaines-Thomas convention uses the equivalent fraction of the exchangeable cations for the activity of the adsorbed ions [*Appelo and Postma*, 1993]. The Vanselow-convention, on the other hand, uses molar fractions of the exchangeable cations for the activities of the adsorbed ions [*Appelo and Postma*, 1993]. The present model allows the consideration of ion-exchange reactions in terms of the Gapon- and Gaines-Thomas conventions. Both solution approaches have advantages. The solution based on the Gaines-Thomas-convention is more popular and the majority of the compilations of exchange parameters are based on the Gaines-Thomas model. On the other hand, the solution based on the Gapon-convention is numerically more efficient (see below). The fundamental formulation is equivalent for both solution approaches. The particular form of these conventions can be used to obtain explicit expressions for the concentrations of the ion-exchanged species. This allows a more convenient incorporation of ion-exchange reactions into the present model.

Gaines-Thomas Convention

The ion-exchange reaction between the mono-valent cation Na^+ and the bi-valent cation Ca^{2+} can be used as an illustrative example. A reaction equation, which fits the format of the Gaines-Thomas convention can be written as

$$Na^+ + \tfrac{1}{2}Ca\text{-}X_2 \rightleftharpoons Na\text{-}X + \tfrac{1}{2}Ca^{2+}, \tag{3.68}$$

where X^- defines an exchanger site with charge -1 [*Appelo and Postma*, 1993]. A general stoichiometric relationship for ion-exchange between the cations A_k^d and A_i^d can be written

as

$$\frac{A_k^d}{Z_k^d} + \frac{A_i^d\text{-}X_{Z_i^d}}{Z_i^d} \rightleftharpoons \frac{A_k^d\text{-}X_{Z_k^d}}{Z_k^d} + \frac{A_i^d}{Z_i^d}, \tag{3.69}$$

where Z_i^d and Z_k^d define the charge of the cations A_i^d and A_k^d [meq mmol^{-1}], while $(Z_i^d)^{-1}$ and $(Z_k^d)^{-1}$ can also be interpreted as the stoichiometric coefficients of the reaction equation. It is at this point convenient to redefine the ion-exchanged species as:

$$A_i^s = A_i^d\text{-}X_{Z_i^d} \tag{3.70}$$

$$A_k^s = A_k^d\text{-}X_{Z_k^d} \tag{3.71}$$

Substituting equation 3.70 and 3.71 into equation 3.69 leads to:

$$\frac{A_k^d}{Z_k^d} + \frac{A_i^s}{Z_i^d} \rightleftharpoons \frac{A_k^s}{Z_k^d} + \frac{A_i^d}{Z_i^d} \tag{3.72}$$

Equation 3.72 can be rearranged to obtain a stoichiometric relationship with a unit stoichiometric coefficient for the ion-exchanged species A_i^s:

$$A_i^s \rightleftharpoons \frac{Z_i^d}{Z_k^d}A_k^s + A_i^d - \frac{Z_i^d}{Z_k^d}A_k^d \tag{3.73}$$

The stoichiometric relationship given by equation 3.73 expresses ion-exchange reactions in a general way involving any pair of dissolved cations. This formulation has to be adjusted to facilitate its incorporation into the existing model equations. In this context, ion-exchange reactions will be limited to exchange reactions involving cations, which are defined as components. Equation 3.73 can be generalized as

$$A_i^s \rightleftharpoons \nu_i^s A_k^s \sum_{j=1}^{N_c} \nu_{ij}^s A_j^c \qquad i = 1, N_s, \tag{3.74}$$

where ν_i^s is the stoichiometric coefficient of the ion-exchanged species A_k^s in the i^{th} ion exchange reaction, which is defined by the ratio of the charge of the two cations. ν_{ij}^s are the stoichiometric coefficients of the components, which can be related to the stoichiometric coefficients in equation 3.73 and N_s defines the number of the ion-exchanged species. The stoichiometric relationship given by equation 3.74 is similar to the one for aqueous complexation (equation 3.45) and gas dissolution-exsolution reactions (equation

3.66). A significant difference does, however, exist, since A_i^s cannot be expressed exclusively in terms of aqueous components, but is dependent on the ion-exchanged species A_k^s. One of the ion-exchanged species has to be chosen to represent A_k^s. Based on the stoichiometry defined in reaction equation 3.74, the law of mass action can be used to obtain a relationship that defines the activities of the ion-exchanged species A_i^s in terms of equivalent fractions

$$\beta_i = (K_i^s)^{-1}(\beta_k)^{\nu_i^s} \prod_{j=1}^{N_c} \left(\gamma_j^c C_j^c\right)^{\nu_{ij}^s} \qquad i = 1, N_s,\ i \neq k, \tag{3.75}$$

where β_i and β_k are the activities of the ion-exchanged species A_i^s and A_k^s [meq meq^{-1}] and K_i^s is the selectivity coefficient for the i^{th} ion-exchange reaction. Equation 3.75 provides only an explicit relationship for the calculation of β_i, if the activity of the ion-exchanged species A_k^s is known. It is not possible to use equation 3.75 to determine β_k, therefore, an additional relationship is needed. This relationship can be defined as the sum of the activities of all ion-exchanged species, which equals 1 by definition [*Appelo and Postma*, 1993]:

$$1 = \sum_{i=1}^{N_s} \beta_i \tag{3.76}$$

Equations 3.75 and 3.76 constitute the set of equations defining the ion-exchange sub-problem.

In order to include ion-exchange reactions into the global mass conservation equations, three approaches are possible:

- Treatment of the ion-exchanged species A_k^s as a component
- Implicit solution of ion-exchange as a sub-problem
- Explicit solution of ion-exchange as a sub-problem. Derivation of an explicit relationship for A_k^s in terms of aqueous components, allows an explicit solution for the concentrations of all ion-exchanged species.

If the ion-exchanged species A_k^s is treated as a component, equation 3.76 has to be added to the global system of mass conservation equations consisting of equations 3.28 and 3.29. In this case, an initial concentration for the ion-exchanged species A_k^s is required,

which constitutes a quantity not generally available. It is therefore preferable to treat ion-exchange reactions as a sub-problem that allows the treatment of all ion-exchanged species as secondary unknowns for the global problem. This can be achieved by substituting the equilibrium expressions for the ion-exchanged species A_i^s (equations 3.75) into equation 3.76.

$$1 = \sum_{i=1}^{N_s} (K_i^s)^{-1} (\beta_k)^{\nu_i^s} \prod_{j=1}^{N_c} \left(\gamma_j^c C_j^c\right)^{\nu_{ij}^s} \tag{3.77}$$

Equation 3.77 implicitly contains the solution for β_k. The activities of all ion-exchanged species can be calculated by solving the system of equations given by equations 3.75 and equation 3.77, provided the concentrations of the components as species in solution are known. An explicit solution cannot always be obtained, because equation 3.77 is nonlinear with respect to the activity β_k. The nonlinearity is introduced by the stoichiometric coefficients ν_i^s defining the ratio between the charges of the ion-exchanged species. An implicit solution of the sub-problem is necessary if ion-exchange reactions involve tri-valent or higher charged cations. Relationship 3.77 simplifies to a quadratic equation if only mono-valent and bi-valent cations are participating in ion-exchange reactions.

In this case, an explicit relationship can be formulated, which allows the computation of the activity of A_k^s

$$\beta_k = \frac{-b + (b^2 - 4ac)^{1/2}}{2a}, \tag{3.78}$$

where the factors a, b and c are defined as:

$$\begin{aligned} a &= \sum_{\substack{i=1 \\ \nu_i^s=2}}^{N_s} (K_i^s)^{-1} \prod_{j=1}^{N_c} \left(\gamma_j^c C_j^c\right)^{\nu_{ij}^s}, \\ b &= \sum_{\substack{i=1 \\ \nu_i^s=1}}^{N_s} (K_i^s)^{-1} \prod_{j=1}^{N_c} \left(\gamma_j^c C_j^c\right)^{\nu_{ij}^s}, \\ c &= -1 \end{aligned}$$

It should be pointed out that equation 3.78 is only applicable for ion exchange reactions involving both mono-valent and bi-valent cations. If only mono-valent species are present, equation 3.77 is linear with respect to β_k, and can be solved directly. The activities of the

remaining ion-exchanged species can subsequently be calculated based on equations 3.75. The actual concentrations of the ion-exchanged species can be obtained by applying the conversion:

$$C_i^s = \frac{\rho_b}{100} CEC (Z_i^s)^{-1} \beta_i \tag{3.79}$$

where C_i^s is the concentration of the ion-exchanged species A_i^s [mol l^{-1} bulk], ρ_b is the dry bulk density of the porous medium [g solid cm^{-3} bulk] and CEC defines the cation exchange capacity [meq $(100g)^{-1}$ solid]. The factor 100 provides the conversion [g $(100g)^{-1}$].

Gapon-Convention

An alternative solution approach can be derived based on the Gapon-convention. In this case the stoichiometric expression for the example ion-exchange reaction can be written as:

$$Na^+ + Ca_{1/2}\text{-}X \rightleftharpoons Na\text{-}X + \tfrac{1}{2}Ca^{2+} \tag{3.80}$$

The differences between equation 3.68 and equation 3.80 lie in the definitions for the activities of the ion-exchanged species. A general stoichiometric relationship can be written as:

$$\frac{A_k^c}{Z_k^c} + A_{i,1/Z_i^c}^c\text{-}X \rightleftharpoons A_{k,1/Z_k^c}^c\text{-}X + \frac{A_i^c}{Z_i^c} \tag{3.81}$$

The ion-exchanged species can again be redefined as:

$$A_i^s = A_{i,1/Z_i^c}^c\text{-}X \tag{3.82}$$

$$A_k^s = A_{k,1/Z_k^c}^c\text{-}X \tag{3.83}$$

Substituting equations 3.82 and 3.83 into equation 3.81 leads to:

$$\frac{A_k^c}{Z_k^c} + A_i^s \rightleftharpoons A_k^s + \frac{A_i^c}{Z_i^c} \tag{3.84}$$

Equation 3.84 can be rearranged and simplified in a similar manner as was done for the Gaines-Thomas-convention:

$$A_i^s = A_k^s \sum_{j=1}^{N_c} \nu_{ij}^s A_j^c \qquad K_i^s \tag{3.85}$$

Equation 3.85 shows that the stoichiometric coefficients of the ion-exchanged species are always unity in the case of the Gapon-convention. An appropriate equilibrium relationship can be expressed as

$$\beta_i = (K_i^s)^{-1} \beta_k \prod_{j=1}^{N_c} \left(\gamma_j^c C_j^c\right)^{\nu_{ij}^s}, \tag{3.86}$$

where β_i and β_k define the fraction of exchange sites with charge -1 occupied by the ion-exchanged species A_i^s and A_k^s respectively [*Appelo and Postma*, 1993]. Substituting equation 3.86 into equation 3.76 leads to:

$$1 = \sum_{i=1}^{N_s} (K_i^s)^{-1} \beta_k \prod_{j=1}^{N_c} \left(\gamma_j^c C_j^c\right)^{\nu_{ij}^s} \tag{3.87}$$

Equation 3.87 is linear with respect to the fraction of exchange sites occupied by the ion-exchanged species. Therefore, β_k can be determined directly based on the activities of the components as species in solution according to:

$$\beta_k = \frac{1}{\sum_{i=1}^{N_s} (K_i^s)^{-1} \prod_{j=1}^{N_c} \left(\gamma_j^c C_j^c\right)^{\nu_{ij}^s}} \tag{3.88}$$

Substituting equation 3.88 into the equilibrium expressions 3.86 yields an explicit solution for the exchanger composition, which is solely based on the activities of the components as species in solution:

$$\beta_i = \frac{(K_i^s)^{-1} \prod_{j=1}^{N_c} \left(\gamma_j^c C_j^c\right)^{\nu_{ij}^s}}{\sum_{k=1}^{N_s} (K_k^s)^{-1} \prod_{j=1}^{N_c} \left(\gamma_j^c C_j^c\right)^{\nu_{kj}^s}} \qquad i = 1, N_s \tag{3.89}$$

Expressing the exchanger composition in terms of concentrations does not require a correction for the charge of the ion-exchanged cation in case of the Gapon-convention because the fractions β_i are related to the exchange sites with charge -1, but not to the charge of

the exchanging cations. The concentrations can be calculated according to:

$$C_i^s = \frac{\rho_b}{100} CEC\beta_i \tag{3.90}$$

The units remain as defined in the previous section for the Gaines-Thomas convention.

3.4.6 Mineral Dissolution-Precipitation

Dissolution-precipitation reactions encompass the dissolution of primary minerals and the formation of secondary mineral phases and are usually complex in nature. The mineral particles are covered by a thin stagnant water film, which may be characterized by a different chemical composition than the bulk solution [*Berner*, 1978, *Schnoor*, 1990]. This implies that reactant species have to be transported from the bulk solution to the mineral surface (Figure 3.1). Diffusion through a stagnant water film is, however, not considered in this study, since it is too rapid to be the rate-determining step for most dissolution-precipitation reactions [*Schnoor*, 1990]. Some minerals will form a leached layer, an alteration rim, or a surface coating during the dissolution process, which may inhibit the transport of the reactant species to the mineral surface significantly and consequently the further dissolution of the mineral (Figure 3.1) [*Murphy et al.*, 1989, *Nicholson et al.*, 1990, *Schnoor*, 1990]. The actual chemical reaction between the dissolved species and the mineral occurs on the mineral surface as a series of elementary steps, including the adsorption of dissolved species onto the mineral surface, followed by the formation and subsequent detachment of an activated complex [*Wieland et al.*, 1988, *Stone and Morgan*, 1990, *Stumm and Wollast*, 1990, *Stumm and Morgan*, 1996]. The reaction progress of overall dissolution-precipitation reactions may also be limited by intermediate reactant or product species, similar to intra-aqueous kinetic reactions. The reaction products are subsequently transported back into the bulk solution [*Stone and Morgan*, 1990].

From these observations it is evident that the reaction progress of dissolution-precipitation reactions may be influenced by many factors. The reaction progress can be limited by either microscale transport processes involving reactant or product species or by the actual chemical reaction taking place on the mineral surface itself [*Berner*, 1978, *Stone and Morgan*, 1990, *Steefel and Lasaga*, 1994]. Dissolution-precipitation reactions can therefore be characterized as "surface-controlled" or "diffusion-controlled" reactions, depending on which process limits the rate of the reaction progress [*Berner*, 1978, *Steefel and Lasaga*, 1994]. The reaction is subject to a "mixed reaction control" if the reaction

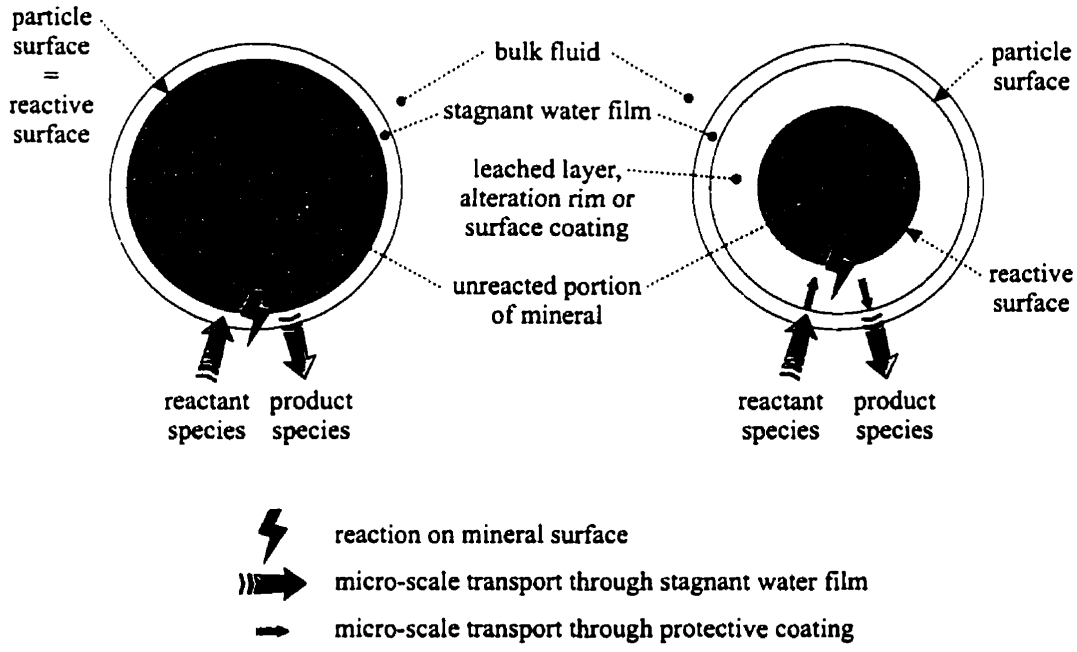

Figure 3.1: Mineral particles with and without protective surface layer

progress is influenced simultaneously by microscale transport and chemical reaction processes [*Stone and Morgan*, 1990, *Steefel and Lasaga*, 1994]. A formulation for "mixed reaction control" is not considered in the present work. The dissolution of most minerals can be described by surface-controlled reactions [*Blum and Lasaga*, 1991], such as the dissolution of aluminosilicate minerals [e.g. *Berner*, 1978, *Blum and Stillings*, 1995, *Dove*, 1995, *Nagy*, 1995], carbonates [*Chou et al.*, 1989, *Greenberg and Tomson*, 1992] and oxy-hydroxides [*Wieland et al.*, 1988].

It is assumed, that the dissolution or precipitation of minerals occurs congruently according to the stoichiometry of the overall reaction. Influences on the reaction stoichiometry due to the formation of a leached layer or an alteration rim are not considered in the present study. The formulation, however, accounts for the formation of secondary minerals from the reaction products. This approach facilitates a suitable description of aqueous species and mineral concentrations, but does not describe the actual form of the secondary precipitates (surface coating, alteration rim or new mineral particles).

The present kinetic formulation facilitates the description of dissolution-precipitation

reactions as irreversible or reversible reactions. Irreversible reactions are assumed to be unaffected by the presence of the reaction products, which is usually the case for reactions, which take place under far-from-equilibrium conditions. In the case of reversible reactions, the build-up of reaction products may, however, lead to a diminution of the reaction progress or even to a change of the reaction direction. Mineral precipitation conceptually only makes sense for surface-controlled reactions. Diffusion-controlled reactions are therefore strictly treated as irreversible dissolution reactions.

A general stoichiometric relationship, which describes the congruent dissolution or precipitation of a mineral in terms of components as species in solution can be written as:

$$A_i^m \rightleftharpoons \sum_{j=1}^{N_c} \nu_{ij}^m A_j^c \qquad i = 1, N_m \tag{3.91}$$

where A_i^m defines the i^{th} mineral, ν_{ij}^m are the stoichiometric coefficients of the components as species in solution comprising the mineral A_i^m, and N_m defines the number of minerals actively participating in dissolution-precipitation reactions.

A number of dissolution-precipitation reactions are defined to illustrate the development of the rate expressions. For example, the stoichiometric relationship describing the dissolution or precipitation of calcite can be written as

$$CaCO_3(s) \rightleftharpoons Ca^{2+} + CO_3^{2-} \tag{3.92}$$

where the arrows in both directions indicate that the reaction is considered reversible. The dissolution of aluminosilicate minerals in shallow groundwater systems on the other hand is usually irreversible. The dissolution of albite, for example, is defined by:

$$NaAlSi_3O_8(s) + 4H^+ + 4H_2O \rightarrow Na^+ + Al^{3+} + 3H_4SiO_4 \tag{3.93}$$

It is often the case that dissolution-precipitation reactions take place along several reaction pathways. Previous studies have shown that the oxidation of pyrite can follow two different reaction pathways [*Singer and Stumm*, 1970, *Moses et al.*, 1987, *Williamson and Rimstidt*, 1994]. Pyrite might either be oxidized by dissolved oxygen:

$$FeS_2(s) + \tfrac{7}{2}O_2(aq) + H_2O \rightarrow Fe^{2+} + 2SO_4^{2-} + 2H^+ \tag{3.94}$$

or by ferric iron:

$$FeS_2(s) + 14Fe^{3+} + 8H_2O \rightarrow 15Fe^{2+} + 2SO_4^{2-} + 16H^+ \quad (3.95)$$

Reaction 3.94 or reaction 3.95 can be controlling the overall reaction progress of pyrite oxidation, depending on the prevailing chemical conditions.

In the following a general framework is presented that allows the consideration of the reaction types discussed above. The formulation of the various reaction mechanisms implemented in the present model is derived. Using a typical example, the appropriate rate equation is presented based on rate expressions obtained from the literature, or is developed further to suit the required format.

Surface Controlled Reactions

Figure 3.2 illustrates symbolically the time-dependent evolution of a mineral particle due to a surface-controlled dissolution process during the time interval t_0 to t_1. The mineral grains are here approximated as spherical particles. The size of a particle of the mineral A_i^m can be described by the representative radius r_i^p [m]. The radius r_i^r [m] defines the location of the reactive surface of the mineral grain. The radii r_i^p and r_i^r are identical for surface-controlled dissolution-precipitation reactions, since a surface coating does not exist at any time. The size of the mineral particle is decreasing during the dissolution process. This also implies that the dissolved species concentrations $C_j^{c,r}$ at the reactive surface of the mineral are equal to the corresponding concentrations in the bulk solution C_j^c. The precipitation of a mineral onto an existing mineral particle can be described similarly and is shown conceptually in Figure 3.3. The reaction rates of surface-controlled dissolution-precipitation reactions are a function of a rate constant, the reactive mineral surface area, and the activities or concentrations of dissolved reactant and product species or intermediate reaction products. A general rate expression for surface-controlled dissolution-precipitation reactions can be developed in a similar manner as for kinetically-controlled intra-aqueous reactions.

Assuming that the dissolution of the mineral A_i^m takes place under far-from-equilibrium conditions and that reaction equation 3.91 represents an elementary process, a rate

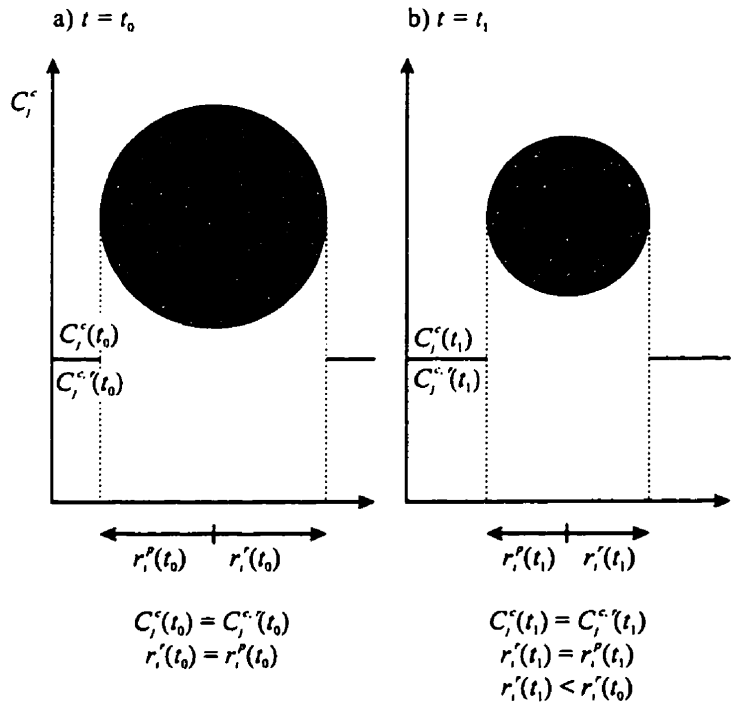

Figure 3.2: Transient evolution of particle, surface-controlled reaction - dissolution

expression for the dissolution of the mineral A_i^m can be written as

$$R_i^{md,s,u} = -k_i^{md,s} \prod_{\nu_{ij}^m < 0} (\gamma_j^c C_j^c)^{-\nu_{ij}^m}, \tag{3.96}$$

where $R_i^{md,s,u}$ defines the rate of dissolution per unit surface area [mol m^{-2} mineral s^{-1}] and $k_i^{md,s}$ is the dissolution rate constant. The superscript s attributes the reaction rate and related reaction parameters to a surface-controlled reaction. The rate expression can be scaled for application in a continuum model by multiplying equation 3.96 with the reactive surface area S_i, which is given in units [m^2 mineral l^{-1} bulk]. A discussion on possible descriptions of the reactive surface area is provided later in this chapter. The bulk porous medium dissolution rate for the mineral A_i^m can then be expressed as:

$$R_i^{md,s} = -S_i k_i^{md,s} \prod_{\nu_{ij}^m < 0} (\gamma_j^c C_j^c)^{-\nu_{ij}^m} \tag{3.97}$$

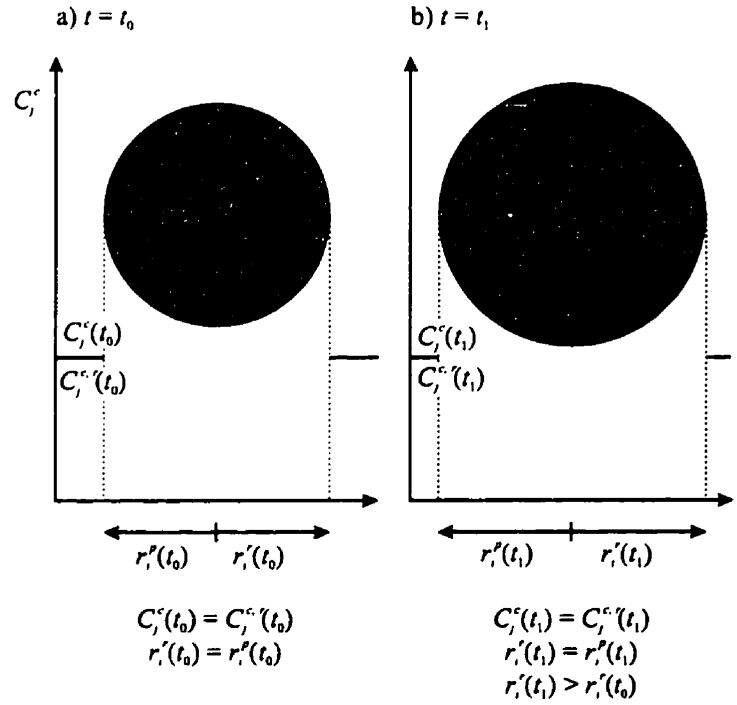

Figure 3.3: Transient evolution of particle, surface-controlled reaction - precipitation

The units of the rate are given in [mol l^{-1} bulk s^{-1}]. A corresponding reaction expression for the precipitation of the i^{th} mineral can be written as

$$R_i^{mp,s} = S_i k_i^{mp,s} \prod_{\nu_{ij}^m > 0} (\gamma_j^c C_j^c)^{\nu_{ij}^m}, \tag{3.98}$$

where $R_i^{mp,s}$ [mol l^{-1} bulk s^{-1}] defines the rate of precipitation of the mineral A_i^m and $k_i^{mp,s}$ is the precipitation rate constant. The dissolution-precipitation rate can be obtained from the sum of rate expressions 3.97 and 3.98, assuming that the reaction as specified in equation 3.91 is reversible:

$$R_i^{m,s} = -S_i \left[k_i^{md,s} \prod_{\nu_{ij}^m < 0} (\gamma_j^c C_j^c)^{-\nu_{ij}^m} - k_i^{mp,s} \prod_{\nu_{ij}^m > 0} (\gamma_j^c C_j^c)^{\nu_{ij}^m} \right] \tag{3.99}$$

The equilibrium constant associated with the dissolution-precipitation reaction can be

defined based on the dissolution and precipitation reaction rates according to the principle of detailed balancing [*Lasaga*, 1981]:

$$K_i^m = \frac{k_i^{md,s}}{k_i^{mp,s}} \tag{3.100}$$

Substituting equation 3.100 into equation 3.99 facilitates the expression of the reaction rate in terms of the dissolution rate constant and the equilibrium constant:

$$R_i^{m,s} = -S_i k_i^{md,s} \prod_{\nu_{ij}^m<0} (\gamma_j^c C_j^c)^{-\nu_{ij}^m} \left[1 - (K_i^m)^{-1} \prod_{j=1}^{N_c} (\gamma_j^c C_j^c)^{\nu_{ij}^m}\right] \tag{3.101}$$

The ion activity product IAP_i^m of the i^{th} dissolution-precipitation reaction is defined as the product of the activities of the reacting species:

$$IAP_i^m = \prod_{j=1}^{N_c} (\gamma_j^c C_j^c)^{\nu_{ij}^m} \tag{3.102}$$

Equation 3.102 can be substituted into reaction expression 3.101 to yield a simplified rate expression for dissolution-precipitation reactions [e.g.: *Steefel and Lasaga*, 1994]:

$$R_i^{m,s} = -S_i k_i^{md,s} \prod_{\nu_{ij}^m<0} (\gamma_j^c C_j^c)^{-\nu_{ij}^m} \left[1 - \frac{IAP_i^m}{K_i^m}\right] \tag{3.103}$$

The dissolution-precipitation rate can alternatively be expressed in terms of the precipitation rate constant:

$$R_i^{m,s} = S_i k_i^{mp,s} \prod_{\nu_{ij}^m>0} (\gamma_j^c C_j^c)^{\nu_{ij}^m} \left[1 - \frac{K_i^m}{IAP_i^m}\right] \tag{3.104}$$

Rate expressions 3.103 and 3.104 can be applied to describe the progress of reversible dissolution-precipitation reactions if the reaction represents an elementary process.

Rate expression 3.103 can be applied to describe the reaction progress of calcite dissolution or precipitation (equation 3.92):

$$R_1^{m,s} = -S_1 k_1^{md,s} \left[1 - \frac{IAP_1^m}{K_1^m}\right],$$

where calcite was defined as the mineral A_1^m, $R_1^{m,s}$ is the calcite dissolution-precipitation rate, S_1 is the reactive surface area of the mineral in the bulk porous medium, $k_1^{md,s}$ is the far-from-equilibrium rate constant for calcite dissolution.

Reaction equation 3.91 usually defines an overall reaction rather than an elementary reaction and the reaction progress may be controlled by the concentrations or activities of intermediate species [*Lasaga*, 1981, *Steefel and Lasaga*, 1994]. It is therefore advantageous to implement a more general dependence of the reaction rate on all dissolved species present in an analogous manner to the formulation for intra-aqueous kinetic reactions. Considering for now only irreversible far-from-equilibrium reactions, a general rate expression for the dissolution of the mineral A_i^m can be deduced from the corresponding rate expression for intra-aqueous kinetic reactions (equation 3.57):

$$R_i^{md,s} = -S_i k_i^{md,s} \prod_{j=1}^{N_c} (T_j^a)^{o_{ij}^{mt,s}} \prod_{j=1}^{N_c} (\gamma_j^c C_j^c)^{o_{ij}^{mc,s}} \prod_{j=1}^{N_x} (\gamma_j^x C_j^x)^{o_{ij}^{mx,s}} \tag{3.105}$$

This rate expression allows the reaction progress to depend on the total aqueous component concentrations, the activities of the components as species in solution, and on the activities of aqueous complexes, where $o_{ij}^{mt,s}$, $o_{ij}^{mc,s}$ and $o_{ij}^{mx,s}$ define the corresponding reaction orders.

The far-from-equilibrium dissolution rate for albite, under low pH-conditions, as given in reaction equation 3.93, can be defined as [*Chou and Wollast*, 1985, *Blum and Lasaga*, 1988, *Blum and Lasaga*, 1991]

$$R_2^{m,s} = -S_2 \left[k_2^{md,s} \{\mathrm{H}^+\}^{0.49} \right] \qquad 2 \leq \mathrm{pH} \leq 6,$$

where albite corresponds to the mineral A_2^m and the reactive surface area of albite is defined by S_2. The reaction order does depend on the activity of the hydrogen ion, as defined in reaction equation 3.93. The order of the reaction with respect to the hydrogen ion does, however, not correspond to the stoichiometric coefficient for the hydrogen ion in the reaction equation.

Another example is the oxidation of pyrite by oxygen as defined in reaction equation 3.94. The rate expression after *Williamson and Rimstidt* [1994] exhibits a square root dependence on the activity of dissolved oxygen and a fractional dependence on pH

$$R_3^{m,s} = -S_3 \left[k_3^{md,s} \{\mathrm{O_2(aq)}\}^{0.50} \{\mathrm{H}^+\}^{-0.11} \right],$$

where pyrite was defined as the mineral A_3^m.

Dissolution or precipitation of a mineral can take place along various reaction pathways, each reaction being dominant under certain conditions and having its own rate constant [*Chou et al.*, 1989, *Sposito*, 1994]. To allow for a more general applicability of the rate expression, the different reaction pathways have to be taken into account. Albite dissolution under basic pH-conditions, for example, is also dependent on the hydrogen ion activity, however, the reaction order is different under these conditions [*Blum and Lasaga*, 1988]:

$$R_2^{m,s} = -S_2 \left[k_2^{md,s} \{\mathrm{H}^+\}^{-0.30} \right] \qquad 8 \leq \mathrm{pH} \leq 12$$

The rate of albite dissolution under far-from-equilibrium conditions over a pH-range from 2-12 can be expressed as

$$R_2^{m,s} = -S_2 \left[k_{21}^{md,s} \{\mathrm{H}^+\}^{0.49} + k_{22}^{md,s} \{\mathrm{H}^+\}^{-0.30} \right],$$

if the reactions under acidic and basic conditions are considered as parallel reactions.

A general relationship for the surface-controlled dissolution of the i^{th} mineral, where the reaction can occur along several reactions pathways can be defined as

$$R_i^{md,s} = -S_i \sum_{k=1}^{N_i^{mp}} k_{ik}^{md,s} \prod_{j=1}^{N_c} (T_j^a)^{o_{ijk}^{mt,s}} \prod_{j=1}^{N_c} (\gamma_j^c C_j^c)^{o_{ijk}^{mc,s}} \prod_{j=1}^{N_x} (\gamma_j^x C_j^x)^{o_{ijk}^{mx,s}}, \tag{3.106}$$

where N_i^{mp} defines the number of parallel reaction pathways contributing to the overall dissolution rate, and k_{ik}^{md} is the rate constant for the dissolution of mineral A_i^m for the k^{th} parallel reaction pathway. $o_{ijk}^{mc,s}$, $o_{ijk}^{mc,s}$ and $o_{ijk}^{mx,s}$ are the reaction orders with respect to the total aqueous component concentrations, the activities of the components as species in solution and the activities of the complexed species, respectively.

The overall precipitation rate of a mineral under far-from-equilibrium conditions can similarly be expressed as:

$$R_i^{mp,s} = S_i \sum_{k=1}^{N_i^{mp}} k_{ik}^{mp,s} \prod_{j=1}^{N_c} (T_j^a)^{o_{ijk}^{mt,s}} \prod_{j=1}^{N_c} (\gamma_j^c C_j^c)^{o_{ijk}^{mc,s}} \prod_{j=1}^{N_x} (\gamma_j^x C_j^x)^{o_{ijk}^{mx,s}} \tag{3.107}$$

where k_{ik}^{mp} is the precipitation rate constant for the k^{th} parallel reaction pathway.

The fact that dissolution-precipitation reactions can take place along different reac-

tion pathways not only affects the overall dissolution-precipitation rate itself, but also influences the concentrations of dissolved reactant and product species. The reaction stoichiometries of the various reaction pathways have to be considered separately if the reactant or product species undergo consumption or production due to kinetically-controlled intra-aqueous reactions. The reaction stoichiometry describing dissolution-precipitation reactions defined by equation 3.91 has therefore to be modified for a general description of parallel kinetically-controlled dissolution-precipitation reactions. An appropriate stoichiometric relationship for the dissolution-precipitation of the i^{th} mineral along the k^{th} reaction pathway can be written as

$$A_i^m \rightleftharpoons \sum_{j=1}^{N_c} \nu_{ijk}^m A_j^c \qquad i = 1, N_m,\ k = 1, N_i^{mp}, \tag{3.108}$$

where ν_{ijk}^m are the stoichiometric coefficients of the components comprising the mineral A_i^m, if the dissolution takes place along the k^{th} reaction pathway.

The oxidation of pyrite, for example, can take place along parallel reaction pathways [*Singer and Stumm*, 1970, *Moses et al.*, 1987, *Williamson and Rimstidt*, 1994]. Pyrite can be oxidized by dissolved oxygen according to reaction equation 3.94 or by ferric iron according to equation 3.95. Considering the reactions as parallel reactions and combining the rate expressions given by *Williamson and Rimstidt* [1994] leads to:

$$R_3^{m,s} = -S_3 \left[k_{31}^{md,s} \{O_2(aq)\}^{0.50} \{H^+\}^{-0.11} + k_{32}^{md,s} \{Fe^{3+}\}^{0.93} \{Fe^{2+}\}^{-0.40} \right]$$

A separate reaction stoichiometry defined by reaction equations 3.94 and 3.95 has to be used for each reaction pathway if the oxidation of ferrous iron in the aqueous phase is also considered kinetically limited.

Rate expression 3.106 can be expanded to allow the description of reversible dissolution-precipitation reactions in a similar way as intra-aqueous kinetic reactions. The dissolution of calcite, for example, can occur as a simple hydrolysis reaction, but also depends on the availability of carbonic acid and protons [*Chou et al.*, 1989]. The corresponding reaction equations are:

$$CaCO_3(s) + H_2O \rightleftharpoons Ca^{2+} + HCO_3^- + OH^- \tag{3.109}$$

$$CaCO_3(s) + H_2CO_3 \rightleftharpoons Ca^{2+} + 2HCO_3^- \tag{3.110}$$

$$CaCO_3(s) + H^+ \rightleftharpoons Ca^{2+} + HCO_3^- \tag{3.111}$$

A rate expression for calcite dissolution-precipitation along parallel reaction pathways as defined by equations 3.109 - 3.111 can be written as [*Chou et al.*, 1989]:

$$\begin{aligned} R_1^{md,s} = -S_1 \Bigg[& k_{11}^{md,s}\{\mathrm{H_2O}\}\left[1 - \frac{IAP_{11}^m}{K_{11}^m}\right] \\ & + k_{12}^{md,s}\{\mathrm{H_2CO_3}\}\left[1 - \frac{IAP_{12}^m}{K_{12}^m}\right] \\ & + k_{13}^{md,s}\{\mathrm{H^+}\}\left[1 - \frac{IAP_{13}^m}{K_{13}^m}\right]\Bigg] \end{aligned}$$

where the ion activity product and the equilibrium constants were specified separately for the parallel reaction pathways.

A general rate expression for reversible dissolution-precipitation reactions along parallel reaction pathways can be written as

$$\begin{aligned} R_i^{md,s} = & -S_i \sum_{k=1}^{N_i^{mp}} k_{ik}^{md,s} \prod_{j=1}^{N_c} (T_j^a)^{o_{ijk}^{mt,s}} \prod_{j=1}^{N_c} (\gamma_j^c C_j^c)^{o_{ijk}^{mc,s}} \\ & \prod_{j=1}^{N_x} (\gamma_j^x C_j^x)^{o_{ijk}^{mx,s}} \left[1 - \left(\frac{IAP_{ik}^m}{K_{ik}^m}\right)^{(\bar{\sigma}_{ik}^m)^{-1}}\right], \end{aligned} \tag{3.112}$$

where $\bar{\sigma}_{ik}^m$ defines the Tempkin-number, which has been introduced to allow the application of rate expression 3.112 to reversible overall reactions [*Lichtner*, 1996b]. A rate expression for the dissolution-precipitation of the i^{th} mineral along N_i^{mp} parallel reaction pathways can alternatively be expressed in terms of the precipitation rate constants:

$$\begin{aligned} R_i^{mp,s} = & \sum_{k=1}^{N_i^{mp}} k_{ik}^{mp,s} \prod_{j=1}^{N_c} (T_j^a)^{o_{ijk}^{mt,s}} \prod_{j=1}^{N_c} (\gamma_j^c C_j^c)^{o_{ijk}^{mc,s}} \\ & \prod_{j=1}^{N_x} (\gamma_j^x C_j^x)^{o_{ijk}^{mx,s}} \left[1 - \left(\frac{IAP_{ik}^m}{K_{ik}^m}\right)^{\bar{\sigma}_{ik}^m}\right] \end{aligned} \tag{3.113}$$

It should be noted at this point that the rate expression for reversible dissolution-precipitation reactions can be simplified if equilibrium between all dissolved reactant and product species exists. The rate expression for the dissolution and precipitation of

calcite, for example, can be simplified as:

$$R_1^{md,s} = -S_1 \left[k_{11}^{md,s}\{H_2O\} + k_{12}^{md,s}\{H_2CO_3\} + k_{13}^{md,s}\{H^+\}\right]\left[1 - \frac{IAP_1^m}{K_i^m}\right]$$

The application of rate expression 3.106 to the dissolution of albite might lead to an over-prediction of the dissolution rate. The rate constants have been determined under far-from-equilibrium conditions and may not be valid, if reaction products accumulate in solution. On the other hand, it is also not correct to apply a rate expression according to equation 3.112 to the weathering of albite because this reaction expression allows the precipitation of albite, which is not thermodynamically favored under low-temperature and low-pressure conditions. An approximate dissolution rate, which accounts for the build-up of reaction products can be written as:

$$R_2^{md,s} = -\max\left[\left[S_2\left[k_{21}^{md,s}\{H^+\}^{0.49} + k_{21}^{md,s}\{H^+\}^{-0.30}\right]\left[1 - \frac{IAP_{11}^m}{K_{11}^m}\right]\right], 0\right]$$

A general rate expression for an irreversible dissolution reaction that accounts for the build-up of reaction products in solution can then be expressed as:

$$R_i^{md,s} = -\max\left[\left[S_i \sum_{k=1}^{N_i^{mp}} k_{ik}^{md,s} \prod_{j=1}^{N_c} (T_j^a)^{o_{ijk}^{mt,s}} \prod_{j=1}^{N_c} (\gamma_j^c C_j^c)^{o_{ijk}^{mc,s}} \prod_{j=1}^{N_x} (\gamma_j^x C_j^x)^{o_{ijk}^{mx,s}} \left[1 - \frac{IAP_{ik}^m}{K_{ik}^m}\right]\right], 0\right] \tag{3.114}$$

The corresponding relationship for the irreversible precipitation of the i^{th} mineral can be written as:

$$R_i^{mp,s} = \max\left[\left[S_i \sum_{k=1}^{N_i^{mp}} k_{ik}^{mp,s} \prod_{j=1}^{N_c} (T_j^a)^{o_{ijk}^{mt,s}} \prod_{j=1}^{N_c} (\gamma_j^c C_j^c)^{o_{ijk}^{mc,s}} \prod_{j=1}^{N_x} (\gamma_j^x C_j^x)^{o_{ijk}^{mx,s}} \left[1 - \left(\frac{IAP_{ik}^m}{K_{ik}^m}\right)^{-1}\right]\right], 0\right] \tag{3.115}$$

The product of the concentrations and/or activities controlling the reaction progress

dissolution far-from-equilibrium	$R_i^{md,s}$	$=$	$-\left[S_i \sum_{k=1}^{N_i^{mp}} k_{ik}^{md,s} RP_{ik}^{m,s}\right]$
precipitation far-from-equilibrium	$R_i^{mp,s}$	$=$	$\left[S_i \sum_{k=1}^{N_i^{mp}} k_{ik}^{mp,s} RP_{ik}^{m,s}\right]$
reversible dissolution rate constant	$R_i^{m,s}$	$=$	$-\left[S_i \sum_{k=1}^{N_i^{mp}} k_{ik}^{md,s} RP_{ik}^{m,s}\right]\left[1-\left(\frac{IAP_{ik}^m}{K_{ik}^m}\right)^{(\sigma_{ik}^m)^{-1}}\right]$
reversible precipitation rate constant	$R_i^{m,s}$	$=$	$\left[S_i \sum_{k=1}^{N_i^{mp}} k_{ik}^{mp,s} RP_{ik}^{m,s}\right]\left[1-\left(\frac{IAP_{ik}^m}{K_{ik}^m}\right)^{\sigma_{ik}^m}\right]$
dissolution towards equilibrium	$R_i^{md,s}$	$=$	$-\max\left[\left[S_i \sum_{k=1}^{N_i^{mp}} k_{ik}^{md,s} RP_{ik}^{m,s}\left[1-\frac{IAP_{ik}^m}{K_{ik}^m}\right]\right],0\right]$
precipitation towards equilibrium	$R_i^{mp,s}$	$=$	$\max\left[\left[S_i \sum_{k=1}^{N_i^{mp}} k_{ik}^{mp,s} RP_{ik}^{m,s}\left[1-\left(\frac{IAP_{ik}^m}{K_{ik}^m}\right)^{-1}\right]\right],0\right]$

Table 3.2: Rate expressions for surface-controlled dissolution-precipitation reactions

of surface-controlled dissolution-precipitation reactions can be defined as:

$$RP_{ik}^{m,s} = \prod_{j=1}^{N_c} (T_j^a)^{o_{ijk}^{mt,s}} \prod_{j=1}^{N_c} (\gamma_j^c C_j^c)^{o_{ijk}^{mc,s}} \prod_{j=1}^{N_x} (\gamma_j^x C_j^x)^{o_{ijk}^{mx,s}} \tag{3.116}$$

Equation 3.116 can be substituted to simplify rate expressions 3.106, 3.107, 3.112, 3.113, 3.114 and 3.115. This set of reaction expressions can be used to define the reaction progress of reversible and irreversible dissolution-precipitation reactions under far-from-equilibrium conditions and near equilibrium. Table 3.2 summarizes the rate expressions and defines their range of applicability.

Diffusion-Controlled Reactions

The dissolution of minerals might also be controlled by diffusive transport of reactant and product species through a protective surface layer covering the reactive mineral surface. The derivation of the present formulation is based on the shrinking core model developed

by *Levenspiel* [1972] and applied by *Davis and Ritchie* [1986] and *Wunderly et al.* [1996] among others. Figure 3.4 shows the transient evolution of a reacting mineral particle covered by a protective surface coating between the times t_0 and t_1. The radius r_i^p of the

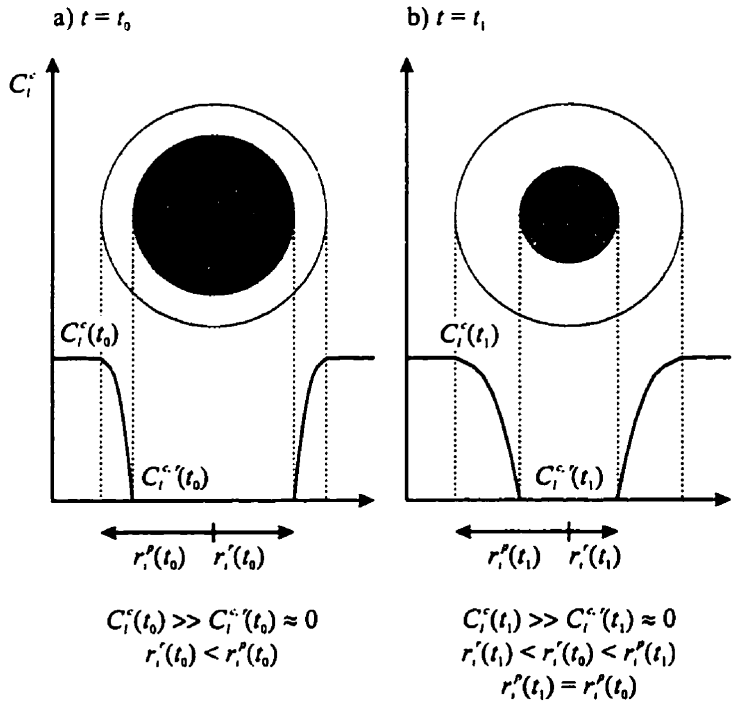

Figure 3.4: Transient evolution of particle, diffusion-controlled reaction - dissolution

particle remains unchanged during the dissolution process, the original mineral is replaced by a protective surface layer. This is a reasonable assumption if a leached layer or an alteration rim is forming, but is not necessarily the case if a surface coating is forming on the mineral particles due to the precipitation of secondary minerals. The shrinking core model can, nevertheless, be used as an approximation for the latter case. The reactive core shrinks during the dissolution process, which leads to progressively decreasing reaction rates with increasing surface layer thickness. The reacting species have to be transported through the surface layer before the reaction between the unreacted core of the mineral and the reacting species can occur. The location of the unreacted core of the mineral is defined by the radius r_i^r. The reaction will be limited in many cases by the availability of one reacting species, here defined as the primary reactant A_l^c. It is practical to reformulate

reaction equation 3.91 to account for the special role of the primary reactant A_l^c. An appropriate stoichiometric relationship can be written as

$$A_i^m + \nu_{il}^m A_l^c + \rightarrow \sum_{\substack{j=1 \\ j \neq l}}^{N_c} \nu_{ij}^m A_j^c \qquad i = 1, N_m, \tag{3.117}$$

where ν_{il}^m is the stoichiometric coefficient of the primary reactant species for the i^{th} mineral. The present formulation assumes that other reactant species A_j^c involved in the dissolution reaction are available in sufficient concentrations and do not limit the progress of the reaction. The primary reactant is consumed at the reactive mineral surface causing a concentration gradient to develop within the surface coating through which the primary reactant is transported to the reactive surface. The concentration at the particle surface is assumed to be equal to the concentration in the bulk solution C_l^c, while the concentration on the reactive surface of the mineral is defined by $C_l^{c,r}$, and is less than the bulk concentration. A purely diffusion-controlled reaction implies that the time scales of the transport of the primary reactant through the surface coating is much longer than the time scale of the chemical reaction taking place on the reactive mineral surface. This implies, in practical terms, that the primary reactant is consumed immediately at the reactive mineral surface. The concentration of the primary reactant at the mineral surface can therefore be approximated by $C_l^{c,r} \approx 0$, which simplifies the determination of the reaction rate. The rate-limiting step under these conditions is the supply of the primary reactant to the reactive surface. The rate expression that describes diffusion-controlled dissolution of minerals can therefore be based on the diffusional mass flux of the primary reactant through the protective surface coating. An example for this type of behavior is the oxidation of sulfide minerals such as pyrrhotite and pyrite after an initial period of surface-controlled dissolution [*Davis and Ritchie*, 1986].

The formulation requires the specification of an initial surface coating thickness defined by $r_i^p - r_i^r$ at $t = t_0$. However, the present formulation does not account for the formation of a leached layer from the original primary mineral due to an incongruent dissolution process, neither does it identify the composition of the protective layer. The model formulation is strictly only valid under the assumption that the reactants diffusing towards the reactive mineral surface do not interact with the reaction products diffusing back into the bulk solution.

The dissolution rate is proportional to the diffusional mass flux of the primary reactant

species through the protective surface layer. Steady state conditions can be assumed if the time scale of the core shrinking is much longer than the time scale of diffusive transport. *Levenspiel* [1972] reported that diffusional transport of the primary reactant through the protective surface layer is much faster than the rate at which the unreacted core is shrinking. Fick's first law can therefore be applied to approximate the flux of the primary reactant through the protective surface layer. Assuming that the mineral particle is spherical, the flux per unit area reactive mineral surface can be expressed as:

$$J_i^{md,t,u} = 10^3 D_i^m \frac{r_i^p}{(r_i^p - r_i^r) r_i^r} (C_l^c - C_l^{c,r}) \tag{3.118}$$

where $J_i^{md,t,u}$ [mol m^{-2} mineral s^{-1}] defines the mass flux of the primary reactant species at the surface of the unreacted core per unit reactive surface area of the mineral A_i^m [*Levenspiel*, 1972]. The flux is given in units [mol m^{-2} mineral s^{-1}]. D_i^m [m^2 s^{-1}] is the diffusion coefficient of the primary reactant through the water filled porosity of the surface coating. The factor 10^3 is necessary to convert dissolved species concentrations, which are usually given in units [mol l^{-1} water], to units [mol m^{-3} water] to be consistent with the formulation for surface-controlled reactions. Equation 3.118 can be simplified because it is assumed that the concentration of the primary reactant species on the reactive mineral surface is negligibly small. This simplification leads to:

$$J_i^{md,t,u} = 10^3 D_i^m \frac{r_i^p}{(r_i^p - r_i^r) r_i^r} C_l^c \tag{3.119}$$

The dissolution rate of the mineral per unit surface area is proportional to the stoichiometric coefficient of the primary reactant in reaction equation 3.117 and can thus be written as:

$$R_i^{md,t,u} = -10^3 \frac{D_i^m}{\nu_{il}^m} \frac{r_i^p}{(r_i^p - r_i^r) r_i^r} C_l^c \tag{3.120}$$

where $R_i^{md,t,u}$ is defined in units [mol m^{-2} mineral s^{-1}]. The bulk porous medium dissolution rate can be obtained by multiplying rate expression 3.120 by the reactive surface area of the mineral:

$$R_i^{md,t} = -10^3 S_i \frac{D_i^m}{\nu_{il}^m} \frac{r_i^p}{(r_i^p - r_i^r) r_i^r} C_l^c \tag{3.121}$$

The reaction rate $R_i^{md,t}$ is given in units [mol l^{-1} bulk s^{-1}], provided that the reactive

surface area is given in units [m^2 mineral l^{-1} bulk].

The oxidation of pyrite, for example, is often described as a diffusion-controlled reaction [e.g. *Davis and Ritchie*, 1986, *Ritchie*, 1994, *Wunderly et al.*, 1996]. Assuming that pyrite is represented by the mineral A_3^m and that the overall oxidation of pyrite can be expressed in terms of dissolved oxygen following the reaction stoichiometry given in equation 3.94, an appropriate rate expression can be written as

$$R_3^{md,t} = -10^3 S_3 \frac{D_3^m}{3.5} \frac{r_3^p}{(r_3^p - r_3^r) r_3^r} [O_2(aq)],$$

where D_3^m defines the bulk diffusion coefficient for dissolved oxygen through the surface coating on the pyrite particles.

The rate expression given by equation 3.121 can be generalized as:

$$R_i^{md,t} = -10^3 S_i D_i^m \frac{r_i^p}{(r_i^p - r_i^r) r_i^r} \left[\sum_{j=1}^{N_c} o_{ij}^{mt,t} T_j^a + \sum_{j=1}^{N_c} o_{ij}^{mc,t} C_j^c + \sum_{j=1}^{N_x} o_{ij}^{mx,t} C_j^x \right] \quad (3.122)$$

The factors $o_{ij}^{mc,t}$ are here used to represent the inverse of the stoichiometric coefficient ν_{il}^m of the primary reactant in reaction equation 3.117. The use of the factors $o_{ij}^{mx,t}$ facilitates the consideration of aqueous complexes as primary reactants and $o_{ij}^{mt,t}$ allows the specification of total aqueous component concentrations. At this point it should be noted that this formulation requires that only one of the factors $o_{ij}^{mt,t}$, $o_{ij}^{mc,t}$ and $o_{ij}^{mx,t}$ be a positive real number, while all remaining factors must be set to zero.

The oxidation of pyrite, for example, may take place along two primary reaction pathways as was discussed previously. It is therefore necessary to allow the consideration of parallel reaction pathways also for diffusion-controlled dissolution reactions. An appropriate stoichiometric relationship for the k^{th} parallel reaction pathway can be written as:

$$A_i^m + \nu_{ilk}^m A_l^c \rightarrow \sum_{\substack{j=1 \\ j \neq l}}^{N_c} \nu_{ijk}^m A_j^c \qquad i = 1, N_m,\ k = 1, N_i^{mp} \quad (3.123)$$

where ν_{ilk}^m is the stoichiometric coefficient of the primary reactant in the k^{th} parallel reaction pathway. The subscript l defines a different species for each parallel reaction

pathway. Expanding reaction expression 3.122 for parallel reaction pathways leads to:

$$R_i^{md,t} = -10^3 S_i \frac{r_i^p}{(r_i^p - r_i^r) r_i^r} \sum_{k=1}^{N_i^{mp}} D_{ik}^m \left[\sum_{j=1}^{N_c} o_{ijk}^{mt,t} T_j^a + \sum_{j=1}^{N_c} o_{ijk}^{mc,t} C_j^c + \sum_{j=1}^{N_x} o_{ijk}^{mx,t} C_j^x \right] \quad (3.124)$$

where $o_{ijk}^{mt,t}$, $o_{ijk}^{mc,t}$ and $o_{ijk}^{mx,t}$ define the inverse of the stoichiometric coefficient ν_{ilk}^m of the primary reactant in the k^{th} parallel reaction pathway. An appropriate reaction expression for the diffusion-controlled oxidative dissolution of pyrite with dissolved oxygen and ferric iron as oxidants can be written as:

$$R_3^{md,t} = -10^3 S_3 \frac{r_3^p}{(r_3^p - r_3^r) r_3^r} \left[\frac{D_{31}^m}{3.5} [\mathrm{O_2(aq)}] + \frac{\mathrm{D_{32}^m}}{14} [\mathrm{Fe^{3+}}] \right]$$

A rate expression for diffusion-controlled reactions that accounts for the build-up of reaction products in the bulk solution, can be written as:

$$R_i^{md,t} = -\max \left[\left[10^3 S_i \frac{r_i^p}{(r_i^p - r_i^r) r_i^r} \sum_{k=1}^{N_i^{mp}} D_{ik}^m \left[\sum_{j=1}^{N_c} o_{ijk}^{mt,t} T_j^a + \sum_{j=1}^{N_c} o_{ijk}^{mc,t} C_j^c + \sum_{j=1}^{N_x} o_{ijk}^{mx,t} C_j^x \right] \left[1 - \frac{IAP_{ik}^m}{K_{ik}^m} \right] \right], 0 \right] \quad (3.125)$$

It should be noted that this formulation is essentially very similar to the formulation for surface-controlled reactions. Comparing, for example, the rate expressions for dissolution under far-from-equilibrium conditions (equations 3.106 and 3.122) shows that the rate constant for surface-controlled reactions is replaced by a diffusion coefficient and geometrical mineral parameters that will influence the reaction progress. A pseudo rate constant for the diffusion-controlled dissolution of the mineral A_i^m can be expressed in terms of the diffusion coefficient of the primary reactant and the geometrical parameters of the mineral:

$$k_{ik}^{md,t} = 10^3 D_{ik}^m \left[\frac{r_i^p}{(r_i^p - r_i^r) r_i^r} \right] \quad (3.126)$$

The quotient $RP_{ik}^{m,t}$ of the concentration and the stoichiometric coefficient of the primary

reactant can be defined as:

$$RP_{ik}^{m,t} = \sum_{j=1}^{N_c} o_{ijk}^{mt,t} T_j^a + \sum_{j=1}^{N_c} o_{ijk}^{mc,t} C_j^c + \sum_{j=1}^{N_x} o_{ijk}^{mx,t} C_j^x \tag{3.127}$$

Equation 3.126 and 3.127 can be substituted into rate expressions 3.122 and 3.125 for simplification. The resulting set of reaction equations can be used to describe the reaction progress of diffusion-controlled dissolution reactions under far-from-equilibrium conditions and when the reaction rate becomes influenced by the build-up of reaction products.

dissolution far-from-equilibrium	$R_i^{md,t}$	$=$	$-$	$\left[S_i \sum_{k=1}^{N_i^{mp}} k_{ik}^{md,t} RP_{ik}^{m,t} \right]$
dissolution towards equilibrium	$R_i^{md,t}$	$=$	$-$ max	$\left[\left[S_i \sum_{k=1}^{N_i^{mp}} k_{ik}^{md,t} RP_{ik}^{m,t} \left[1 - \frac{IAP_{ik}^m}{K_{ik}^m} \right] \right], 0 \right]$

Table 3.3: Rate expressions for diffusion-controlled dissolution-precipitation reactions

Reactive Surface Area

All rate expressions developed in the previous section are scaled by the reactive surface area S_i, which defines the mineral surface that is actively participating in dissolution precipitation reactions. The reactive surface area has to be defined in units [m^2 mineral l^{-1} bulk] to be consistent with the rate expressions developed in the previous sections.

It is possible to define the reactive surface area in terms of the geometric mineral parameters [e.g. *White and Peterson*, 1990, *Steefel and Lasaga*, 1994]. The geometric surface area [m^2 mineral] of a mineral particle can be defined as:

$$S_i^{g,p} = 4\pi (r_i^r)^2 \tag{3.128}$$

The volume of a single mineral particle [m^3 mineral] is given by:

$$V_i^p = \frac{4}{3}\pi (r_i^r)^3 \tag{3.129}$$

The reactive surface area can therefore be defined as

$$S_i = 10^{-3}\varphi_i \frac{S_i^{g,p}}{V_i^p} = 3 \cdot 10^{-3}\frac{\varphi_i}{r_i^r}, \tag{3.130}$$

where φ_i is the volume fraction of the mineral defined in units [m^3 mineral m^{-3} bulk] and 10^{-3} is a conversion factor [m^3 bulk l^{-1} bulk]. Calculating the reactive surface area based on geometric mineral parameters can only be a coarse approximation due to deviations of the mineral grains from sphericity and surface roughness [*White and Peterson*, 1990]. It is often the case that the geometric surface area does not coincide with the reactive surface area observed in laboratory experiments or in the field. *White and Peterson* [1990], reported that reactive surface areas are commonly 1 to 3 orders of magnitudes lower than geometric surface areas. *Schnoor* [1990] reported discrepancies between laboratory and field determined reaction rates on the order of 1-2 magnitudes. The discrepancies were attributed to preferential flow and limited contact between the bulk solution and the mineral surface. It is therefore useful to include a scaling factor F_i into equation 3.130, which can be used to adjust the reaction rate to the observed conditions:

$$S_i = 3 \cdot 10^{-3} F_i \frac{\varphi_i}{r_i^r} \tag{3.131}$$

In many cases, it is more practical to specify a measured or empirically determined reactive surface area independent of geometrical mineral parameters:

$$S_i = 10^{-3} S_i^e \tag{3.132}$$

where S_i^e defines an empirically determined reactive surface area in units [m^2 mineral m^{-3} bulk]. Physical surface areas can, for example, be determined using the BET-method [*White and Peterson*, 1990].

The change of reactive surface area during the dissolution of a mineral phase can also be approximated by a two-thirds power relationship of the form [*Lichtner*, 1992, 1996a]

$$S_i = S_i^0 \left(\frac{\phi_i}{\phi_i^0}\right)^{2/3} \tag{3.133}$$

where S_i^0 represents the initial reactive surface area of the i^{th} mineral and ϕ_i^0 defines the initial volume fraction of the mineral phase. This relationship has the advantage of being completely independent of geometric mineral parameters and can therefore be applied to

update the reactive surface area specified in equation 3.132.

Symbolic Representation and Source-Sink Terms

The general rate expressions for surface-controlled dissolution-precipitation reactions as summarized in Table 3.2 and for diffusion-controlled dissolution reactions as shown in Table 3.3 can be expressed in symbolic form. The rate expressions can be written as a function of the dissolution and precipitation rate constants, the diffusion coefficients of the primary reactant species through a protective surface layer, geometric parameters such as the representative mineral particle radius, the thickness of the protective surface layer, and the reactive mineral surface area. The rate expression will depend in addition on the activities of the components as species in solution and aqueous complexes, total aqueous component concentrations, and the equilibrium constant of the reaction. The symbolic representation of the rate expressions can be written as:

$$R_i^m = f(k_{ik}^{md}, k_{ik}^{mp}, D_{ik}^m, r_i^p, r_i^r, S_i, a_j^c, a_i^x, T_j^a, K_i^m) \qquad i = 1, N_m,\ k = 1, N_i^{mp} \tag{3.134}$$

The source-sink term defining the consumption or production of aqueous components due to mineral dissolution-precipitation reactions can be defined as

$$Q_j^{a,m} = -\sum_{i=1}^{N_m} \sum_{k=1}^{N_i^{mp}} \nu_{ijk}^m R_{ik}^m \qquad j = 1, N_c, \tag{3.135}$$

where the parallel reaction pathways are considered separately. If all dissolved species with non-stoichiometric coefficients in the parallel dissolution-precipitation reactions are at equilibrium, the source and sink term can be simplified to:

$$Q_j^{a,m} = -\sum_{i=1}^{N_m} \nu_{ij}^m R_i^m \qquad j = 1, N_c \tag{3.136}$$

Chapter 4

Numerical Methods

This chapter introduces the numerical techniques used for the solution of the governing equations for variably-saturated flow and reactive transport. The governing equations are approximated by discretized equations and global mass balance calculations are described for the flow and reactive transport solutions. Several numerical techniques have been used or developed to increase the accuracy, efficiency and robustness of the present model. These techniques are described briefly and their influence on the performance of the model and the accuracy of the model results is investigated using an example test problem. In particular spatial weighting schemes [*van Leer*, 1974, *Unger et al.*, 1996] are addressed, as well as an adaptive time stepping and update modification algorithm, activity update techniques [*Lichtner*, personal communication, 1997], sparse matrix data structures and the treatment of finite mineral phases. The test problem deals with the generation of acid mine drainage in variably-saturated media and subsequent reactive transport. The problem is designed to include the majority of the model capabilities and involves transport processes in the aqueous and gaseous phase, gas dissolution-exsolution reactions, complexation and oxidation-reduction reactions and dissolution-precipitation reactions.

4.1 Spatial and Temporal Discretization

The governing equations presented in the previous chapter have been implemented using the finite volume discretization method, which is equivalent to the block-centered finite difference method for regular geometries. The method is locally mass-conservative, which

is a general requirement for a physically meaningful solution and is a necessity for the solution of reactive transport using the global implicit solution method. The governing equations are discretized in one, two and three spatial dimensions. The influence coefficients are calculated prior to the assembly of the global matrix equation. Therefore, other spatial discretization methods can be implemented during future model development without major re-structuring of the code.

Fully implicit time weighting is used for temporal discretization of the governing equations. Centered time weighting is not practical for reactive transport problems, because the wide range in time scales of physical and geochemical processes leads to a stiff system of equations [*Hindmarsh and Petzold*, 1995a]. The partly explicit nature of centered time weighting may limit the time step size dramatically [*Hindmarsh and Petzold*, 1995a] and is therefore not considered here. The implementation of other, more suitable higher order methods [e.g. *Hindmarsh and Petzold*, 1995b] is beyond the scope of the present model development.

4.1.1 Variably-Saturated Flow

Spatial and temporal discretization of the mass conservation equation for variably-saturated flow (equation 3.1) using the finite volume technique leads to

$$\left[S_{a,k}^{N+1} S_s \frac{h_k^{N+1} - h_k^N}{\Delta t} + \phi \frac{S_{a,k}^{N+1} - S_{a,k}^N}{\Delta t}\right] V_k$$
$$- \sum_{l \in \eta_k} k_{ra,kl} \gamma_{kl} \left[h_l^{N+1} - h_k^{N+1}\right] - Q_{a,k}^{N+1} = 0 \quad k = 1, N_v, \tag{4.1}$$

where the subscript k defines the k^{th} control volume. η_k defines the number of adjacent control volumes, which can vary from $\eta_k = 1$ for a boundary control volume in case of a one-dimensional problem to $\eta_k = 6$ for an internal control volume (assuming blocks) in case of a three-dimensional spatial discretization. The subscript l identifies the adjacent control volumes, Δt is the time increment, $N + 1$ represents the new time level and N defines the old time level. V_k is the volume of the k^{th} control volume. N_v defines the number of control volumes in the solution domain. $k_{ra,kl}$ is the representative relative permeability used for the flux calculation between control volumes k and l. Different spatial weighting schemes can be applied to define this quantity, as will be discussed in

section 4.7. The influence coefficients γ_{kl} can be calculated according to

$$\gamma_{kl} = \frac{A_{kl}}{d_{kl}} K_{kl}, \tag{4.2}$$

where A_{kl} is the interfacial area between the control volumes k and l, and d_{kl} is the distance between the centroids of the control volumes. All material properties are here defined on a control volume basis. It is therefore necessary to determine averaged hydraulic conductivities and relative permeabilities for the calculation of interfacial fluxes. K_{kl} is the representative hydraulic conductivity used for the flux calculation between control volumes k and l, and can be calculated based on the distance-weighted harmonic mean:

$$K_{kl} = \frac{2K_{i,k}K_{i,l}d_{kl}}{K_{i,k}d_{i,l} + K_{i,l}d_{i,k}}, \tag{4.3}$$

where $K_{i,k}$ and $K_{i,l}$ are the hydraulic conductivities of the control volumes k and l, respectively, perpendicular to the interfacial area A_{kl}. The subscript i identifies here the spatial coordinates x, y and z. $d_{i,k}$ and $d_{i,l}$ define the spatial extent of the two adjacent control volumes perpendicular to the interfacial area A_{kl}. Porosity changes due to chemical processes such as the dissolution or precipitation of minerals is at this time not considered in equation 4.1.

4.1.2 Reactive Transport

The global mass conservation equations 3.28 for the components A_j^c can be discretized in space using the finite volume technique and by applying fully implicit time weighting. The discretized equations can be written as:

$$\begin{aligned}
&\frac{\phi V_k}{\Delta t}\left[S_{a,k}^{N+1}T_{j,k}^{a,N+1} - S_k^{a,N}T_{j,k}^{a,N}\right] + \frac{\phi V_k}{\Delta t}\left[S_{g,k}^{N+1}T_{j,k}^{g,N+1} - S_k^{g,N}T_{j,k}^{g,N}\right] \\
&\quad + \sum_{l\in\eta_k} v_{a,kl}T_{j,kl}^{a,N+1} - \sum_{l\in\eta_k}\gamma_{a,kl}^{d}\left[T_{j,l}^{a,N+1} - T_{j,k}^{a,N+1}\right] - \sum_{l\in\eta_k}\gamma_{g,kl}^{d}\left[T_{j,l}^{g,N+1} - T_{j,k}^{g,N+1}\right] \\
&\quad + \frac{V_k}{\Delta t}\left[T_{j,k}^{s,N+1} - T_{j,k}^{s,N+1}\right] - Q_{j,k}^{a,a,N+1}V_k - Q_{j,k}^{a,m,M}V_k = 0 \qquad j = 1, N_c
\end{aligned} \tag{4.4}$$

$v_{a,kl}$ is the aqueous phase flux between control volumes k and l, $\gamma_{a,kl}^{d}$ defines the influence coefficient for the dispersive flux in the aqueous phase and $\gamma_{g,kl}^{d}$ is the influence coefficient for the diffusive flux in the gaseous phase. $T_{j,kl}^{a,N+1}$ defines the total aqueous component

concentration used for the advective flux calculations across the interface between the control volumes k and l. This quantity is discussed further in Section 4.7 below. Equation 4.4 is based on the assumption that porosity changes due to physical and chemical processes are negligible, the storage terms due to porosity changes have therefore been omitted. The interfacial flux $v_{a,kl}$ can be obtained directly from the solution of the flow equation:

$$v_{a,kl} = k_{ra,kl}\gamma_{kl}\left[h_l^{N+1} - h_k^{N+1}\right] \tag{4.5}$$

The influence coefficients $\gamma^d_{a,kl}$ for the dispersive flux terms can be calculated in a similar manner as the influence coefficients for the flow solution and are defined as [*Unger et al.*, 1996]

$$\gamma^d_{a,kl} = \frac{A_{kl}}{d_{kl}} S^{N+1}_{a,kl}\phi_{kl}D_{a,kl}, \tag{4.6}$$

where $D_{a,kl}$ defines the effective dispersion coefficient in the aqueous phase between control volumes k and l. The computation of the dispersion coefficient is based on the implementation by *Forsyth et al.* [1998], which makes use of a pseudo-finite element formulation based on equations 3.6-3.11 and 3.12. This formulation allows the consideration of cross-derivative terms in the framework of a finite volume discretization [*Forsyth et al.*, 1998]. $S_{a,kl}$ is an average aqueous phase saturation used for the calculation of the aqueous phase dispersive flux between control volumes k and l. $S_{a,kl}$ can be evaluated using volume-weighted harmonic averaging according to:

$$S_{a,kl} = \frac{S_{a,k}S_{a,l}(V_k + V_l)}{S_{a,k}V_l + S_{a,l}V_k} \tag{4.7}$$

ϕ_{kl} is the corresponding averaged porosity, which can be calculated according to:

$$\phi_{kl} = \frac{\phi_k\phi_l(V_k + V_l)}{\phi_k V_l + \phi_l V_k} \tag{4.8}$$

Influence coefficients $\gamma^d_{g,kl}$ for the diffusive flux between control volumes k and l in the gaseous phase can be calculated according to

$$\gamma^d_{g,kl} = \frac{A_{kl}}{d_{kl}} S^{N+1}_{g,kl}\phi_{kl}D_{g,kl}, \tag{4.9}$$

where $D_{g,kl}$ is the effective diffusion coefficient in the gaseous phase perpendicular to the interfacial area A_{kl}, which can be obtained using equations 3.20-3.22 and 3.12. The averaged gas phase saturation $S_{g,kl}$ can be calculated as defined in equation 4.7 for the aqueous phase.

It can be generally assumed that mineral parameters will change slowly in comparison to the changes in aqueous concentrations [e.g. *Lichtner*, 1988]. All mineral parameters are therefore updated explicitly in time. This approach is particularly beneficial because it reduces the number of primary unknowns per control volume by the number of minerals N_m. For the present model formulation, this implies that the number of primary unknowns is $N_p = N_c$ instead of $N_p = N_c + N_m$. A similar approach has been used, for example, by *Steefel and Lasaga* [1994]. The assumption of slowly changing mineral parameters is not always valid. Problems can occur if a mineral becomes depleted during a single time step. The complete dissolution of a mineral phase requires special treatment to avoid mass balance errors. This issue will be discussed in more detail in Section 4.5 below.

The volume fraction of the mineral A_i^m can be obtained after completion of a time step by discretizing equation 3.29 in time and solving for the volume fraction at the new time level [*Steefel and Lasaga*, 1994]:

$$\varphi_i^{N+1} = \varphi_i^N + V_i^m R_i^{m,N+1} \Delta t \tag{4.10}$$

The radius $r_i^{r,N+1}$, which defines the location of the mineral's reactive surface and is an essential parameter in the case of diffusion-controlled dissolution reactions, can be updated using:

$$r_i^{r,N+1} = \left[\frac{\varphi_i^{N+1}}{\varphi_i^N} \left[r_i^{r,N} \right]^3 \right]^{(1/3)} \tag{4.11}$$

The mineral reactive surface area S_i^{N+1} can be calculated based on φ_i^{N+1} and $r_i^{r,N+1}$ if the reactive surface area is computed based on geometric parameters:

$$S_i^{N+1} = 3 \cdot 10^{-3} F_i \varphi_i^{N+1} r_i^{r,N+1} \tag{4.12}$$

An alternative method is given by a two-thirds power relationship [*Lichtner*, 1996a]:

$$S_i^{N+1} = S_i^0 \left(\frac{\varphi_i^{N+1}}{\varphi_i^0} \right)^{2/3} \tag{4.13}$$

S_i^0 and φ_i^0 define the initial reactive surface area and volume fraction of the mineral A_i^m, respectively. It can be shown that equations 4.12 and 4.13 lead to equivalent results if the initial reactive surface area is calculated using the geometrical mineral parameters. Equation 4.13 has the advantage of being defined even if the mineral in question becomes completely depleted. A further, more important, advantage is that the reactive surface area can be determined independent of average particle sizes. The model also allows the specification of a constant reactive surface area, which is specifically useful for the formation of secondary minerals, or when the model is used to approximate equilibrium behavior. In the latter case, the reactive surface area has to be chosen large enough that the local equilibrium assumption is satisfied.

The source-sink-term due to mineral dissolution-precipitation reactions $Q_j^{a,m,M}$ is only implicit in time with respect to the aqueous parameters, but not with respect to the mineral parameters [*Steefel and Lasaga*, 1994], as is indicated by the superscript M replacing $N+1$. The source-sink term depends directly on the dissolution-precipitation rates, as defined in equation 3.135 and 3.136. The far-from-equilibrium dissolution rate of a mineral is given here in time-discretized form as an illustrative example:

$$\begin{aligned} R_i^{md,s,M} = & - S_i^N \sum_{k=1}^{N_i^{mp}} k_{ik}^{md,s} \\ & \prod_{j=1}^{N_c} (T_j^{a,N+1})^{o_{ijk}^{mt,s}} \prod_{j=1}^{N_c} (\gamma_j^{c,L} C_j^{c,N+1})^{o_{ijk}^{mc,s}} \prod_{j=1}^{N_x} (\gamma_j^{x,L} C_j^{x,N+1})^{o_{ijk}^{mx,s}} \end{aligned} \tag{4.14}$$

The superscript L on the activity coefficients indicates the time level at which the activity coefficients are evaluated [*Lichtner*, personal communication, 1997]. How the time level chosen influences the accuracy and robustness of the solution is discussed in more detail in Section 4.8.

4.2 Mass Balance Calculations

The present model formulation includes detailed mass balance calculations for variably-saturated flow and reactive transport. This is specifically useful for the reactive transport simulations, because it facilitates the evaluation of the interactions between aqueous, gaseous, and solid species. Mass balance calculations include absolute and relative mass balance errors per time step and the corresponding cumulative errors. Mass balance calculations also include the total mass of the species contained in the solution domain, the total mass gain and mass loss due to fluxes across the boundaries, change in storage, and mass transfer between the phases in the case of reactive transport. Mass balance calculations for variably-saturated flow are formulated in a standard way and consequently not explicitly reported.

The determination of absolute and relative mass balance errors is performed for the aqueous phase in terms of total aqueous component concentrations. All gaseous species, sorbed species, and mineral phases are treated as secondary unknowns, and therefore, do not require the computation of mass balance errors. It is nevertheless useful to determine the total system mass for all aqueous, gaseous, sorbed and mineral species. The total system mass [mol] of the component A_j^c in terms of total aqueous component concentrations can be calculated according to

$$M_j^{a,N+1} = 10^3 \sum_{k=1}^{N_v} V_k S_{a,k}^{N+1} \phi_k T_{j,k}^{a,N+1}, \tag{4.15}$$

where the factor 10^3 defines the conversion [l m^{-3}]. The total system mass [mol] in the gaseous phase for the i^{th} gas can be defined similarly:

$$M_i^{g,N+1} = 10^3 \sum_{k=1}^{N_v} V_k S_{g,k}^{N+1} \phi_k C_{i,k}^{g,N+1} \tag{4.16}$$

The total system mass [mol] of mineral A_i^m contained in the solution domain is defined by:

$$M_i^{m,N+1} = 10^3 \sum_{k=1}^{N_v} \frac{V_k}{V_i^m} \varphi_{i,k}^{N+1} \tag{4.17}$$

The total system mass [mol] can also be calculated for the sorbed species A_i^s according

to:

$$M_i^{s,N+1} = 10^3 \sum_{k=1}^{N_v} V_k C_{i,k}^{s,N+1} \tag{4.18}$$

The present model formulation also allows determination of the total system mass for selected aqueous species A_i^d, where the dissolved species can be either a component as species in solution or an aqueous complex. For example, it is more useful to calculate the system mass for dissolved oxygen in terms of the species concentration rather than in terms of total aqueous component concentrations, because the total aqueous oxygen concentration is not a physically meaningful quantity, if O_2(aq) is chosen as the redox master variable. The total system mass [mol] for the selected aqueous species A_i^d is given by:

$$M_i^{d,N+1} = 10^3 \sum_{k=1}^{N_v} V_k S_{a,k}^{N+1} \phi_k C_{i,k}^{d,N+1} \tag{4.19}$$

The determination of mass balance errors for the aqueous phase is based on the calculation of all contributions of mass over the solution domain during a time step and in a cumulative sense. It is most appropriate to express all contributions to the mass balance as rates rather than absolute changes over a single time step to facilitate an analysis of transient conditions. The total mass gain [mol s^{-1}] due to aqueous mass fluxes across the domain boundary can be calculated according to

$$Q_j^{a,\text{in},N+1} = 10^3 \sum_{k=1}^{N_b} J_k^b(T_j^{a,N+1}) \quad \text{if} \quad J_k^b(T_j^{a,N+1}) \geq 0, \tag{4.20}$$

where $J_k^b(T_j^{a,N+1})$ defines the gain due to mass fluxes across the domain boundary for control volume k in terms of total aqueous component concentrations. N_b defines the number of control volumes located adjacent to the domain boundary. The total mass loss [mol s^{-1}] for component A_j^c due to aqueous mass fluxes across the domain boundary is given by:

$$Q_j^{a,\text{out},N+1} = -10^3 \sum_{k=1}^{N_b} J_k^b(T_j^{a,N+1}) \quad \text{if} \quad J_k^b(T_j^{a,N+1}) < 0 \tag{4.21}$$

The rate of change in storage [mol s^{-1}] for component A_j^c in the aqueous phase is given

by:

$$\Delta M_j^{a,N+1} = \frac{10^3}{\Delta t} \sum_{k=1}^{N_v} V_k \phi_k \left(S_{a,k}^{N+1} T_{j,k}^{a,N+1} - S_{a,k}^{N} T_{j,k}^{a,N} \right) \tag{4.22}$$

It is necessary to compute the mass gain, mass loss, and the change in storage for all gases to obtain the source-sink term for the aqueous phase concentrations due to gas dissolution-exsolution reactions. The total mass gain [mol s^{-1}] for the gas A_i^g due to mass fluxes across the domain boundary can be calculated according to:

$$Q_i^{g,\text{in},N+1} = 10^3 \sum_{k=1}^{N_b} J_k^b(C_i^{g,N+1}) \quad \text{if} \quad J_k^b(C_i^{g,N+1}) \geq 0 \tag{4.23}$$

The corresponding total mass loss [mol s^{-1}] due to gas fluxes across the boundary can be obtained from:

$$Q_i^{g,\text{out},N+1} = 10^3 \sum_{k=1}^{N_b} J_k^b(C_i^{g,N+1}) \quad \text{if} \quad J_k^b(C_i^{g,N+1}) < 0 \tag{4.24}$$

The rate of change in storage [mol s^{-1}] for the i^{th} gas is given by:

$$\Delta M_i^{g,N+1} = \frac{10^3}{\Delta t} \sum_{k=1}^{N_v} V_k \phi_k \left(S_{g,k}^{N+1} C_{i,k}^{g,N+1} - S_{g,k}^{N} C_{i,k}^{g,N} \right) \tag{4.25}$$

The source-sink term [mol s^{-1}] for the total aqueous component concentrations due to gas dissolution-exsolution reactions can then be computed according to:

$$Q_j^{a,g,N+1} = \sum_{i=1}^{N_g} \nu_{ij}^g \left[\Delta M_i^{g,N+1} - Q_i^{g,\text{in},N+1} + Q_i^{g,\text{out},N+1} \right] \tag{4.26}$$

A similar approach can be taken for the sorbed species. These species are not subject to physical transport. The only term to consider is the rate of change in storage [mol s^{-1}]:

$$\Delta M_i^{s,N+1} = \frac{10^3}{\Delta t} \sum_{k=1}^{N_v} V_k [C_{i,k}^{s,N+1} - C_{i,k}^{s,N}] \tag{4.27}$$

The source-sink term [mol s^{-1}] for the total aqueous component concentrations due to

sorption-desorption reactions can be obtained from:

$$Q_j^{a,s,N+1} = \sum_{i=1}^{N_s} \nu_{ij}^s \Delta M_i^{s,N+1} \tag{4.28}$$

Source-sink terms due to kinetically-controlled dissolution-reactions and intra-aqueous kinetic reactions can be related directly to the corresponding reaction rates. The total source-sink term for the mineral A_i^m can be calculated using

$$\Delta M_i^{m,N+1} = 10^3 \sum_{k=1}^{N_v} V_k R_{i,k}^{m,N+1}, \tag{4.29}$$

where the reaction rates can be calculated based on rate expressions 3.106, 3.107, 3.112-3.115, 3.122 and 3.125. The source-sink term [mol s^{-1}] for the total aqueous component concentrations due to kinetically-controlled dissolution-precipitation reactions is then defined by

$$Q_j^{a,m,N+1} = -\sum_{i=1}^{N_m} \nu_{ij}^m \Delta M_i^{m,N+1}, \tag{4.30}$$

while the source-sink term [mol s^{-1}] towards the total aqueous component concentrations due to intra-aqueous kinetic reactions is defined by

$$Q_j^{a,a,N+1} = -10^3 \sum_{k=1}^{N_v} S_{a,k} \phi V_k \sum_{i=1}^{N_a} \nu_{ij}^a R_{i,k}^{a,N+1}, \tag{4.31}$$

where the reaction rate can be calculated based on rate expressions 3.57, 3.61 and 3.62.

The absolute mass balance error [mol] per time step for component A_j^c in terms of total aqueous component concentrations for the entire solution domain can then be obtained from:

$$\begin{aligned} EA_j^{a,N+1} = \big[& \Delta M_j^{a,N+1} - Q_j^{a,\text{in},N+1} + Q_j^{a,\text{out},N+1} \\ & + Q_j^{a,g,N+1} + Q_j^{a,s,N+1} \\ & + Q_j^{a,m,N+1} + Q_j^{a,a,N+1} \big] \Delta t \end{aligned} \tag{4.32}$$

It is also useful to determine relative mass balance errors. The relative mass balance error can be obtained by comparing the absolute mass balance error to a quantity such as the

mass gain or mass loss due to fluxes across the model boundary. Choosing a meaningful quantity is particularly difficult for reactive transport problems. The mass gain due to fluxes across the boundary may be negligible for one species, but may be very large for another species. The total mass contained in the aqueous phase as defined by equation 4.15, has been chosen as the representative quantity in this study. The relative mass balance error [%] for component A_j^c for a single time step can be calculated according to:

$$ER_j^{a,N+1} = 100\frac{EA_j^{a,N+1}}{M_j^{a,N+1}} \tag{4.33}$$

The absolute cumulative mass balance error [mol] can be obtained from the sum of all absolute mass balance errors over all time steps

$$EAC_j^{a,N_t} = \sum_{N=1}^{N_t} EA_j^{a,N}, \tag{4.34}$$

where N_t defines the total number of time steps completed. The corresponding relative mass balance error can be calculated by comparing the cumulative absolute mass balance error to the total system mass in the aqueous phase:

$$ERC_j^{a,N_t} = 100\frac{EAC_j^{a,N_t}}{M_j^{a,N_t}} \tag{4.35}$$

4.3 Solution Method

The solution of the system of equations consists of the solution of the variably-saturated flow problem and the subsequent solution of the reactive transport problem based on the fluxes and phase saturations obtained from the flow solution. In case of steady state groundwater flow, it is sufficient to solve the flow problem only once prior to solving the reactive transport problem in a transient manner.

It should be pointed out that the consideration of transient variably-saturated flow can lead to non-physical results when solving the reactive transport problem. This is due to changes of aqueous phase saturations, which may lead to the rapid advective displacement or possibly entrapment of gaseous species. The latter case will render both the flow and the reactive-transport solution inaccurate. Advective gas transport by itself does not likely affect the flow solution, since gas pressures are small, but it may affect the reactive

transport solution significantly. The assumption of a passive gas phase does not account for these transport processes and computed partial gas pressures as well as dissolved gas concentrations may not represent physically reasonable values. The correct solution of the fully transient problem is only possible using a compositional approach, which considers advective and dispersive transport processes in both the aqueous and gaseous phases simultaneously with geochemical reactions. The present model can nevertheless be used as an approximate solution for the fully transient problem. Errors can be controlled by limiting the time step size in order to constrain the saturation changes during a single time step.

The systems of algebraic nonlinear equations for variably-saturated flow (equations 4.1) and reactive transport (equations 4.4) are both linearized using Newton's method. The Newton-linearization for the variably-saturated flow problem has been implemented following standard techniques [e.g. *Paniconi and Putti*, 1994] and is therefore not repeated here. The linearized set of equations for the reactive transport problem can be written as

$$\frac{\partial F(C_j^c)}{\partial C_i^c} \Delta C_i^c = -F(C_j^c), \tag{4.36}$$

where $F(C_j^c)$ is defined by equation 4.4 and ΔC_i^c is the update for the concentrations C_i^c. The concentrations of the components as species in solution at the new iteration level can be obtained from

$$C_j^{c,N+1,I+1} = C_j^{c,N+1,I} + \Delta C_j^c, \tag{4.37}$$

where the superscript I has been introduced to define the iteration level. $I+1$ identifies the concentrations at the new iteration level, while I defines the concentrations at the old iteration level.

Newton's method has to be modified for the solution of reactive transport problems [*Steefel and Lasaga*, 1994], because the concentrations of the components as species in solution can vary over tens of orders of magnitude during the course of a simulation. This results in a Jacobian matrix characterized by a large condition number, which may even be singular or at least numerically singular [*Holm*, 1989]. This is a significant problem for reactive transport simulations characterized by complex chemistry in combination with a fine spatial resolution. The size of the problem requires the use of sparse iterative solution methods that may fail to converge for such ill-conditioned systems. A more appropriate

method is to solve the system of equations in terms of relative concentration increments defined on a logarithmic scale instead of solving for absolute concentration increments [e.g.: *Steefel and Lasaga*, 1994]

$$\frac{\partial F(C_j^c)}{\partial \ln C_i^c} \Delta \ln C_i^c = -F(C_j^c), \tag{4.38}$$

where the derivative of the function $F(C_j^c)$ with respect to ln C_i^c can be obtained from:

$$\frac{\partial F(C_j^c)}{\partial \ln C_i^c} = \frac{\partial F(C_j^c)}{\partial C_i^c} C_i^c \tag{4.39}$$

This modification greatly reduces the condition number of the Jacobian matrix [*Holm*, 1989], leads often to better convergence properties [*Steefel and Lasaga*, 1994] and facilitates the use of sparse matrix solvers for multi-dimensional problems. The concentrations at the new iteration level can be obtained from:

$$\ln C_j^{c,N+1,I+1} = \ln C_j^{c,N+1,I} + \Delta \ln C_j^c \tag{4.40}$$

The solution for one time step consists of a series of iterations and can be considered complete if all updates are smaller than a prescribed tolerance. This tolerance has to be expressed in relative terms to account for the generally poor scaling properties of reactive transport problems:

$$\Delta \ln C_{\text{act}}^c < \varepsilon \tag{4.41}$$

where ε is the prescribed tolerance and $\Delta \ln C_{\text{act}}^c$ is the actual maximum update in the solution domain for all components defined by:

$$\Delta \ln C_{\text{act}}^c = \left[\Delta \ln C_{j,k}^c, \Delta \ln C_{\text{act}}^c\right] \quad k = 1, N_v, \; j = 1, N_c \tag{4.42}$$

The partial derivatives $\partial F(C_j^c)/\partial \ln C_i^c$ can be obtained using numerical differentiation. This is particularly advantageous because complex nonlinear functions can be considered with ease. Complex rate laws for dissolution-precipitation reactions or intra-aqueous kinetic reactions can be implemented without need of deriving analytical derivatives, which may be costly to evaluate numerically. Numerical derivatives have been extensively used in variably-saturated flow models [e.g. *Forsyth et al.*, 1995] and multiphase-

multicomponent compositional simulators [e.g. *Forsyth and Simpson*, 1991, *Forsyth and Shao*, 1991] and appear to perform sufficiently well for reactive transport problems. The partial derivative of the concentration of aqueous complex A_i^x with respect to the concentration of the free species A_j^c can, for example, be obtained using

$$\frac{\partial C_i^x}{\partial C_j^c} = \frac{C_i^x(C_j^c + \zeta) - C_i^x(C_j^c)}{\zeta},$$

where ζ_j is the increment for numerical differentiation for component A_j^c, which is defined relative to the species concentration of component A_j^c:

$$\zeta_j = \xi C_j^c \tag{4.43}$$

ξ is a user defined factor for numerical differentiation, which is usually defined in the range of:

$$10^{-6} \leq \xi \leq 10^{-4}$$

Analytical partial derivatives for law-of-mass-action-based expressions and simple reaction expressions are documented in the literature [e.g. *Lichtner*, 1992]. It may be most efficient to make use of a combination of numerical and analytical derivatives in future model developments.

The set of algebraic equations 4.4 leads to a large Jacobian matrix of the size $N_v N_c$ by $N_v N_c$. The global matrix is characterized by a block structure defined by the spatial discretization scheme. The size of the local matrices is therefore N_c by N_c. The final system of matrix equations is solved using the sparse iterative solver package WATSOLV [*VanderKwaak et al.*, 1997]. The same solver package is used for the solution of the variably-saturated flow problem. The solution is obtained using a CGSTAB acceleration method [*van der Vorst*, 1992] in combination with a level-based preconditioning and natural or RCM-ordering. Given the local matrices are treated as full matrices, the sparse iterative solver works as a direct solver for one-dimensional problems and the level of preconditioning is arbitrary. Good performance for most multi-dimensional reactive transport simulations were obtained with a level-zero or level-one preconditioner matrix.

Only the local matrices containing non-zero entries are stored. Optionally, the local matrices themselves can be stored as full matrices, or in compressed format. Making use of the sparsity of the local matrices can lead to a significant memory savings and to a decrease of CPU-time for a single solver iteration. For the same level of preconditioning,

the disadvantage of this method is usually the increase of the number of solver iterations, which may offset the CPU-savings for a single iteration. Whether making use of the sparsity of the local matrices is beneficial is largely problem-dependent. For complex geochemical systems including multiple dissolution-precipitation fronts, it appears to be better to retain the local matrices as full matrices, while problems approaching a quasi-steady state are often solved more efficiently by making use of the sparsity of the local matrices. Using a higher factorization level in combination with compressed local matrices (one or two levels higher than for full local matrices) generally did not improve the efficiency of the solution above the level that was obtained with full local matrices. These results indicate that using the full local matrices allows constructing an efficient preconditioner matrix for the global problem. These findings may be affected by the ordering scheme used in most simulations (RCM-ordering). Independent of the ordering scheme, storing the local matrices as full matrices will tend to keep the unknowns associated with each control volume together [*Forsyth*, personal communication, 1999].

4.4 Compressed Data Structure for Reaction Matrices

A compressed data structure, which stores only non-zero entries, is not only applied for the Jacobian matrices resulting from the discretization of the variably-saturated flow and reactive-transport problems, but also for the local geochemical reactions matrices. These matrices contain the stoichiometric coefficients of the components in the secondary species, but are also used to store the reaction orders of the reactant species in the case of kinetically-controlled reactions. Compressed storage in general has the advantage of minimizing the memory requirements and the number of floating point operations when performing matrix operations. Memory savings is not an issue in the case of reaction matrices; however, the computational effort might be decreased significantly.

The dissociation of sulfuric acid into the components H^+ and SO_4^{2-} can be taken as an illustrative example:

$$H_2SO_4 \rightleftharpoons 2H^+ + SO_4^{2-}$$

This reaction will be part of a reaction network containing N_c components. Only the stoichiometric coefficients for H^+ and SO_4^{2-} are non-zero. The concentration of sulfuric acid can be determined by applying the law of mass action (equation 3.46), repeated here

for illustrative purposes:

$$C_i^x = (K_i^x \gamma_i^x)^{-1} \prod_{j=1}^{N_c} (\gamma_j^c C_j^c)^{\nu_{ij}^x} \qquad i = 1, N_x$$

The computation of C_i^x involves the evaluation of a product over all N_c components. Computational savings can be substantial if the stoichiometric coefficients are stored in compressed format. Assuming that the reaction network contains 20 components, 20 multiplications have to be carried out for the case of full storage, while only two multiplications are conducted in the case of sparse storage. The present model utilizes row and column pointers to retrieve data from the compressed matrices. This data storage is applied for all stoichiometric coefficients and reaction orders defined in Chapter 3.

4.5 Treatment of Finite Mineral Phases

One of the major difficulties for the solution of the reactive transport equations is that the masses of mineral phases are limited. This is a particular problem when minerals are treated as secondary unknowns, even though dissolution-precipitation reactions are formulated as kinetically-controlled reactions. The reactive surface area term and all other mineral parameters in reaction expressions 3.106, 3.107, 3.112, 3.113, 3.114 and 3.115 are defined at the old time level when calculating the reaction rate for the solution at the new time level (see Section 4.1.2, equation 4.14). Therefore, the solution of equations 4.4 does not indicate the depletion of a mineral phase during a time step and it is possible that non-physical negative mineral volume fractions are obtained when updating the mineral volume fractions with equations 4.10.

It is consequently necessary to implement special provisions into the model in order to avoid the computation of negative mineral volume fractions. The general idea is to check whether a sufficient amount of a mineral is available to sustain the computed dissolution rate during a particular time step. If this is not the case, the reaction rate has to be adjusted in order to just deplete the particular mineral phase. This reaction rate can then be inserted in the right-hand-side vector as a known source-sink term. An appropriate algorithm is given by:

$$\Delta C_i^m = R_i^{m,N+1} \Delta t$$
$$\texttt{if } (C_i^{m,N} + \Delta C_i^m < 0) \texttt{ then}$$
$$R_i^{m,N+1} = -C_i^{m,N} / \Delta t$$
$$\texttt{end if}$$

A formal proof that this method does not affect the velocities of mineral dissolution fronts is not included here. However, a direct comparison of the model results for the benchmark problem presented in section 5.5 with the results of an established model [*Lichtner*, 1996a] prove the functionality of the approach. The depletion of a mineral phase results in a discontinuity in the system of governing equations and time step reductions may occur as a result of the manipulations described above. Mineral phases could alternatively be retained as primary unknowns. This approach may improve the convergence properties, but will simultaneously increase the size of the Jacobian matrix and will thus lead to additional memory and computational requirements.

4.6 Adaptive Time Stepping and Update Modification Schemes

Adaptive time stepping and update modification schemes are needed to ensure a reliable and robust solution of the nonlinear equations describing variably-saturated flow and reactive transport. An adaptive time stepping scheme reported by *Forsyth and Sammon* [1986] and an underrelaxation scheme modified after *Cooley* [1983] are included in the present model for the solution of the variably-saturated flow problem in a similar manner as implemented in the variably-saturated flow model FRAC3DVS [*Therrien and Sudicky*, 1996]. These techniques are not described in more detail; the focus of this section lies in the algorithm employed for the solution of the reactive transport equations.

The infiltration of surface water characterized by a different chemical composition relative to the background groundwater and the propagation of atmospheric gases into the unsaturated zone lead to steep geochemical gradients resulting in numerical difficulties when solving the reactive transport equations. Moving redox zones pose a particular problem due to extreme concentration changes on a small spatial scale [*Engesgaard and Kipp*, 1992, *Abrams et al.*, 1998]. A further complication arises due to the appearance and disappearance of mineral phases leading to pronounced local geochemical changes. Fast kinetically-controlled reactions and rapid transport processes increase the stiffness of

the system of equations. Diffusive gas transport imposes a particular stress on the system as a result of the short characteristic time scale. On the other hand, it is also possible that quasi steady-state conditions develop during a simulation. Physical transport and geochemical reaction processes are, in this case, balanced, and concentration changes in the aqueous and gaseous phases become negligible (compare Chapter 2, Section 2.4.4). It is also possible that a series of temporary quasi steady-state conditions develop during the course of a simulation, which are interrupted by rapid geochemical changes. Such a behavior is characteristic when pH- or E_h-buffer minerals are less abundant and the complete dissolution of mineral phases occurs frequently.

It is necessary to provide an adaptive time stepping scheme, which adjusts the time increment to the present difficulty of the problem. The estimate should be based on the expected geochemical changes. Short time steps during rapid geochemical changes ensure a robust solution, while large time steps during periods of quasi steady-state make the solution more efficient. The present time stepping scheme does not include provisions for Courant constraints, because a fully implicit time integration is chosen and these Courant-criteria do not have to be obeyed to warrant numerical stability [*Unger et al.*, 1996]. The time stepping scheme also does not include an error control as provided by more sophisticated methods such as the DAE-solvers DASSL or DASPK [*Hindmarsh and Petzold*, 1995b]. A maximum time increment can, however, be specified to ensure a sufficiently accurate solution.

A simple but efficient adaptive time stepping scheme has been developed and implemented in the present model. The size of the time increment is determined based on the relative change in aqueous concentrations and the number of Newton iteration during the last time step. The update-based and iteration-based time increment adjustment can be used simultaneously or as stand-alone schemes. A flow chart of the time stepping scheme is presented in Table 4.1. The time increment for the next time step Δt^{N+1} is initially limited by the minimum of the user-specified maximum time increment $\Delta t_{\max}$ and the previous time increment multiplied by a factor α_{inc}, which determines the maximum tolerable time increment increase. In the following the new time increment is estimated based on the geochemical changes which have occurred during the previous time step using a method similar to the one proposed by *Forsyth and Sammon* [1986]. Employing a first order scheme, the new time increment can be based on the maximum actual update $\Delta \log C^c_{\text{act}}$, which is determined based on the local updates for all components in the entire solution domain, and an user-specified anticipated update $\Delta \log C^c_{\text{ant}}$. These

1.	set maximum new time increment	$\Delta t^{N+1} = \min[\Delta t_{\max}, \alpha_{\text{inc}} \Delta t^N]$
2.	determine maximum actual update $\Delta \log C^c_{\text{act}}$	for $k = 1, N_v$ for $j = 1, N_c$ $\Delta \log C^c_{\text{act}} = \max[\Delta \log C^c_{\text{act}}, \Delta \log C^c_{j,k}]$ end for end for
3.	determine new time increment based on anticipated and maximum actual update	$\Delta t^{N+1} = \min[\Delta t^{N+1}, \Delta \log C^c_{\text{ant}} / \Delta \log C^c_{\text{act}} \Delta t^N]$
4.	determine new time increment based on actual and anticipated number of iterations	$\Delta t^{N+1} = \min[\Delta t^{N+1}, f(N^{\text{act}}_{it}, N^{\text{ant}}_{it}) \Delta t^N]$
5.	limit decrease of time increment	$\Delta t^{N+1} = \max[\Delta t^{N+1}, \alpha_{\text{dec}} \Delta t^N]$
6.	lower bound - minimum time increment	$\Delta t^{N+1} = \max[\Delta t^{N+1}, \Delta t_{\min}]$

Table 4.1: Adaptive time stepping scheme for solution of reactive transport equations

updates have to be defined on a logarithmic scale to account for the large concentration ranges characteristic for reactive transport problems. A second possibility is to base the new time increment on the number of Newton-iterations N^{act}_{it} which were required for the solution of the previous time step and an anticipated number of Newton-iterations N^{ant}_{it}. Various functional relationships between these parameters can be employed to yield a rapid adjustment towards the anticipated time increment. The new time increment can now be defined as the minimum of the estimated time increments. The time increment is finally checked against a maximum tolerable decrease in comparison to the previous time increment, defined by the factor α_{dec} and a user-specified minimum time increment.

It is nevertheless possible that convergence cannot be achieved using the estimated time increment, where non-convergence is based on exceeding a maximum number of Newton-iterations without meeting the specified convergence tolerance for all components.

In this case, the time step is restarted with a reduced time increment. This algorithm ensures that the only possibility for complete convergence failure is if the solution does not converge for the minimum time increment specified. A primary reason for time step failures is that the adaptive time stepping scheme presented here poorly accounts for rapid geochemical changes caused by the complete depletion of mineral phases, because the mineral volume fractions and related parameters are updated explicitly (see Section 4.1.2 and Section 4.5).

It is also important to ensure that a non-convergent solution is not induced during the early stages of the Newton-iteration loop, when quadratic convergence behavior is not yet encountered. If the updates become too large, unrealistic concentrations may be determined, which will provide an even poorer approximation of the solution than the estimate obtained from the previous iteration. Such unrealistic updates prohibit the further solution of the model equations. It is therefore necessary to constrain the updates within specified limits to force the solution into the zone of quadratic convergence [*Crerar*, 1975, *Leeming et al.*, 1998]. Common techniques for equilibrium systems are presented by *van Zeggeren and Storey* [1970] and include line search methods [*Fletcher*, 1987, *I and Nancollas*, 1972] and curve crawler techniques [*Crerar*, 1975]. The present model makes use of simple, but efficient local update corrections as described by the following algorithm:

```
for k = 1, N_v
   for j = 1, N_c
      if (Δlog C^c_{j,k} > Δlog C^c_max) then
         Δlog C^c_{j,k} = Δlog C^c_max
      elseif (Δlog C^c_{j,k} < −Δlog C^c_max)
         Δlog C^c_{j,k} = −Δlog C^c_max
      end if
   end for
end for
```

Leeming et al. [1998] have shown that more sophisticated techniques, such as line search methods do not lead to a significant improvement of the convergence behavior in comparison to the update modification scheme presented above. Experiments with global underrelaxation have proven to perform worse than the local update modification scheme presented here.

4.7 Spatial Weighting Schemes

Spatial weighting schemes may have a significant impact on the accuracy and efficiency of the solution of the model equations. An ideal spatial weighting scheme ensures a physically meaningful solution, while minimizing numerical dispersion. The spatial weighting schemes used in this work for variably-saturated flow and reactive transport are presented below.

4.7.1 Variably-Saturated Flow

The present model allows the option of using centered spatial weighting or upstream weighting for the relative permeability term $k_{ra,kl}$ (equation 4.1). The relative permeability using centered spatial weighting can be calculated as [*Forsyth et al.*, 1995]:

$$k_{ra,kl} = \frac{k_{ra,k} + k_{ra,l}}{2} \tag{4.44}$$

Relative permeabilities can alternatively be determined using upstream weighting [*Forsyth et al.*, 1995]:

$$\begin{aligned} k_{ra,kl} &= k_{ra,k} \quad \text{if } h_k \geq h_l \\ k_{ra,kl} &= k_{ra,l} \quad \text{if } h_k < h_l \end{aligned} \tag{4.45}$$

Upstream weighting usually increases the efficiency of the solution and ensures its physical correctness, but leads to significant numerical dispersion, which decreases the accuracy of the numerical solution. However, *Forsyth et al.* [1995] showed that the use of upstream weighting for the relative permeability term does not lead to an appreciable loss of accuracy for variably-saturated flow problems. This is due to the self-sharpening nature of variably-saturated flow problems [*Forsyth et al.*, 1995].

4.7.2 Reactive Transport

The present reactive transport model contains three different spatial weighting schemes for the advective mass flux in the aqueous phase. These consist of centered weighting, upstream weighting, and a van Leer flux limiter [*van Leer*, 1974, *Unger et al.*, 1996]. The

spatial weighting scheme determines the definition of the total aqueous component concentrations $T^a_{j,kl}$ at the interface between adjacent control volumes. These concentrations are used for the advective flux calculations in equation 4.4.

A common technique to define these interfacial concentrations is to use centered spatial weighting. $T^a_{j,kl}$, in this case, is simply defined as the arithmetic average of the total aqueous component concentrations in control volumes k and l.

$$T^a_{j,kl} = \frac{T^a_{j,k} + T^a_{j,l}}{2} \tag{4.46}$$

Centered spatial weighting can lead to non-physical results if the appropriate Peclet criterion is not obeyed (see also Section 2.4.2), and may limit the size of the time increment severely. Experience gained during the development of the present model indicated that centered spatial weighting may even lead to a non-convergent solution. This is essentially due to the fact that the total aqueous component concentrations may vary over many orders of magnitude between control volumes k and l. Such a concentration gradient can occur as a result of boundary conditions, but also as a result of the complete depletion of a mineral phase in spatially limited areas of the solution domain. The dissolution of the mineral maintains the concentration of the components constituting the particular mineral in the downstream control volume, while the control volume located upstream is unaffected by this concentration increase, except for diffusive transport processes. It is possible that the application of centered spatial weighting for such a problem will lead to negative concentrations in the control volume located upstream. The present model does not allow for physically incorrect solutions and responds with a reduction of the time step size, which ultimately leads to convergence failure when the minimum tolerable time step is reached (see also Section 4.6).

Optionally, upstream weighting can be used to circumvent these problems:

$$\begin{aligned} T^a_{j,kl} &= T^a_{j,k} \quad \text{if } v_{a,kl} \geq 0 \\ T^a_{j,kl} &= T^a_{j,l} \quad \text{if } v_{a,kl} < 0 \end{aligned} \tag{4.47}$$

This method ensures convergence and a physically correct solution. However, the disadvantage of this technique is extensive numerical dispersion for moving concentration fronts.

Flux limiter schemes can be employed to make use of the benefits of upstream weight-

ing, while limiting numerical dispersion. Various flux limiter schemes have been developed in recent years, as reported, for example, by *Cirpka* [1997]. The van Leer flux limiter [*van Leer*, 1974], modified by *Unger et al.* [1996], has been implemented in the present reactive transport model. The interfacial total aqueous component concentrations are in this case defined as

$$T^a_{j,kl} = T^a_{j,k} + \sigma(r_{kl}) \frac{T^a_{j,l} - T^a_{j,k}}{2}, \tag{4.48}$$

where $\sigma(r_{kl})$ is the van Leer flux limiter and r_{kl} is a smoothness sensor, which is used to define the numerical value of $\sigma(r_{kl})$. For a definition of $\sigma(r_{kl})$ and r_{kl} refer to *Unger et al.* [1996]. The numerical values of the van Leer flux limiter range from

$$0 \leq \sigma(r_{kl}) \leq 2$$

$\sigma(r_{kl})$ is determined dynamically with the goal to ensure a physically meaningful solution, while minimizing numerical dispersion. By examining equation 4.48, it can be seen that upstream weighting is obtained for $\sigma(r_{kl}) = 0$, while $\sigma(r_{kl}) = 2$ leads to downstream weighting, which is the most anti-dispersive scheme possible [*Unger et al.*, 1996].

4.8 Activity Update Techniques

The governing equations for reactive transport are highly nonlinear due to the interactions between physical and geochemical processes. The nonlinearity of the equations is further increased by the concentration dependency of the activity corrections. Activity coefficients are calculated based on the ionic strength, which in turn depends on the concentration and the charge of the dissolved species (see Chapter 3, Section 3.4.2). The application of the standard Newton-linearization requires the consideration of the partial derivatives of the activity coefficients with respect to the concentrations C^c_j directly in the Jacobian matrix [*Lichtner*, 1992]. Alternative approaches are based on updating the activity coefficients once [*I and Nancollas*, 1972] or twice [*Wolery et al.*, 1990] after each Newton-iteration. These methods may lead to numerical instabilities during the Newton-iteration loop, because intermediate iterates of the concentrations may enter unrealistic concentration ranges and are often a poor approximation of the true solution. Activity coefficients calculated using these concentrations may therefore have an adverse effect on the convergence behavior. Modified update techniques limit the size of the updates for

the activity coefficients [*Crerar*, 1975] in order to reduce convergence problems. An alternative possibility is a time-lagged or explicit update of the activity coefficients [*Lichtner*, personal communication, 1997], which means that the solution for the time level $N + 1$ is obtained using the activity coefficients based on the concentrations at the time level N. This method can significantly improve the convergence properties of the reactive transport equations with negligible effect on the results.

The present model formulation includes the double update technique as described by *Wolery et al.* [1990] and the time-lagged update as proposed by *Lichtner* [personal communication, 1997]. The model also gives the option to neglect activity corrections all together in order to facilitate comparisons with verification examples that exclude activity corrections.

4.9 Choice of Redox Master Variable

The concentrations of the components as species in solution that are primary unknowns may vary over many orders of magnitudes in space and time, and can pose significant numerical difficulties for the solution of reactive transport problems. This is particularly true for problems involving oxidation-reduction reactions [e.g. *Engesgaard and Kipp*, 1992]. Various numerical techniques have been developed for geochemical equilibrium models in order to facilitate a more stable and efficient solution. A commonly used method is basis switching [*Bethke*, 1996]. Any species as part of the total concentration term defined by equation 3.23 can be chosen as the primary unknown; assuming that only aqueous species can be used as components. Basis switching is possible, because the choice of the basis species is not unique [e.g. *Steefel and MacQuarrie*, 1996]. This technique ensures that the most abundant species is selected as the primary unknown, which leads to a more diagonally dominant Jacobian matrix and therefore to a more stable solution. Basis switching has, on the other, hand the disadvantage that it requires the frequent transformation of the reaction matrices [*Bethke*, 1996], which can be computationally quite expensive. The implementation of basis switching is particularly difficult when the global implicit solution method is employed. The difficulties arise from the potential for adjacent control volumes to have a different set of components, while being spatially connected by advective and dispersive fluxes. Nevertheless, *Steefel and Lasaga* [1994] and *Lichtner* [1992] have implemented basis-switching into their reactive transport models. However, *Steefel and MacQuarrie* [1996] reported that basis switching does not significantly improve the

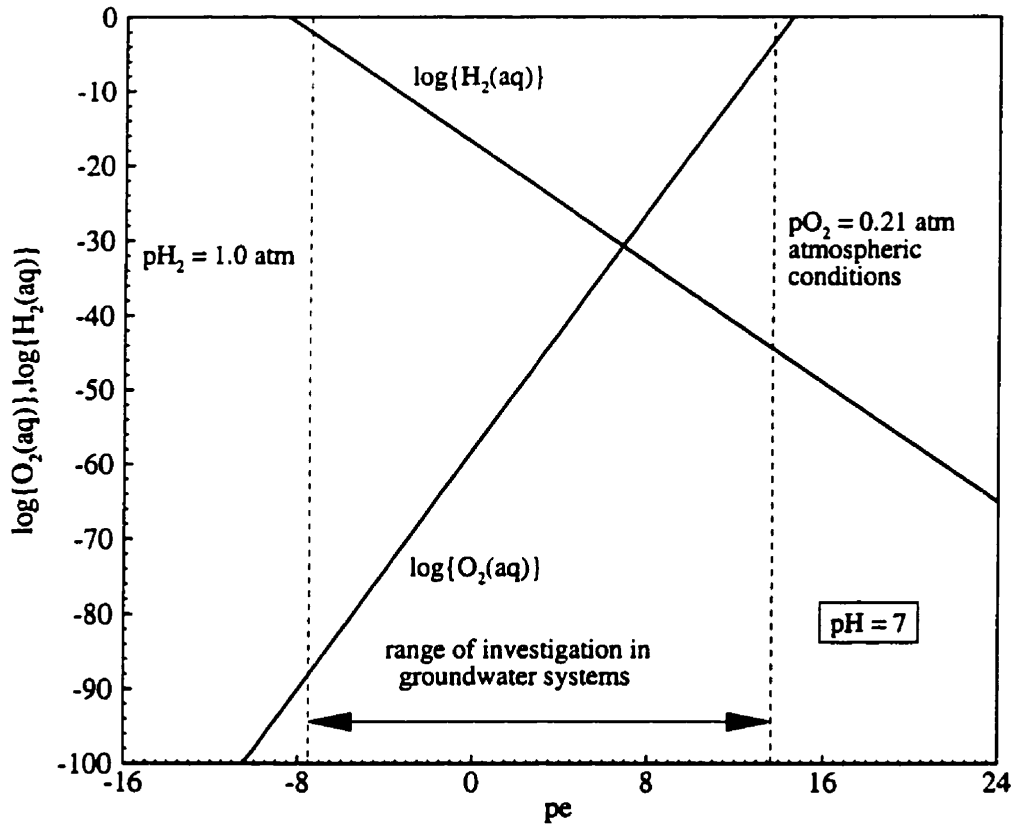

Figure 4.1: Dissolved oxygen and hydrogen gas concentrations as a function of pe at pH=7 (equilibrium conditions)

efficiency of the solution for reactive transport problems if solved on a logarithmic scale.

The relative ineffectiveness of basis switching for reactive transport problems can be explained by conceptual differences between reactive transport and geochemical equilibrium batch problems. The governing equations for reactive transport describe the transient evolution of geochemical conditions in space and time instead of the final equilibrium conditions in a batch reactor. The estimate for the solution at the new time level of a reactive transport problem is based on the solution from the old time level and is therefore often much better than the initial concentration estimates for a geochemical equilibrium batch problem. How efficiently the solution at the new time level can be obtained will not exclusively depend on the abundance of the species chosen as the primary unknown,

but will also be affected significantly by the relative change of the concentrations of the primary unknowns over a single time step. Large changes over a single time step will inhibit the solvability of the governing equations. This can be deduced directly from the adaptive time stepping scheme presented in Section 4.6, because the time increment is made dependent on the relative concentration changes of the components as species in solution. It can therefore be recommended to choose species as primary unknowns whose change of concentrations is as small as possible during a simulation. The choice of the components is not straightforward, however, it appears reasonable that the efficiency of the solution will generally benefit if the components are rather insensitive with respect to changes in the master variables pH and pe.

It is instructive to apply this concept to the choice of the redox master variable - the component used to express all oxidation-reduction reactions in the reactive transport equations. The present model allows the option of $O_2(aq)$, $H_2(aq)$ or the electron as the redox master variable. Each choice has advantages and disadvantages from a theoretical point of view (see Chapter 3, Section 3.4.1). Figure 4.1 shows the distribution of dissolved oxygen and hydrogen gas concentrations at equilibrium as a function of pe for pH = 7. Most computations will take place for a pe ranging from -7.5 (pH_2 = 1 atm) to 13.8 (pO_2 = 0.21 atm), as indicated by the range of investigation in Figure 4.1. The change in dissolved oxygen and hydrogen gas concentrations is directly related to the pe-change and is defined by the reaction stoichiometry of the half reactions:

$$\begin{aligned} H^+ + e^- &\rightleftharpoons \tfrac{1}{2}H_2(aq) \\ \tfrac{1}{4}O_2(aq) + H^+ + e^- &\rightleftharpoons \tfrac{1}{2}H_2O \end{aligned}$$

The change of the species concentrations ($O_2(aq)$:$H_2(aq)$:e^-) is therefore related to the ratio 4:2:1, which is shown in Figure 4.1. The pe changes over approximately 21 orders of magnitude over the possible range of investigation, while the dissolved hydrogen gas concentration changes over almost 43 orders of magnitude. Even more extreme are the changes of dissolved oxygen concentrations which exceeds 85 orders of magnitude. Choosing the electron as the primary unknown is therefore numerically more efficient. However, this approach is not most generally applicable; care has to be taken when the method is applied in combination with kinetically-controlled reactions or in multiphase systems to warrant a consistent solution. The progress of kinetically-controlled reactions has to be expressed in terms of the actual electron acceptors and donors.

4.10 Test Problem

The following sections focus on the evaluation of the numerical techniques discussed above. The present model is applied to a test problem to investigate how numerical methods and parameters can affect the efficiency of the solution and the accuracy of the model results. The test problem addresses the generation and subsequent reactive transport of acid mine drainage in variably-saturated media. Figure 4.2 depicts the corresponding conceptual model. Atmospheric oxygen can penetrate into the tailings material due to the existence of an unsaturated zone. Gaseous oxygen subsequently partitions into the aqueous phase, where it causes the oxidation of sulfide minerals such as pyrite. The oxidation of pyrite leads to an increase in acidity, dissolved iron, and sulfate concentrations. The low pH-water is buffered, as the pore water migrates downwards into the tailings impoundment.

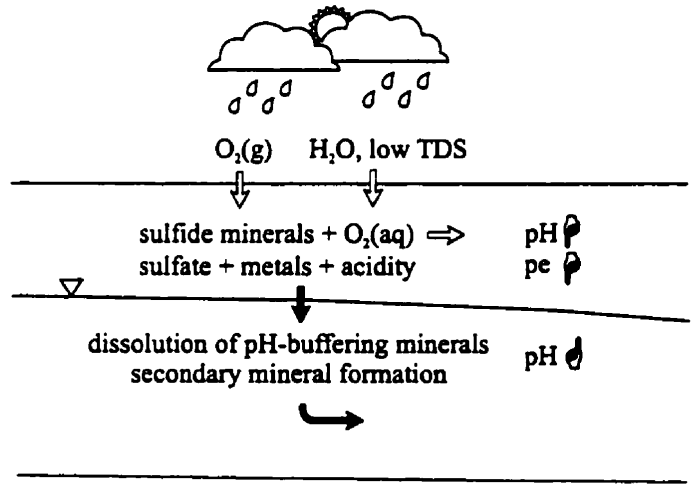

Figure 4.2: Concept of sulfide mineral oxidation in tailings impoundments

The test problem considers a one-dimensional soil column of 5 m length, which is discretized into 101 control volumes yielding a discretization interval of 5 cm for the interior control volumes and 2.5 cm for the control volumes on the boundary. Boundary conditions for the flow problem consist of a specified flux boundary at the top of 300 mm y^{-1}, which represents recharge, and a fixed head boundary of $h = 2.5$ m at the bottom boundary. These boundary conditions lead to the development of an unsaturated zone,

which extends from the surface to a depth of 2.45 m with variable moisture content. The physical parameters used for the simulations are summarized in Table 4.2. The free phase diffusion coefficients are representative for oxygen at T = 25°C and were taken from the compilation of *Glinski and Stepniewski* [1985].

Parameter		unit	value
length of solution domain	L	[m]	5.0
porosity	ϕ	[-]	0.5
infiltration rate	q_{in}	[m y^{-1}]	0.3
hydraulic conductivity	K_{zz}	[m s^{-1}]	$1.0 \cdot 10^{-6}$
residual saturation	S_{ra}	[-]	0.05
soil hydraulic function	α	[-]	3.5
parameters	n	[-]	1.4
longitudinal dispersivity	α_l	[m]	$5.0 \cdot 10^{-4}$
free phase diffusion coefficient in gaseous phase	D_g^*	[m^2 s^{-1}]	$2.07 \cdot 10^{-5}$
free phase diffusion coefficient in aqueous phase	D_a^*	[m^2 s^{-1}]	$2.38 \cdot 10^{-9}$

Table 4.2: Physical input parameters - test problem for numerical performance

Table 4.3 defines the reaction stoichiometry of all intra-aqueous reactions considered in the test problem. These intra-aqueous reactions are treated as equilibrium reactions. For the base case, O_2(aq) has been used as the redox master variable. H_2(aq) is considered an excluded species. Table 4.4 shows the gas dissolution-exsolution reactions considered and Table 4.5 defines the reaction stoichiometries for the mineral-dissolution precipitation reactions considered. The equilibrium constants for oxidation-reduction, complexation and gas dissolution-exsolution reactions are also given in Tables 4.3-4.4. Table 4.6 defines the equilibrium constants for dissolution-precipitation along with the effective reaction rate constants. The kinetically-controlled dissolution and precipitation of minerals is assumed to be surface-controlled and is here described in terms of effective rate constants, which are based on the combined effect of reactive surface area and the rate constant for surface-controlled dissolution reactions:

$$k_{i,\text{eff}} = S_i k_i^{md,s}$$

Mineral dissolution-precipitation rates are described by transition state rate expressions

given by:

$$R_i^m = -k_{i,\text{eff}} \left[1 - \frac{IAP_i^m}{K_i^m} \right]$$

Reaction			$\log K_i^T$
Oxidation-reduction reactions			
(1)	Fe^{3+}	$\rightleftharpoons Fe^{2+} + 0.25O_2(aq) + H^+ - 0.5H_2O$	8.473
(2)	HS^-	$\rightleftharpoons SO_4^{2-} + H^+ - 2O_2(aq)$	-138.376
Complexation reactions			
(3)	OH^-	$\rightleftharpoons H_2O - H^+$	-13.998
(4)	H_3SiO4^-	$\rightleftharpoons H_4SiO_4 - H^+$	-9.830
(5)	$CaHCO_3^+$	$\rightleftharpoons Ca^{2+} + CO_3^{2-} + H^+$	11.440
(6)	$CaCO_3(aq)$	$\rightleftharpoons Ca^{2+} + CO_3^{2-}$	3.220
(7)	$CaSO_4(aq)$	$\rightleftharpoons Ca^{2+} + SO_4^{2-}$	2.309
(8)	KSO_4^-	$\rightleftharpoons K^+ + SO_4^{2-}$	0.850
(9)	$Al(OH)_2^+$	$\rightleftharpoons Al^{3+} + 2H_2O - 2H^+$	-10.100
(10)	$Al(OH)_4^-$	$\rightleftharpoons Al^{3+} + 4H_2O - 4H^+$	-22.700
(11)	$Al(OH)_3(aq)$	$\rightleftharpoons Al^{3+} + 3H_2O - 3H^+$	-16.900
(12)	$Fe(OH)^+$	$\rightleftharpoons Fe^{2+} + H_2O - H^+$	-9.500
(13)	$FeSO_4(aq)$	$\rightleftharpoons Fe^{2+} + SO_4^{2-}$	2.250
(14)	HCO_3^-	$\rightleftharpoons H^+ + CO_3^{2-}$	10.330
(15)	$H_2CO_3(aq)$	$\rightleftharpoons 2H^+ + CO_3^{2-}$	16.681
(16)	$Al(OH)^{2+}$	$\rightleftharpoons Al^{3+} + H_2O - H^+$	-4.990
(17)	$AlSO_4^+$	$\rightleftharpoons Al^{3+} + SO_4^{2-}$	3.500
(18)	$Al(SO_4)_2^-$	$\rightleftharpoons Al^{3+} + 2SO_4^{2-}$	5.000
(19)	$H_SO_4^-$	$\rightleftharpoons H^+ + SO_4^{2-}$	1.987
(20)	$Fe(OH)^{2+}$	$\rightleftharpoons Fe^{3+} + H_2O - H^+$	-2.190
(21)	$Fe(SO_4)^+$	$\rightleftharpoons Fe^{3+} + SO_4^{2-}$	4.040
(22)	$Fe(OH)_2^+$	$\rightleftharpoons Fe^{3+} + 2H_2O - 2H^+$	-5.670
(23)	$Fe(OH)_3(aq)$	$\rightleftharpoons Fe^{3+} + 3H_2O - 3H^+$	-12.560
(24)	$H_2(aq)$	$\rightleftharpoons H_2O - 0.5O_2(aq)$	-46.133

Table 4.3: Oxidation-reduction and complexation reactions - test problem for numerical performance

The mineral volume fractions present are loosely based on field data from the Nordic Main Tailings at Elliot Lake [*Dubrovsky*, 1986] and are defined in Table 4.6. The tailings material consists primarily of quartz, K-feldspar, muscovite, but also contains a significant amount of pyrite and small amounts of primary buffer minerals including calcite, siderite

and gibbsite. The geochemical composition of the initial tailings water and the infiltrating recharge water are given in Table 4.7 and are based on the data from *Smyth* [1981] as modified by *Wunderly et al.* [1996]. Cl- and Mg-concentrations have been altered to investigate the effect of spatial weighting schemes and time discretization on the behavior of dissolved species, which are transported conservatively.

Reaction			$\log K_i^g$
(1)	$O_2(g)$	$\rightleftharpoons O_2(aq)$	2.898
(2)	$CO_2(g)$	$\rightleftharpoons 2H^+ + CO_3^{2-} - H_2O$	18.160

Table 4.4: Gas dissolution-exsolution reactions - test problem for numerical performance

Mineral phase		Reaction	
Primary minerals			
(1)	pyrite	$FeS_2(s) + 3.5O_2(aq) + H_2O$	$\rightleftharpoons Fe^{2+} + 2SO_4^{2-} + 2H^+$
(2)	calcite	$CaCO_3(s)$	$\rightleftharpoons Ca^{2+} + CO_3^{2-}$
(3)	siderite	$FeCO_3(s)$	$\rightleftharpoons Fe^{2+} + CO_3^{2-}$
(4)	gibbsite	$Al(OH)_3(s) + 3H^+$	$\rightleftharpoons Al^{3+} + 3H_2O$
(5)	gypsum	$CaSO_4 \cdot 2H_2O(s)$	$\rightleftharpoons Ca^{2+} + SO_4^{2-} + 2H_2O$
(6)	K-feldspar	$KAlSi_3O_8 + 4H^+ + 4H_2O$	$\rightleftharpoons K^+ + Al^{3+} + 3H_4SiO_4$
(7)	muscovite	$KAl_2(AlSi_3O_{10})(OH)_2 + 10H^+$	$\rightleftharpoons K^+ + 3Al^{3+} + 3H_4SiO_4$
(8)	quartz	$SiO_2(s) + 2H_2O$	$\rightleftharpoons H_4SiO_4$
Secondary minerals			
(9)	ferrihydrite	$Fe(OH)_3(s) + 3H^+$	$\rightleftharpoons Fe^{3+} + 3H_2O$
(11)	jarosite	$KFe_3(SO_4)_2(OH)_6 + 6H^+$	$\rightleftharpoons K^+ + 3Fe^{3+} + 2SO_4^{2-} + 6H_2O$
(10)	silica(am)	$SiO_2(am) + 2H_2O$	$\rightleftharpoons H_4SiO_4$

Table 4.5: Dissolution-precipitation reactions - test problem for numerical performance

All simulations were carried out with an update-based adaptive time stepping scheme ($\Delta \log C^c_{ant} = 2.0$, $\Delta \log C^c_{max} = 3.0$, $N^{ant}_{it} = 60$), upstream weighting for the advective transport of dissolved species, and a time-lagged activity update, unless otherwise noted.

Figures 4.3a-d summarize the results for the test problem for a simulation time of t = 10 years. Figure 4.3d shows a rapid decline of gaseous oxygen concentrations versus depth. This is primarily due to the oxidation of pyrite, which becomes depleted in the zone where oxygen is present, as shown in Figure 4.3b. Figure 4.3a shows a pronounced decrease pH and pe in the zone of pyrite oxidation. The pe decreases rapidly, when oxygen

Mineral phase		log K_i^m	$k_{i,eff}$ [mol cm^{-3} s^{-1}]	volume fraction [-]
Primary minerals				
(1)	pyrite	-215.264	$1.0 \cdot 10^{-12}$	$1.37 \cdot 10^{-2}$
(2)	calcite	8.475	$5.0 \cdot 10^{-11}$	$1.15 \cdot 10^{-3}$
(3)	siderite	10.450	$1.0 \cdot 10^{-11}$	$3.50 \cdot 10^{-4}$
(4)	gibbsite	-8.110	$1.0 \cdot 10^{-11}$	$8.30 \cdot 10^{-4}$
(5)	gypsum	4.580	$1.0 \cdot 10^{-10}$	$6.50 \cdot 10^{-3}$
(6)	K-feldspar	-0.080	$5.0 \cdot 10^{-14}$	$2.68 \cdot 10^{-2}$
(7)	muscovite	-12.990	$1.0 \cdot 10^{-14}$	$7.31 \cdot 10^{-2}$
(8)	quartz	3.980	$1.0 \cdot 10^{-15}$	$3.78 \cdot 10^{-1}$
Secondary minerals				
(9)	ferrihydrite	2.710	$1.0 \cdot 10^{-10}$	0.0
(10)	jarosite	9.210	$1.0 \cdot 10^{-10}$	0.0
(11)	silica(am)	2.710	$1.0 \cdot 10^{-11}$	0.0

Table 4.6: Equilibrium constants, rate constants and mineral volume fractions for dissolution-precipitation reactions - test problem for numerical performance

component		tailings water	recharge water	unit
(1)	Ca^{2+}	$1.43 \cdot 10^{-02}$	$1.90 \cdot 10^{-03}$	[mol l^{-1}]
(2)	K^+	$9.00 \cdot 10^{-03}$	$9.00 \cdot 10^{-03}$	[mol l^{-1}]
(3)	Mg^{2+}	$1.04 \cdot 10^{-08}$	$1.04 \cdot 10^{-03}$	[mol l^{-1}]
(4)	Al^{3+}	$2.59 \cdot 10^{-08}$	$1.28 \cdot 10^{-08}$	[mol l^{-1}]
(5)	Cl^-	$1.14 \cdot 10^{-03}$	$1.14 \cdot 10^{-08}$	[mol l^{-1}]
(6)	CO_3^{2-}	$2.49 \cdot 10^{-03}$	$1.10 \cdot 10^{-05}$	[mol l^{-1}]
(7)	H_4SiO_4	$1.93 \cdot 10^{-03}$	$1.99 \cdot 10^{-04}$	[mol l^{-1}]
(8)	Fe^{2+}	$1.45 \cdot 10^{-04}$	$1.29 \cdot 10^{-11}$	[mol l^{-1}]
(9)	Fe^{3+}	$7.16 \cdot 10^{-12}$	$5.36 \cdot 10^{-05}$	[mol l^{-1}]
(10)	SO_4^{2-}	$1.97 \cdot 10^{-02}$	$7.48 \cdot 10^{-03}$	[mol l^{-1}]
(11)	HS^-	$3.31 \cdot 10^{-12}$	$2.55 \cdot 10^{-139}$	[mol l^{-1}]
(12)	pH	7.00	5.00	[-]
(13)	pO_2	$7.73 \cdot 10^{-66}$	$2.10 \cdot 10^{-01}$	[atm]

Table 4.7: Initial composition of tailings water and infiltrating groundwater - test problem for numerical performance

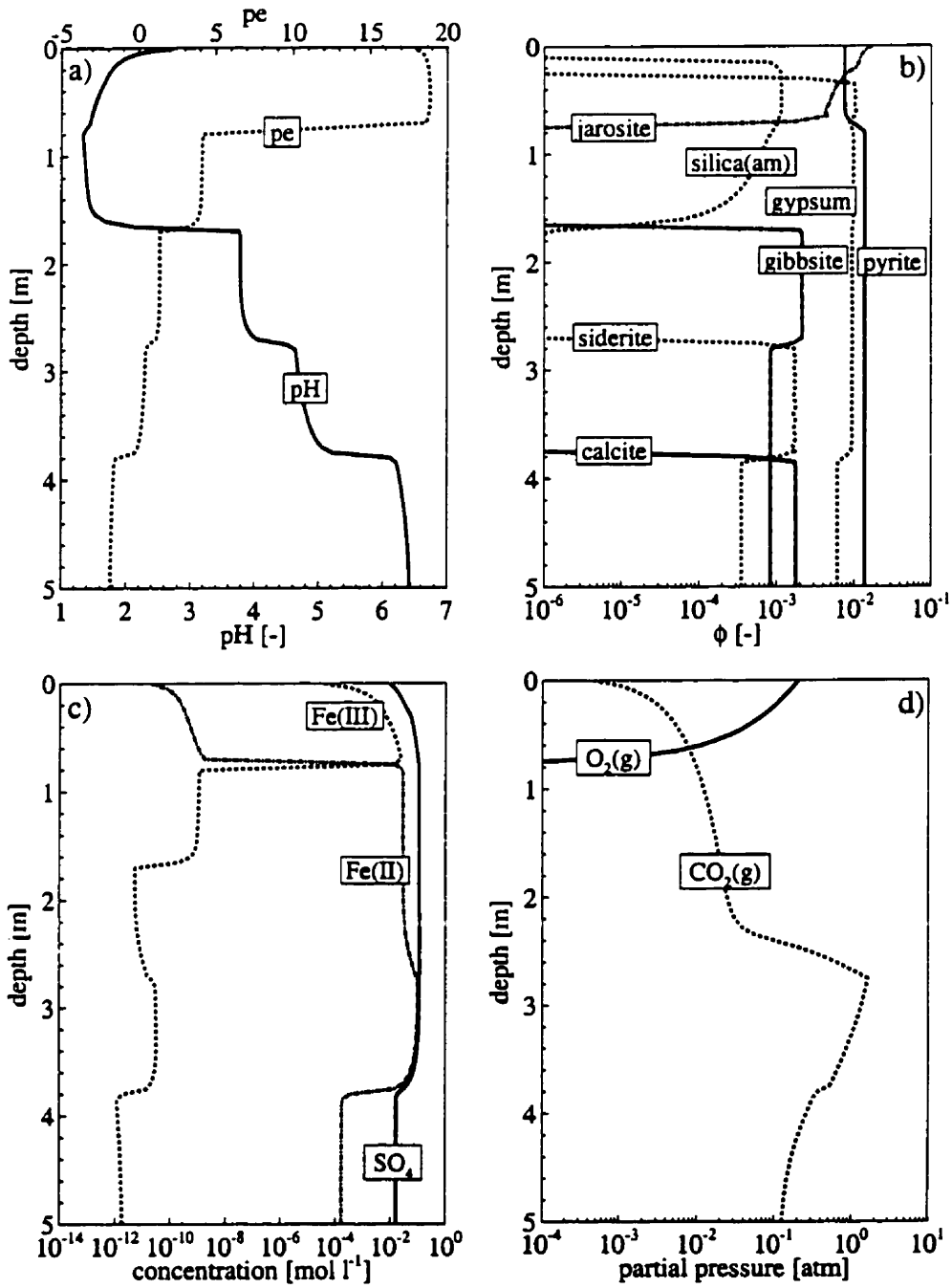

Figure 4.3: Results for test problem after $t = 10$ years, a) pH and pe, b) mineral volume fractions, c) selected total aqueous component concentrations, d) partial gas pressures

and ferric iron become depleted. The step-wise increase of pH at greater depth can be attributed to the dissolution of calcite (pH $\approx$ 6.4), siderite (pH $\approx$ 4.8) and gibbsite (pH $\approx$ 4.0), which is depicted in Figure 4.3b). The primary alumniosilicate minerals K-feldspar and muscovite also dissolve due to the excessively low pH-conditions (not shown), but have only a secondary influence on the groundwater composition due to the slow dissolution rates. As a result of the dissolution of these primary mineral phases, secondary minerals such as jarosite, amorphous silica and gypsum form within the column. After 10 years, elevated concentrations of dissolved iron and sulfate have penetrated deep into the column, as shown in Figure 4.3c). Ferric iron prevails close to the ground surface where oxidizing conditions prevail, while dissolved ferrous iron dominates below the zone of active oxidation. The test problem is characterized by steep geochemical gradients in the transition zone from oxic to anoxic conditions and in the zones of pH-buffering due to mineral dissolution.

4.10.1 Mass Balance Calculations

The mass balance calculations included in the present model can be used to investigate the interactions between the components within a single phase and between the phases. Figure 4.4 examines the fate of oxygen gas for the test problem, as it enters the subsurface. The mass balance calculations presented here consider the entire tailings column. Oxygen diffuses into the subsurface primarily through the gas filled porosity. Aqueous mass fluxes of dissolved oxygen are negligible in comparison to oxygen ingress through the gaseous phase due to its limited solubility and the small diffusion coefficient in water and are therefore not shown. Figure 4.4 shows that the infiltrating oxygen partitions into the aqueous phase, where it is consumed by the oxidation of pyrite and by the oxidation of ferrous iron to ferric iron, which subsequently precipitates in the form of ferrihydrite and jarosite. The pyrite oxidation rate and the dissolution-precipitation rates of ferrihydrite and jarosite can be related directly to the oxygen influx, if their reaction rates are normalized with respect to oxygen:

$$\begin{aligned}
\tfrac{2}{7}FeS_2(s) + O_2(aq) + \tfrac{2}{7}H_2O &\rightarrow \tfrac{2}{7}Fe^{2+} + \tfrac{4}{7}SO_4^{2-} + \tfrac{4}{7}H^+ \\
4Fe^{2+} + O_2(aq) + 10H_2O &\rightarrow 4Fe(OH)_3(s) + 8H^+ \\
\tfrac{4}{3}K^+ + 4Fe^{2+} + O_2(aq) + \tfrac{8}{3}SO_4^{2-} + 6H_2O &\rightarrow \tfrac{4}{3}KFe_3(SO_4)_2(OH)_6(s) + 4H^+
\end{aligned}$$

Examination of Figure 4.4 indicates that the majority of oxygen is ultimately consumed

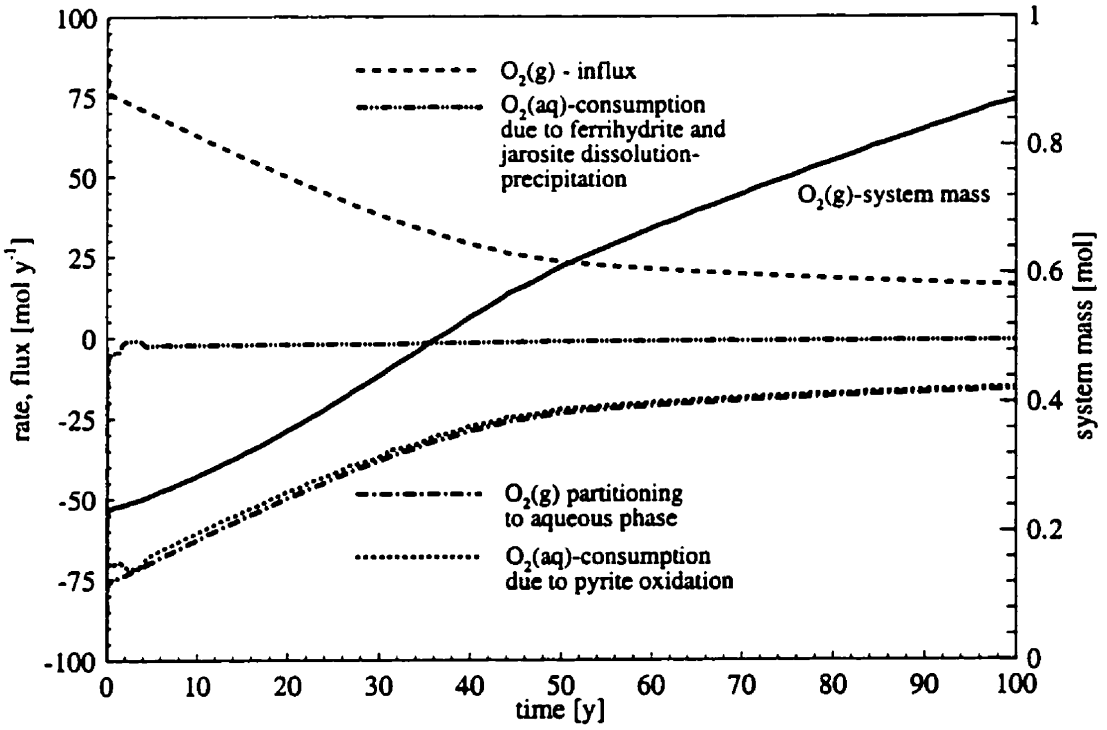

Figure 4.4: Mass balance for oxygen over a simulation period of $t = 100$ years

by pyrite oxidation. A small amount is, however, consumed by Fe(II)-oxidation, and subsequent precipitation of the mineral phases ferrihydrite and jarosite immobilizing some ferric iron in the oxidizing zone. This effect is more pronounced during the first two years of the simulation. The pH in the oxidizing zone during this time period is still buffered, allowing the precipitation of ferrihydrite. Primary minerals such as calcite, siderite and gibbsite become depleted in the oxidizing zone at later times, and ferrihydrite becomes unstable. This leads to the dissolution of ferrihydrite and an increase in Fe(III)-concentrations. This, in turn, causes jarosite to precipitate. This reaction can be written as an overall reaction:

$$3Fe(OH)_3(s) + K^+ + 2SO_4^{2-} + 3H_2O \rightarrow KFe_3(SO_4)_2(OH)_6(s) + 3H^+$$

Because this reaction does not consume dissolved oxygen, oxygen remains available for the oxidation of pyrite, manifesting itself in an increased pyrite oxidation rate. These conditions prevail until ferrihydrite becomes completely dissolved in the tailings column, occurring after approximately four years. At later times, the oxygen consumption can be attributed exclusively to pyrite oxidation and the oxidation of Fe(II) with the subsequent precipitation of jarosite.

Figure 4.4 also shows that the oxygen influx decreases over time. This is a result of the depletion of pyrite near the surface, causing the reaction to become increasingly limited by oxygen diffusion through the gaseous phase. Increasing water saturations further inhibit the diffusion of oxygen with increasing depth.

Furthermore, Figure 4.4 indicates that the yearly influx of oxygen is large in comparison to the total mass of oxygen contained in the tailings column (scale on right y-axis), implying that the residence time of oxygen is short. A residence time of less than a day can be calculated for the conditions prevailing at early time.

The maximum cumulative mass balance error, according to equation 4.35, was determined for dissolved oxygen and was $1.26 \cdot 10^{-3}$ % for a 10 year simulation. This error is very small considering the minute amount of dissolved oxygen and the high oxygen influxes. All other components are characterized by mass balance errors of less than 10^{-4} %. The convergence tolerance of the Newton-iteration, according to equation 4.41, was set to 10^{-6} log-cycles for this simulation.

4.10.2 Adaptive Time Stepping and Update Modification Schemes

The update- and iteration-based methods incorporated in the adaptive time stepping algorithm have been tested separately. Parameters which are independent of the method encompassing the maximum update ($\Delta \log C^c_{max}$) and the maximum number of Newton-iterations per time step (N^{max}_{it}) are varied over the same range for both techniques:

$$\begin{aligned} 2.0 &\leq \Delta \log C^c_{max} \leq 5.0 \\ 20 &\leq N^{max}_{it} \leq 80 \end{aligned}$$

A series of simulations for a time period of four years was carried out for each method and the model performance was examined based on the total number of time steps (N^{tot}_t), the total number of failed time steps (N^{tot}_{ft}), the total number of Newton-iterations (N^{tot}_{it})and

the actual CPU-time. All simulations were performed on an IBM-workstation (RS6000-590).

To test the performance of the update-based adaptive time stepping scheme, the anticipated update per time step was varied over the specified range:

$$0.5 \leq \Delta \log C^c_{\text{ant}} \leq 3.0$$

A total of 60 simulations were carried out; the results of these simulations are shown in Appendix A. The alternative iteration-based adaptive time stepping method was tested by varying the anticipated number of iterations within the range defined below:

$$10 \leq N^{\text{ant}}_{it} \leq 40$$

In this case a total of 48 simulations was carried out, the performance results are summarized in Tables A.3 and A.4 in Appendix A.

method	$\Delta \log C^c_{\text{ant}}$	N^{ant}_{it}	$\Delta \log C^c_{\text{max}}$	N^{max}_{it}	N^{tot}_{t}	N^{tot}_{ft}	N^{tot}_{it}	CPU [h:m:s]
update	2.0	-	3.0	60	163	7	2358	0:31:30
iteration	-	30	3.0	40	104	20	2229	0:29:56

Table 4.8: Optimal parameters and performance for update and iteration-based adaptive time stepping scheme - $t = 4$ years

Table 4.8 shows the parameters which resulted in the best model performance for each method along with the performance results. The results indicate that both methods perform best for a maximum update of $\Delta \log C^c_{\text{max}} = 3.0$ and a high maximum number of Newton-iterations per time step. The iteration-based method performed somewhat better than the update-based method in terms of CPU-time, however, the ratio between successful and failed time steps is much worse in this case. The total number of successful time steps is significantly higher for the update-based method with little more computational cost and allows therefore a higher temporal resolution of the model results. The update-based method appears to adjust the time increment to the physico-chemical conditions in the solution domain in a better way and is therefore considered superior.

The results in Appendix A show that a small number of maximum Newton-iterations leads to a large number of unsuccessful time steps, because the iteration loop is prema-

turely terminated. A very large number of maximum Newton-iterations, on the other hand, leads to the continuation of the Newton-iteration for time steps for which convergence can not be achieved at all. A small anticipated update or a small number of anticipated Newton-iterations result in small time steps and therefore in a large number of total time steps. Very large anticipated updates or a very large number of anticipated Newton-iterations, however, cause in the contrary frequent convergence failures. Execution times are prolonged in all cases.

The update modification scheme generally performed best for values of $\Delta \log C^c_{max} = 2$-3. The model results indicate that large maximum updates within a Newton-iteration increase the total number of iterations because the solution space is unsuccessfully searched, i.e. the quadratic convergence mode is never attained.

It is difficult to make a general recommendation for the choice of the adaptive time stepping parameters, as can be seen from the model performance for various parameter combinations in Appendix A. Tables A.1-A.4 do, however, clarify that the time stepping parameters have to be adjusted with respect to each other to obtain an efficient solution. It is likely, that the optimal parameter set for the present test example will not perform best for other reactive transport problems. However, experience with the modelling of other problems has confirmed that the parameters presented in Table 4.9 are usually a reasonable choice:

parameter	proposed range
$\Delta \log C^c_{ant}$	1-2
$\Delta \log C^c_{max}$	2-3
N^{ant}_{it}	20-30
N^{max}_{it}	40-60

Table 4.9: Recommended parameters for adaptive time stepping scheme

The test problem was then run for a simulation period of 100 years using the update-based adaptive time stepping scheme with the parameters shown in Table 4.8. Figure 4.5 shows the development of the time step versus simulation time along with a scale showing the maximum Courant numbers for advective transport of the dissolved species and diffusive gas transport in the gas phase.

It can be seen that the time increments are small during the initial period and show a gradually increasing trend as a function of elapsed time. The time increment during

the initial period is limited by the short time scale of oxygen diffusion into the tailings material and rapidly moving dissolution fronts of the primary buffer minerals such as calcite, siderite and gibbsite. Figure 4.5 shows frequent time step decreases during the course of the simulation, which are due to the depletion of mineral phases resulting in rapid geochemical changes in the aqueous phase concentrations. A series of quasi-steady states develop once calcite and siderite are depleted throughout the entire column. These quasi-steady state conditions are characterized by a dynamic equilibrium between the oxidation of pyrite, the weathering of aluminosilcate minerals and the dissolution and formation of secondary mineral phases such as jarosite, gypsum, amorphous silica and gibbsite. The periods of quasi-steady state are interrupted when pyrite or one of the remaining secondary mineral phases becomes completely depleted at a specific depth.

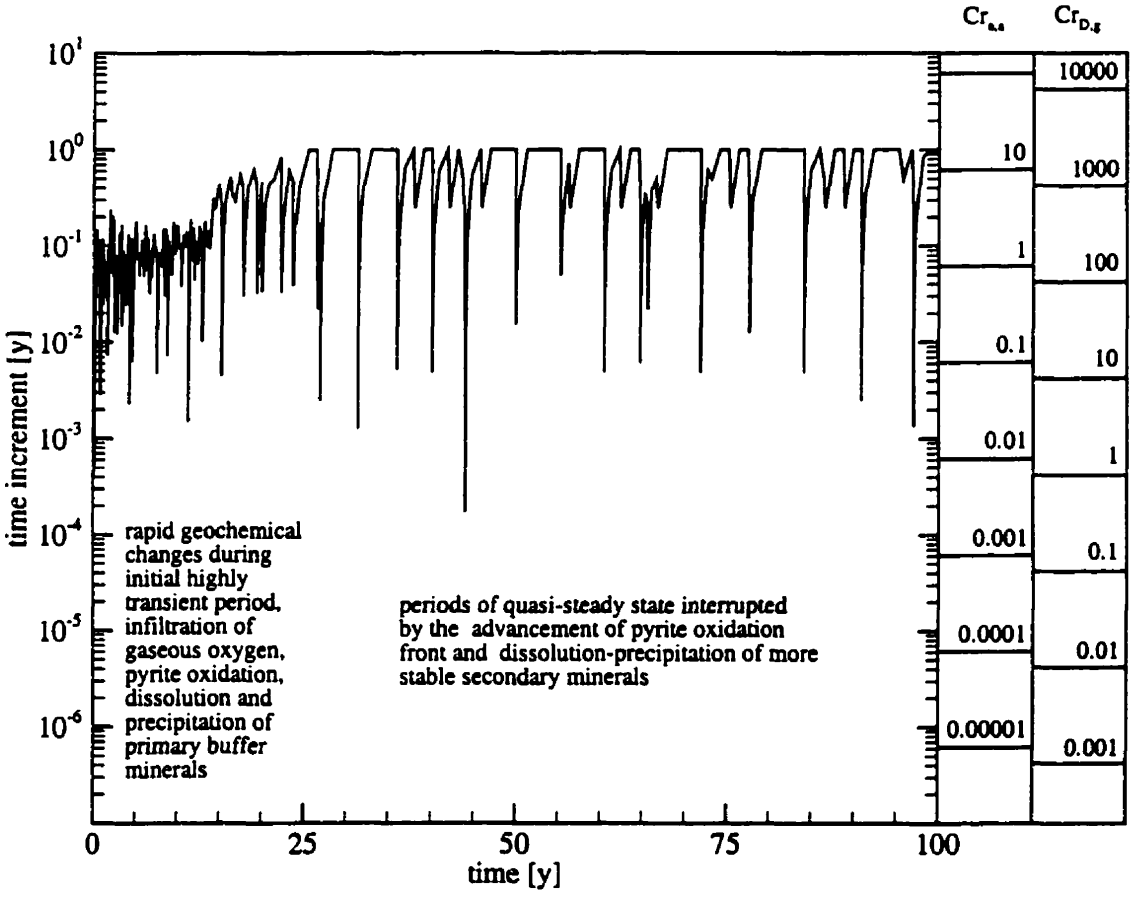

Figure 4.5: Development of time increment versus simulation time and corresponding Courant numbers

Figure 4.5 shows that the time stepping scheme is capable of dynamically adjusting to the geochemical changes in the solution domain. Large time steps are taken whenever the geochemical conditions are characterized by a state of dynamic equilibrium. Therefore, the adaptive time stepping algorithm allows an efficient solution of the example problem. The simulation required a total number of $N_t^{tot} = 487$ time steps excluding 82 time step failures. The total number of Newton-iterations was 9771, yielding a simulation time of 1 hour, 51 minutes and 15 seconds for the 100 year simulation.

The Courant numbers shown in Figure 4.5 are calculated based on the time increment and the physico-chemical and discretization parameters used in this study. The maximum Courant-number for the advective transport of dissolved species can be calculated as

$$Cr_{a,a} = \frac{v_{a,\max}\Delta t}{\Delta z},$$

where Δt is the time increment and Δz is the spatial discretization interval. $v_{a,\max}$ defines the maximum average linear groundwater velocity in the soil column and is defined by

$$v_{a,\max} = \frac{q_{\text{in}}}{S_{a,\min}\phi},$$

where q_{in} is the recharge rate and $S_{a,\min}$ is the minimum water saturation in the soil column, which is characteristic for conditions near to the ground surface.

The maximum Courant number for diffusive gas transport can be obtained from

$$Cr_{D,g} = \frac{2D_{g,\text{eff}}\Delta t}{\Delta z^2},$$

where $D_{g,\text{eff}}$ is the effective diffusion coefficient in the gas phase defined by

$$D_{g,\text{eff}} = S_{g,\max}^{10/3}\phi^{4/3}D_g^*,$$

where $S_{g,\max}$ is the maximum saturation of the gas phase, which occurs directly adjacent to the ground surface, and D_g^* is the free phase diffusion coefficient for oxygen in air. The parameters q_{in}, D_g^* and ϕ are defined in Table 4.2. The minimum saturation in the water phase is $S_{a,\min} = 0.7382$, which yield a maximum gas phase saturation of $S_{g,\max} = 0.2618$. The discretization interval used for this simulation is, as was previously defined, $\Delta z = 5$ cm.

Comparing the Courant numbers for advective and diffusive transport shows clearly

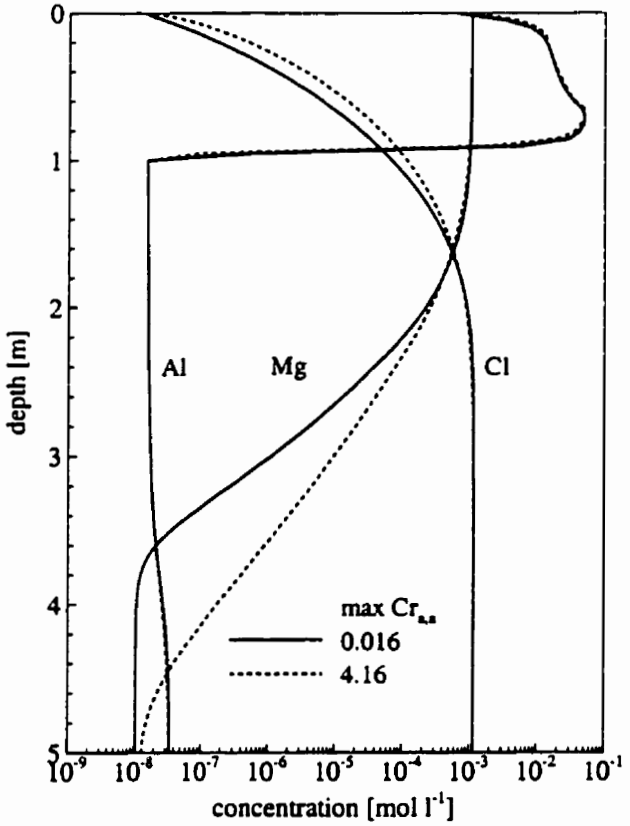

Figure 4.6: Effect of time step size on conservative and reactive species, $t = 2$ years

that the time scale of diffusive gas transport is much shorter than the time scale of advective transport in the aqueous phase. This would be even more pronounced for lower water saturations due to the nonlinear dependence of the effective diffusion coefficient on the gas phase saturation. Figure 4.5 also shows that the global implicit method allows simulations with high Courant numbers. In this particular case a maximum time increment of 1.0 years was specified. This time increment is used by the model during periods of quasi-steady state, the maximum Courant numbers for advective transport of dissolved species and diffusive gas transport are $Cr_{a,a} = 16.3$ and $Cr_{D,g} = 2379.2$ respectively. The use of a non-iterative operator-splitting method (SNIA) for such a simulation would require exceedingly small time increments. If $Cr_{D,g} > 1$, gaseous oxygen can be transported further than one grid cell without reacting, leading to erroneous results. Such a Courant-constraint would require a time increment of approximately

$\Delta t = 4.2 \cdot 10^{-4}$ years for this simulation, which corresponds to over 200,000 time steps for the 100-year simulation. The simulation conducted here on the other hand required only 487 time steps. This discussion implies that the global implicit solution method is particularly well suited for problems which are characterized by Damköhler numbers smaller than 1 or quasi-steady state problems, as already shown in Chapter 2 based on theoretical considerations.

In order to investigate the influence of the time step size on the accuracy of the model results, the test problem was run with a small maximum time increment, which was set to 10^{-3} years corresponding to a maximum advective Courant-number of $Cr_{a,a} = 0.016$. The simulation was carried out for a time period of 4 years. A simulation with no upper time step limit was conducted for comparative purposes, which yielded a maximum advective Courant-number of $Cr_{a,a} = 4.16$ during the 4 year-period.

Figure 4.6 compares the results for both cases for $t = 2$ years. The comparison includes components which are reactive (Al) and non-reactive (Cl and Mg). The input concentrations for Cl were chosen to evaluate the accuracy of the solution for components characterized by low source concentrations and high background concentrations, while Mg-concentrations are representative of the model accuracy for high source concentrations and low background concentrations. The accuracy of the solution for Cl and Mg are significantly degraded for the base case due to numerical dispersion. Artificial dispersion appears to be more pronounced for Mg, however, the Cl-concentration distribution may be affected by the boundary condition. The most notable finding for the comparison is that the concentration distribution for the reactive component Al shows no significant decrease in accuracy for the solution with the large time steps.

4.10.3 Spatial Weighting Schemes

Two simulations using centered spatial weighting and the van Leer flux limiter scheme have been conducted for a time period of 4 years.

The simulations were carried out with a small maximum time increment ($\Delta t_{max} = 10^{-3}$ years) to minimize numerical dispersion due to the time discretization. The results are compared to the simulation with upstream weighting ($\Delta t_{max} = 10^{-3}$ years) conducted in the previous section. The effect of the weighting schemes on the accuracy of the solution for reactive and non-reactive species is depicted in Figure 4.7 for $t = 2$ years. It can be observed that the higher order weighting schemes lead to less numerical dispersion for

the non-reactive species Cl and Mg. The van Leer-flux limiter performs somewhat better than centered spatial weighting. The results also show that the accuracy for reactive species (e.g. Al) is not significantly affected by the spatial weighting scheme.

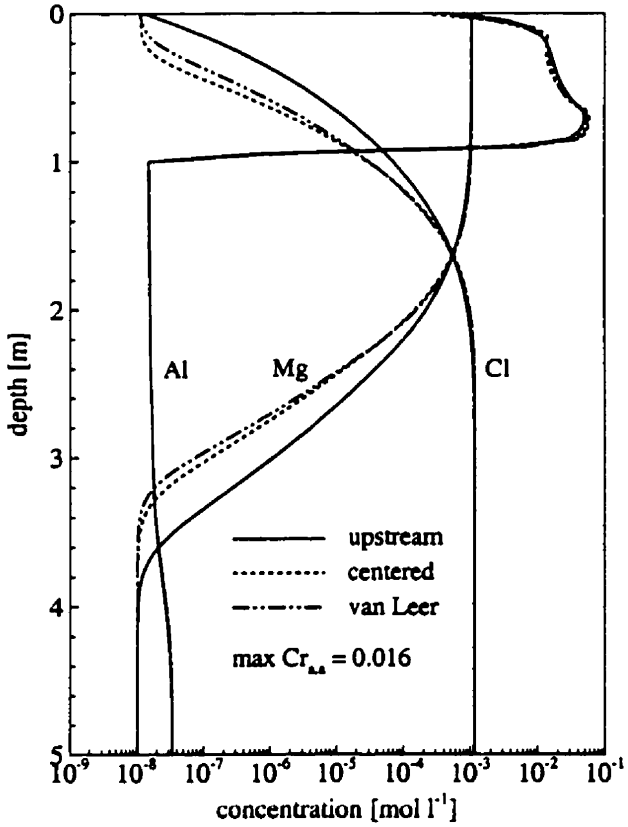

Figure 4.7: Effect of spatial weighting schemes on conservative and reactive species, t = 2 years

Two additional simulations were carried out to evaluate how the higher order weighting schemes affect the execution times of the simulations, if the maximum time step is not restricted. This comparison is necessary to determine whether the higher order weighting schemes are applicable to practical simulations. The disadvantage of flux limiters is that additional non-linearity is introduced into the model equations. Convergence may therefore be inhibited, particularly in the vicinity of domain boundaries and internal source-sink terms [*Unger et al.*, 1996]. Reactive transport solutions are unfortunately characterized by many local internal sources and sinks, primarily due to dissolution-

precipitation reactions. The efficiency of the solution may be influenced adversely under certain circumstances. Table 4.10 shows that the computational requirements increase for centered spatial weighting and the van Leer-flux limiter in comparison to upstream weighting. The increases are, however, not dramatic, and it appears that flux limiter methods are useful for a more accurate description of the transport of non-reactive species in comparison with upstream or centered weighting.

weighting scheme	N_t^{tot}	N_{ft}^{tot}	N_{it}^{tot}	CPU [h:m:s]
upstream	163	7	2358	0:31:30
centered	179	25	2859	0:38:52
van Leer	168	14	2745	0:38:32

Table 4.10: Numerical performance dependent on spatial weighting scheme, $t = 4$ years

4.10.4 Activity Update Techniques

This section compares the influence of the activity update techniques on the accuracy of the model results and the performance of the model. The simulations were conducted for a time period of 10 years. Only the time-lagged and the double update methods are compared because the use of unity activity coefficients would lead to different model results, thereby preventing a direct comparison.

Figure 4.8 presents selected mineral volume fractions for both methods after $t = 10$ years. It can be seen that the results are practically identical; the time-lagged activity update method does not decrease the accuracy notably. The execution times for the simulations, however, differ significantly, as shown in Table 4.11. The method using the double update during each Newton-iteration requires more than 23 times the execution time than the time-lagged method. This is primarily due to the additional non-linearity introduced in the system of equations. The parameters for the adaptive time stepping algorithm had to be adjusted to the values reported in Table 4.11 to obtain a solution within less than a day.

update technique	$\Delta \log C_{ant}^c$	$\Delta \log C_{max}^c$	N_{it}^{ant}	N_{it}^{max}	N_t^{tot}	N_{ft}^{tot}	N_{it}^{tot}	CPU [h:m:s]
time-lagged	2.0	3.0	-	60	448	11	4951	0:58:29
double	0.5	1.5	12	30	6756	1993	105895	22:54:09

Table 4.11: Numerical performance dependent on activity update technique, $t = 10$ years

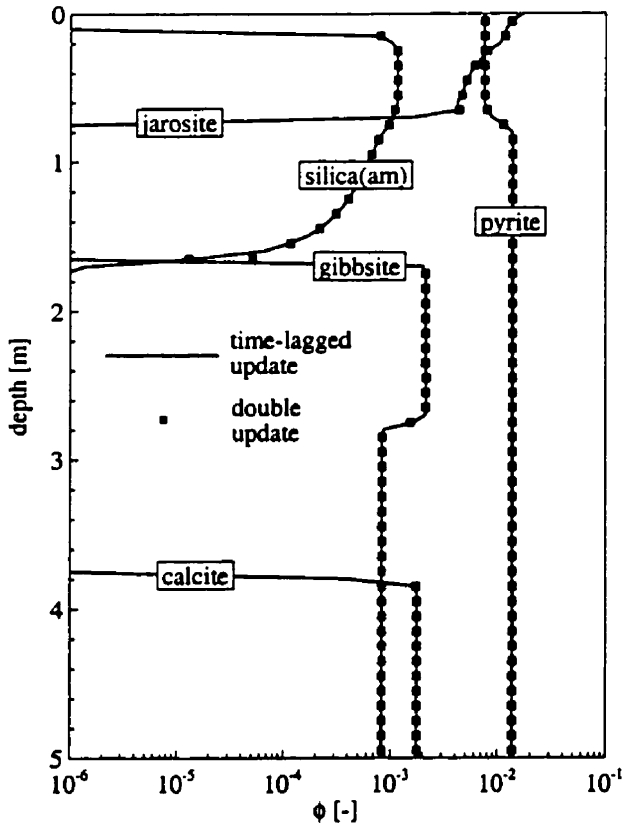

Figure 4.8: Effect of activity update method on selected mineral volume fractions, t = 10 years

4.10.5 Choice of Redox Master Variable

The test problem is now used to compare for two different choices of the redox master variable, namely O_2(aq) and H_2(aq). Reactions affected are the oxidation of ferrous iron in the aqueous phase, gaseous and aqueous oxygen concentrations, and the equilibrium condition for pyrite oxidation. Table 4.12 summarizes these reactions in terms of the different redox master variables and furthermore defines the pe calculation for the different cases.

Figure 4.9 compares the results for the different choices of master variables for pH and pe. The results are virtually identical for both methods. It is interesting to note,

Reaction			log K
redox master variable: $O_2(aq)$			
(1)	Fe^{3+}	$= Fe^{2+} + 0.25O_2(aq) + H^+ - 0.5H_2O$	8.473
(2)	HS^-	$= SO_4^{2-} + H^+ - 2O_2(aq)$	-138.376
(3)	$O_2(g)$	$= O_2(aq)$	2.898
(4)	$H_2(aq)$	$= H_2O - 0.5O_2(aq)$	-46.133
(5)	$FeS_2(s)$	$= Fe^{2+} + 2SO_4^{2-} + 2H^+ - 3.5O_2(aq) - H_2O$	-215.264
	pe	$= 21.5045 - pH + 0.25\log\{O_2(aq)\} - 0.5\log\{H_2O\}$	
redox master variable: $H_2(aq)$			
(1)	Fe^{3+}	$= Fe^{2+} + H^+ - 0.5H_2(aq)$	-14.594
(2)	HS^-	$= SO_4^{2-} + H^+ + 4H_2(aq) - 4H_2O$	-46.156
(3)	$O_2(g)$	$= 2H_2O - 2H_2(aq)$	-89.368
(4)	$O_2(aq)$	$= 2H_2O - 2H_2(aq)$	-92.266
(5)	$FeS_2(s)$	$= Fe^{2+} + 2HS^- - H_2(aq)$	-14.675
	pe	$= -1.562 - pH - 0.5\log\{H_2(aq)\}$	

Table 4.12: Oxidation-reduction reactions for different redox master variables - test problem for numerical performance

Master variable	$\Delta\log C^c_{ant}$	$\Delta\log C^c_{max}$	N^{ant}_{it}	N^{max}_{it}	N^{tot}_{t}	N^{tot}_{ft}	N^{tot}_{it}	CPU [h:m:s]
$O_2(aq)$	2.0	3.0	-	60	448	11	4951	0:58:29
	-	3.0	30	40	163	54	4546	0:53:12
$H_2(aq)$	1.5	2.0	-	60	270	20	4486	0:51:49
	-	2.0	30	40	146	41	4252	0:48:56

Table 4.13: Numerical performance dependent on redox master variable, $t = 10$ years

however, that the simulation using $H_2(aq)$ required a smaller number of time steps and less CPU-time than the simulation which used $O_2(aq)$ as the redox master variable. This indicates that the magnitude of the concentration of the master variable does not exclusively determine the efficiency of the solution. The relative change in concentration from one time step to the next also affects the performance. The reduction in simulation time using $H_2(aq)$ is, however, not very dramatic. This can be explained by the fact that the time step size is frequently limited by other primary unknowns such as dissolved Fe and Al. The effect of the choice of the redox master variable is therefore somewhat diluted. Table 4.13 summarizes the numerical performance of the model for the different

cases. It can be observed that the model required approximately 8% less CPU-time when using H_2(aq).

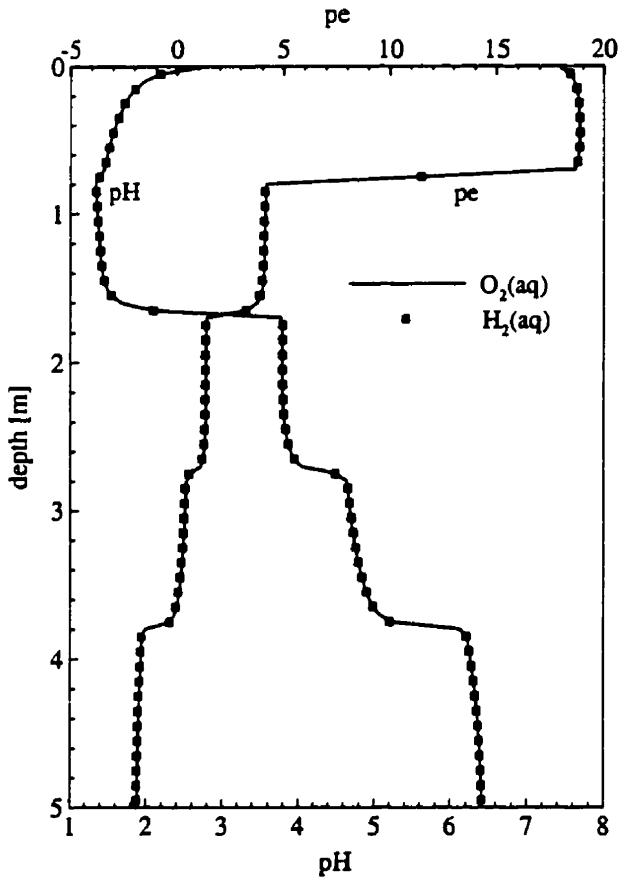

Figure 4.9: Distribution of pH and pe versus depth for different redox master variables, $t = 10$ years

4.11 Summary of Results

The test problem presented in this chapter has shown that appropriate numerical methods, which are incorporated in the present model formulation, must be used to allow an efficient and accurate solution of reactive transport problems. The findings of this study can be summarized as follows:

- The mass balance calculations are a powerful tool for the interpretation of the interactions between the gaseous, dissolved and solid species.
- The adaptive time stepping scheme allows for the efficient solution of complex problems and allows large Courant-numbers during periods of quasi-steady state. The update-based scheme is considered superior because it achieves the same degree of efficiency with smaller time increments and less time step failures, resulting in a higher accuracy of the solution.
- The global implicit method appears to be particularly well suited for multiphase problems because it allows very large time steps in comparison to the time scale of the gas transport processes.
- Large time steps affect the accuracy of the solution significantly for non-reactive components, but do not affect the distributions of component concentrations controlled by fast dissolution-precipitation reactions.
- Flux limiter schemes can be used to improve the accuracy of the model results; an improvement can be obtained specifically for non-reactive species. Centered spatial weighting can be used alternatively, but is not appropriate for all simulations. Upstream weighting of the advective term provides a sufficient degree of accuracy for the determination of mineral assemblages, particularly if mineral dissolution-precipitation reactions are fast.
- Based on the previous two points it can be concluded that the dissolution or precipitation of a particular mineral phase can have an self-sharpening effect on concentration fronts. This overrules the effect of transport-induced numerical dispersion. This property may also explain the comparably small errors introduced when using operator-splitting techniques (SIA, SNIA approaches) for the solution of reactive-transport problems for which concentration distributions are largely controlled by equilibrium dissolution-precipitation reactions [e.g.: *Walter et al.*, 1994a].
- The accuracy of the solution at late time is only slightly affected by the time step size and the spatial weighting scheme if several pore volumes pass through the solution domain during the course of a simulation. This is because the concentration gradients are controlled by geochemical reaction processes and not by transport processes.

- The time-lagged update of the activity coefficients does not decrease the accuracy of the results notably, but allows a much more efficient solution.
- A more efficient solution could be obtained for the test problem using $H_2(aq)$ as the redox master variable instead of $O_2(aq)$. These results show that the relative concentration change of the components over a single time step influence the efficiency of the solution, indicating that the relative concentration changes may have a larger influence than the actual magnitude of the concentrations in the case of reactive transport problems.

Most of these findings should be applicable in a general sense for more complex, multidimensional reactive transport problems. However, it can be expected that the performance of spatial weighting schemes is affected in a different manner for two- or three-dimensional problems.

Chapter 5

Model Verification

Analytical solutions are not available for complex multicomponent reactive transport problems. An alternative model verification approach has been employed to overcome this shortfall. The verification of the present model consists of direct comparisons of MIN3P to established numerical models and comparison tests involving the individual modules of MIN3P and analytical solutions for transport problems. One verification problem involves the comparison of the model results to field data.

Verification problems addressing variably-saturated flow, conservative transport of dissolved species and gas diffusion will only be discussed generically for reasons of brevity. This discussion is followed by four verification problems of various difficulty. The first problem is a comparison of MIN3P with the numerical model PYROX [*Wunderly et al.*, 1996] and it assesses the functionality of the code for problems involving the oxidation of sulfide minerals described by the shrinking core model [*Levenspiel*, 1972]. The second problem assesses the model's capability for simulating reactive transport involving ion-exchange reactions. The model has been applied to match field data reported by *Valocchi et al.* [1981]. The remaining problems involve comparisons with the multiphase-multicomponent reactive transport model MULTIFLO [*Lichtner*, 1996a] and are based on two benchmark problems presented at the "Workshop on Subsurface Reactive Transport Modeling" in Richland, WA, 1997. The first of these comparisons describes the generation of acid mine drainage in a partially-saturated porous medium and subsequent reactive transport [*Lichtner*, 1997a]. The last problem is a two-dimensional scenario and describes the leaching of copper from a five-spot well pattern [*Lichtner*, 1997b].

5.1 Verification of Flow and Transport Modules

Several comparisons have been performed to verify the variably-saturated flow module. These comparisons encompassed one-dimensional drainage and infiltration problems as reported by *Forsyth et al.* [1995]. Simulation results for a two-dimensional infiltration problem based on laboratory data from *Vauclin et al.* [1979] as reported by *Clement et al.* [1994] have been compared directly to the results obtained by FRAC3DVS [*Therrien and Sudicky*, 1996]. To evaluate the performance of the seepage-face algorithm a comparison between the present model and UNSAT2 [*Davis and Neuman*, 1983] has been carried out. Example problem #2 of the UNSAT2 Documentation and User's Guide [*Davis and Neuman*, 1983] has been chosen for this comparison. The results for all problems were in close agreement with respect to hydraulic head, pressure head and saturation distributions. The model proved to be very robust and computationally efficient for all simulations conducted.

Non-reactive transport has been verified by comparing the results of a two-dimensional test case with a strip boundary condition to an analytical solution of the advection-dispersion equation developed by *Cleary and Ungs* [1978]. Gas diffusion has been verified by comparing the results of a one-dimensional test case involving gas diffusion in a porous medium with constant moisture content to the Ogata-Banks solution [*Ogata and Banks*, 1961].

5.2 Comparison with PYROX

This comparison is designed to verify both the formulation for diffusive gas transport in unsaturated porous media and the formulation for the diffusion-controlled dissolution of minerals as presented in Chapter 3, Section 3.4.6. Results from the newly developed reactive transport model MIN3P are compared to the model results from PYROX [*Wunderly et al.*, 1996]. PYROX was designed exclusively for the simulation of sulfide mineral oxidation in the unsaturated zone due to the infiltration of atmospheric oxygen. The model PYROX couples the bulk porous medium diffusion of oxygen in the gas phase with the diffusion-controlled oxidation of pyrite or pyrrhotite based on the shrinking core model [*Wunderly et al.*, 1996]. This comparison involves the simulation of pyrite oxidation in the unsaturated zone of a porous medium consisting entirely of pyrite particles. The

overall reaction stoichiometry of pyrite oxidation is defined by:

$$FeS_2(s) + \frac{7}{2}O_2(aq) + H_2O \rightarrow Fe^{2+} + 2SO_4^{2-} + 2H^+ \quad (5.1)$$

PYROX and MIN3P can be used to predict the mass of oxygen and pyrite consumed as well as the mass of the reaction products generated due to the reaction above. The actual masses can be calculated based on the reaction stoichiometry defined in equation 5.1.

5.2.1 Problem Definition

Table 5.1 presents the input parameters used for the present verification problem. A vertical column of 1.5 m length has been chosen as the solution domain. The free phase diffusion coefficient for gaseous oxygen has been taken from the compilation of *Glinski and Stepniewski* [1985] for 10°C. Diffusion in the aqueous phase is neglected because the formulation of PYROX does not include transport processes in the aqueous phase. A porosity of $\phi = 0.5$ has been assumed throughout the column. A first type boundary condition with a hydraulic head of h = -0.2 m is defined as the bottom boundary 1.5 m below the ground surface and a second type boundary with zero flux is specified as the top boundary. The hydraulic conductivity is arbitrary, since no flow occurs as a result of the specified boundary conditions. Soil hydraulic function parameters and the residual saturation for the van Genuchten equations are specified in Table 5.1. These parameters are needed to compute the saturations of the aqueous and gaseous phase.

Parameter		unit	value
length of solution domain	L	[m]	1.5
porosity	ϕ	[-]	0.5
oxygen diffusion coefficient	D_g	[m^2s^{-1}]	$1.89 \cdot 10^{-5}$
residual saturation	S_{ra}	[-]	0.05
soil hydraulic function	α	[-]	3.5
parameters	n	[-]	1.5
pyrite volume fraction	φ_{Pyr}	[-]	0.5
initial grain size	r^p_{Pyr}	[m]	$7.0 \cdot 10^{-5}$
diffusion coefficient through surface coating	D^m_{Pyr}	[m^2s^{-1}]	$1.0 \cdot 10^{-14}$

Table 5.1: Physical and chemical input parameters - comparison with PYROX

Of particular importance are the phase saturations in the gaseous phase, which are used to compute the effective diffusion coefficients for oxygen. The phase saturations are presented in Figure 5.1 as a function of depth.

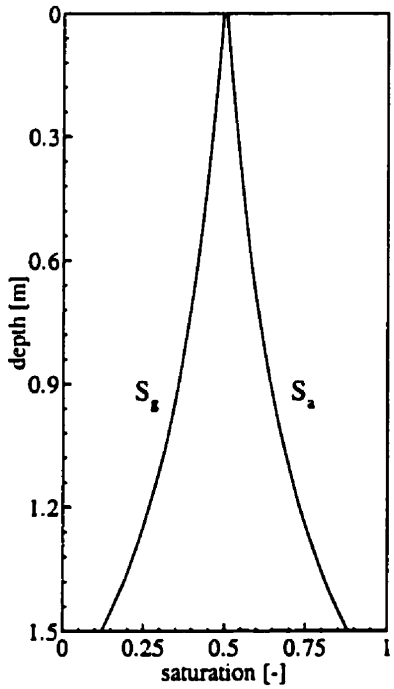

Figure 5.1: Phase saturations - comparison with PYROX

The MIN3P-simulation requires the specification of four components, SO_4^{2-}, Fe^{2+}, O_2(aq) and H^+, which all participate in reaction 5.1. Complexation reactions have been neglected. O_2(g) has been specified as the only gas, and pyrite has been defined as the only mineral phase. Arbitrarily low concentrations for all dissolved species and gaseous oxygen are specified as an initial condition within the solution domain. A first type boundary condition has been assigned for oxygen in the gas phase, while a third type boundary condition is specified for all dissolved species. A partial oxygen pressure of 0.21 atm has been specified at the top boundary. To facilitate comparison with PYROX, it has been assumed that the solid phase is made up entirely of pyrite, resulting in a pyrite volume

fraction of $\varphi_{Pyr} = 0.5$. Other parameters influencing the rate of pyrite oxidation are the initial representative grain radius of the pyrite particles and the diffusion coefficient of dissolved oxygen through the surface coating formed on the unreacted portion of the pyrite particles. It is assumed that all pyrite particles react in a uniform manner and that the particles are unreacted to 99% initially.

The simulation has been conducted for a period of 20 years with a maximum time increment of 0.1 years using a spatial discretization of 121 control volumes with half cells on the boundary corresponding to a spatial discretization increment of 1.25 cm.

The model PYROX was slightly modified for this comparison. The empirical relationship for the calculation of the effective diffusion coefficient for oxygen developed by *Reardon and Moddle* [1985] implemented in the original code was replaced by the relationship reported by *Millington* [1959] as described in equation 3.12. The time weighting of PYROX was also changed from centered to the fully-implicit scheme to concentrate the comparison on the kinetic formulation for diffusion-controlled dissolution reactions. Unit activity coefficients were used in the MIN3P simulation to allow a direct comparison with PYROX.

5.2.2 Evaluation of Results

Figure 5.2a compares the pyrite oxidation rate obtained from the MIN3P and PYROX simulations. The oxidation rate is here given in units of mol d^{-1} and represents the cumulative rate for the entire column. It can be seen that the reaction rate decreases gradually over time. This behavior is primarily caused by the accumulation of a surface coating on pyrite particles, which acts as a protective layer inhibiting the oxidation process. A second reason for decreasing reaction rates is an increase in the average diffusion length for oxygen in the bulk porous medium, since oxygen enters deeper regions of the column as pyrite becomes gradually depleted. The results of both models agree very well. Figure 5.2b presents the total mass of pyrite oxidized during the 20 year simulation period. This quantity is given in units of [mol] and is also representative for the entire column. The mass of pyrite oxidized is steadily increasing, however, the increase becomes less pronounced over time due to the decreasing reaction rates. The mass of oxygen consumed as well as the mass of sulfate and ferrous iron produced can be calculated based on the reaction stoichiometry given in equation 5.1 and is therefore not shown here.

Figure 5.3a shows depth-dependent oxygen profiles after 10 and 20 years simulation

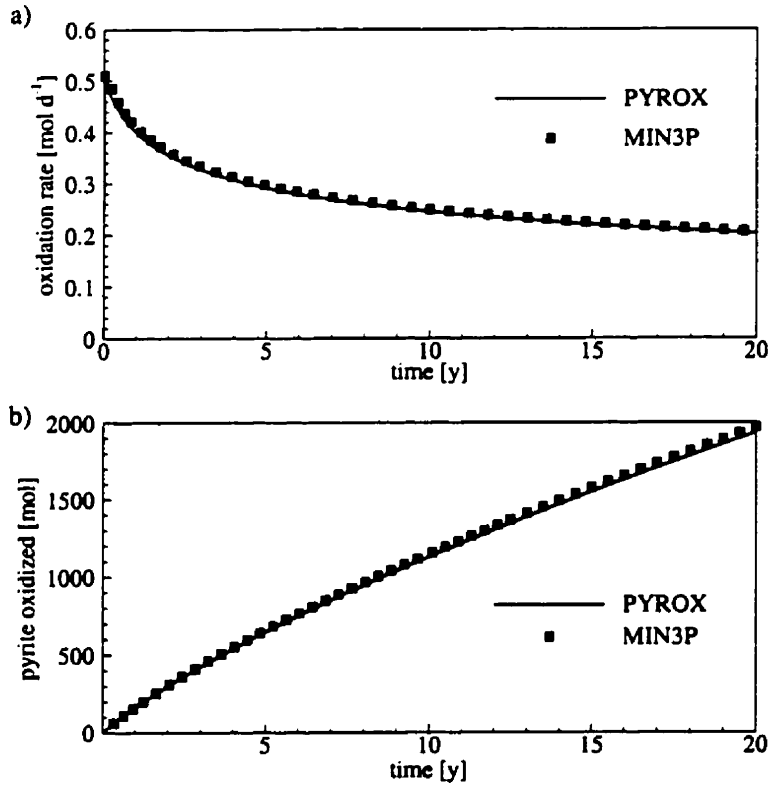

Figure 5.2: Comparison MIN3P versus PYROX: a) total pyrite oxidation rate, b) total mass of pyrite oxidized

time. The gradient of the oxygen profile is caused by the consumption of oxygen by pyrite oxidation and the increasing resistance to gas transport due to increasing moisture content with depth. The pyrite volume fractions are presented in Figure 5.3b and show an inverse behavior in relation to the oxygen profiles. The results of both models again agree very well.

The PYROX solution treats the mineral parameters as primary unknowns and provides an implict solution with respect to the fraction of pyrite reacted. MIN3P, on the other hand, uses an explicit update for the mineral parameters. The reaction rates calculated using the explicit approach will overpredict pyrite oxidation rates, while the implicit approach will underestimate the reaction rates. Figure 5.2a indicates these differences; however, the discrepancies between the results are only minor, at least for the problem

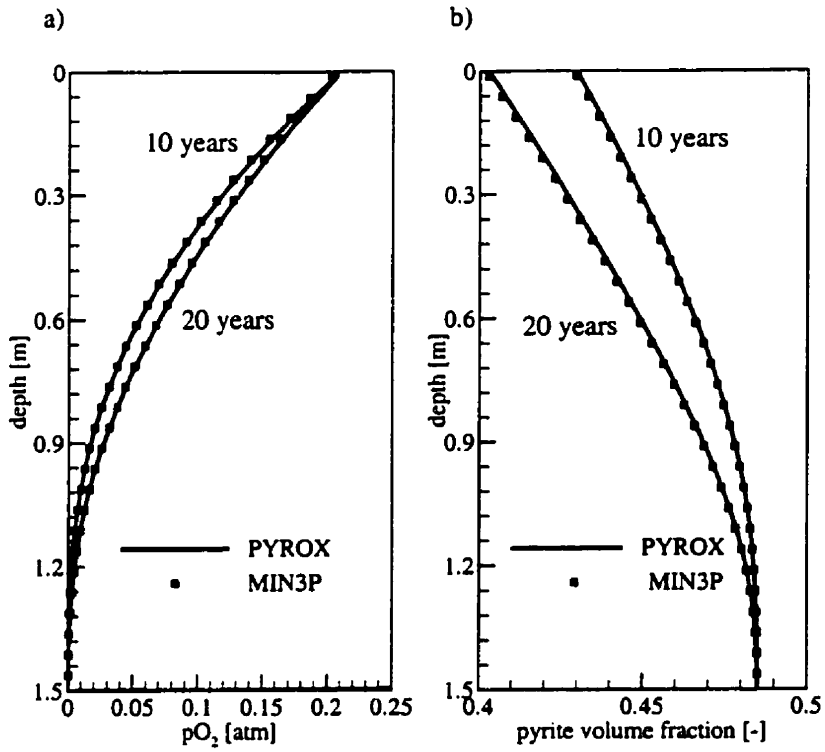

Figure 5.3: Comparison MIN3P versus PYROX: a) partial oxygen pressures, b) pyrite volume fractions

presented here. Results using fully-implicit and centered time weighting for PYROX were also compared in this context and, again, the differences proved to be insignificant.

5.2.3 Numerical Settings and Performance

The solution of the verification problem required a total 292 time steps; no time step failures occurred. The total number of Newton iterations was 1163. A CPU-time of 36 seconds is required on a Pentium P2/266 MHz.

5.3 Ion Exchange

The ability of MIN3P to solve physical transport coupled with ion-exchange has been tested by comparing the model results to the classical field example from the Palo Alto Baylands Region as reported by *Valocchi et al.* [1981]. Fresh water from a sewage treatment plant with near drinking water quality is injected into a shallow alluvial aquifer containing brackish water [*Valocchi et al.*, 1981, *Appelo and Postma*, 1993]. The brackish water contains high concentrations of Na^+ and Mg^{2+} while the fresh water contains relatively high calcium concentrations. The injection of the fresh water leads to a series of ion-exchange reactions, which ultimately results in the replacement of sodium and magnesium by calcium on the exchange sites. Stoichiometric relationships describing these ion-exchange reactions, based on the Gaines-Thomas-convention, can be written as:

$$Na^+ + \tfrac{1}{2}Ca\text{-}X_2 \rightleftharpoons Na\text{-}X + \tfrac{1}{2}Ca^{2+}$$
$$Na^+ + \tfrac{1}{2}Mg\text{-}X_2 \rightleftharpoons Na\text{-}X + \tfrac{1}{2}Mg^{2+}$$

5.3.1 Problem Definition

The injection results in a two-dimensional radial flow field, which is here simply approximated by one-dimensional uniform flow-field in a cartesian coordinate system. This simplification can be justified, since the focus of this comparison is limited to the reproduction of the general chromatographic pattern reported by *Valocchi et al.* [1981]. A constant Darcy flux was used and represents an average quantity between the injection and the observation well. The physical input parameters used for this verification problem are summarized in Table 5.2.

A cation-exchange capacity of $CEC = 10$ meq/100g solid, determined from laboratory batch experiments [*Valocchi et al.*, 1981], was used for the simulations. The corresponding selectivity coefficients are listed in Table 5.3. The chemical composition of the injected water and the background water are summarized in Table 5.4. Complexation reactions are neglected in order to be consistent with the original simulation. The problem was solved using unity activity coefficients. The initial condition for the ion-exchanged species was calculated based on the aqueous concentrations reported in Table 5.4.

Parameter	unit	value	reference
length of solution domain	[m]	16.0	*Valocchi et al.* [1981]
porosity	[-]	0.25	*Valocchi et al.* [1981]
Darcy flux	[m hour^{-1}]	0.35	calibrated
longitudinal dispersivity	[m]	1.0	*Valocchi et al.* [1981]
dry bulk density	[gcm^{-3}]	1.875	*Valocchi et al.* [1981]
cation exchange capacity	[meq/100g solid]	10.0	*Valocchi et al.* [1981]

Table 5.2: Physical input parameters - ion-exchange verification problem after *Valocchi et al.* [1981]

ion-exchanged species	log K_i^s
Mg^{2+}-X	0.355
Ca^{2+}-X	0.602

Table 5.3: Selectivity coefficients with Na^+ - ion-exchange verification problem after *Valocchi et al.* [1981]

component	Injection water [mg l^{-1}]	Background water [mg l^{-1}]
Na^+	216.0	1990.0
Mg^{2+}	12.0	436.0
Ca^{2+}	85.0	444.0
Cl^-	320.0	5700.0

Table 5.4: Chemical input parameters - ion-exchange verification problem after *Valocchi et al.* [1981] - Well S23

5.3.2 Evaluation of Results

Figure 5.4 shows the total aqueous component concentrations for sodium, magnesium and calcium versus time at observation well S23 [*Valocchi et al.*, 1981]. The injection of fresh water leads initially to the desorption of all cations, which is indicated by the concentration drop during the first 50 hours of operation (≈1,000 m^3 injected). The remaining concentration changes are due to the replacement of ion-exchanged Na^+ and Mg^{2+} by Ca^{2+}.

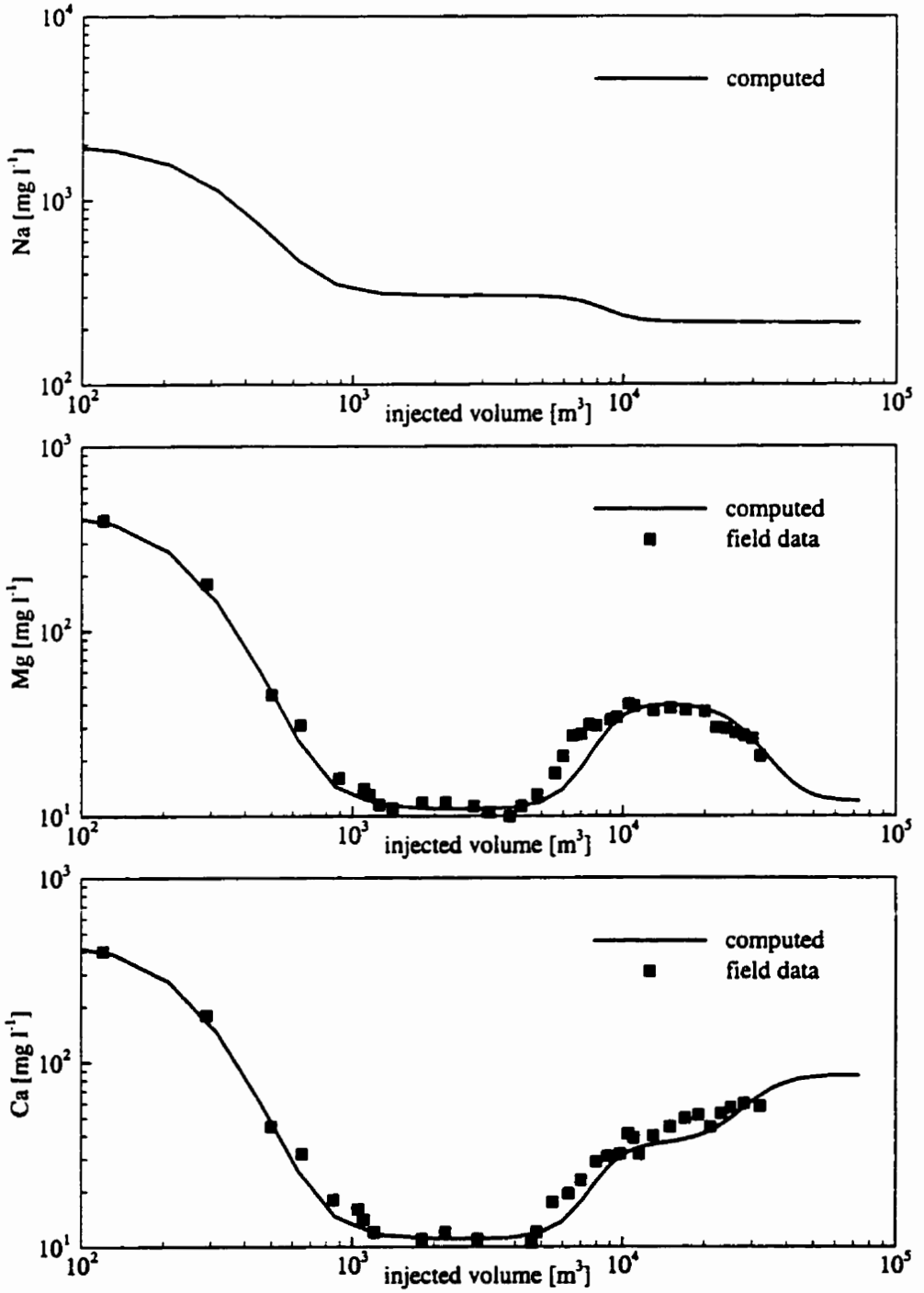

Figure 5.4: Comparison of simulated and actual breakthrough of Na^+, Mg^{2+} and Ca^{2+} at observation well S23 (field data for Na^+ not available)

Na^+ is replaced first by Mg^{2+} and Ca^{2+}, which can be seen by the decreasing sodium concentrations after approximately 380 hours (≈8,000 m^2 injected) accompanied by increasing calcium and magnesium concentrations. Finally Ca^{2+} displaces most of the ion-exchanged Mg^{2+} starting after approximately 950 hours (≈20,000 m^3 injected), which leads to the decrease of the observed magnesium concentrations accompanied by a further increase of calcium concentrations at the observation well. The modelled data agrees very well to the field data from *Valocchi et al.* [1981]. A comparison with sodium data was not possible because this data was not provided in the original reference.

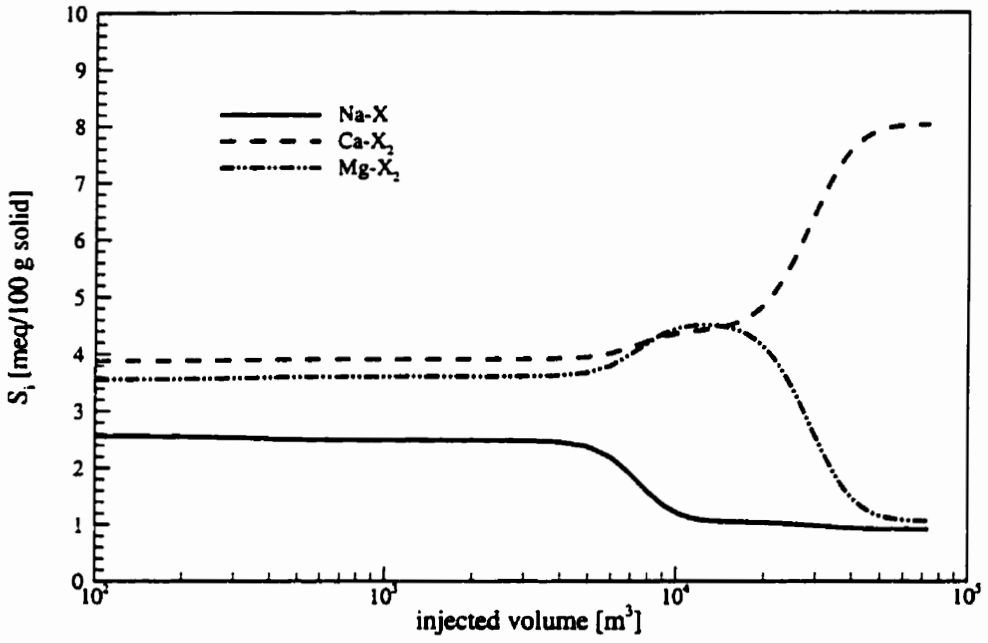

Figure 5.5: Concentrations of ion-exchanged species at monitoring well S23 as a function of time

It is also instructive to consider the concentrations of the ion-exchanged species. Figure 5.5 depicts the concentrations of the ion-exchanged species in the vicinity of observation well S23 as a function of time. The aquifer material in contact with the brackish background water has already Ca^{2+} as the dominant ion-exchanged cation, more abundant than Mg^{2+} and Na^+ despite the comparably low calcium concentrations. This

behavior reflects the selectivity sequence $Ca^{2+} > Mg^{2+} > Na^{+}$ [*Valocchi et al.*, 1981]. Towards the end of the simulation time, almost 80% of the available exchange sites are occupied by Ca^{2+}, while the remaining 20% are shared by sodium and magnesium. Such a behavior is expected, since the injected fresh water is comparably rich in calcium.

5.3.3 Numerical Settings and Performance

The problem was solved to a final solution time of 3500 hours (58.3 days) using a spatial increment of 16 cm and a maximum time step of 50 hours. The simulation required a total number of 101 time steps or 322 Newton iterations; no time step failures occurred during the solution. The required CPU-time on a Pentium P2/266 MHz is 27 seconds.

5.4 Benchmark Problem: Acid Mine Drainage

This benchmark problem considers the generation of acid mine drainage due to pyrite oxidation. Gaseous oxygen enters the subsurface due to the existence of an unsaturated zone and partitions into the aqueous phase where it is consumed as an electron acceptor for the oxidation of pyrite:

$$FeS_2(s) + \tfrac{7}{2}O_2(aq) + H_2O \rightarrow Fe^{2+} + 2SO_4^{2-} + 2H^{+} \tag{5.2}$$

Dissolved oxygen can alternatively be consumed by the oxidation of ferrous iron:

$$Fe^{2+} + \tfrac{1}{4}O_2(aq) + H^{+} \rightarrow Fe^{3+} + \tfrac{1}{2}H_2O \tag{5.3}$$

Ferric iron produced by the oxidation of ferrous iron is subsequently available as an oxidizing agent for the oxidation of pyrite:

$$FeS_2(s) + 14Fe^{3+} + 8H_2O \rightarrow 15Fe^{2+} + 2SO_4^{2-} + 16H^{+} \tag{5.4}$$

Pyrite oxidation produces acidity and leads to an increase of iron and sulfate concentrations in the pore water. The resulting low-pH water is buffered by the dissolution of primary minerals, which subsequently leads to the formation of secondary mineral phases. This test example was originally developed by *Lichtner* [1997a] for the "Workshop on Subsurface Reactive Transport Modeling" in Richland, WA, 1997 and is also documented by

Lichtner [1996b]. The test example contains a wide range of transport and reaction processes, including processes in the unsaturated zone. Therefore, it is ideally suited for the verification of the present model. The model results are directly compared to the results obtained by *Lichtner* [1996b, 1997a] using MULTIFLO [*Lichtner*, 1996a].

5.4.1 Problem Definition

A vertical soil column of 20 m length is considered for this simulation. Steady state flow conditions are assumed, the water table is located 10 m below the ground surface and a recharge rate of 0.1 m y^{-1} is applied to the top boundary. The saturated hydraulic conductivity throughout the column is constant. Model input data for hydraulic conductivity, residual saturation and soil hydraulic function parameters are presented in Table 5.5. Pyrite is initially present below 1 m depth, resulting in a non-uniform porosity distribution as documented in Table 5.5. Free phase diffusion coefficients are assumed to be equivalent for all gaseous and dissolved species respectively. The effect of tortuosity on the transport of gaseous and dissolved species and dispersive mass transport in the aqueous phase has been neglected.

Parameter		unit	value
length of solution domain	L	[m]	20.0
porosity	ϕ	[-]	0.20 (0-1 m depth)
			0.16 (1-20 m depth)
infiltration rate	q_{in}	[m y^{-1}]	0.1
hydraulic conductivity	K_{zz}	[m s^{-1}]	$1.09 \cdot 10^{-7}$
residual saturation	S_{ra}	[-]	0.05
soil hydraulic function	α	[-]	0.195
parameters	n	[-]	6.67
free phase diffusion coefficient in gaseous phase	D_g	[m^2 s^{-1}]	$2.13 \cdot 10^{-5}$
free phase diffusion coefficient in aqueous phase	D_a	[m^2 s^{-1}]	$1.0 \cdot 10^{-9}$

Table 5.5: Physical input parameters - acid mine drainage benchmark problem after *Lichtner* [1997a]

The chemical system considered can be expressed in terms of the components K^+, Fe^{2+}, Al^{3+}, CO_3^{2-}, SO_4^{2-}, H_4SiO_4(aq), H^+ and O_2(aq). Table 5.6 summarizes aqueous oxidation-reduction and complexation reactions considered along with the equilibrium

constants. The MIN3P database was altered for this simulation to ensure that the equilibrium constants are consistent with the parameters used by *Lichtner* [1997a]. Gas dissolution-exsolution reactions considered and the corresponding equilibrium constants are summarized in Table 5.7. The primary mineral phases pyrite, K-feldspar, kaolinite and quartz comprise the soil material. Secondary minerals forming under the given conditions include principally ferric hydroxides and hydroxy-sulfates. The mineral phases considered here are presented in Table 5.8, along with the reaction stoichiometries of the corresponding dissolution-precipitation reactions.

Reaction			$\log K_i^x$
Oxidation-reduction reactions			
(1)	Fe^{3+}	$\rightleftharpoons Fe^{2+} + 0.25O_2(aq) + H^+ - 0.5H_2O$	8.4900
(2)	HS^-	$\rightleftharpoons SO_4^{2-} + H^+ - 2O_2(aq)$	-138.3200
Complexation reactions			
(3)	$H_2CO_3(aq)$	$\rightleftharpoons 2H^+ + CO_3^{2-}$	16.6737
(4)	$FeOH_2^+$	$\rightleftharpoons Fe^{3+} + 2H_2O - 2H^+$	-5.6700
(5)	$Fe(OH)_3(aq)$	$\rightleftharpoons Fe^{3+} + 3H_2O - 3H^+$	-12.0000
(6)	$FeOH^{2+}$	$\rightleftharpoons Fe^{3+} + H_2O - H^+$	-2.1900
(7)	HSO_4^-	$\rightleftharpoons H^+ + SO_4^{2-}$	1.9791
(8)	KSO_4^-	$\rightleftharpoons K^+ + SO_4^{2-}$	0.8796
(9)	$AlOH^{2+}$	$\rightleftharpoons Al^{3+} + H_2O - H^+$	-4.9571
(10)	$H_3SiO_4^-$	$\rightleftharpoons H_4SiO_4 - H^+$	-9.9525
(11)	$Al(OH)_2^+$	$\rightleftharpoons Al^{3+} + 2H_2O - 2H^+$	-10.5950
(12)	OH^-	$\rightleftharpoons H_2O - H^+$	-13.9950
(13)	$Al(OH)_3(aq)$	$\rightleftharpoons Al^{3+} + 3H_2O - 3H^+$	-16.1580
(14)	HCO_3^-	$\rightleftharpoons H^+ + CO_3^{2-}$	10.3290
(15)	$Al(OH)_4^-$	$\rightleftharpoons Al^{3+} + 4H_2O - 4H^+$	-22.8830
(16)	$Fe(OH)_4^-$	$\rightleftharpoons Fe^{3+} + 4H_2O - 4H^+$	-21.6000
(17)	$KHSO_4(aq)$	$\rightleftharpoons K^+ + H^+ + SO_4^{2-}$	0.8136
(18)	$FeSO_4(aq)$	$\rightleftharpoons Fe^{2+} + SO_4^{2-}$	2.2000
(19)	$H_2SO_4(aq)$	$\rightleftharpoons 2H^+ + SO_4^{2-}$	-1.0209
(20)	$H_2SiO_4^{2-}$	$\rightleftharpoons H_4SiO_4 - 2H^+$	-22.9600
(21)	$H_2(aq)$	$\rightleftharpoons H_2O - 0.5O_2(aq)$	-46.1070
(22)	$H_2S(aq)$	$\rightleftharpoons HS^- + H^+$	6.9900

Table 5.6: Oxidation-reduction and complexation reactions - acid mine drainage benchmark problem after *Lichtner* [1997a]

The dissolution and precipitation of minerals is assumed to be surface-controlled and

Reaction			$\log K_i^g$
(1)	$O_2(g)$	$\rightleftharpoons O_2(aq)$	2.8980
(2)	$CO_2(g)$	$\rightleftharpoons 2H^+ + CO_3^{2-} - H_2O$	18.1426
(3)	$H_2(g)$	$\rightleftharpoons H_2O - 0.5O_2(aq)$	-43.0015
(4)	$H_2S(g)$	$\rightleftharpoons HS^- + H^+$	7.9759

Table 5.7: Gas dissolution-exsolution reactions - acid mine drainage benchmark problem after *Lichtner* [1997a]

is here described in terms of effective rate constants, which consider the combined effect of reactive surface area and the rate constant for surface-controlled dissolution reactions:

$$k_{i,\text{eff}} = S_i k_i^{md,s} \tag{5.5}$$

Mineral dissolution-precipitation rates are described by transition state theory rate expressions of the form:

$$R_i^m = -k_{i,\text{eff}} \left[1 - \frac{IAP_i^m}{K_i^m}\right] \tag{5.6}$$

Mineral phase		Reaction	
Primary minerals			
(1)	pyrite	$FeS_2(s) + 3.5O_2(aq) + H_2O$	$\rightleftharpoons Fe^{2+} + 2SO_4^{2-} + 2H^+$
(2)	K-feldspar	$KAlSi_3O_8 + 4H^+ + 4H_2O$	$\rightleftharpoons K^+ + Al^{3+} + 3H_4SiO_4$
(3)	kaolinite	$Al_2Si_2O_5(OH)_4 + 6H^+$	$\rightleftharpoons 2Al^{3+} + 2H_4SiO_4 + H_2O$
(4)	quartz	$SiO_2(s) + 2H_2O$	$\rightleftharpoons H_4SiO_4$
Secondary minerals			
(5)	ferrihydrite	$Fe(OH)_3(s) + 3H^+$	$\rightleftharpoons Fe^{3+} + 3H_2O$
(6)	alunite	$KAl_3(SO_4)_2(OH)_6 + 6H^+$	$\rightleftharpoons K^+ + 3Al^{3+} + 2SO_4^{2-} + 6H_2O$
(7)	jarosite	$KFe_3(SO_4)_2(OH)_6 + 6H^+$	$\rightleftharpoons K^+ + 3Fe^{3+} + 2SO_4^{2-} + 6H_2O$
(8)	jurbanite	$Al(OH)SO_4 \cdot 5H_2O + H^+$	$\rightleftharpoons Al^{3+} + SO_4^{2-} + 6H_2O$

Table 5.8: Dissolution-precipitation reactions - acid mine drainage benchmark problem after *Lichtner* [1997a]

An exception is the oxidation of pyrite, which is described by two parallel rate expressions [*Lichtner*, 1996b]. The overall reaction rate is determined as the sum of the experimentally derived rate law from *Williamson and Rimstidt* [1994], which accounts for

Mineral phase		log K_i^m	rate constant
Primary minerals			
(1)	pyrite	-217.4	$k_{11}^{md,s} = 1.0 \cdot 10^{-12.0}$ [mol cm^{-2} s^{-1}]
			$k_{12}^{md,s} = 2.5 \cdot 10^{-14.0}$ [mol cm^{-2} s^{-1}]
(2)	K-feldspar	0.2753	$k_{2,\text{eff}} = 1.0 \cdot 10^{-14.0}$ [mol cm^{-3} s^{-1}]
(3)	kaolinite	-6.810	$k_{3,\text{eff}} = 1.0 \cdot 10^{-13.5}$ [mol cm^{-3} s^{-1}]
(4)	quartz	3.999	$k_{4,\text{eff}} = 1.0 \cdot 10^{-15.0}$ [mol cm^{-3} s^{-1}]
Secondary minerals			
(5)	ferrihydrite	-4.896	$k_{5,\text{eff}} = 1.0 \cdot 10^{-11.0}$ [mol cm^{-3} s^{-1}]
(6)	alunite	0.348	$k_{6,\text{eff}} = 1.0 \cdot 10^{-11.0}$ [mol cm^{-3} s^{-1}]
(7)	jarosite	9.371	$k_{7,\text{eff}} = 1.0 \cdot 10^{-11.0}$ [mol cm^{-3} s^{-1}]
(8)	jurbanite	3.805	$k_{8,\text{eff}} = 1.0 \cdot 10^{-11.0}$ [mol cm^{-3} s^{-1}]

Table 5.9: Parameters for dissolution-precipitation reactions - acid mine drainage benchmark problem after *Lichtner* [1997a]

the dependency of the reaction progress on dissolved oxygen concentrations and pH, and a transition state theory rate law. The resulting rate expression describing the overall reaction progress can be written as:

$$R_1^m = -S_1 \left[k_{11}^{md,s} \{O_2(aq)\}^{0.5} \{H^+\}^{-0.11} + k_{12}^{md,s} \right] \left[1 - \frac{IAP_1^m}{K_i^m} \right] \tag{5.7}$$

The equilibrium and rate constants defining the reaction progress are summarized in Table 5.9.

The infiltrating groundwater is assumed to be saturated with oxygen under atmospheric conditions (pO_2 = 0.2 atm), is slightly acidic (pH = 5) and is in equilibrium with quartz and ferrihydrite. The water initially contained in the porous medium is in equilibrium with the primary mineral phases quartz, kaolinite, K-feldspar, pyrite and additionally muscovite [*Lichtner*, 1996b] with a neutral pH. The total aqueous component concentrations used in this test problem are presented, along with the simulation results, in Tables 5.12 and 5.17. The mineralogical composition of the porous medium is described in Table 5.10. The composition is assumed to be uniform, except for the absence of pyrite at shallow depth. The reactive surface area for pyrite is 10^3 m^{-1}.

The solution domain was discretized in 201 control volumes with half cells on the boundary, resulting in a spatial discretization interval of 10 cm for interior control volumes

Mineral phase		volume fraction [-]
Primary minerals		
(1)	pyrite	0.00 (0-1 m depth) 0.04 (1-20 m depth)
(2)	K-feldspar	0.2
(3)	kaolinite	0.2
(4)	quartz	0.4
Secondary minerals		
(5)	ferrihydrite	0.0
(6)	alunite	0.0
(7)	jarosite	0.0
(8)	jurbanite	0.0

Table 5.10: Mineralogical composition - acid mine drainage benchmark problem after *Lichtner* [1997a]

and 5 cm for boundary control volumes. The simulation was conducted to a final solution time of 50 years. Activity corrections have been neglected in this study and upstream weighting has been applied for the advective transport of dissolved species.

5.4.2 Evaluation of Results

Composition of the Initial Aqueous Solution and Infiltrating Groundwater

As a first step the batch chemistry module of MIN3P has been used to compute the composition of the infiltrating groundwater and the groundwater initially contained in the porous medium. The results obtained using MIN3P are directly compared to the model output from MULTIFLO [*Lichtner*, 1997a], which was used for the solution of the original benchmark problem.

A direct comparison of the modelled compositions of the initial groundwater are presented in Tables 5.11 - 5.15. A comparison of the calculated compositions of the infiltrating groundwater is given in Tables 5.16 - 5.20. Master variables such as ionic strength, pH, pe and E_H, total aqueous component concentrations, aqueous species concentrations, gas concentrations and mineral saturation indices are compared directly. The results for the equilibration of both the initial and infiltrating groundwater agree very well.

Flow Solution

As a second step the steady state flow solution was computed using the flow module of MIN3P. Hydraulic conductivities, recharge rates and soil hydraulic function parameters were taken from the benchmark problem [*Lichtner*, 1996b, *Lichtner*, 1997a] as summarized in Table 5.5. The computed water saturations are shown in Figure 5.6. Water saturations increase continuously from $S_a = 0.36$ to fully saturated conditions at approximately 8 m depth. An approximately 2 m thick capillary fringe is located between 8 and 10 m depth.

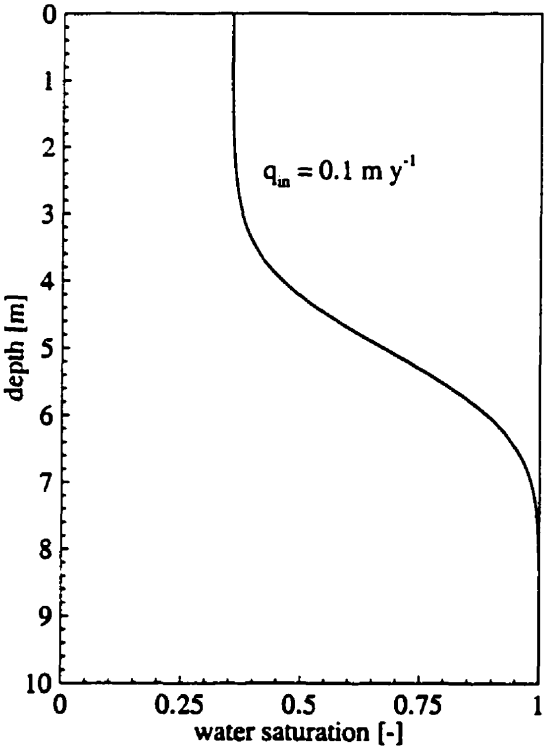

Figure 5.6: Water saturation as a function of depth at steady state

Reactive Transport Solution

The reactive transport simulation was conducted using the equilibrated chemistry for the initial and the infiltrating groundwater, and the velocities and saturations obtained

from the steady state flow solution. The results presented in Figures 5.7 - 5.12 indicate that the MIN3P solution agrees favorably with the original solution by *Lichtner* [1996b, 1997a]. Small differences might be attributed to the slightly different spatial discretization schemes employed by the two models.

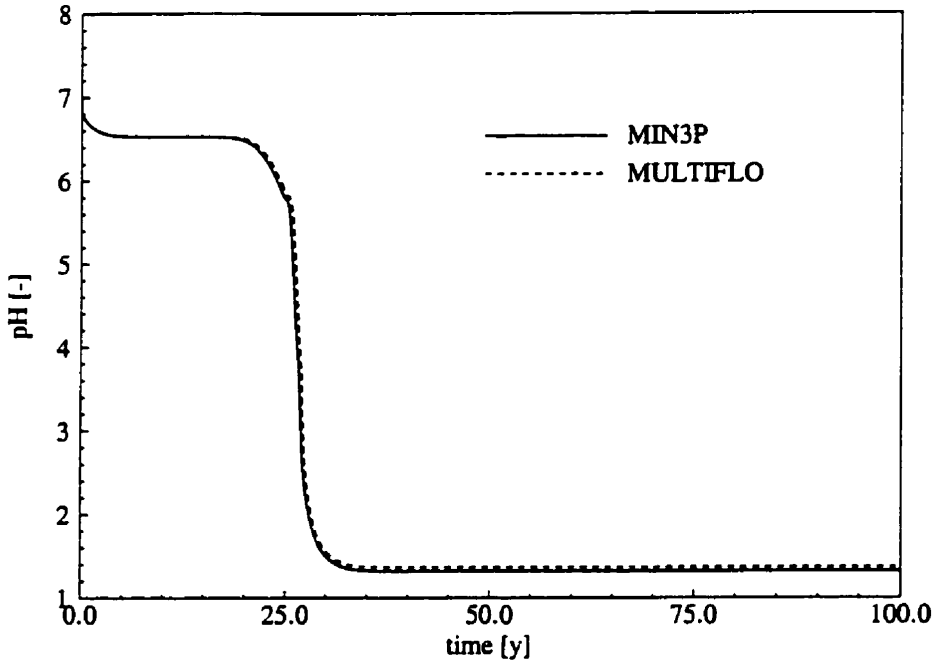

Figure 5.7: pH as a function of time at a depth of 20 m

Figure 5.7 shows the transient evolution of pH at a depth of 20 m. Both models predict a breakthrough of acidified water after approximately 27 years of simulation time. Figure 5.8 shows the transient evolution of pH profiles versus depth. A sharp pH-decrease develops during the first 0.1 years at the upper limit of the pyrite containing zone located 1 m below the ground surface. A pH-drop develops at later time (starting at approximately 1 year), when Fe^{3+} containing water reaches a depth of approximately 5.5 m. Gaseous oxygen is not able to penetrate deeper than 5.5 m at a significant rate and the oxidation of pyrite and Fe^{2+} by oxygen below this depth is no longer possible. Pyrite oxidation continues nevertheless due to high dissolved Fe^{3+} concentrations. Pyrite oxidation by ferric iron, as defined in reaction 5.4, produces comparably large amounts of acidity which cannot be neutralized any longer by the acid-consuming oxidation of

ferrous iron in the aqueous phase. The results of MULTIFLO and MIN3P agree very well.

Figure 5.9 shows the reaction rates of pyrite oxidation due to the two parallel rate laws as defined in the benchmark problem at $t = 25$ years. Oxidation rates for the sqrt $O_{2(aq)}$ rate law approach zero when oxygen concentrations approach zero (see also Figure 5.10). Oxidation rates due to the transition state theory rate law continues up to a depth of approximately 6.0 m, where the groundwater approaches equilibrium with respect to pyrite.

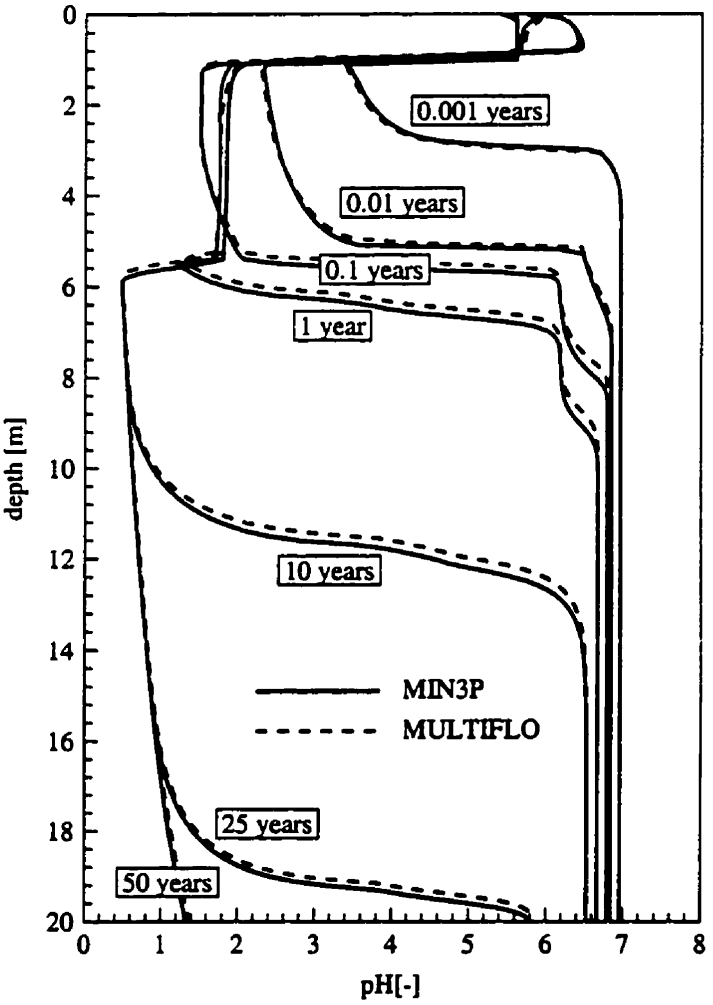

Figure 5.8: pH as a function of depth and elapsed time

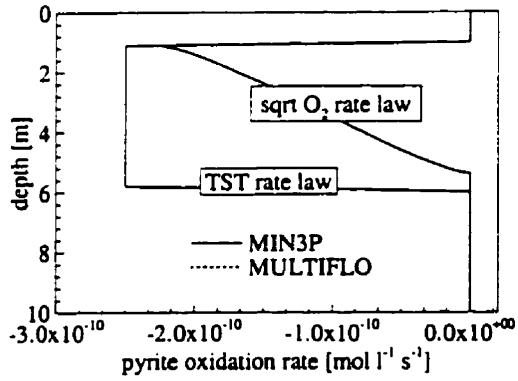

Figure 5.9: Pyrite oxidation rate as a function of depth after $t = 25$ years

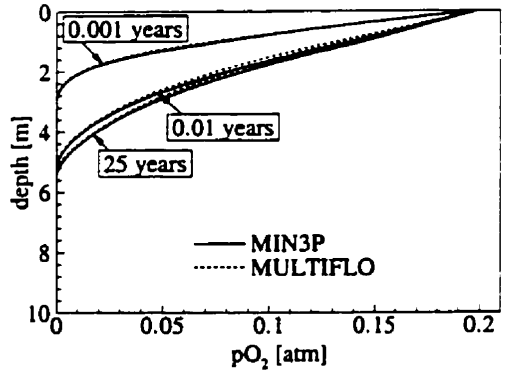

Figure 5.10: pO_2 as a function of depth and elapsed time

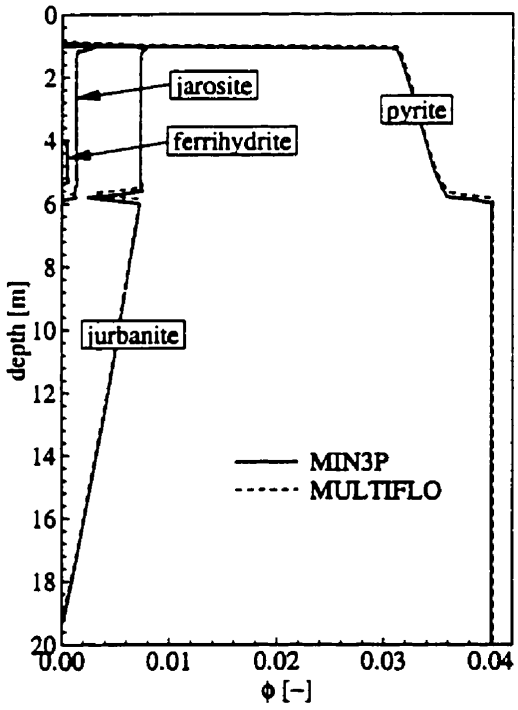

Figure 5.11: Mineral volume fractions as a function of depth after $t = 25$ years

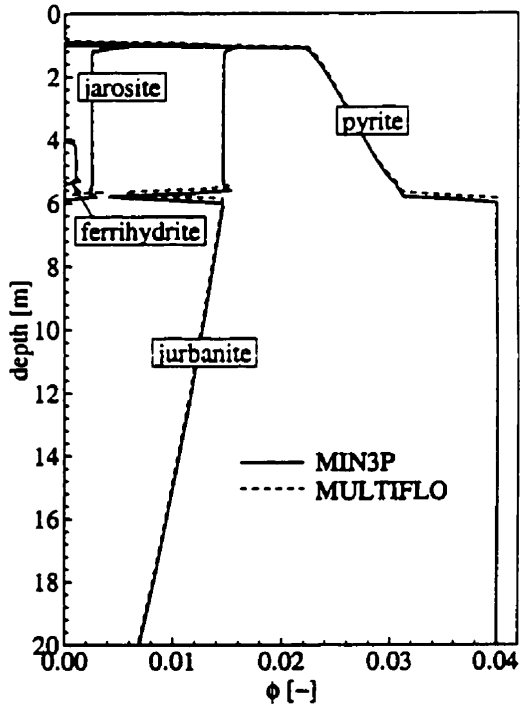

Figure 5.12: Mineral volume fractions as a function of depth after $t = 50$ years

The transient evolution of the partial oxygen pressures versus depth are shown in Figure 5.10. It is evident that the time scale of oxygen diffusion is fast in comparison to most other processes in the system. Quasi steady state is achieved between 0.01 and 0.1 years.

Finally, the mineral volume fractions for selected minerals are presented at times $t =$ 25 and 50 years. Pyrite is being depleted in the zone of active oxidation in Figures 5.11 and 5.12, respectively. The depletion is more pronounced in the upper portion of the column, where oxygen is present and the sqrt $O_{2(aq)}$ rate law is active. Mineral volume fractions of the secondary mineral phases ferrihydrite, jurbanite and jarosite are also presented. Jurbanite was found to be the most abundant secondary mineral phase in this scenario. The precipitation of this mineral phase limits dissolved SO_4^{2-}- and Al^{3+}-concentrations that originate from pyrite oxidation and from the dissolution of kaolinite, respectively. Ferrihydrite and jarosite only form in the zone of active oxidation. At greater depth anoxic conditions prevail; dissolved Fe^{3+} is, therefore, not abundant in this zone and the water remains undersaturated with respect to ferric hydroxides or hydroxy-sulfates.

Figure 5.13 compares the transient evolution of the oxygen inflow from the ground surface with the total oxygen consumption in the soil column due to the oxidation of pyrite and ferrous iron. Figure 5.13 shows clearly that the oxygen inflow increases very rapidly during a very short time period and only changes slowly thereafter. Envelope curves for the overall oxygen consumption are given based on the stoichiometry of reaction 5.3 and:

$$FeS_2(s) + \tfrac{15}{4}O_2(aq) + \tfrac{1}{2}H_2O \rightarrow Fe^{3+} + 2SO_4^{2-} + H^+ \qquad (5.8)$$

Equation 5.3 implies that only S^- becomes oxidized to sulfate, while equation 5.8 also allows for the oxidation of Fe^{2+}. As long as oxidizing conditions prevail in the zone of pyrite oxidation, it can be expected that most of the iron will also be oxidized and therefore 15/4 mol of oxygen will be consumed per mole of pyrite oxidized. As mentioned previously, once pyrite oxidation takes place below the depth of oxygen penetration, ferrous iron produced will not be oxidized any longer and will remain in the reduced state. The total amount of oxygen consumed per mole of pyrite dissolved is therefore closer to the stoichiometry given by equation 5.3 at later times. This behavior is indicated by the actual oxygen influx which lies in between the two envelope curves calculated form the pyrite oxidation rates according to the reaction stoichiometries form equations 5.3 and 5.8. Initially iron remains in the overall reaction in its oxidized state, while ferric iron is at later times consumed by pyrite oxidation in the anoxic zone below a depth of 5.5 m.

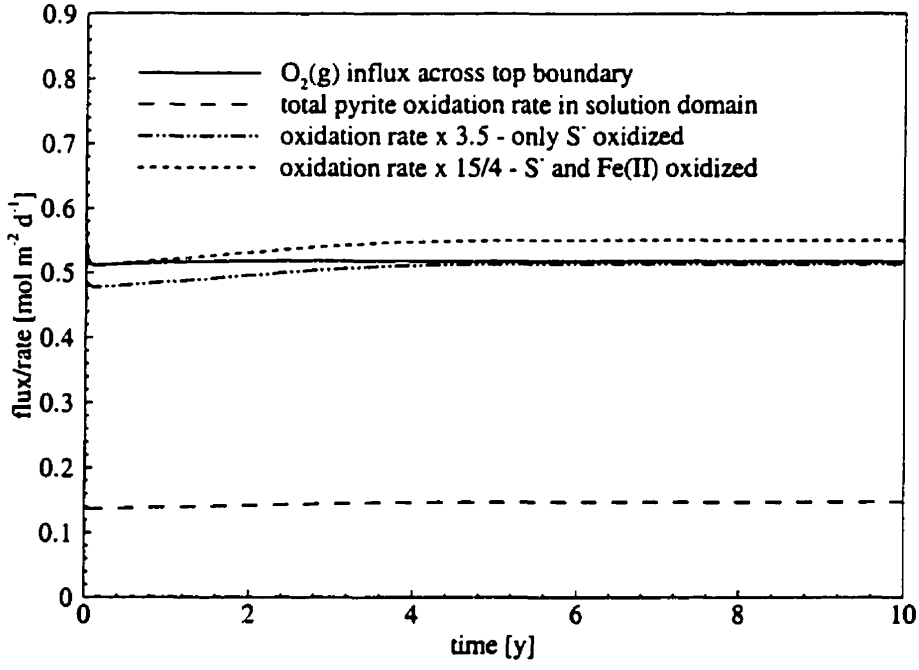

Figure 5.13: Oxygen influx and pyrite oxidation rate in column as a function of time

5.4.3 Numerical Settings and Performance

An anticipated update of 3 log concentration cycles or an anticipated number of 12 Newton iterations per time step were used as control parameters for the adaptive time stepping scheme. The maximum tolerable concentration update before modifying the updates was limited to 5 log concentration cycles, and the maximum number of iterations before restarting a time step was limited to 15 iterations. The solution of this problem required 3306 time steps or 21468 Newton iterations. The memory required was 2.8 MB, which shows that memory requirements of the global implicit method are, at least for one-dimensional problems, not of concern. The required CPU-time was 2 hours 45 minutes and 7 seconds on a Pentium P2/266 MHz. Most of the computational effort was spent on tracking the infiltrating oxygen front during the first 10^{-2} years. A more efficient solution, without affecting the results in a significant way, could likely be obtained by assuming atmospheric conditions throughout the column as an initial condition.

	MULTIFLO	MIN3P
computed pH of solution:	7.0000	7.0000
computed pe of solution:	−2.6863	−2.6870
computed E_H of solution:	−0.1589	−0.1585
ionic strength:	$9.4157 \cdot 10^{-03}$	$9.4157 \cdot 10^{-03}$

Table 5.11: Master variables, initial groundwater

	MULTIFLO	MIN3P
K^+	$6.3368 \cdot 10^{-03}$	$6.3368 \cdot 10^{-03}$
Al^{3+}	$1.7303 \cdot 10^{-09}$	$1.7303 \cdot 10^{-09}$
H^+	$3.3808 \cdot 10^{-05}$	$2.2146 \cdot 10^{-04}$
$H_4SiO_4(aq)$	$1.0027 \cdot 10^{-04}$	$1.0027 \cdot 10^{-04}$
CO_3^{2-}	$1.8765 \cdot 10^{-04}$	$1.8765 \cdot 10^{-04}$
$O_2(aq)$	$-1.7507 \cdot 10^{-10}$	$-1.7414 \cdot 10^{-10}$
Fe^{2+}	$1.0000 \cdot 10^{-04}$	$1.0000 \cdot 10^{-04}$
SO_4^{2-}	$3.1915 \cdot 10^{-03}$	$3.1915 \cdot 10^{-03}$

Table 5.12: Total aqueous component concentrations [mol l^{-1}], initial groundwater

	MULTIFLO	MIN3P
$O_2(g)$	$1.4194 \cdot 10^{-66}$	$1.4189 \cdot 10^{-66}$
$CO_2(g)$	$1.0000 \cdot 10^{-03}$	$1.0000 \cdot 10^{-03}$
$H_2(g)$	$2.3521 \cdot 10^{-09}$	$2.3525 \cdot 10^{-09}$
$H_2S(g)$	$4.2761 \cdot 10^{-10}$	$4.2429 \cdot 10^{-10}$

Table 5.13: Partial gas pressures [atm], initial groundwater

	MULTIFLO	MIN3P
ferrihydrite	−3.762	−3.762
pyrite	0.000	0.001
kaolinite	−0.948	−0.948
quartz	0.000	0.000
K-feldspar	0.000	0.000
jurbanite	−5.785	−5.785
alunite	−7.109	−7.109
jarosite	−15.480	−15.477

Table 5.14: Mineral saturation indices [-], initial groundwater

	MULTIFLO	MIN3P
K^+	$6.1951 \cdot 10^{-03}$	$6.1951 \cdot 10^{-03}$
Al^{3+}	$8.5222 \cdot 10^{-15}$	$8.5206 \cdot 10^{-15}$
H^+	$1.0000 \cdot 10^{-07}$	$1.0000 \cdot 10^{-07}$
$H_4SiO_4(aq)$	$1.0016 \cdot 10^{-04}$	$1.0016 \cdot 10^{-04}$
CO_3^{2-}	$7.2044 \cdot 10^{-08}$	$7.2013 \cdot 10^{-08}$
$O_2(aq)$	$1.7939 \cdot 10^{-69}$	$1.7945 \cdot 10^{-69}$
Fe^{2+}	$6.7648 \cdot 10^{-05}$	$6.7648 \cdot 10^{-05}$
SO_4^{2-}	$3.0174 \cdot 10^{-03}$	$3.0174 \cdot 10^{-03}$
Fe^{3+}	$1.3605 \cdot 10^{-20}$	$1.3606 \cdot 10^{-20}$
HS^-	$4.5201 \cdot 10^{-11}$	$4.4850 \cdot 10^{-11}$
$H_2CO_3(aq)$	$3.3970 \cdot 10^{-05}$	$3.3971 \cdot 10^{-05}$
$Fe(OH)_2^+$	$2.9086 \cdot 10^{-12}$	$2.9090 \cdot 10^{-12}$
$Fe(OH)_3(aq)$	$1.3605 \cdot 10^{-11}$	$1.3606 \cdot 10^{-11}$
$Fe(OH)^{2+}$	$8.7838 \cdot 10^{-16}$	$8.7850 \cdot 10^{-16}$
HSO_4^-	$2.8757 \cdot 10^{-08}$	$2.8757 \cdot 10^{-08}$
KSO_4^-	$1.4167 \cdot 10^{-04}$	$1.4167 \cdot 10^{-04}$
$AlOH^{2+}$	$9.4070 \cdot 10^{-13}$	$9.4052 \cdot 10^{-13}$
$H_3SiO_4^-$	$1.1174 \cdot 10^{-07}$	$1.1173 \cdot 10^{-07}$
$Al(OH)_2^+$	$2.1680 \cdot 10^{-11}$	$2.1651 \cdot 10^{-11}$
OH^-	$1.0114 \cdot 10^{-07}$	$1.0116 \cdot 10^{-07}$
$Al(OH)_3(aq)$	$5.9272 \cdot 10^{-10}$	$5.9220 \cdot 10^{-10}$
HCO_3^-	$1.5360 \cdot 10^{-04}$	$1.5361 \cdot 10^{-04}$
$Al(OH)_4^-$	$1.1149 \cdot 10^{-09}$	$1.1155 \cdot 10^{-09}$
$Fe(OH)_4^-$	$3.4173 \cdot 10^{-14}$	$3.4178 \cdot 10^{-14}$
$KHSO_4(aq)$	$1.2170 \cdot 10^{-11}$	$1.2170 \cdot 10^{-11}$
$FeSO_4(aq)$	$3.2352 \cdot 10^{-05}$	$3.2352 \cdot 10^{-05}$
$H_2SO_4(aq)$	$2.8757 \cdot 10^{-18}$	$2.8757 \cdot 10^{-18}$
$H_2SiO_4^{2-}$	$1.0983 \cdot 10^{-13}$	$1.0982 \cdot 10^{-13}$
$H_2(aq)$	$1.8469 \cdot 10^{-12}$	$1.8451 \cdot 10^{-12}$
$H_2S(aq)$	$4.3939 \cdot 10^{-11}$	$4.3829 \cdot 10^{-11}$

Table 5.15: Species concentrations [mol l^{-1}], initial groundwater

	MULTIFLO	MIN3P
computed pH of solution:	5.0000	5.0000
computed pe of solution:	15.6010	15.6002
computed E_H of solution:	0.9229	0.9204
ionic strength:	$1.6000 \cdot 10^{-04}$	$1.6000 \cdot 10^{-04}$

Table 5.16: Master variables, infiltrating groundwater

	MULTIFLO	MIN3P
K^+	$1.0000 \cdot 10^{-04}$	$1.0000 \cdot 10^{-04}$
Al^{3+}	$1.0000 \cdot 10^{-08}$	$1.0000 \cdot 10^{-08}$
H^+	$3.4790 \cdot 10^{-04}$	$3.4789 \cdot 10^{-04}$
$H_4SiO_4(aq)$	$1.0016 \cdot 10^{-04}$	$1.0016 \cdot 10^{-04}$
CO_3^{2-}	$3.5506 \cdot 10^{-04}$	$3.5506 \cdot 10^{-04}$
$O_2(aq)$	$2.5323 \cdot 10^{-04}$	$2.5322 \cdot 10^{-04}$
Fe^{2+}	$1.8123 \cdot 10^{-06}$	$1.8123 \cdot 10^{-13}$
SO_4^{2-}	$4.8245 \cdot 10^{-05}$	$4.8245 \cdot 10^{-05}$

Table 5.17: Total aqueous component concentrations [mol l^{-1}], infiltrating groundwater

	MULTIFLO	MIN3P
$O_2(g)$	$2.0000 \cdot 10^{-01}$	$2.0000 \cdot 10^{-01}$
$CO_2(g)$	$1.0000 \cdot 10^{-02}$	$1.0000 \cdot 10^{-02}$
$H_2(g)$	$6.2659 \cdot 10^{-42}$	$6.2681 \cdot 10^{-42}$
$H_2S(g)$	$3.4376 \cdot 10^{-138}$	$3.4132 \cdot 10^{-138}$

Table 5.18: Partial gas pressures [atm], infiltrating groundwater

	MULTIFLO	MIN3P
ferrihydrite	0.000	0.000
pyrite	−236.100	−236.139
kaolinite	−1.580	−1.579
quartz	0.000	0.000
K-feldspar	−4.108	−4.108
jurbanite	−3.898	−3.898
alunite	−7.443	−7.443
jarosite	−3.576	−3.576

Table 5.19: Mineral saturation indices [-], infiltrating groundwater

	MULTIFLO	MIN3P
K^+	$9.9964 \cdot 10^{-05}$	$9.9964 \cdot 10^{-05}$
Al^{3+}	$4.1168 \cdot 10^{-09}$	$4.1174 \cdot 10^{-09}$
H^+	$1.0000 \cdot 10^{-05}$	$1.0000 \cdot 10^{-05}$
$H_4SiO_4(aq)$	$1.0016 \cdot 10^{-04}$	$1.0016 \cdot 10^{-04}$
CO_3^{2-}	$7.2044 \cdot 10^{-11}$	$7.2010 \cdot 10^{-11}$
$O_2(aq)$	$2.5277 \cdot 10^{-04}$	$2.5277 \cdot 10^{-04}$
Fe^{2+}	$2.0200 \cdot 10^{-13}$	$2.0199 \cdot 10^{-13}$
SO_4^{2-}	$4.8163 \cdot 10^{-05}$	$4.8163 \cdot 10^{-05}$
Fe^{3+}	$7.8705 \cdot 10^{-11}$	$7.8706 \cdot 10^{-11}$
HS^-	$3.6337 \cdot 10^{-141}$	$3.6079 \cdot 10^{-141}$
$H_2CO_3(aq)$	$3.3970 \cdot 10^{-04}$	$3.3970 \cdot 10^{-04}$
$Fe(OH)_2^+$	$1.6827 \cdot 10^{-06}$	$1.6827 \cdot 10^{-06}$
$Fe(OH)_3(aq)$	$7.8705 \cdot 10^{-08}$	$7.8706 \cdot 10^{-08}$
$Fe(OH)^{2+}$	$5.0816 \cdot 10^{-08}$	$5.0817 \cdot 10^{-08}$
HSO_4^-	$4.5900 \cdot 10^{-08}$	$4.5900 \cdot 10^{-08}$
KSO_4^-	$3.6488 \cdot 10^{-08}$	$3.6488 \cdot 10^{-08}$
$AlOH^{2+}$	$4.5442 \cdot 10^{-09}$	$4.5449 \cdot 10^{-09}$
$H_3SiO_4^-$	$1.1174 \cdot 10^{-09}$	$1.1174 \cdot 10^{-09}$
$Al(OH)_2^+$	$1.0473 \cdot 10^{-09}$	$1.0462 \cdot 10^{-09}$
OH^-	$1.0114 \cdot 10^{-09}$	$1.0116 \cdot 10^{-09}$
$Al(OH)_3(aq)$	$2.8633 \cdot 10^{-10}$	$2.8617 \cdot 10^{-10}$
HCO_3^-	$1.5360 \cdot 10^{-05}$	$1.5360 \cdot 10^{-05}$
$Al(OH)_4^-$	$5.3869 \cdot 10^{-12}$	$5.3904 \cdot 10^{-12}$
$Fe(OH)_4^-$	$1.9770 \cdot 10^{-12}$	$1.9770 \cdot 10^{-12}$
$KHSO_4(aq)$	$3.1344 \cdot 10^{-13}$	$3.1344 \cdot 10^{-13}$
$FeSO_4(aq)$	$1.5420 \cdot 10^{-15}$	$1.5418 \cdot 10^{-15}$
$H_2SO_4(aq)$	$4.5900 \cdot 10^{-16}$	$4.5900 \cdot 10^{-16}$
$H_2SiO_4^{2-}$	$1.0983 \cdot 10^{-17}$	$1.0982 \cdot 10^{-17}$
$H_2(aq)$	$4.9202 \cdot 10^{-45}$	$4.9163 \cdot 10^{-45}$
$H_2S(aq)$	$3.5323 \cdot 10^{-139}$	$3.5258 \cdot 10^{-139}$

Table 5.20: Species concentrations [mol l^{-1}], infiltrating groundwater

5.5 Benchmark Problem: Copper Leaching

This test problem describes an *in-situ* leaching operation for the retrieval of copper from a porphyry copper deposit and was originally developed by *Lichtner* [1996b] for the "Workshop on Subsurface Reactive Transport Modeling" in Richland, WA, 1997 [*Lichtner*, 1997b]. The problem is used to test MIN3P's capabilities for modelling reactive transport in two spatial dimensions. The copper ore is dissolved by the injection of a leach solution and is removed from the subsurface by means of extraction wells. The results obtained using MIN3P are compared to the original results obtained by *Lichtner* [1996b, 1997b].

5.5.1 Problem Definition

Figure 5.14 shows a schematic of the leaching operation. The leaching of the 30 by 30 m ore body is performed using a five-spot well pattern with four injection wells and an extraction well in the center. Symmetry allows reduction of the problem to a quarter of the original problem size with quarter strength injection and extraction rates. Copper ore is present in the form of chrysocolla and is recovered by injecting a low-pH leach solution.

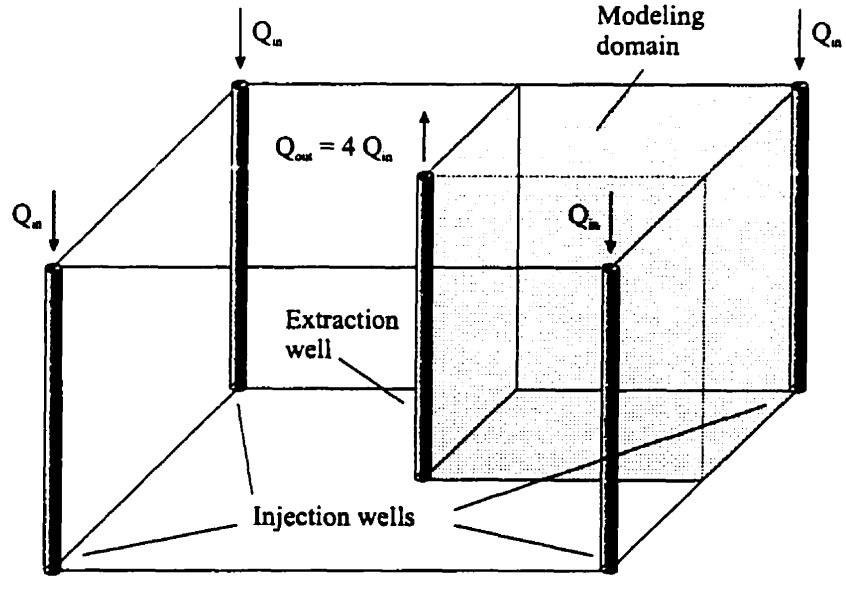

Figure 5.14: Modelling domain - copper leaching benchmark problem after *Lichtner*, [1997b]

The gangue material of the ore body consists of goethite, kaolinite, muscovite and quartz. Since chrysocolla dissolves preferentially at low pH-values a fast removal of the copper ore can be expected upon injection of the leach-solution. Gangue minerals will also dissolve and secondary mineral phases such as amorphous silica, gypsum, jarosite, jurbanite and alunite will form. Table 5.21 summarizes the physical parameters used in the present study. All equilibrium relationships and rate expressions can be expressed in

Parameter		unit	value
dimensions of solution	L_x	[m]	15.0
domain	L_y	[m]	15.0
	L_z	[m]	120.0
porosity	ϕ	[-]	0.1
injection rate	Q_{in}	[l s^{-1}]	2.52
hydraulic conductivity	$K_{xx} = K_{yy}$	[m s^{-1}]	$1.635 \cdot 10^{-6}$
free phase diffusion coefficient in aqueous phase	D_a	[m^2 s^{-1}]	$1.0 \cdot 10^{-9}$

Table 5.21: Physical input parameters - copper leaching benchmark problem after *Lichtner* [1997b]

terms of 12 components: the cations Na^+, K^+, Cu^{2+}, Fe^{2+}, Ca^{2+}, Al^{3+}, the anions Cl^-, CO_3^{2-}, SO_4^{2-}, as well as H_4SiO_4, O_2(aq) and H^+. Table 5.22 summarizes the oxidation-reduction and complexation reactions considered. Stoichiometric relationships for the dissolution-precipitation reactions involving the 10 specified primary and secondary minerals are shown in Table 5.24.

The dissolution and precipitation of minerals are assumed to be surface-controlled and are described in terms of effective rate constants similar to the benchmark problem on acid mine drainage. The rate expression for the dissolution of the ore mineral chrysocolla accounts for the pH-dependency of the reaction and takes the form:

$$R_1^m = -k_{1,\text{eff}}\{H^+\}^{0.39}\left[1 - \frac{IAP_1^m}{K_1^m}\right]$$

Dissolution-precipitation of the remaining minerals are described by transition state rate expressions as defined by equation 5.6. Equilibrium coefficients, effective rate constants and the volume fractions of the minerals comprising the porphyry copper deposit are presented in Table 5.23.

Reaction			$\log K_i^T$
Oxidation-reduction reactions			
(1)	Fe^{3+}	$= Fe^{2+} + 0.25O_2(aq) + H^+ - 0.5H_2O$	8.4900
(2)	Cu^+	$= Cu^{2+} + 0.5H_2O - 0.25O_2(aq) - H^+$	18.7703
Complexation reactions			
(3)	OH^-	$= H_2O - H^+$	-13.9951
(4)	$H_2CO_3(aq)$	$= 2H^+ + CO_3^{2-}$	16.6735
(5)	HCO_3^-	$= H^+ + CO_3^{2-}$	10.3288
(6)	$CaSO_4(aq)$	$= Ca^{2+} + SO_4^{2-}$	2.1111
(7)	$CaHCO_3^+$	$= Ca^{2+} + CO_3^{2-} + H^+$	11.3757
(8)	$CaCO_3(aq)$	$= Ca^{2+} + CO_3^{2-}$	3.3271
(9)	$CuOH^+$	$= Cu^{2+} + H_2O - H^+$	-7.2875
(10)	$Al(OH)_4^-$	$= Al^{3+} + 4H_2O - 4H^+$	-22.8830
(11)	$CaOH^+$	$= Ca^{2+} + H_2O - H^+$	-12.8500
(12)	$Al(OH)_3(aq)$	$= Al^{3+} + 3H_2O - 3H^+$	-16.1577
(13)	HSO_4^-	$= H^+ + SO_4^{2-}$	1.9791
(14)	$CuSO_4(aq)$	$= Cu^{2+} + SO_4^{2-}$	2.3100
(15)	$CuCl^+$	$= Cu^{2+} + Cl^-$	0.4370
(16)	$Al(OH)_2^+$	$= Al^{3+} + 2H_2O - 2H^+$	-10.5950
(17)	$Fe(OH)_3(aq)$	$= Fe^{3+} + 3H_2O - 3H^+$	-12.0000
(18)	$Fe(OH)_4^-$	$= Fe^{3+} + 4H_2O - 4H^+$	-21.6000
(19)	$Fe(OH)_2^+$	$= Fe^{3+} + H_2O - H^+$	-2.1900
(20)	$CuCl_2(aq)$	$= Cu^{2+} + 2Cl^-$	4.8210
(21)	$AlOH^{2+}$	$= Al^{3+} + H_2O - H^+$	-4.9571
(22)	CuO_2^{2-}	$= Cu^{2+} + 2H_2O - 4H^+$	-39.4497
(23)	$AlSO_4^+$	$= Al^{3+} + SO_4^{2-}$	3.0100
(24)	$CuCl_2^-$	$= Cu^+ + 2Cl^-$	4.8210
(25)	$Al(SO_4)_2^-$	$= Al^{3+} + 2SO_4^{2-}$	4.9000
(26)	$CuCl_3^{2-}$	$= Cu^+ + 3Cl^-$	5.6290
(27)	$H_2SO_4(aq)$	$= 2H^+ + SO_4^{2-}$	-1.0200
(28)	$CuCl_4^{2-}$	$= Cu^{2+} + 4Cl^-$	-4.5681
(29)	$FeSO_4(aq)$	$= Fe^{2+} + SO_4^{2-}$	2.2000
(30)	$FeSO_4^+$	$= Fe^{3+} + SO_4^{2-}$	1.9276
(31)	$Fe(SO_4)_2^-$	$= Fe^{3+} + 2SO_4^{2-}$	3.2137
(32)	$Fe(OH)_2(aq)$	$= Fe^{2+} + 2H_2O - 2H^+$	-20.6000
(33)	$Fe(OH)_3^-$	$= Fe^{2+} + 3H_2O - 3H^+$	-31.0000
(34)	$FeHSO_4^{2+}$	$= Fe^{3+} + SO_4^{2-} + H^+$	1.5400

Table 5.22: Oxidation-reduction and complexation reactions - copper leaching benchmark problem after *Lichtner* [1997b]

Mineral phase		log K_i^m	$k_{i,eff}$ [mol cm^{-3} s^{-1}]	volume fraction [-]
Primary minerals				
(1)	chrysocolla	3.9279	$1.0 \cdot 10^{-10}$	0.005
(2)	goethite	-0.5345	$1.0 \cdot 10^{-11}$	0.025
(3)	kaolinite	6.8100	$1.0 \cdot 10^{-13}$	0.05
(4)	muscovite	-13.5900	$1.0 \cdot 10^{-13}$	0.05
(5)	quartz	3.9993	$1.0 \cdot 10^{-14}$	0.77
Secondary minerals				
(6)	silica(am)	2.7136	$1.0 \cdot 10^{-11}$	0.0
(7)	gypsum	4.4823	$1.0 \cdot 10^{-10}$	0.0
(8)	jarosite	9.3706	$1.0 \cdot 10^{-11}$	0.0
(9)	jurbanite	3.2300	$1.0 \cdot 10^{-11}$	0.0
(10)	alunite	0.3479	$1.0 \cdot 10^{-11}$	0.0

Table 5.23: Parameters for dissolution-precipitation reactions - copper leaching benchmark problem after *Lichtner* [1997b]

Mineral phase		Reaction	
Primary minerals			
(1)	chrysocolla	$CuSiO_3 \cdot 2H_2O + 2H^+$	$\rightleftharpoons Cu^{2+} + H_4SiO_4 + H_2O$
(2)	goethite	$FeOOH + 3H^+$	$\rightleftharpoons Fe^{3+} + 2H_2O$
(3)	kaolinite	$Al_2Si_2O_5(OH)_4 + 6H^+$	$\rightleftharpoons 2Al^{3+} + 2H_4SiO_4 + H_2O$
(4)	muscovite	$KAl_2(AlSi_3O_{10})(OH)_2 + 10H^+$	$\rightleftharpoons K^+ + 3Al^{3+} + 3H_4SiO_4$
(5)	quartz	$SiO_2(s) + 2H_2O$	$\rightleftharpoons H_4SiO_4$
Secondary minerals			
(6)	silica(am)	$SiO_2(am) + 2H_2O$	$\rightleftharpoons H_4SiO_4$
(7)	gypsum	$CaSO_4 \cdot 2H_2O$	$\rightleftharpoons Ca^{2+} + SO_4^{2-} + 2H_2O$
(8)	jarosite	$KFe_3(SO_4)_2(OH)_6 + 6H^+$	$\rightleftharpoons K^+ + 3Fe^{3+} + 2SO_4^{2-} + 6H_2O$
(9)	jurbanite	$Al(OH)SO_4 \cdot 5H_2O + H^+$	$\rightleftharpoons Al^{3+} + SO_4^{2-} + 6H_2O$
(10)	alunite	$KAl_3(SO_4)_2(OH)_6 + 6H^+$	$\rightleftharpoons K^+ + 3Al^{3+} + 2SO_4^{2-} + 6H_2O$

Table 5.24: Dissolution-precipitation reactions - copper leaching benchmark problem after *Lichtner* [1997b]

The initial groundwater contained in the deposit is in equilibrium with the minerals calcite, muscovite, kaolinite, goethite, chalcedony and the copper ore chrysocolla and has a pH of 8. The leach solution is in equilibrium with the minerals jarosite, gypsum, amorphous silica and goethite with pH = 1 [*Lichtner* 1996b, 1997b]. Both aqueous solutions can be characterized as oxidizing. The total concentrations for all components, as specified in the original data set, were used as input parameters and are reported in Table 5.26 and 5.30.

The 15 by 15 m subdomain was discretized in 31 spatial increments in x- and y-direction. Half cells were used on the boundary, leading to a discretization length of 0.25 m for the boundary elements and 0.5 m for all interior elements. The simulation was carried out for a leaching period of two years. Activity coefficients were updated after each time step, upstream weighting was used for advective transport of dissolved species and the mineral volume fractions of the primary minerals were updated based on equation 4.13.

5.5.2 Evaluation of Results

Composition of Initial Aqueous Solution and Leach Solution

The batch chemistry module of MIN3P has been used to compute the composition of the leach solution and the groundwater initially contained in the mineral deposit. The equilibrium constants of the MIN3P database have been adjusted to the data given in the original benchmark problem. A direct comparison of the speciated composition of the initial groundwater is presented in Tables 5.25 - 5.28. A comparison of the modelled composition of the leach solution is given in Tables 5.29 - 5.32. Master variables such as ionic strength, pH, pe and E_H, total aqueous component concentrations, aqueous species concentrations and mineral saturation indices are compared directly. The results for the equilibration of the initial groundwater agree very well. Significant differences can be seen, however, for the composition of the leach solution, which is likely due to the differences in activity correction parameters. The model MIN3P applies activity corrections for charged species based on the Debye-Hückel equation:

$$\log \gamma_i = \frac{-A_d Z_i^2 I^{1/2}}{1 + B_d a_i I^{1/2}} + b_i I$$

The activity correction parameters a_i and b_i were taken from the database of MINTEQA2 (Allison et al., 1991) and WATEQ4F (Ball and Nordstrom, 1991). These activity correction parameters are different than the ones used in the simulation conducted using MULTIFLO. If the same constraints (i.e. equilibration with mineral phases) are enforced, total aqueous component concentrations, specifically for solutions with high ionic strength will be different. MIN3P also applies activity corrections to neutral species, which are calculated according to:

$$\log \gamma_i = 0.1I$$

These corrections are not performed in MULTIFLO (see Table 5.28 and 5.32) and this serves as another explanation for the differences in the composition of high ionic strength solutions such as the leach solution. This comparison clearly shows the importance of activity correction parameters for high ionic strength solutions. Components most affected are $H_4SiO_{4(aq)}$, K^+, Ca^{2+} and Fe^{2+} with a maximum difference for $H_4SiO_{4(aq)}$ of 15%.

Flow Solution

The steady state flow solution was computed using the flow module of MIN3P. Figure 5.15 shows the hydraulic head distribution in the solution domain at steady state. The total head difference between injection and extraction well is approximately 20 m. Steep gradients can be observed close to the injection and extraction wells leading to high flow velocities for the reactive transport simulation.

Reactive Transport Solution

The reactive transport simulation was conducted based on the results for the composition of the initial groundwater and the leach solution and the results of the flow solution. The results obtained are presented in Figures 5.16 - 5.26.

Figure 5.16 shows the copper recovery plotted as a function of time. It can be seen that breakthrough of copper at the extraction well occurs after approximately 0.05 years of leaching operation. The maximum extraction rate is reached after roughly 0.1 years. The depletion of chrysocolla at the extraction well after approximately 0.4 years leads to a decrease in the copper concentrations in the leach solution. The concentrations in the leach solution are now determined by the mixing ratio of pore water stemming from

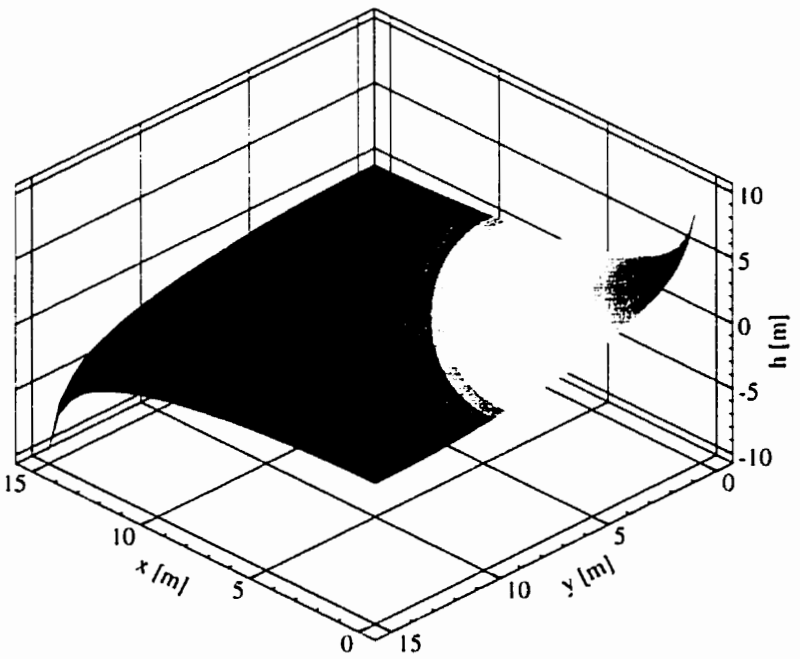

Figure 5.15: Hydraulic head distribution at steady state

the more remote areas of the deposit where chrysocolla is still present and from areas where chrysocolla is depleted. From a practical point of view the copper ore is completely leached out after roughly 1.2 years. Copper is, at this point, only recovered from the far corners of the solution domain, which mark stagnation points from a hydraulic point of view. The results of the solutions obtained by the models MIN3P and MULTIFLO agree closely. The concentrations towards the end of the simulation period are somewhat lower for the MIN3P simulation, which may be attributed to the use of half cells on the domain boundary in the case of MIN3P. MULTIFLO, on the other hand, uses full cells on the domain boundary [*Lichtner*, personal communication, 1997]. The discrepancies may also be attributed to the differing spatial weighting schemes used by the two models. MIN3P makes use of upstream weighting, while the MULTIFLO simulation was performed with a mixed method that uses upstream weighting in areas of high flow velocities close to the injection and extraction wells and centered spatial weighting in the interior of the domain where pore water velocities are slower (Lichtner, personal communication, 1997). It should be pointed out that the copper concentrations in Figure 5.16 are presented on

a log scale, therefore, the differences are from a practical point of view insignificant.

Figure 5.17 shows the pH of the leach solution at the extraction well. The pH drops after a comparably short time-period from an initial value of 8 to a value of approximately 4. This is due to the arrival of the leach solution at the extraction well. At this stage, the leach solution is primarily buffered due to the dissolution of chrysocolla, which consumes 2 mol of hydrogen ions per mol of mineral dissolved. A secondary buffer effect can be attributed to the precipitation and subsequent re-dissolution of alunite and jurbanite. The dominance of chrysocolla as the pH-buffering mineral can also be observed from Figure 5.25, where it is the only mineral dissolving at a significant rate. Once chrysocolla becomes depleted at the extraction well, a similar behavior can be observed as for the copper concentrations. pH-buffered water from remote areas of the mineral deposit mix with higly acidic water in the converging flow field close to the extraction well. pH-buffering after one year of simulation time can be attributed to the dissolution of primary aluminosilicate minerals such as kaolinite and muscovite. The buffering effect is insignificant due to the slow dissolution rates of these minerals in conjunction with the high flow velocities. The results of both models are in excellent agreement.

Figures 5.18 - 5.23 present mineral volume fractions for selected minerals at t = 0.25 years. The computed mineral volume fractions resemble the ones of the original solution closely [see *Lichtner*, 1996b]. The spatial discretization of this test problem is not fine enough to resolve the dissolution-precipitation front for alunite with sufficient accuracy, as is indicated in Figure 5.23. Figure 5.24 presents a direct comparison of the mineral volume fractions obtained from the MIN3P and MULTIFLO [*Lichtner*, 1997b] simulations along the diagonal line connecting the injection and extraction wells. The results agree well, and the discrepancies observed can likely be attributed to the differing activity corrections employed by the two models. From Figure 5.24a it is evident that amorphous silica and jurbanite are the dominant secondary mineral phases. Jurbanite and alunite are only stable between a pH of 1 and 4 and redissolve once chrysocolla becomes completely depleted. Amorphous silica, jarosite and gypsum on the other hand remain stable even at excessively low pH-values as shown in Figures 5.24a and b. This behavior is also supported by examining the dissolution-precipitation rates presented in Figure 5.25.

Figure 5.26 presents a mass balance calculation for copper. Presented are the total amounts of copper contained in the ore body in solid and dissolved form, and the cumulative mass of copper removed from the ore body. Initially, approximately 117 metric tons

of copper are contained in the solution domain in form of chrysocolla. The total copper mass in solid form decreases due to the dissolution of chrysocolla following the injection of the leach solution. The total mass of dissolved copper in the solution domain is increasing as a result. The total dissolved mass ceases to increase, once the copper bearing solution reaches the extraction well and is removed from the ore body. Dissolved copper mass decreases when chrysocolla becomes completely depleted in parts of the solution domain. Figure 5.26 also shows that more than 90% of the available copper is retrieved after 0.7 years of leaching operation.

5.5.3 Numerical Settings and Performance

As mentioned previously, the model was run using upstream weighting. The time-lagged method was used for updating the activity coefficients. Performing double activity updates during each Newton iteration was leading to convergence problems. Time increments were chosen such that an anticipated update of 1 log concentration cycle was attained or that 12 Newton iterations per time step were achieved. The maximum tolerable update before modifying the computed updates was set to 3 log concentration cycles, and the maximum number of Newton iterations before restarting a time step was limited to 15 iterations. The magnitude of the time increment averaged around 10^{-4} and 10^{-3} years during the first 0.2 years of simulation time and then gradually increased to 10^{-2} years, which was the specified maximum time step. The magnitude of the time increment reflected particular difficulties during the early stages of the simulation when high concentration gradients exist in the vicinity of the injection well. The complete depletion of chrysocolla close to the injection well was also leading to computational difficulties because the dissolved copper concentrations decreased by approximately 7 orders of magnitude as a result of the mineral depletion. A final difficulty was the arrival of the leaching front at the extraction well, where the formation and complete depletion of mineral phases take place in a converging flow field.

The solution of this problem required 894 time steps or 8480 Newton iterations. The memory required was 20.2 MB. The required CPU-time was 11 hours and 26 minutes and 20 seconds on a Pentium P2/266 MHz.

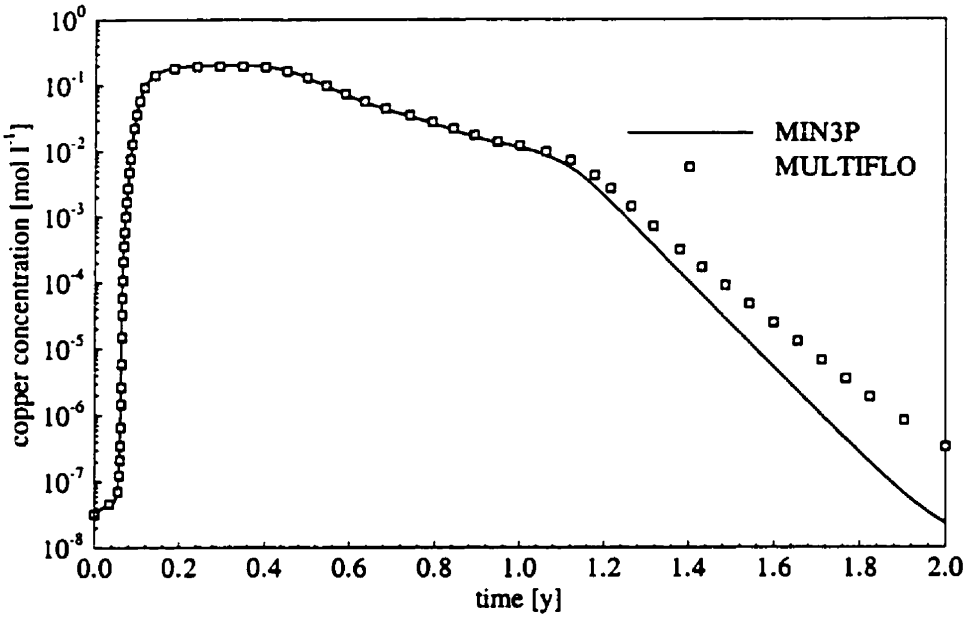

Figure 5.16: Copper recovery plotted as a function of time

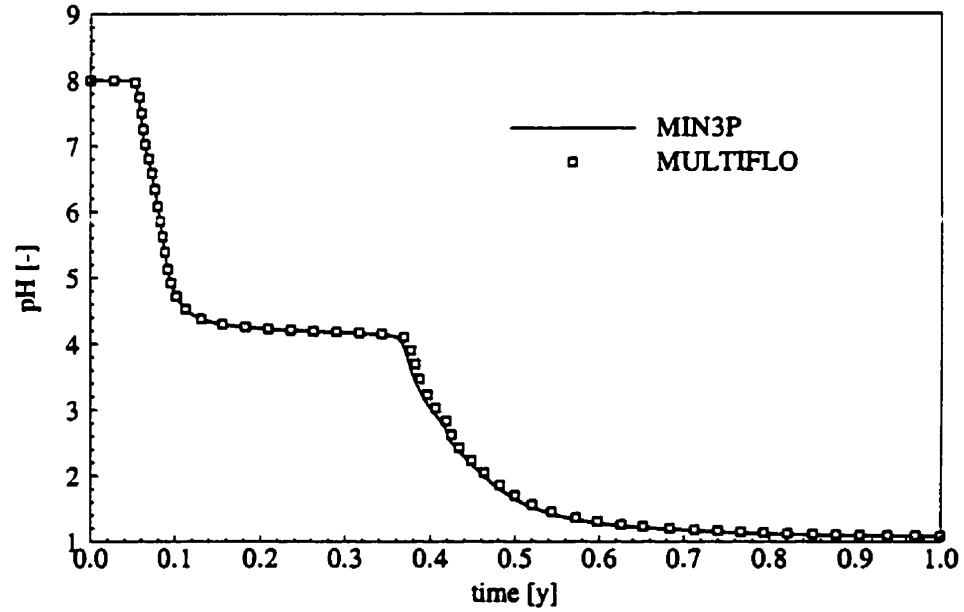

Figure 5.17: pH plotted as a function of time at extraction well

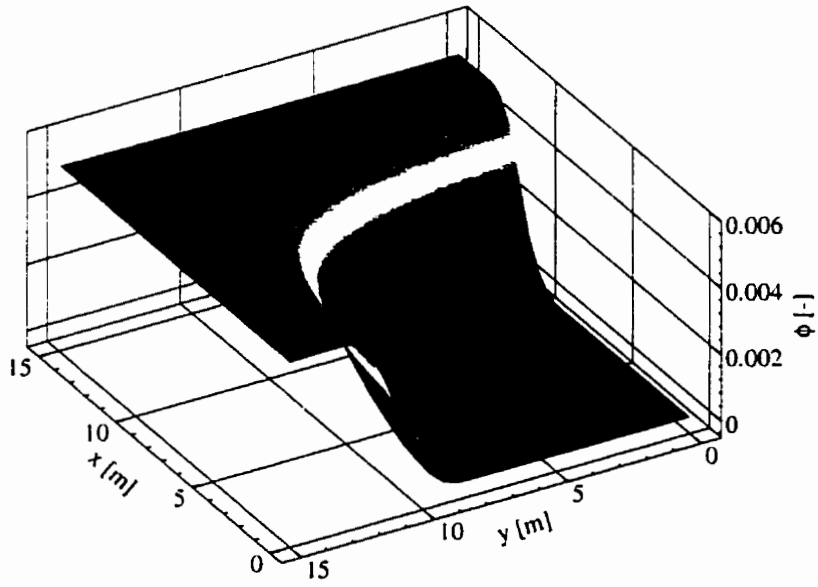

Figure 5.18: Mineral volume fractions after $t = 0.25$ years - chrysocolla

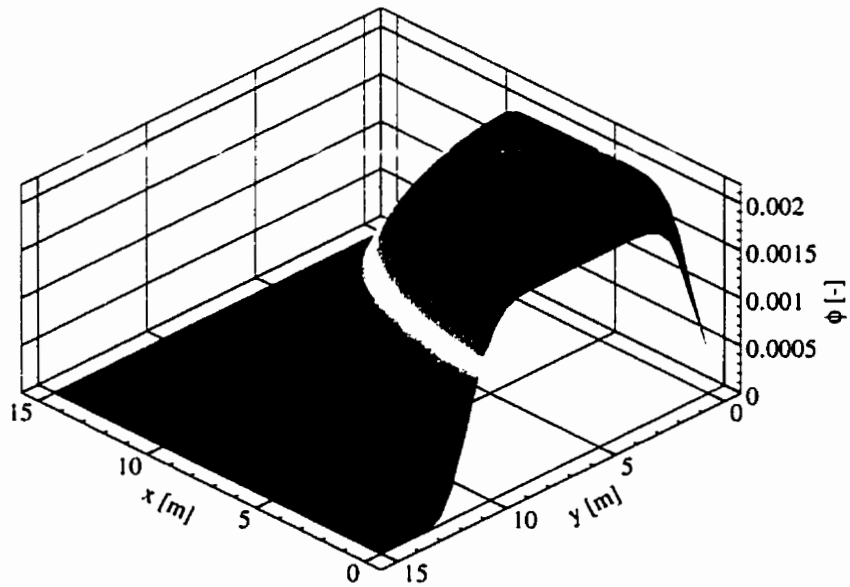

Figure 5.19: Mineral volume fractions after $t = 0.25$ years - silica (am)

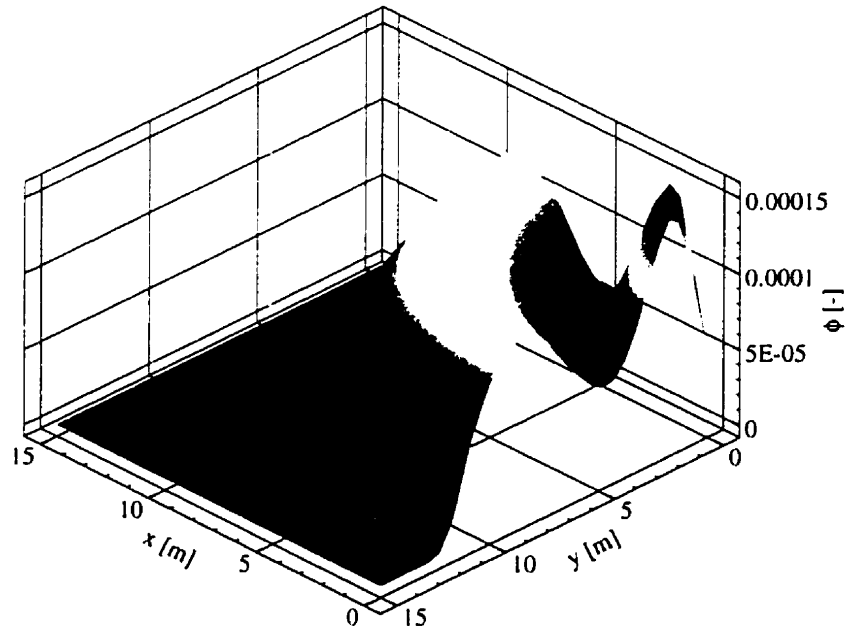

Figure 5.20: Mineral volume fractions after $t = 0.25$ years - gypsum

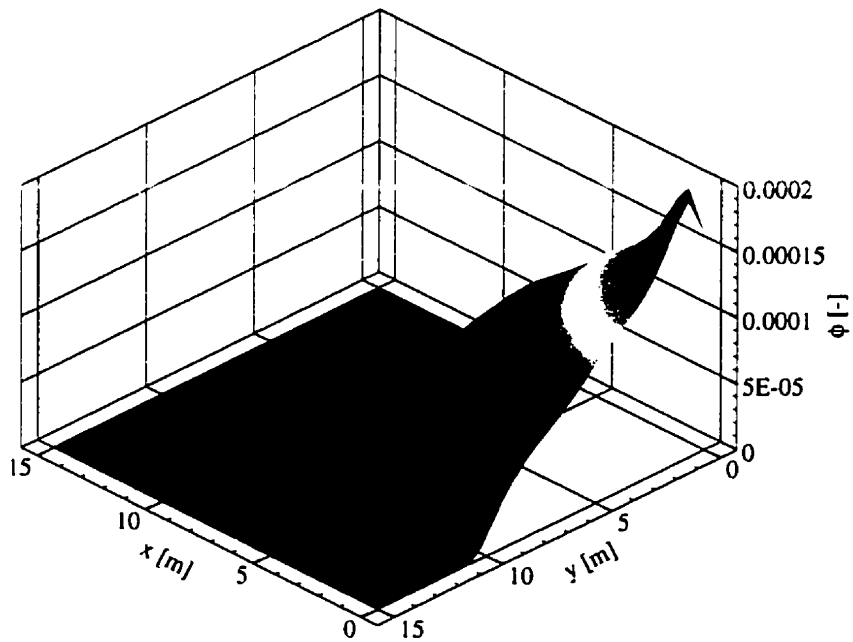

Figure 5.21: Mineral volume fractions after $t = 0.25$ years - jarosite

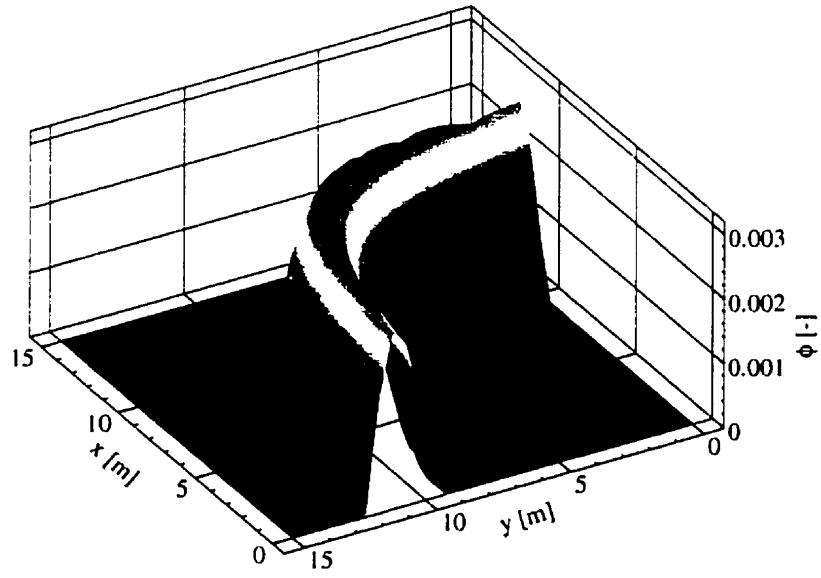

Figure 5.22: Mineral volume fractions after $t = 0.25$ years - jurbanite

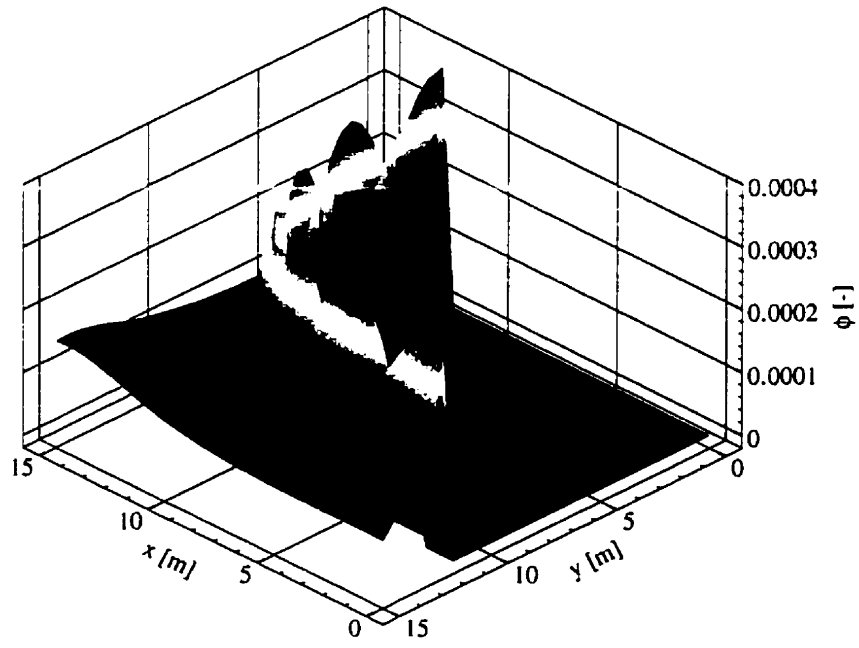

Figure 5.23: Mineral volume fractions after $t = 0.25$ years - alunite

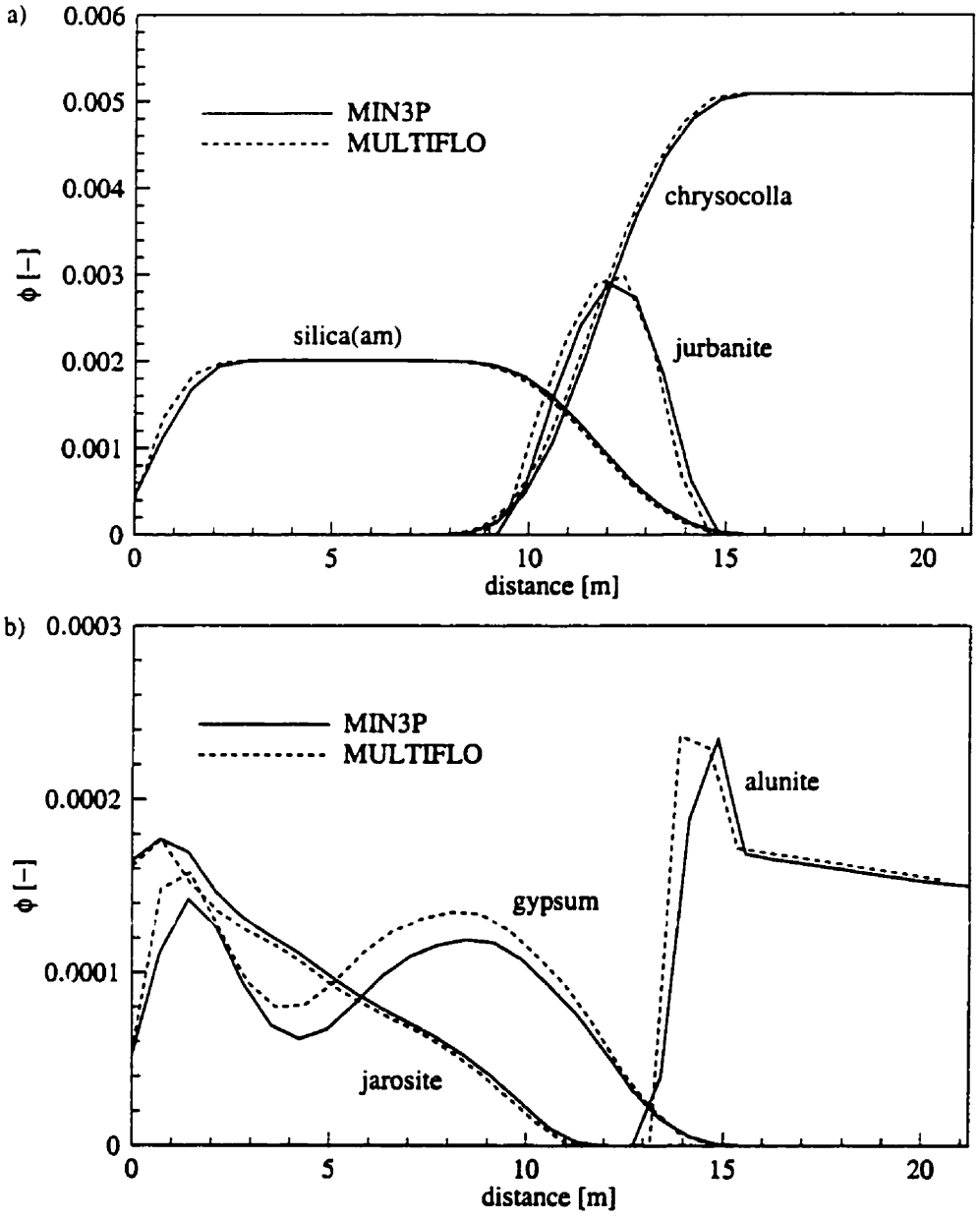

Figure 5.24: Selected mineral volume fractions and pH after $t = 0.25$ years along centerline

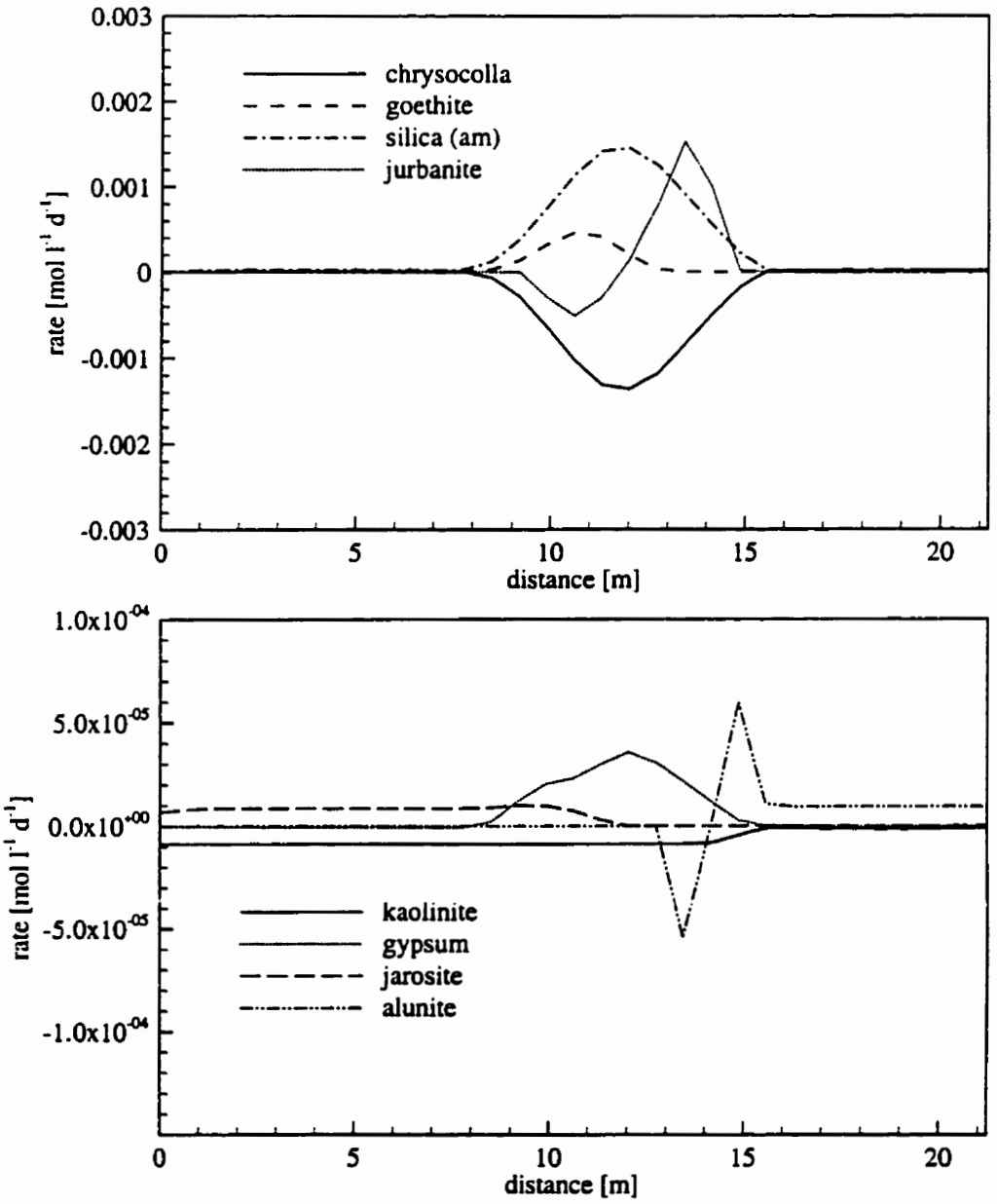

Figure 5.25: Mineral dissolution-precipitation rates after $t = 0.25$ years along centerline

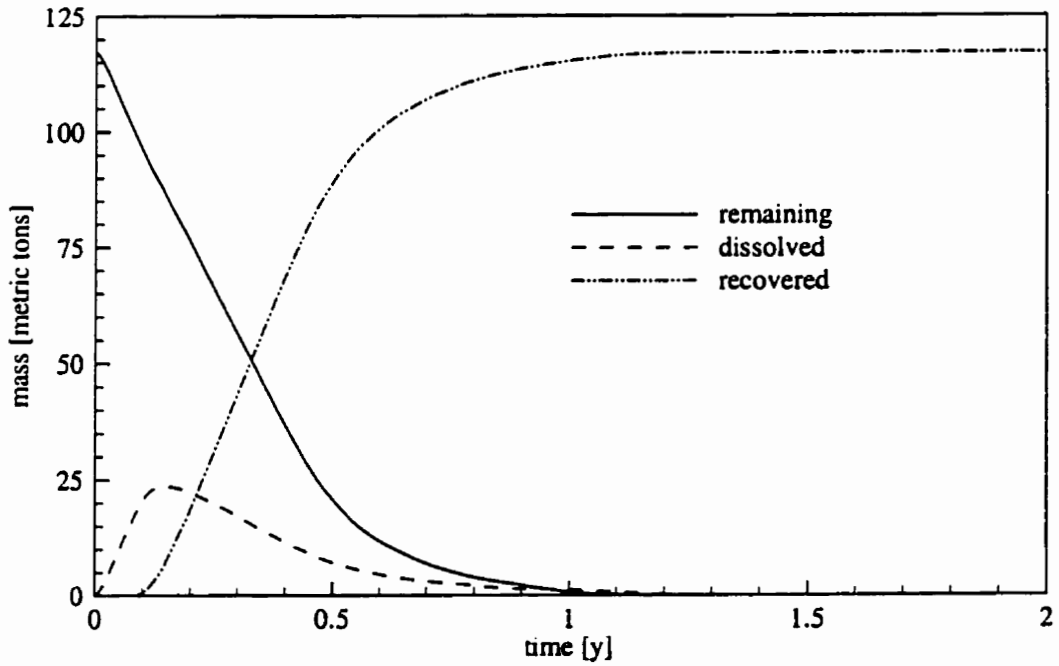

Figure 5.26: Mass balance for copper leaching benchmark problem

	MULTIFLO	MIN3P
computed pH of solution:	8.000	8.0000
computed pe of solution:	12.601	12.6004
computed E_H of solution:	0.7454	0.7434
ionic strength:	$7.4758 \cdot 10^{-03}$	$7.4756 \cdot 10^{-03}$

Table 5.25: Master variables, initial groundwater

	MULTIFLO	MIN3P
Na^+	$5.0000 \cdot 10^{-03}$	$5.0000 \cdot 10^{-03}$
K^+	$2.5768 \cdot 10^{-05}$	$2.5768 \cdot 10^{-05}$
Ca^{2+}	$6.8569 \cdot 10^{-04}$	$6.8569 \cdot 10^{-04}$
H^+	$1.5399 \cdot 10^{-05}$	$1.5500 \cdot 10^{-05}$
Al^{3+}	$2.0413 \cdot 10^{-08}$	$2.0413 \cdot 10^{-08}$
$H_4SiO_4(aq)$	$1.8703 \cdot 10^{-04}$	$1.8703 \cdot 10^{-04}$
HCO_3^-	$1.7418 \cdot 10^{-03}$	$1.7418 \cdot 10^{-03}$
SO_4^{2-}	$5.0000 \cdot 10^{-04}$	$5.0000 \cdot 10^{-04}$
Cl^-	$3.6709 \cdot 10^{-03}$	$3.6709 \cdot 10^{-03}$
$O_2(aq)$	$2.5277 \cdot 10^{-04}$	$2.5277 \cdot 10^{-04}$
Fe^{2+}	$3.5980 \cdot 10^{-12}$	$3.5980 \cdot 10^{-12}$
Cu^{2+}	$3.2342 \cdot 10^{-08}$	$3.2342 \cdot 10^{-08}$

Table 5.26: Total aqueous component concentrations [mol l^{-1}], initial groundwater

	MULTIFLO	MIN3P
chrysocolla	0.000	0.000
goethite	0.000	0.000
kaolinite	0.000	0.000
muscovite	0.000	0.000
quartz	0.271	0.272
silica(am)	−1.015	−1.014
gypsum	−2.332	−2.332
jarosite	−24.61	−24.61
jurbanite	–	−9.115
alunite	−13.84	−13.84

Table 5.27: Mineral saturation indices [-], initial groundwater

	MULTIFLO		MIN3P	
	C [mol l^{-1}]	γ	C [mol l^{-1}]	γ
Na^+	$5.0000 \cdot 10^{-03}$	0.9133	$5.0000 \cdot 10^{-03}$	0.9138
K^+	$2.5768 \cdot 10^{-05}$	0.9111	$2.5768 \cdot 10^{-05}$	0.9109
Ca^{2+}	$6.5026 \cdot 10^{-04}$	0.7067	$6.5023 \cdot 10^{-04}$	0.7085
H^+	$1.0837 \cdot 10^{-08}$	0.9228	$1.0844 \cdot 10^{-08}$	0.9222
Al^{3+}	$2.8166 \cdot 10^{-17}$	0.4824	$2.8185 \cdot 10^{-17}$	0.4824
$H_4SiO_4(aq)$	$1.8703 \cdot 10^{-04}$	1.0000	$1.8703 \cdot 10^{-04}$	1.0017
CO_3^{2-}	$1.0330 \cdot 10^{-03}$	0.6974	$1.0277 \cdot 10^{-05}$	0.7028
SO_4^{2-}	$4.8021 \cdot 10^{-04}$	0.6942	$4.8022 \cdot 10^{-04}$	0.6935
Cl^-	$3.6709 \cdot 10^{-03}$	0.9111	$3.6709 \cdot 10^{-03}$	0.9109
$O_2(aq)$	$2.5277 \cdot 10^{-04}$	1.0000	$2.5277 \cdot 10^{-04}$	1.0017
Fe^{2+}	$1.2435 \cdot 10^{-23}$	0.7067	$1.2464 \cdot 10^{-23}$	0.7064
Cu^{2+}	$6.4090 \cdot 10^{-09}$	0.7067	$6.4088 \cdot 10^{-09}$	0.7064
Fe^{3+}	$7.0969 \cdot 10^{-24}$	0.4824	$7.1135 \cdot 10^{-24}$	0.4824
Cu^+	$6.6733 \cdot 10^{-19}$	0.9133	$6.6967 \cdot 10^{-19}$	0.9094
OH^-	$1.1087 \cdot 10^{-06}$	0.9122	$1.1091 \cdot 10^{-06}$	0.9117
$H_2CO_3(aq)$	$3.3970 \cdot 10^{-05}$	1.0000	$3.3998 \cdot 10^{-05}$	1.0017
HCO_3^-	$1.6819 \cdot 10^{-03}$	0.9133	$1.6819 \cdot 10^{-03}$	0.9156
$CaSO_4(aq)$	$1.9785 \cdot 10^{-05}$	1.0000	$1.9781 \cdot 10^{-05}$	1.0017
$CaHCO_3^+$	$8.6059 \cdot 10^{-06}$	0.9133	$8.6204 \cdot 10^{-06}$	0.9168
$CaCO_3(aq)$	$7.0307 \cdot 10^{-06}$	1.0000	$7.0542 \cdot 10^{-06}$	1.0017
$CuOH^+$	$2.5580 \cdot 10^{-08}$	0.9133	$2.5580 \cdot 10^{-08}$	0.9127
$Al(OH)_4^-$	$1.9465 \cdot 10^{-08}$	0.9133	$1.9466 \cdot 10^{-08}$	0.9138
$CaOH^+$	$7.1072 \cdot 10^{-09}$	0.9133	$7.0965 \cdot 10^{-09}$	0.9168
$Al(OH)_3(aq)$	$9.4504 \cdot 10^{-10}$	1.0000	$9.4352 \cdot 10^{-10}$	1.0017
HSO_4^-	$3.4788 \cdot 10^{-10}$	0.9133	$3.4734 \cdot 10^{-10}$	0.9138
$CuSO_4(aq)$	$3.0827 \cdot 10^{-10}$	1.0000	$3.0732 \cdot 10^{-10}$	1.0017
$CuCl^+$	$4.5366 \cdot 10^{-11}$	0.9133	$4.5365 \cdot 10^{-11}$	0.9127
$Al(OH)_2^+$	$3.7848 \cdot 10^{-12}$	0.9133	$3.7721 \cdot 10^{-12}$	0.9156
$Fe(OH)_3(aq)$	$3.4237 \cdot 10^{-12}$	1.0000	$3.4238 \cdot 10^{-12}$	1.0017
$Fe(OH)_4^-$	$9.4166 \cdot 10^{-14}$	0.9133	$9.4073 \cdot 10^{-14}$	0.9156
$Fe(OH)_2^+$	$8.0149 \cdot 10^{-14}$	0.9133	$8.0101 \cdot 10^{-14}$	0.9156
$CuCl_2(aq)$	$7.2973 \cdot 10^{-14}$	1.0000	$7.2784 \cdot 10^{-14}$	1.0017
$AlOH^{2+}$	$2.1506 \cdot 10^{-14}$	0.6974	$2.1352 \cdot 10^{-14}$	0.7028
CuO_2^{2-}	$2.3163 \cdot 10^{-16}$	0.6942	$2.3180 \cdot 10^{-16}$	0.6932
$AlSO_4^+$	$5.0755 \cdot 10^{-18}$	0.9133	$5.0713 \cdot 10^{-18}$	0.9138
$CuCl_2^-$	$4.9454 \cdot 10^{-19}$	0.9133	$4.9400 \cdot 10^{-19}$	0.9127
$Al(SO_4)_2^-$	$1.3134 \cdot 10^{-19}$	0.9133	$1.3111 \cdot 10^{-19}$	0.9138
$CuCl_3^{2-}$	$1.3975 \cdot 10^{-20}$	0.6942	$1.3835 \cdot 10^{-20}$	0.7003
$H_2SO_4(aq)$	$3.1771 \cdot 10^{-21}$	1.0000	$3.1751 \cdot 10^{-21}$	1.0017
$CuCl_4^{2-}$	$2.2066 \cdot 10^{-23}$	0.6942	$2.1844 \cdot 10^{-23}$	0.7003
$FeSO_4(aq)$	$4.6428 \cdot 10^{-25}$	1.0000	$4.6394 \cdot 10^{-25}$	1.0017
$FeSO_4^+$	$1.0579 \cdot 10^{-25}$	0.9133	$1.0575 \cdot 10^{-25}$	0.9148
$Fe(SO_4)_2^-$	$6.8149 \cdot 10^{-28}$	0.9133	$6.8236 \cdot 10^{-28}$	0.9125
$Fe(OH)_2(aq)$	$2.2072 \cdot 10^{-28}$	1.0000	$2.2069 \cdot 10^{-28}$	1.0017
$Fe(OH)_3^-$	$9.6214 \cdot 10^{-31}$	0.9133	$9.6188 \cdot 10^{-31}$	0.9148
$FeHSO_4^{2+}$	$5.6746 \cdot 10^{-34}$	0.6974	$5.6587 \cdot 10^{-34}$	0.7003

Table 5.28: Species concentrations [mol l^{-1}] and activity coefficients, initial groundwater

	MULTIFLO	MIN3P
computed pH of solution:	1.0000	1.0000
computed pe of solution:	19.601	19.6149
computed E_H of solution:	1.160	1.1573
ionic strength:	$4.995 \cdot 10^{-01}$	$5.2279 \cdot 10^{-01}$

Table 5.29: Master variables, leach solution

	MULTIFLO	MIN3P
Na^+	$5.0000 \cdot 10^{-03}$	$5.0000 \cdot 10^{-03}$
K^+	$1.2647 \cdot 10^{-04}$	$1.4365 \cdot 10^{-04}$
Ca^{2+}	$1.5291 \cdot 10^{-02}$	$1.4008 \cdot 10^{-02}$
H^+	$3.2930 \cdot 10^{-01}$	$3.3173 \cdot 10^{-01}$
Al^{3+}	$2.5000 \cdot 10^{-02}$	$2.5000 \cdot 10^{-02}$
$H_4SiO_4(aq)$	$1.9337 \cdot 10^{-03}$	$1.6883 \cdot 10^{-03}$
CO_3^{2-}	$3.3971 \cdot 10^{-04}$	$3.3971 \cdot 10^{-04}$
SO_4^{2-}	$2.6080 \cdot 10^{-01}$	$2.5955 \cdot 10^{-01}$
Cl^-	$5.0000 \cdot 10^{-03}$	$5.0000 \cdot 10^{-03}$
$O_2(aq)$	$1.1112 \cdot 10^{-02}$	$1.1788 \cdot 10^{-02}$
Fe^{2+}	$4.3435 \cdot 10^{-02}$	$4.6141 \cdot 10^{-02}$
Cu^{2+}	$1.0000 \cdot 10^{-08}$	$1.0000 \cdot 10^{-08}$

Table 5.30: Total aqueous component concentrations [mol l^{-1}] - leach solution

	MULTIFLO	MIN3P
chrysocolla	−13.43	−13.433
goethite	0.000	0.000
kaolinite	−12.71	−12.714
muscovite	−25.53	−25.489
quartz	1.286	1.286
silica(am)	0.000	0.000
gypsum	0.000	0.000
jarosite	0.000	0.000
jurbanite	–	−0.983
alunite	−11.34	−11.336

Table 5.31: Mineral saturation indices [-] - leach solution

	MULTIFLO		MIN3P	
	C [mol l^{-1}]	γ	C [mol l^{-1}]	γ
Na^+	$5.0000 \cdot 10^{-03}$	0.6810	$5.0000 \cdot 10^{-03}$	0.7034
K^+	$1.2647 \cdot 10^{-04}$	0.6420	$1.4365 \cdot 10^{-04}$	0.6235
Ca^{2+}	$1.1037 \cdot 10^{-02}$	0.2610	$1.0178 \cdot 10^{-02}$	0.3019
H^+	$1.249 \cdot 10^{-01}$	0.8009	$1.3112 \cdot 10^{-01}$	0.7626
Al^{3+}	$6.2276 \cdot 10^{-03}$	0.0923	$6.7465 \cdot 10^{-03}$	0.0873
$H_4SiO_4(aq)$	$1.9337 \cdot 10^{-03}$	1.0000	$1.6883 \cdot 10^{-03}$	1.1279
CO_3^{2-}	$3.4981 \cdot 10^{-18}$	0.2060	$3.6056 \cdot 10^{-18}$	0.2254
SO_4^{2-}	$6.1235 \cdot 10^{-02}$	0.1867	$6.5354 \cdot 10^{-02}$	0.1666
Cl^-	$5.0000 \cdot 10^{-03}$	0.6420	$5.0000 \cdot 10^{-03}$	0.6235
$O_2(aq)$	$2.5277 \cdot 10^{-04}$	1.0000	$2.5277 \cdot 10^{-04}$	1.1279
Fe^{2+}	$3.3666 \cdot 10^{-09}$	0.2610	$3.5069 \cdot 10^{-09}$	0.2460
Cu^{2+}	$6.2008 \cdot 10^{-09}$	0.2610	$6.7203 \cdot 10^{-09}$	0.2460
Fe^{3+}	$3.6834 \cdot 10^{-02}$	0.0929	$3.9840 \cdot 10^{-02}$	0.0873
Cu^+	$3.1980 \cdot 10^{-26}$	0.6810	$3.6670 \cdot 10^{-26}$	0.5865
OH^-	$1.5267 \cdot 10^{-13}$	0.6625	$1.5967 \cdot 10^{-13}$	0.6286
$H_2CO_3(aq)$	$3.3970 \cdot 10^{-04}$	1.0000	$3.3971 \cdot 10^{-04}$	1.1279
HCO_3^-	$2.2555 \cdot 10^{-09}$	0.6810	$2.5145 \cdot 10^{-09}$	0.6890
$CaSO_4(aq)$	$4.2540 \cdot 10^{-03}$	1.0000	$3.8299 \cdot 10^{-03}$	1.1279
$CaHCO_3^+$	$7.2349 \cdot 10^{-11}$	0.6810	$8.4203 \cdot 10^{-11}$	0.7043
$CaCO_3(aq)$	$4.4075 \cdot 10^{-18}$	1.0000	$4.7009 \cdot 10^{-18}$	1.1279
$CuOH^+$	$1.2258 \cdot 10^{-15}$	0.0681	$1.3087 \cdot 10^{-15}$	0.6466
$Al(OH)_4^-$	$1.1120 \cdot 10^{-22}$	0.6810	$1.1274 \cdot 10^{-22}$	0.6630
$CaOH^+$	$5.9749 \cdot 10^{-15}$	0.6810	$6.1151 \cdot 10^{-15}$	0.7043
$Al(OH)_3(aq)$	$4.0259 \cdot 10^{-17}$	1.0000	$3.5477 \cdot 10^{-17}$	1.1279
HSO_4^-	$1.6001 \cdot 10^{-01}$	0.6810	$1.5649 \cdot 10^{-01}$	0.6630
$CuSO_4(aq)$	$3.7784 \cdot 10^{-09}$	1.0000	$3.2579 \cdot 10^{-09}$	1.1279
$CuCl^+$	$2.0865 \cdot 10^{-11}$	0.6810	$2.1801 \cdot 10^{-11}$	0.6466
$Al(OH)_2^+$	$2.1622 \cdot 10^{-12}$	0.6810	$2.1381 \cdot 10^{-12}$	0.6890
$Fe(OH)_3(aq)$	$3.4237 \cdot 10^{-12}$	1.0000	$3.0122 \cdot 10^{-12}$	1.1279
$Fe(OH)_4^-$	$1.2628 \cdot 10^{-20}$	0.6810	$1.2291 \cdot 10^{-20}$	0.6890
$Fe(OH)_2^+$	$1.0748 \cdot 10^{-06}$	0.6810	$1.0624 \cdot 10^{-06}$	0.6890
$CuCl_2(aq)$	$2.4020 \cdot 10^{-14}$	1.0000	$2.0517 \cdot 10^{-14}$	1.1279
$AlOH^{2+}$	$3.1024 \cdot 10^{-07}$	0.2060	$2.8615 \cdot 10^{-07}$	0.2254
CuO_2^{2-}	$3.0774 \cdot 10^{-44}$	0.1867	$2.3110 \cdot 10^{-44}$	0.2501
$AlSO_4^+$	$9.9451 \cdot 10^{-03}$	0.6810	$9.8930 \cdot 10^{-03}$	0.6630
$CuCl_2^-$	$2.1830 \cdot 10^{-26}$	0.6810	$2.1407 \cdot 10^{-26}$	0.6466
$Al(SO_4)_2^-$	$8.8270 \cdot 10^{-03}$	0.6810	$8.3603 \cdot 10^{-03}$	0.6630
$CuCl_3^{2-}$	$1.6413 \cdot 10^{-27}$	0.1867	$1.3127 \cdot 10^{-27}$	0.2113
$H_2SO_4(aq)$	$1.0897 \cdot 10^{-05}$	1.0000	$9.2175 \cdot 10^{-06}$	1.1279
$CuCl_4^{2-}$	$2.4873 \cdot 10^{-23}$	0.1867	$1.9980 \cdot 10^{-23}$	0.2113
$FeSO_4(aq)$	$1.5924 \cdot 10^{-09}$	1.0000	$1.3197 \cdot 10^{-09}$	1.1279
$FeSO_4^+$	$4.8657 \cdot 10^{-03}$	0.6810	$4.7258 \cdot 10^{-03}$	0.6780
$Fe(SO_4)_2^-$	$1.0751 \cdot 10^{-03}$	0.6810	$9.5308 \cdot 10^{-04}$	0.7072
$Fe(OH)_2(aq)$	$2.2072 \cdot 10^{-28}$	1.0000	$1.8919 \cdot 10^{-28}$	1.1279
$Fe(OH)_3^-$	$1.2903 \cdot 10^{-37}$	0.6810	$1.2435 \cdot 10^{-37}$	0.6780
$FeHSO_4^{2+}$	$6.5908 \cdot 10^{-04}$	0.2060	$6.2127 \cdot 10^{-04}$	0.2113

Table 5.32: Species concentrations [mol l^{-1}] and activity coefficients - leach solution

Chapter 6

Generation and Fate of Acid Mine Drainage

Groundwater contamination by acidic drainage from mines and mine wastes is an important environmental problem [e.g. *Nordstrom and Alpers*, 1998]. Mining activities disturb natural geologic settings on a large scale and move minerals which have been buried deeply to the surface, where they are exposed to atmospheric conditions. This exposure leads to a high degree of disequilibrium between the mineral phases and the infiltrating recharge water. In mine waste dumps, the development of an unsaturated zone facilitates the ingress of atmospheric oxygen through the gaseous phase. This leads to the rapid oxidation of sulfide mineral phases resulting in the acidification of the pore water, high concentrations of dissolved iron, sulfate, and often heavy metals.

Due to the severity of the problem, many investigations have been conducted contributing to our knowledge of the generation and fate of acid mine drainage. Studies have been carried out on the laboratory scale [e.g. *Nicholson et al.*, 1990, *Schulz*, 1995, *Al et al.*, 1997] and on the field scale [e.g. *Smyth*, 1981, *Dubrovsky*, 1986 *Blowes and Jambor*, 1990, *Blowes et al.*, 1992]. Processes studied include reaction kinetics of sulfide mineral oxidation [e.g. *McKibben and Barnes*, 1986, *Moses et al.*, 1987, *Nicholson et al.*, 1988, *Nicholson et al.*, 1990, *Moses and Herman*, 1991, *Williamson and Rimstidt*, 1994], the oxidation of dissolved ferrous iron [*Singer and Stumm*, 1970, *Millero*, 1985, *Eary and Schramke*, 1990), biological catalysis of oxidation reactions [*Bodo and Lundgren*, 1974, *Ahonen and Tuovinen*, 1989, *Southam and Beveridge*, 1992, *Blowes et al.*, 1995, *Nordstrom and Southam*, 1997], transport of atmospheric oxygen through the unsaturated

zone of the tailings material [e.g. *Pantelis and Ritchie*, 1991, *Ritchie*, 1994], pH-buffering due to mineral dissolution [e.g. *Morin et al.*, 1988, *Blowes and Ptacek*, 1994] and the precipitation and/or dissolution of minerals containing ferric iron [*Baron*, 1996, *Bigham et al.*, 1996, *Jambor*, 1996]. The actual mechanisms of acid mine drainage generation are complex and may change in time and space.

Modelling studies of acid mine drainage have previously been conducted by *Jaynes et al.* [1984a], *Morin et al.* [1988], *Narasimhan et al.* [1986], *Liu and Narasimhan* [1989a], *Brand et al.* [1994], *Prein* [1994], *Walter et al.* [1994a] and [1994b], *Wunderly et al.* [1996] and *Gerke et al.* [1998] among others. These studies addressed the conceptual description of acid mine drainage generation and/or transport, or the matching of laboratory experiments or conditions observed in the field.

This study shows how MIN3P can be used to investigate the effect of transport and kinetic reaction processes on the generation and fate of acid mine drainage. Several simulations were conducted to illustrate the model capabilities for the evaluation of rate-limiting factors affecting sulfide mineral oxidation. Common sulfide minerals include pyrite and pyrrhotite. Marcasite, arsenopyrite, galena, sphalerite, chalcopyrite and covellite may also be of importance [*Nordstrom and Alpers*, 1998]. In this study, the oxidation of pyrite is investigated. Processes considered are the kinetics of pyrite and ferrous iron oxidation, the formation of secondary minerals phases, and diffusive oxygen transport through the gas phase. In addition, mass balance calculations for the ultimate electron acceptor oxygen are conducted.

The initial composition of the tailings material plays a significant role for pH-buffering and controls the evolution of the pore water in the saturated zone. The dissolution of various mineral phases, primarily carbonates, but also hydroxides and aluminosilicate minerals [*Morin et al.*, 1988, *Blowes and Ptacek*, 1994] leads to the the consumption of acidity. In this study, two different idealized tailings materials are considered to delineate the geochemical evolution in well and poorly buffered mine waste environments. Material A consists entirely of K-feldspar, while the mineralogy of material B is made up of calcite and K-feldspar. The importance of CO_2-degassing as a pH-buffer mechanism is also investigated.

Simulations are conducted for a batch system and for a 1D vertical profile. Data obtained from laboratory and field studies were used to establish the framework for the simulations.

6.1 Conceptual Model

The focus of this section is to describe a conceptual model (Figure 6.1), which includes important processes controlling the generation and the fate of acid mine drainage. Among others, *Cathles* [1979] and *Davis and Ritchie* [1986] reported that the overall rate of pyrite oxidation in tailings impoundments or waste rock piles is largely dominated by the rate of oxygen transport through the gas-filled pore space. High moisture contents decrease effective diffusion coefficients and limit the capability of oxygen to penetrate into the tailings limiting pyrite oxidation rates. The effective diffusion coefficient for transport of gaseous oxygen can be estimated as [*Millington*, 1959]

$$D_g^{\text{eff}} = D_g^{\star} S_g^{10/3} \phi^{4/3}, \tag{6.1}$$

where $D_g^{\star}$ is the free phase diffusion coefficient for oxygen in air, S_g is the saturation of the gas phase and ϕ is the porosity of the tailings material. Gas phase saturations are determined by the capability of the material to transport recharge water and is therefore ultimately related to the pore size distribution (permeability) of the tailings material. This process is here referred to as a "macroscopic transport control".

Because $O_2(aq)$ is the ultimate electron acceptor during the oxidation of mine wastes, the oxidation of pyrite is often expressed as an overall reaction in terms of oxygen as the primary oxidant (see for example the modelling studies by *Davis and Ritchie* [1986] and *Wunderly et al.* [1996]):

$$FeS_2(s) + \tfrac{7}{2}O_2(aq) + H_2O \rightarrow Fe^{2+} + 2SO_4^{2-} + 2H^+ \tag{6.2}$$

However, pyrite can alternatively be oxidized by ferric iron [e.g. *Garrels and Thompson*, 1960, *Singer and Stumm*, 1970, *McKibben and Barnes*, 1986]:

$$FeS_2(s) + 14Fe^{3+} + 8H_2O \rightarrow 15Fe^{2+} + 2SO_4^{2-} + 16H^+ \tag{6.3}$$

During the initiation of sulfide oxidation aqueous iron concentrations are low. Therefore, oxidation rates by Fe(III) are negligible and pyrite oxidation is almost exclusively by dissolved oxygen. Over time dissolved iron concentrations increase. If oxygen is present, ferrous iron will be oxidized to ferric iron:

$$Fe^{2+} + \tfrac{1}{4}O_2(aq) + H^+ \rightarrow Fe^{3+} + \tfrac{1}{2}H_2O \tag{6.4}$$

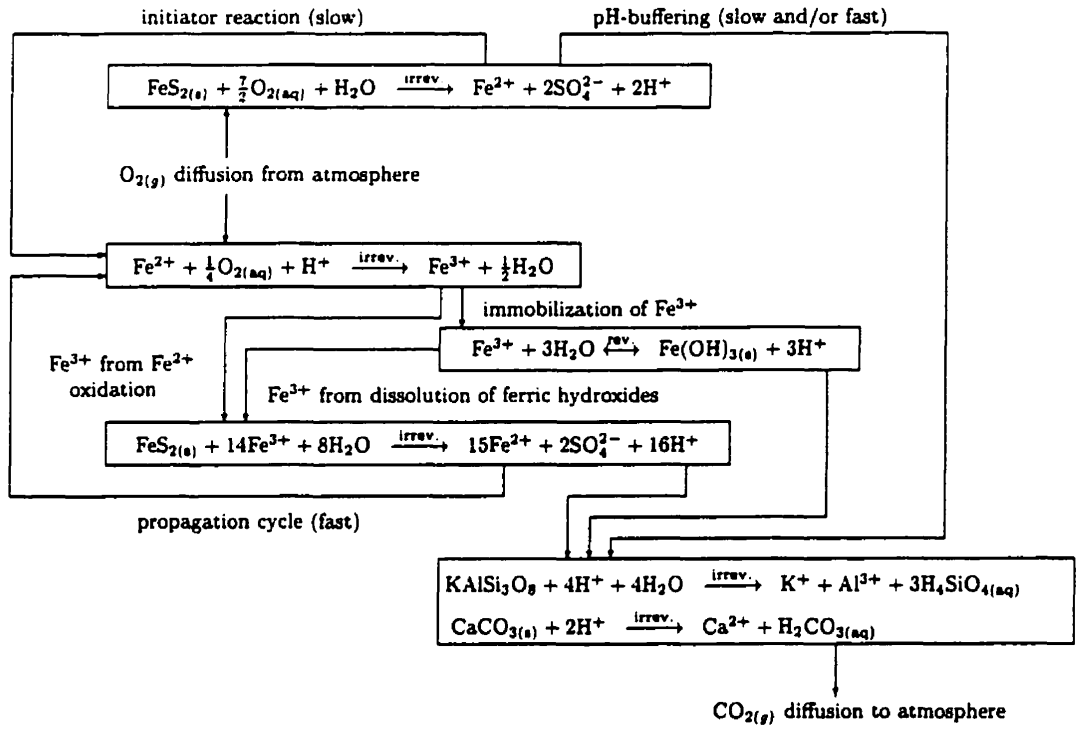

Figure 6.1: Conceptual model of pyrite oxidation, modified from *Singer and Stumm* [1970]

Reactions 6.2 and 6.3 provide parallel reaction pathways for the oxidation of pyrite. Many studies have shown that under low pH-conditions the oxidation by ferric iron is the preferred pathway for pyrite oxidation [*Singer and Stumm*, 1970, *Moses et al.*, 1987, *Nordstrom and Alpers*, 1998]. However, *Moses et al.* [1987] reported that low Fe(III)-concentrations are sufficient to oxidize pyrite and that the oxidation of pyrite by Fe(III) is dominant over the oxidation by dissolved oxygen up to pH = 9, although the difference decreases with increasing pH. *Singer and Stumm* [1970] determined that the direct oxidation of pyrite by O_2(aq) according to reaction 6.2 provides a significant contribution to the overall oxidation of pyrite at early times only and, therefore, defined this reaction as the "initiator reaction". Reactions 6.3 and 6.4 are sequential reactions and the progress of the combined reaction will be determined by the slower reaction of the sequence. *Singer and Stumm* [1970] have defined reactions 6.3 and 6.4 as the "propagation cycle". Reactions 6.2 and 6.4 are parallel reactions with respect to the consumption of dissolved oxygen. If conditions are favorable, i.e. if the rates of reactions 6.3 and 6.4 are both faster than

the rate of reaction 6.2, then the oxidation of pyrite by Fe^{3+} will be more rapid than oxidation by dissolved oxygen.

Singer and Stumm [1970] define the oxidation of ferrous iron to ferric iron according to reaction 6.4 as the rate-determining step under abiotic conditions. Many researchers have found that the rate of ferrous iron oxidation under low pH-conditions is significantly faster if the reaction is catalyzed by the bacteria *Thiobacillus Ferrooxidans* [*Southam and Beveridge*, 1992, *Bodo and Lundgren*, 1974, *Singer and Stumm*, 1970]. *Bodo and Lundgren* [1974] reported that ideal conditions for biological catalysis of ferrous iron oxidation by *Thiobacillus Ferrooxidans* exist in a pH-range between 2 and 3.5. They observed a sharp drop of catalysis rates when approaching higher pH-values. *Southam and Beveridge* [1992], on the other hand, reported that catalysis at a lower rate might also take place under circumneutral pH-conditions. For high pH-values (pH > 7), the abiotic rate of ferrous iron oxidation is rapid [*Singer and Stumm*, 1970, *Millero*, 1985]. Considerable differences exist with respect to estimates of the degree of biological catalysis in comparison to the abiotic rate. *Singer and Stumm* [1970] reported that microbial mediation might accelerate the rate of ferrous iron oxidation by a factor larger than 10^6. *Nordstrom and Alpers* [1998] suggested that the oxidation of pyrite by ferric iron is the rate-controlling step of the propagation cycle, implying that the biologically catalyzed rate of ferrous iron oxidation is potentially faster than the oxidation of pyrite by ferric iron.

Another influence on pyrite oxidation rates may be the availability of ferric iron as a species in solution, which hydrolyzes at pH-values above 2:

$$Fe^{3+} + H_2O \rightleftharpoons FeOH^{2+} + H^+ \quad (6.5)$$

$$Fe^{3+} + 2H_2O \rightleftharpoons Fe(OH)_2^+ + H^+ \quad (6.6)$$

$$Fe^{3+} + 3H_2O \rightleftharpoons Fe(OH)_3(aq) + H^+ \quad (6.7)$$

$$Fe^{3+} + 4H_2O \rightleftharpoons Fe(OH)_4^- + H^+ \quad (6.8)$$

Most laboratory studies of pyrite oxidation by Fe(III) were conducted under low pH-conditions [*McKibben and Barnes*, 1986, *Williamson and Rimstidt*, 1994] and therefore do not address the possible influence of hydrolysis reactions. As mentioned previously, *Moses et al.* [1987] showed that pyrite oxidation by Fe(III) is of importance over a pH-range from 2 - 9, and, even at high pH-values, is at least as fast as the oxidation of pyrite by oxygen. These findings indicate that the effect of ferric iron hydrolysis may not be

as pronounced and most importantly, that it may be appropriate to express the pyrite oxidation rate in terms of the total Fe(III)-concentrations instead of the Fe^{3+}-species concentrations.

A likely explanation for decreasing pyrite oxidation rates by ferric iron under mildly acidic and circumneutral pH-conditions is the significant decrease in the solubility of ferric iron. The precipitation of ferric oxides/hydroxides or hydroxy-sulfates such as ferrihydrite, schwertmannite and jarosite [*Bigham et al.*, 1996] limit dissolved Fe(III)-concentrations and therefore the availability of ferric iron for the oxidation of pyrite. Under these conditions pyrite oxidation by ferric iron becomes more dependent on the Fe-recycling reaction according to equation 6.4 [*Moses et al.*, 1987]. Precipitation reactions for ferrihydrite and jarosite can be written as:

$$Fe^{3+} + 3H_2O \rightleftharpoons Fe(OH)_3(s) + 3H^+ \quad (6.9)$$

$$K^+ + 3Fe^{3+} + 2SO_4^{2-} + 6H_2O \rightleftharpoons KFe_3(SO_4)_2(OH)_6 + 6H^+ \quad (6.10)$$

If secondary minerals containing ferric iron precipitate, reactions 6.3, 6.9 and 6.10 are parallel reactions with respect to the consumption of ferric iron. To what degree the precipitation of these secondary minerals will affect the oxidation of pyrite depends on the relative rates for secondary mineral precipitation and pyrite oxidation, and the solubility of the secondary mineral phases.

The dissolution of ferric oxides/hydroxides and hydroxy-sulfates is a potential source of ferric iron, which may also affect the rate of pyrite oxidation by providing the oxidant. In this case reactions 6.4, 6.9 and 6.10 are parallel with respect to the production of ferric iron.

The precipitation of secondary minerals may inhibit the oxidation of pyrite by their formation on the surface of the sulfide mineral particles, where they form a surface coating [e.g. *Cathles*, 1979, *Hiskey and Schlitt*, 1982, *Jaynes et al.*, 1984a, *Davis and Ritchie*, 1986, *Nicholson et al.*, 1990, *Wunderly et al.*, 1996]. This protective layer limits the access of the electron acceptors, dissolved oxygen and ferric iron, to the reactive pyrite surface.

The pH of the pore water affects the solubility and hydrolysis of ferric iron, the rate of oxidation of ferrous iron [*Singer and Stumm*, 1970, *Lowson*, 1982], and the bacterial catalysis of oxidation reactions [e.g. *Nordstrom and Southam*, 1997]. By extension, the pH affects the rate of pyrite oxidation by ferric iron. Acidification of the pore water is primarily due to the oxidation of sulfide minerals and the precipitation of ferric hydroxides

(see equations 6.2, 6.3, 6.9 and 6.10). Acid production can be offset by the dissolution of pH-buffering minerals contained in the tailings material. Depending on the particular mineral phase dissolving, the pH will be buffered to a specific value [*Morin et al.*, 1988, *Blowes and Ptacek*, 1994]. Another influence on the degree of pH-buffering is the effective rate of mineral dissolution in comparison to pyrite oxidation rates. Calcite, for example, is a fast dissolving mineral with a high pH-buffer capacity:

$$CaCO_3(s) + H^+ \rightleftharpoons Ca^{2+} + HCO_3^- \tag{6.11}$$

pH-buffering due to the dissolution of aluminosilicate minerals is a relatively slow process. The dissolution of K-feldpar is an example of a slowly dissolving mineral:

$$KAlSi_3O_8 + 4H^+ + 4H_2O \rightarrow K^+ + Al^{3+} + 3H_4SiO_4(aq) \tag{6.12}$$

If carbonate minerals are dissolving in the unsaturated zone, the pH may be buffered additionally by the degassing of carbon dioxide:

$$HCO_3^- + H^+ \rightarrow CO_2(g) + H_2O \tag{6.13}$$

6.2 Example Applications

A number of simulations were conducted to evaluate the relative importance of several processes affecting the rate of pyrite oxidation, the pH of the pore water, and the composition of the aqueous and solid phases. Simulations were carried out for a batch reactor and for a vertical profile of partially-saturated tailings material of varying composition. The following topics were addressed:

Batch reactor simulations:

- Initiator reaction and propagation cycle - What are the contributions of pyrite oxidation by dissolved oxygen and ferric iron to the overall pyrite oxidation rate? How does the propagation cycle evolve over time?
- Kinetically-controlled oxidation of ferrous iron - Under what conditions is the oxidation of ferrous iron by dissolved oxygen rate-limiting for the overall progress of pyrite oxidation?

- Precipitation of ferric-bearing minerals - How does the precipitation of ferric-bearing secondary minerals affect the rate of pyrite oxidation by ferric iron?

Reactive transport simulations:

- Macroscopic transport control - How does pore size distribution (hydraulic conductivity) affect water saturations, oxygen transport, and pyrite oxidation rates?
- pH-buffering - How does the presence of pH-buffering minerals affect the transient evolution of the pore water composition and the tailings mineralogy?
- Oxygen mass balance - What are the oxygen consuming processes and what is the relative importance of the various processes?
- Degassing of carbonic acid - How does exsolution of carbonic acid to the gaseous phase and subsequent loss to the atmosphere affect the pH in the presence of carbonate minerals? How important is CO_2-degassing as an acid-consuming process?

6.2.1 Definition of Reaction Network

Reaction stoichiometries, equilibrium and rate constants common to both the batch reactor and reactive transport simulations are presented in this section. Table 6.1 lists aqueous complexation and oxidation-reduction reactions along with the corresponding equilibrium constants. Table 6.2 defines the reaction stoichiometries for the dissolution and exsolution of oxygen and carbon dioxide and their equilibrium constants. Table 6.3 summarizes the dissolution-precipitation reactions which are considered here. The oxidation of pyrite and the dissolution of K-feldspar are treated as irreversible reactions, while the remaining mineral phases may dissolve or precipitate in response to changes in the saturation state of the solution with respect to each mineral phase.

Dissolution-precipitation reactions are treated as surface-controlled reactions, unless otherwise noted. The reaction rates of reversible dissolution-precipitation reactions are described by transition state theory rate expressions of the form [*Lasaga*, 1998]:

$$R_i^m = -k_{\mathrm{eff},i}\left[1 - \frac{IAP_i^m}{K_i^m}\right], \tag{6.14}$$

Reaction			$\log K_i^x$
Oxidation-reduction reactions			
(1)	Fe^{3+}	$= Fe^{2+} + 0.25O_2(aq) + H^+ - 0.5H_2O$	8.473
Complexation reactions			
(2)	OH^-	$= H_2O - H^+$	-13.998
(3)	H_3SiO4^-	$= H_4SiO_4 - H^+$	-9.830
(4)	$CaHCO_3^+$	$= Ca^{2+} + CO_3^{2-} + H^+$	11.440
(5)	$CaCO_3(aq)$	$= Ca^{2+} + CO_3^{2-}$	3.220
(6)	$CaSO_4(aq)$	$= Ca^{2+} + SO_4^{2-}$	2.309
(7)	KSO_4^-	$= K^+ + SO_4^{2-}$	0.850
(8)	$Al(OH)_2^+$	$= Al^{3+} + 2H_2O - 2H^+$	-10.100
(9)	$Al(OH)_4^-$	$= Al^{3+} + 4H_2O - 4H^+$	-22.700
(10)	$Al(OH)_3(aq)$	$= Al^{3+} + 3H_2O - 3H^+$	-16.900
(11)	$Fe(OH)^+$	$= Fe^{2+} + H_2O - H^+$	-9.500
(12)	$FeSO_4(aq)$	$= Fe^{2+} + SO_4^{2-}$	2.250
(13)	HCO_3^-	$= H^+ + CO_3^{2-}$	10.330
(14)	$H_2CO_3(aq)$	$= 2H^+ + CO_3^{2-}$	16.681
(15)	$Al(OH)^{2+}$	$= Al^{3+} + H_2O - H^+$	-4.990
(16)	$AlSO_4^+$	$= Al^{3+} + SO_4^{2-}$	3.500
(17)	$Al(SO_4)_2^-$	$= Al^{3+} + 2SO_4^{2-}$	5.000
(18)	$H_SO_4^-$	$= H^+ + SO_4^{2-}$	1.987
(19)	$Fe(OH)^{2+}$	$= Fe^{3+} + H_2O - H^+$	-2.190
(20)	$Fe(SO_4)^+$	$= Fe^{3+} + SO_4^{2-}$	4.040
(21)	$Fe(OH)_2^+$	$= Fe^{3+} + 2H_2O - 2H^+$	-5.670
(22)	$Fe(OH)_3(aq)$	$= Fe^{3+} + 3H_2O - 3H^+$	-12.560

Table 6.1: Oxidation-reduction and complexation reactions

Reaction			$\log K_i^g$
(1)	$O_2(g)$	$= O_2(aq)$	2.898
(2)	$CO_2(g)$	$= 2H^+ + CO_3^{2-} - H_2O$	18.160

Table 6.2: Gas dissolution-exsolution reactions

$k_{\text{eff},i}$ defines the effective dissolution rate for the mineral phase A_i^m. The equilibrium and estimated effective rate constants for reversible dissolution-precipitation reactions are given in Table 6.4.

Mineral phase		Reaction	
irreversible			
(1a)	pyrite	$FeS_2(s) + 3.5O_2(aq) + H_2O$	$\rightarrow Fe^{2+} + 2SO_4^{2-} + 2H^+$
(1b)	pyrite	$FeS_2(s) + 14Fe^{3+} + 8H_2O$	$\rightarrow 15Fe^{2+} + 2SO_4^{2-} + 16H^+$
(2)	K-feldspar	$KAlSi_3O_8 + 4H^+ + 4H_2O$	$\rightarrow K^+ + Al^{3+} + 3H_4SiO_4$
reversible			
(3)	calcite	$CaCO_3(s)$	$\rightleftharpoons Ca^{2+} + CO_3^{2-}$
(4)	siderite	$FeCO_3(s)$	$\rightleftharpoons Fe^{2+} + CO_3^{2-}$
(5)	gibbsite	$Al(OH)_3(s) + 3H^+$	$\rightleftharpoons Al^{3+} + 3H_2O$
(6)	gypsum	$CaSO_4 \cdot 2H_2O(s)$	$\rightleftharpoons Ca^{2+} + SO_4^{2-} + 2H_2O$
(7)	ferrihydrite	$Fe(OH)_3(s) + 3H^+$	$\rightleftharpoons Fe^{3+} + 3H_2O$
(8)	jarosite	$KFe_3(SO_4)_2(OH)_6 + 6H^+$	$\rightleftharpoons K^+ + 3Fe^{3+} + 2SO_4^{2-} + 6H_2O$
(9)	silica(am)	$SiO_2(am) + 2H_2O$	$\rightleftharpoons H_4SiO_4$
(10)	jurbanite	$Al(OH)SO_4 \cdot 5H_2O + H^+$	$\rightleftharpoons Al^{3+} + SO_4^{2-} + 6H_2O$
(11)	melanterite	$FeSO_4 \cdot 7H_2O$	$\rightleftharpoons Fe^{2+} + SO_4^{2-} + 7H_2O$

Table 6.3: Dissolution-precipitation reactions

Mineral phase		$\log K_i^m$	$k_{\text{eff},i}$ [mol m^{-3} s^{-1}]
(3)	calcite	8.475	$5.0 \cdot 10^{-5}$
(4)	siderite	10.450	$1.0 \cdot 10^{-5}$
(5)	gibbsite	-8.110	$1.0 \cdot 10^{-5}$
(6)	gypsum	4.580	$1.0 \cdot 10^{-4}$
(7)	ferrihydrite	2.710	$1.0 \cdot 10^{-6}$
(8)	jarosite	9.210	$1.0 \cdot 10^{-6}$
(9)	silica(am)	2.710	$1.0 \cdot 10^{-5}$
(10)	jurbanite	3.805	$1.0 \cdot 10^{-5}$
(11)	melanterite	2.209	$1.0 \cdot 10^{-4}$

Table 6.4: Parameters for reversible dissolution-precipitation reactions

The irreversible dissolution of K-feldspar is described by a pH-dependent rate expression [*Blum and Stillings*, 1995] and is given by:

$$R_2^{md} = -\max\left[\left[S_2\left[k_{21}^{md,s}\{H^+\}^{0.5} + k_{22}^{md,s}\{H^+\}^{-0.58}\right]\left[1 - \frac{IAP_2^m}{K_2^m}\right]\right], 0\right] \tag{6.15}$$

The rate constants are $k_{21}^{md,s} = 3.19 \cdot 10^{-10}$ mol m^{-2} s^{-1} and $k_{22}^{md,s} = 7.30 \cdot 10^{-19}$ mol m^{-1} s^{-1}. The equilibrium constant is K_2^m = -0.08. The rate expressions used for the description of pyrite oxidation are discussed separately for batch and reactive transport simulations in Sections 6.2.2 and 6.2.3.

6.2.2 Batch Reactor Simulations

A series of simulations has been conducted using a batch reactor as shown in Figure 6.2. The porous material in the batch reactor has a porosity of 50% and contains 0.5 vol% pyrite and 49.5 vol% K-feldspar. The initial reactive surface areas for pyrite and K-feldspar are assumed $S_1 = 12$ m^2 m^{-3} and $S_2 = 594$ m^2 m^{-3}, respectively. The void pore space is partially-saturated and the phase saturations for water and gas are both 50%. It was assumed that the system is open to the atmosphere and that the pore water is in equilibrium with atmospheric gases. The initial pore water composition is characterized by a pH = 2 and a total sulfate concentration of $6.95 \cdot 10^{-3}$ mol l^{-1}. The low pH was used as a starting condition to utilize available laboratory-derived rate expressions for pyrite oxidation by Fe(III) only within their range of applicability. The concentrations of the remaining constituents were assumed to be negligibly low.

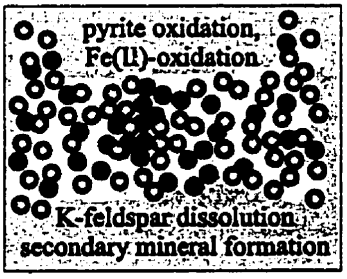

fixed:
$pO_2 = 0.21$ atm, $pCO_2 = 10^{-3.5}$ atm,
$S_a = S_g = 0.5$
initial condition:
pH = 2, $SO_4 = 6.95 \times 10^{-3}$ mol l^{-1}
$\phi = 0.5$, $\phi_{pyrite} = 5 \times 10^{-3}$, $\phi_{K\text{-feldspar}} = 0.495$

Figure 6.2: Batch reactor for numerical study of acid mine drainage generation

Pyrite oxidation is here described by a combined rate expression based on the laboratory experiments from *Williamson and Rimstidt* [1994] and *McKibben and Barnes* [1986]. The combined rate expression takes the form:

$$R_1^{md,s} = -\max\left[\left[S_1\left[k_{11}^{md,s}\{O_2(aq)\}^{0.5}\{H^+\}^{-0.11}\right]\left[\frac{IAP_{11}^m}{K_{11}^m}\right] + \left[k_{12}^{md,s}[Fe(III)]^{0.5}\{H^+\}^{-0.50}\right]\left[\frac{IAP_{12}^m}{K_{12}^m}\right]\right], 0\right], \quad (6.16)$$

This rate expression accounts for the irreversibility of pyrite oxidation. IAP_{11}^m and IAP_{12}^m are the ion activity products for pyrite oxidation by oxygen and by ferric iron, as defined by the reaction stoichiometries of reactions 1a and 1b in Table 6.3. The corresponding equilibrium constants are log K_{11}^m = -215.264 and log K_{12}^m = -98.541. The rate constant for pyrite oxidation by dissolved oxygen is defined by $k_{11}^{md,s} = 10^{-8.19}$ mol m^{-2} s^{-1} [*Williamson and Rimstidt*, 1994] and the rate constant for pyrite oxidation by ferric iron is $k_{12}^{md,s} = 10^{-7.52}$ mol m^{-2} s^{-1} [*McKibben and Barnes*, 1986].

Initiator Reaction and Propagation Cycle

Figure 6.3a shows the time-dependent evolution of pyrite oxidation and K-feldspar dissolution rates plotted on a log-log scale. Pyrite oxidation by dissolved oxygen is initially the dominant reaction path for the oxidation of pyrite. Oxidation by ferric iron gains importance as dissolved iron concentrations increase. The simulation results coincide with the "initiator reaction" and "propagation cycle" model introduced by *Singer and Stumm* [1970]. The overall rate of pyrite oxidation by ferric iron increases with time. This behavior can be attributed to the autocatalytic nature of the propagation cycle, which is due to the net-gain in dissolved total iron concentrations during pyrite oxidation. It was assumed that Fe(II)-oxidation is fast in comparison to pyrite oxidation by ferric iron. Therefore, equilibrium conditions have been assumed for the Fe(II)/Fe(III)-redox couple. The degree of autocatalysis in a real system will strongly depend on the Fe(III)-availability, which is determined by the rate of ferrous iron oxidation by dissolved oxygen (equation 6.4), and will be discussed later. The simulation shows that pyrite oxidation rates by ferric iron exceed the oxidation rates by dissolved oxygen by 2-3 orders of magnitude, which is in close agreement with the results of the laboratory experiments of *Moses et al.* [1987] and *Williamson and Rimstidt* [1994].

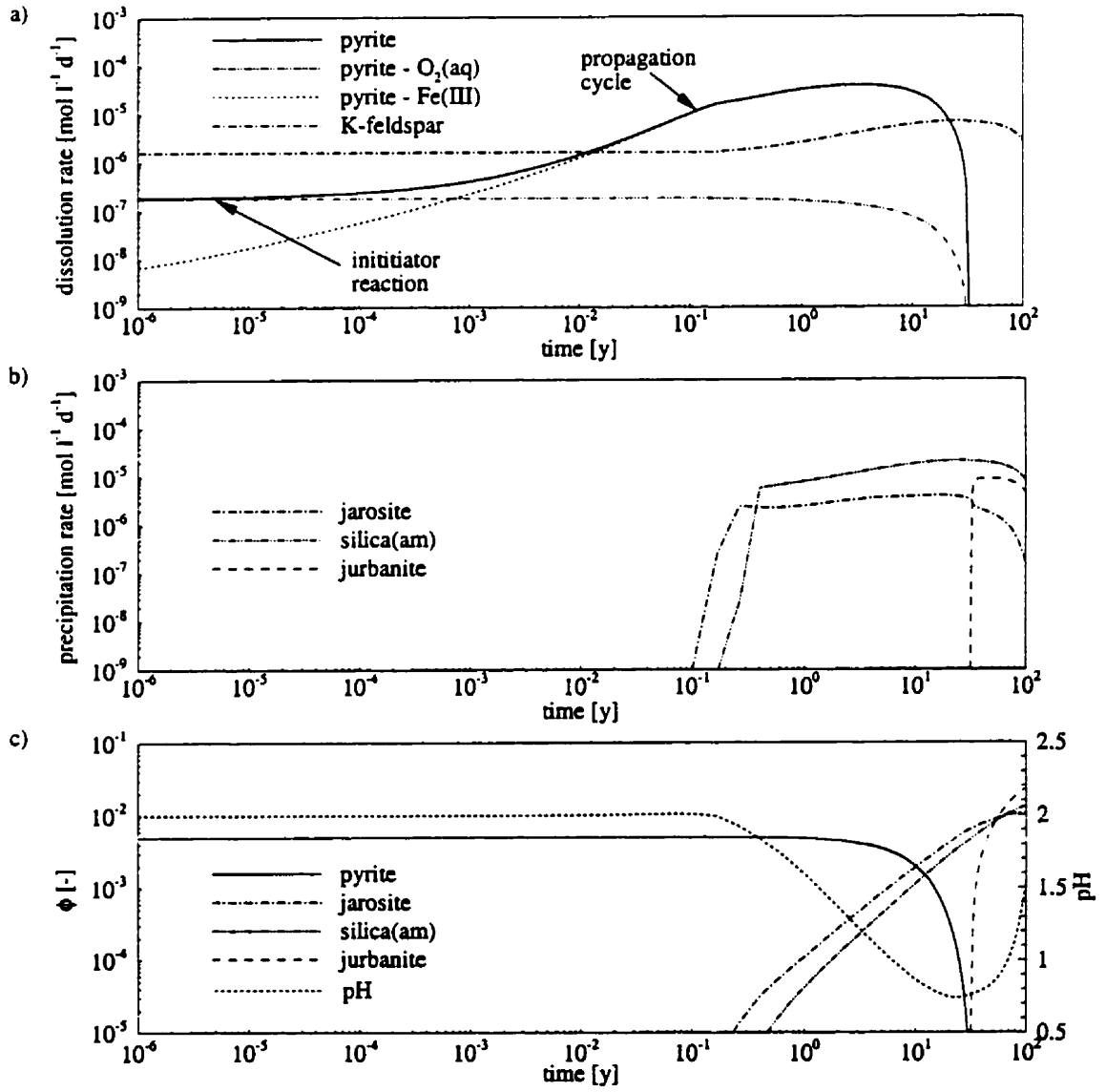

Figure 6.3: Initiator reaction and propagation cycle: a) dissolution rates of primary minerals, b) precipitation rates of secondary minerals, c) selected mineral volume fractions and pH

Jarosite precipitates as a result of the increasing dissolved iron, sulfate and potassium concentrations [*Bigham et al.*, 1996]. Once saturation is reached, jarosite provides a limit to dissolved ferric iron concentrations and thus, the overall oxidation rate of pyrite (Figures 6.3b and c). This behavior is indicated by the break in the increase of pyrite oxidation rates after approximately 0.2 years (Figure 6.3a).

The oxidation of pyrite increases the acidity of the pore water (Figure 6.3c) and leads to an enhanced dissolution of K-feldspar (Figure 6.3a). However, despite the abundance of this mineral phase, the rate of K-feldspar dissolution is slow in comparison to the rate of pyrite oxidation. Significant pH-buffering can only be observed when pyrite becomes completely depleted. The secondary minerals amorphous silica and jurbanite form as a result of K-feldspar dissolution (Figures 6.3b and 6.3c). The solution remained undersaturated with respect to other potential secondary mineral phases including kaolinite, ferrihydrite, gibbsite and alunite.

Pyrite oxidation leads to high concentrations of dissolved iron (max. 0.46 mol l^{-1}) and sulfate (max. 1.38 mol l^{-1}). The ionic strength of the solution reaches a maximum of $I = 1.25$ when pyrite oxidation rates are highest. The present model uses the extended Debye-Hückel equation, which is strictly only applicable up to an ionic strength of $I = 0.7$ [*Allison et al.*, 1991]. This may affect the accuracy of the modelled results. Nevertheless, the qualitative behavior is believed to be represented correctly. It is also possible that other ferric-bearing mineral phases such as coquimbite ($Fe_2(SO_4)_3 \cdot 9H_2O$) or kornelite ($Fe_2(SO_4)_3 \cdot 7H_2O$) precipitate under the prevailing low pH- and high TDS-conditions [*Nordstrom and Alpers*, 1998].

Kinetically-Controlled Oxidation of Ferrous Iron

The simulation conducted in the previous section was based on the assumption that the oxidation of ferrous iron by dissolved oxygen is fast in comparison to the rate of pyrite oxidation by ferric iron. However, *Singer and Stumm* [1970] reported that the oxidation of ferrous iron is the rate-determining step for pyrite oxidation in abiotic systems under low pH-conditions. The abiotic oxidation rate for ferrous iron oxidation for a pH-range from approximately 1 to 8 can be expressed as [*Singer and Stumm*, 1970]:

$$R_1^{af} = -\max\left[\left[k_{11}^{af}[\mathrm{Fe(II)}]\{\mathrm{O_2(aq)}\} + k_{12}^{af}[\mathrm{Fe(II)}]\{\mathrm{O_2(aq)}\}\{\mathrm{H^+}\}^{-2}\right], 0\right] \tag{6.17}$$

The first term dominates the reaction rate for acidic pH-values (pH < 3.5) and is characterized by slow reaction kinetics, while the second term controls the overall reaction rate above pH = 4.5 and accounts for increasing oxidation rates with increasing pH. This rate expression takes into account the irreversibility of ferrous iron oxidation in natural systems. The corresponding rate constants are given by *Singer and Stumm* [1970] and are $k_{11}^{af} = 3.2 \cdot 10^{-5}$ [l mol^{-1} s^{-1}] and $k_{12}^{af} = 2.6 \cdot 10^{-12}$ [l^{-1} mol s^{-1}].

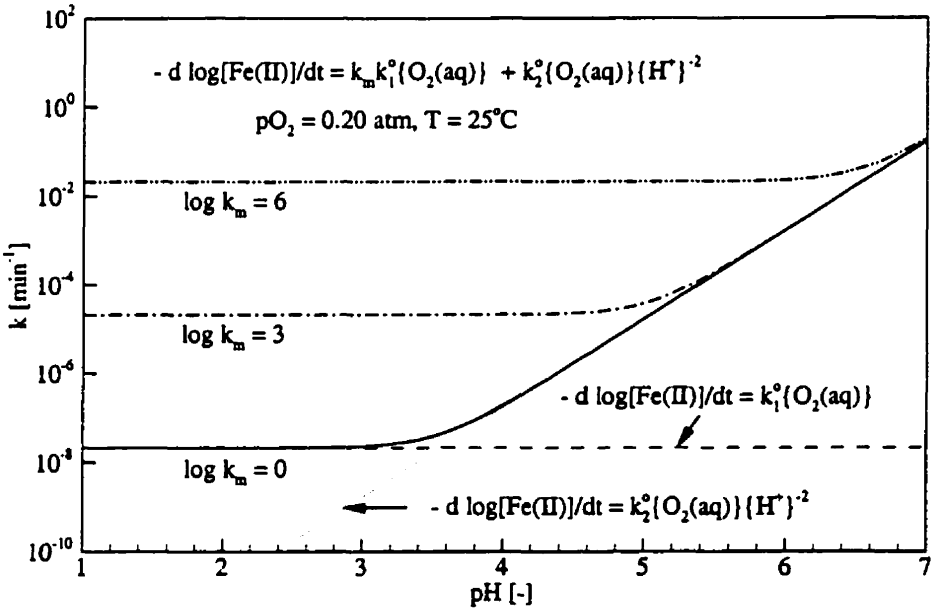

Figure 6.4: Abiotic and biologically catalyzed oxidation rates of ferrous iron

On the other hand, biological catalysis occurs under low-pH conditions in natural environments [e.g.: *Southam and Beveridge*, 1992, *Nordstrom and Alpers*, 1998, *Nordstrom and Southam*, 1997]. Estimates of biological catalysis factors reported in the literature differ significantly [e.g. *Singer and Stumm*, 1970, *Nicholson*, 1994, *Nordstrom and Alpers*, 1998] and range from 10^2 to 10^6 in comparison to the abiotic rate. It is therefore of general interest to determine the sensitivity of pyrite oxidation rates to biological catalysis of ferrous iron oxidation. Rate expression 6.17 can be modified to allow the consideration of biological catalysis under low pH-conditions by introducing the biological catalysis factor k_m:

$$R_1^{af} = -\max\left[\left[k_m k_{11}^{af}[\text{Fe(II)}]\{O_2(aq)\} + k_{12}^{af}[\text{Fe(II)}]\{O_2(aq)\}\{H^+\}^{-2}\right], 0\right], \tag{6.18}$$

The abiotic ($\log k_m = 0$) and microbially mediated (for $\log k_m = 3$ and 6) rates of ferrous iron oxidation are presented in Figure 6.4 for $pO_2 = 0.2$ atm and T = 25°C as a function of pH (modified after *Singer and Stumm*, 1970).

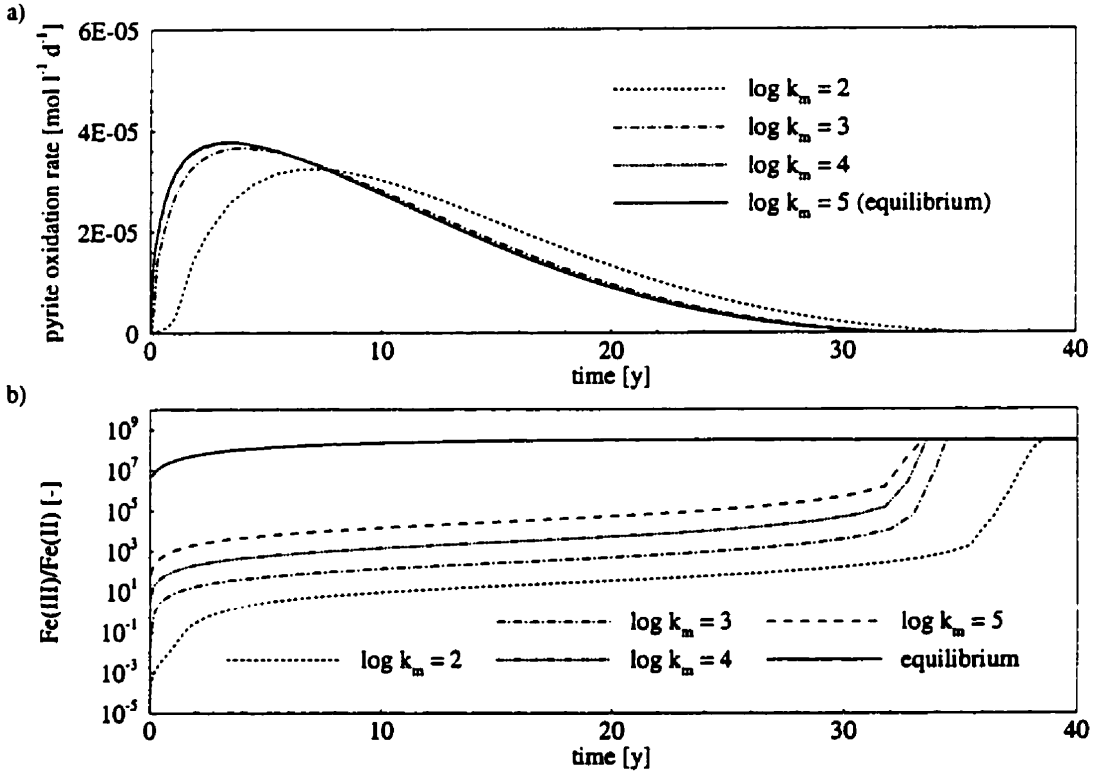

Figure 6.5: Sensitivity with respect to biological catalysis of ferrous iron oxidation: a) pyrite oxidation rates, b) Fe(III)/Fe(II) concentration ratio

Figure 6.5a shows overall pyrite oxidation rates for different biological catalysis factors ($\log k_m$ = 2-5) and for equilibrium conditions for the Fe(II)/Fe(III) redox couple. It can be seen that overall rates of pyrite oxidation are virtually identical for catalysis factors

k_m	10^2	10^3	10^4	10^5	equilibrium
time [y]	22.4	18.9	18.7	18.7	18.7
Fe(II) [mol l^{-1}]	$1.0 \cdot 10^{-2}$	$1.0 \cdot 10^{-3}$	$1.1 \cdot 10^{-4}$	$1.6 \cdot 10^{-5}$	$1.4 \cdot 10^{-9}$
Fe(III) [mol l^{-1}]	$4.3 \cdot 10^{-1}$	$4.5 \cdot 10^{-1}$	$4.5 \cdot 10^{-1}$	$4.5 \cdot 10^{-1}$	$4.5 \cdot 10^{-1}$

Table 6.5: Maximum Fe(III) and corresponding Fe(II) concentrations depending on biological catalysis of ferrous iron oxidation

greater 10^3 and are, for practical purposes, equivalent to pyrite oxidation rates under equilibrium conditions for the Fe(II)/Fe(III) redox couple. However, the oxidation of ferrous iron becomes rate-limiting for catalysis factors $k_m \leq 10^3$. The effect is strongest at early times, when dissolved iron concentrations are low. For low catalysis factors, a considerable fraction of dissolved iron remains in the reduced state. This leads to a decrease of dissolved ferric iron and increased ferrous iron concentrations and most notably a time lag, which proceeds the onset of the propagation cycle (see Figure 6.5a). During this time lag secondary ferrous bearing minerals such as melanterite ($FeSO_4 \cdot 7H_2O$) or ferrous and ferric-bearing minerals, such as copiapite ($Fe(II)Fe(III)_4(SO_4)_6(OH)_2 \cdot 20H_2O$) could precipitate [*Nordstrom and Alpers*, 1998]. The precipitation of these mineral phases may inhibit pyrite oxidation by removing dissolved iron from solution. However, in these simulations the pore water remained undersaturated with respect to melanterite. Equilibrium constants for other ferrous-bearing soluble iron-sulfate minerals were not available, and these minerals were therefore not considered in this analysis. *Blowes et al.* [1991] observed the precipitation of melanterite under field conditions, however, the formation took place below the zone of active oxidation, where ferrous iron is the dominant dissolved state.

Nordstrom and Alpers [1998] hypothesized that ferrous iron oxidation rates are potentially much faster than pyrite oxidation rates by ferric iron and concluded that the rate-determining step for pyrite oxidation in natural environments is the heterogeneous reaction, i.e. the oxidation of pyrite by ferric iron. The present study shows that relatively small catalysis factors ($k_m > 10^3$) appear sufficient to maintain ferric iron concentrations near equilibrium levels (Table 6.5). For these catalysis factors, pyrite oxidation rates do not differ substantially from the rates under equilibrium conditions for the Fe(II)/Fe(III) redox couple (Figure 6.5a). However, ferrous iron concentrations are much higher than the corresponding equilibrium values (Table 6.5), which is also reflected by the Fe(III)/Fe(II) concentration ratio (Figure 6.5b). Differences become less significant for higher catalysis

rates. A comparison to equilibrium conditions for the Fe(II)/Fe(III) redox couple (Figure 6.5b) shows that a biological catalysis factor $k_m \gg 10^6$ would be required to reproduce true equilibrium conditions.

The results indicate that biological catalysis of ferrous iron oxidation can accelerate the oxidation of pyrite by ferric iron. However, field observations show that a significant fraction of total dissolved iron remains as Fe(II) in the zone of active oxidation [*Dubrovsky et al.*, 1984: Elliot Lake, $\approx$ 36% Fe(II); *Johnson*, 1993: Nickel Rim, 52-82% Fe(II); *Bain*, personal communication, 1999: Moose Lake, Ontario, > 85% Fe(II)]. These data indicate that there is some kinetic limitation for ferrous iron oxidation in natural systems. Although not directly comparable, such an Fe(III)/Fe(II) ratio would correspond to a biological catalysis factor of 10^1 to 10^3 for the simulations conducted in the present study (Figure 6.5b). It can be concluded that field-measured Fe(III)/Fe(II) ratios provides a good indicator to determine if kinetic limitations apply in the field. The heterogeneous reaction is the rate-determing step, if Fe(III)/Fe(II) > 100. Ferrous iron oxidation limits pyrite oxidation for Fe(III)/Fe(II) ratios < 100. In this context, it should be mentioned that dissolved Fe(III)-concentrations may also be influenced by the precipitation of Fe(III)-hydroxide or hydroxy-sulfate mineral phases, which limits the applicability of the Fe(III)/Fe(II) ratio to identify the rate-determining step for sulfide mineral oxidation.

It should be pointed out that the results are only applicable to acidic conditions and may differ significantly for pyrite oxidation at circumneutral pH. Simulations in pH-buffered solutions were not possible, because well-defined rate expressions for the oxidation of pyrite are not available at the higher pH-range. It is postulated that pyrite oxidation by ferric iron becomes more dependent on the rate of ferrous iron oxidation due to the limited solubility of iron under circumneutral pH-conditions [*Moses et al.*, 1987].

Results may also differ for tailings material with a higher pyrite content, where dissolved concentrations will be higher. The activity corrections in the present model are not suitable for such extreme conditions, therefore, such a scenario was not considered here.

Precipitation of Ferric-Bearing Minerals

Simulations were conducted to determine the effect of decreasing the rate of jarosite precipitation on pyrite oxidation (Figure 6.6). The envelope conditions are provided by equilibrium conditions for jarosite and no jarosite precipitation. Figure 6.6 shows that

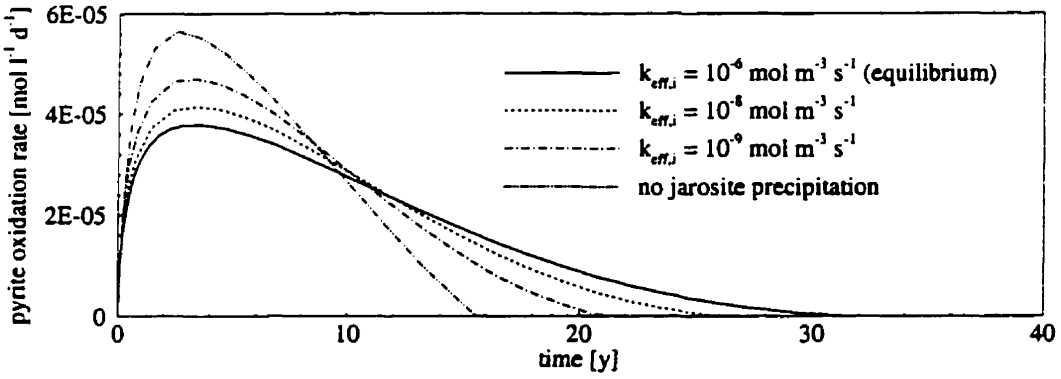

Figure 6.6: Sensitivity of pyrite oxidation rates with respect to jarosite precipitation rates

pyrite oxidation rates increase with decreasing jarosite precipitation rates. If jarosite precipitation is kinetically inhibited, higher dissolved Fe(III)-concentrations result. However, the differences are not as pronounced as might be expected. This is due to the high solubility of ferric iron under low pH-conditions. The effect would likely be more pronounced for pyrite oxidation in pH-buffered solutions, where mineral phases such as schwertmannite or ferrihydrite control the solubility of ferric iron [*Bigham et al.*, 1996]. As mentioned previously, these simulations cannot be conducted due to the lack of an appropriate rate expression for pyrite oxidation by ferric iron under circumneutral pH-conditions.

6.2.3 Reactive Transport Simulations

The numerical simulations are performed for a 1D vertical profile as shown in Figure 6.7. The profile is 4 m long and the upper 2.5 m are unsaturated. A recharge rate of 300 mm y^{-1} is applied at the top boundary and a fixed hydraulic head (h = 1.5 m) is specified at the outflow. A mixed boundary condition is used at the ground surface for reactive transport. Fixed concentrations are applied for gaseous species, while a third type boundary condition is used for dissolved species. A second type boundary condition is specified at the outflow. The physical parameters are summarized in Table 6.6 and are typical for conditions encountered in tailings impoundments [e.g. *Dubrovsky*, 1986, *Smyth*, 1981, *Blowes et al.*, 1987]. A discretization interval of 5 cm has been used in this study. Dispersion has been neglected.

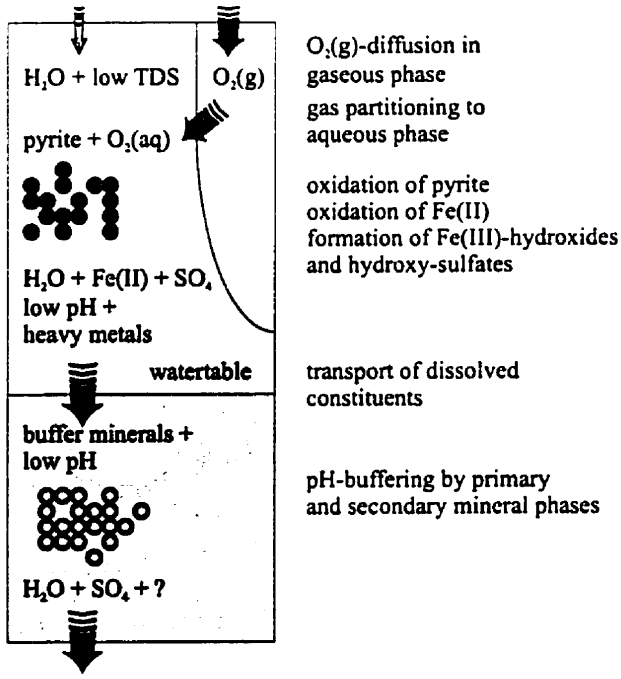

Figure 6.7: 1D-vertical profile for numerical study of acid mine drainage generation

Parameter		unit	value
length of solution domain	L	[m]	4.0
porosity	ϕ	[-]	0.5
infiltration rate	q_{in}	[m y^{-1}]	0.3
hydraulic conductivity	K_{zz}	[m s^{-1}]	$5.0 \cdot 10^{-6}$
residual saturation	S_{ra}	[-]	0.05
soil hydraulic function	α	[-]	3.5
parameters	n	[-]	1.4
longitudinal dispersivity	α_l	[m]	-
free phase diffusion coefficient in gaseous phase	D_g^*	[m^2 s^{-1}]	$2.07 \cdot 10^{-5}$
free phase diffusion coefficient in aqueous phase	D_a^*	[m^2 s^{-1}]	$2.38 \cdot 10^{-9}$

Table 6.6: Physical input parameters - reactive transport simulations

component		tailings water	recharge water	unit
(1)	Ca^{2+}	$4.17 \cdot 10^{-03}$	$1.34 \cdot 10^{-03}$	[mol l^{-1}]
(2)	K^{+}	$9.00 \cdot 10^{-03}$	$1.00 \cdot 10^{-03}$	[mol l^{-1}]
(3)	Al^{3+}	$2.59 \cdot 10^{-08}$	$1.28 \cdot 10^{-08}$	[mol l^{-1}]
(4)	CO_3^{2-}	$5.67 \cdot 10^{-03}$	$1.10 \cdot 10^{-05}$	[mol l^{-1}]
(5)	SO_4^{2-}	$6.29 \cdot 10^{-03}$	$1.85 \cdot 10^{-03}$	[mol l^{-1}]
(6)	H_4SiO_4	$1.93 \cdot 10^{-03}$	$1.99 \cdot 10^{-04}$	[mol l^{-1}]
(7)	Fe^{2+}	$4.40 \cdot 10^{-05}$	$3.24 \cdot 10^{-14}$	[mol l^{-1}]
(8)	Fe^{3+}	$2.55 \cdot 10^{-12}$	$1.89 \cdot 10^{-07}$	[mol l^{-1}]
(9)	pH	7.00	5.00	[-]
(10)	pO_2	$3.93 \cdot 10^{-66}$	$2.10 \cdot 10^{-01}$	[atm]

Table 6.7: Initial composition of tailings water and infiltrating groundwater - reactive transport simulations

Table 6.7 defines the composition of the infiltrating water and the water initially contained in the tailings material. The recharge water is in equilibrium with oxygen and carbon dioxide at atmospheric concentrations and is slightly acidic (pH = 5). This water is characterized by low total dissolved concentrations and is undersaturated with respect to all mineral phases specified in Table 6.3. The initial tailings water, on the other hand, is reducing and is characterized by a neutral pH. The tailings water is similar to the pore water composition from the Nordic Main Tailings at Elliot Lake based on data from *Smyth* [1981], modified by *Wunderly et al.* [1996]. This data was chosen because it represents the typical characteristics of process water disposed with mine waste materials. Undersaturated conditions exist with respect to ferrihydrite, jarosite and gypsum; the water is assumed to be in equilibrium with pyrite, calcite, siderite, gibbsite and amorphous silica, and supersaturated with respect to K-feldspar.

The following sensitivity analyses are based on two different tailings materials (material A: 1 vol% pyrite, 49 vol% K-feldspar; material B: 1 vol% pyrite, 25 vol% K-feldspar, 24 vol% calcite). It has been assumed that the mineral particles have a representative grain size of 50 μm. The reactive surface areas of the primary minerals were determined based on grain size as 1% of the geometric surface area assuming spherical particle geometry. The initial reactive surface area for pyrite is $S_1 = 12$ m^2 m^{-3} for both materials. The reactive surface areas for K-feldspar are $S_2 = 588$ m^2 m^{-3} for material A (no calcite) and 300 m^2 m^{-3} for material B (calcite present). An effective rate constant has been used to describe calcite dissolution, the estimation of a reactive surface area is therefore not necessary.

Applicability of Laboratory-Derived Rate Expressions for Pyrite Oxidation

A number of laboratory studies [e.g. *McKibben and Barnes*, 1986, *Moses et al.*, 1987, *Williamson and Rimstidt*, 1994] and the batch reactor simulations conducted here have shown that pyrite is primarily oxidized by ferric iron. It appears to be logical to apply rate expression 6.16 directly in reactive transport simulations to describe the generation of acid mine drainage in tailings impoundments. However, examining pyrite oxidation rates shown in Figure 6.3a indicates that it requires more than one year until the maximum rate of pyrite oxidation is reached. This is due to the autocatalytic nature of pyrite oxidation, as was discussed previously. It is instructive to compare the time required to reach the maximum oxidation rate to the characteristic time of advective transport in tailings material. This characteristic time is defined by:

$$t_{a,a} = \frac{\Delta z S_a \phi}{q_{\text{in}}}$$

The spatial discretization interval Δz was chosen as the characteristic transport length. For $\Delta z = 5$ cm, a water saturation of $S_a = 0.5$ (as was used for the batch reactor simulations), a porosity of $\phi = 0.5$ and a recharge rate of 300 mm y^{-1} yields $t_{a,a} =$ 0.04 y. For $S_a = 0.8$ (as used in the reactive transport simulations) a characteristic time of 0.07 years is obtained. A direct comparison shows that the characteristic time of advective transport is in any case much shorter than the time required for the rate of pyrite oxidation to reach its maximum value.

This result implies that applying laboratory-derived rate expressions for pyrite oxidation leads to unrealistic results in a continuum reactive transport model. Comparably rapid advective transport results in the migration of dissolved iron into deeper regions before the maximum oxidation rate is achieved. This effect was observed in preliminary simulations, where pyrite oxidation close to the ground surface was slower than pyrite oxidation at greater depth. These results are inconsistent with field observations, which usually show that the depletion of sulfide minerals is most pronounced close to the ground surface and that alteration decreases with increasing depth [e.g.: *Dubrovsky et al.*, 1984, *Blowes and Jambor*, 1990]. Laboratory-derived rate expressions for pyrite oxidation can only be employed in continuum reactive transport models, if the model accounts for the different scales. It is therefore necessary to define a separate rate expression for the simulation of reactive transport, which represents pyrite oxidation on the macro-scale.

Pyrite oxidation in reactive transport models is commonly described as an overall

reaction with oxygen as the primary reactant [e.g.: *Davis and Ritchie*, 1986, *Wunderly et al.*, 1996]. This approach may yield reasonable results in the zone of active oxidation, but will greatly overpredict the redox potential below this zone, because Fe(III)-reduction is neglected. Therefore, it is necessary to include pyrite oxidation by ferric iron. For these simulations, pyrite oxidation is described by a rate expression with a first order dependence on dissolved oxygen and a fractional dependence on ferric iron. This rate expression describes the overall reaction progress due to pyrite oxidation by oxygen and by ferric iron. The contribution due to the oxidation by ferric iron is merely used to adjust the redox potential below the zone of active oxidation:

$$R_1^{md,s} = -\max\left[\left[S_1\left[k_{11}^{md,s}\{O_2(aq)\} + k_{12}^{md,s}[Fe(III)]^{0.3}\right]\left[1 - \frac{IAP_{11}^m}{K_{11}^m}\right]\right], 0\right] \tag{6.19}$$

Using this rate expression allows the reproduction of conditions similar to those observed under field conditions. The rate constant $k_{11}^{md,s}$ was determined based on laboratory-derived reaction rates from *Williamson and Rimstidt* [1994]. These authors reported pyrite oxidation rates ranging from $10^{-10.54}$ - $10^{-8.48}$ mol m^{-2} s^{-1} for oxidation by dissolved oxygen to $10^{-7.68}$ - $10^{-6.20}$ mol m^{-2} s^{-1} for oxidation by Fe(III). A reaction rate of $10^{-6.50}$ mol m^{-2} s^{-1} and a partial oxygen pressure of 0.21 atm was used to determine the rate constant $k_{11}^{md,s}$ ($10^{-2.92}$ mol m^{-2} s^{-1}) for the overall reaction progress. The rate constant $k_{12}^{md,s}$ ($10^{-7.94}$ mol m^{-2} s^{-1}) was determined by calibration to yield a reasonable redox-potential below the zone of active oxidation while minimizing the effect on the overall oxidation rate. This rate expression does not account for the pH-dependence of pyrite oxidation and implies that the Fe^{2+}/Fe^{3+} redox couple is adequately described by the equilibrium condition. Information justifying the inclusion of pH-dependence on a macroscopic scale is not available to date.

Macroscopic Transport Control

The influence of hydraulic conductivity of the tailings material on gas phase saturations and overall pyrite oxidation rates is investigated. The simulations were conducted for tailings material A (no calcite).

Figure 6.8a presents the gas phase saturations as a function of hydraulic conductivity. Three cases have been considered ($K_1 = 5 \cdot 10^{-7}$ m s^{-1}, $K_2 = 5 \cdot 10^{-6}$ m s^{-1}, $K_3 = 5 \cdot 10^{-5}$ m s^{-1}), which fall in the range of measured hydraulic conductivities in mine tailings [e.g.:

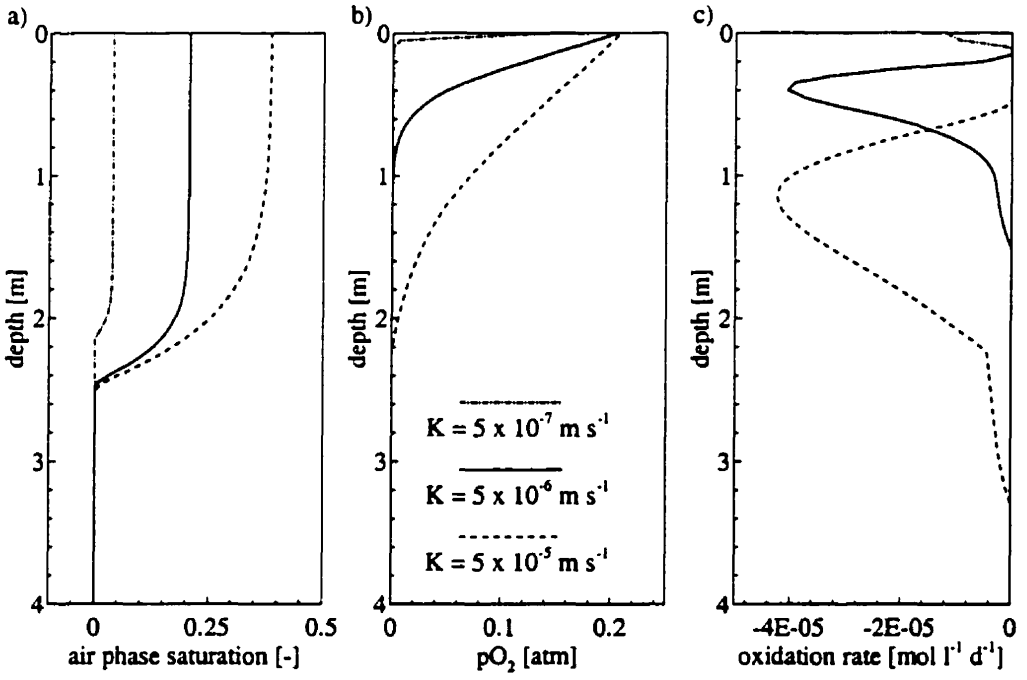

Figure 6.8: Sensitivity with respect to hydraulic conductivity, t = 20 years: a) gas phase saturation, b) partial oxygen gas pressure, c) pyrite oxidation rate

Blowes and Jambor, 1990, *Blowes et al.*, 1991]. The gas phase saturations decrease significantly with decreasing hydraulic conductivity (Figure 6.8a). This decrease has a pronounced impact on the effective diffusion coefficient for oxygen (equation 6.1). A smaller effective diffusion coefficient inhibits the transport of atmospheric oxygen into the tailings material (Figure 6.8b) and decreases the rate of pyrite oxidation (Figure 6.8c). Figure 6.9a compares the oxygen influx across the ground surface for the different cases. Oxygen fluxes for the lowest hydraulic conductivity are almost negligible (max: 2.5 mol m^{-2} y^{-1}). Higher hydraulic conductivities lead to increased oxygen influxes (a maximum of 65 and 190 mol m^{-2} y^{-1}, respectively). The calculated oxygen fluxes are in reasonable agreement with oxygen fluxes measured in the field [e.g.: *Tibble and Nicholson*, 1997].

The width of the oxidation zone increases with increasing gas phase saturation, indicating that macroscopic transport control for oxygen transport becomes less important for more permeable materials. The characteristic thickness of the zone of active oxidation in mine tailings is usually in the cm to 10's of cm range [*Blowes and Jambor*, 1990]. Such

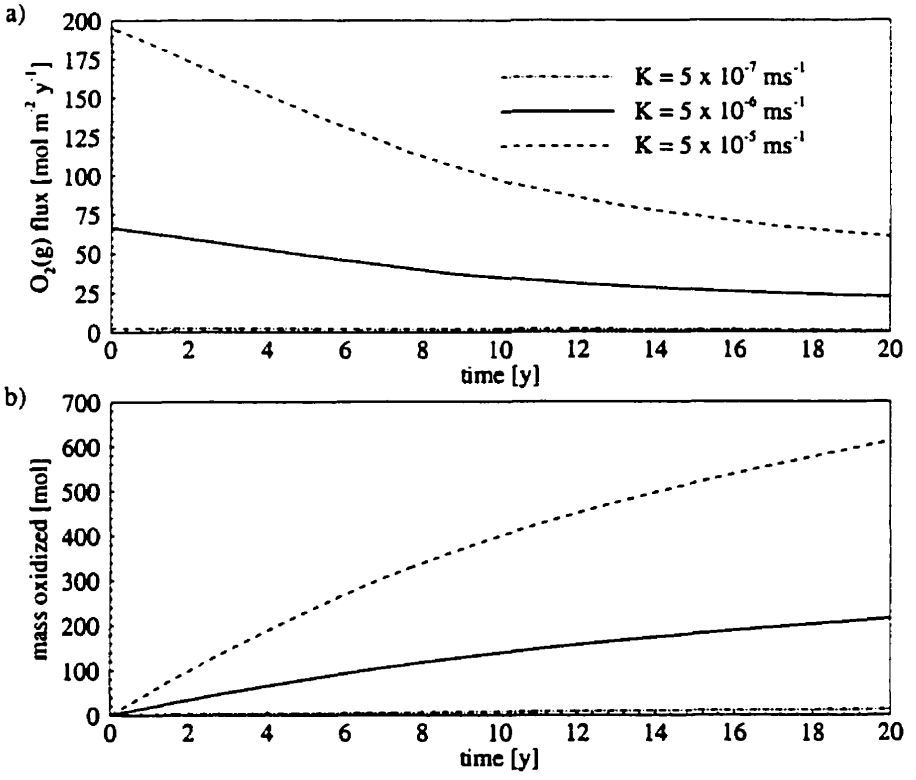

Figure 6.9: Sensitivity with respect to hydraulic conductivity: a) O_2(g) influx, b) pyrite mass oxidized

a narrow zone of active oxidation indicates that macroscopic transport control plays a significant role for controlling the progress of pyrite oxidation.

Furthermore, Figure 6.9a shows a decrease of oxygen influxes over time. This can be attributed to two factors: decreasing reactive surface areas of pyrite, and the advance of the zone of active oxidation into deeper areas of the tailings material, which increases the diffusion length and, therefore, the importance of macroscopic transport control. Figure 6.9b presents the mass of pyrite depleted over a 20 year time interval. Considering $K_2 = 5 \cdot 10^{-6}$ m s^{-1} as a benchmark shows that pyrite depletion after 20 years is 95% less for a ten-fold decrease in hydraulic conductivity and increased by 185% for a ten-fold increase in hydraulic conductivity. $K_2 = 5 \cdot 10^{-6}$ m s^{-1} is used for all the following simulations.

pH-buffering

The following analysis compares the compositional evolution of the pore water and the tailings mineralogy for materials A (no calcite) and B (calcite present). Figure 6.10a-c present the results for tailings material A (no calcite). The acidity generated by pyrite oxidation decreases pH to < 2 (Figure 6.10a) and subsequently leads to the dissolution of K-feldspar (Figure 6.10 c). The rates of pyrite oxidation are much faster than the rates of dissolution or precipitation of any other mineral phase (Figure 6.10c) and pH-buffering is insignificant. Amorphous silica and jarosite precipitate as a result of increased concentrations of H_4SiO_4, K^+, Fe^{3+} and SO_4^{2-} produced by the oxidation of pyrite and dissolution of K-feldspar. The solution remains undersaturated with respect to other potential secondary mineral phases summarized in Table 6.3. Amorphous silica redissolves as pyrite becomes depleted.

The simulation results differ significantly for material B (calcite present) (Figure 6.10d-f). The dissolution of calcite is rapid in comparison to the oxidation of pyrite and effectively buffers the pH of the pore water (Figures 6.10d and f). The oxidation of pyrite and the dissolution of calcite lead to the precipitation of the secondary minerals phases gypsum and ferrihydrite (Figure 6.10e). Significant precipitation of other potential secondary mineral phases did not occur in this simulation. The model results indicate that gypsum redissolves once pyrite becomes depleted, while ferrihydrite remains stable. The redox potential decreases in both simulations to values characteristic for reducing conditions (Figures 6.10a and d) indicating that rate expression 6.19 adequately describes the depletion of the electron acceptors O_2(aq) and ferric iron in the zone of active oxidation.

Figure 6.10e shows that secondary mineral formation is more pronounced for material B (calcite present) (compare to Figure 6.10b). This implies that the formation of surface coatings, which may inhibit the oxidation of pyrite, is more likely to occur in tailings materials containing carbonate minerals. Material B is also more susceptible to the formation of hardpan layers [*Blowes et al.*, 1991] as a result of extensive secondary mineral precipitation. Decreasing reaction rates due to the formation of surface coatings can be considered by replacing rate expression 6.19 with a rate expression which accounts for the build-up of reaction products on the reactive pyrite surface (see Chapter 3). This approach was previously used by *Jaynes et al.* [1984a], *Davis and Ritchie* [1986], *Wunderly et al.* [1996].

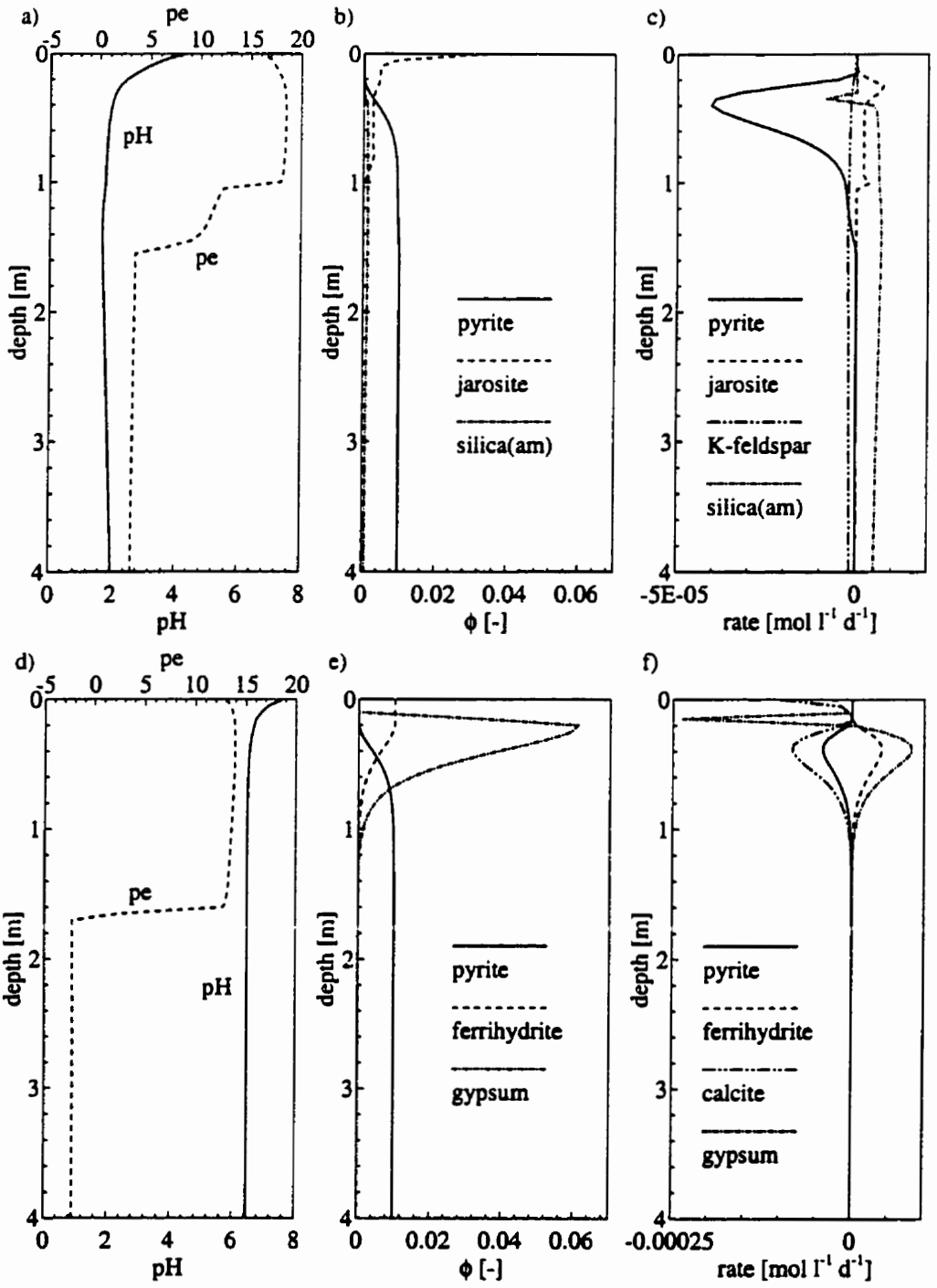

Figure 6.10: Sensitivity with respect to initial mineralogy (pH-buffering), $t = 20$ years: a)-c) material A (no calcite), d)-f) material B (calcite present)

Oxygen Mass Balance

An additional comparison is conducted for the two tailings materials to investigate the use of the ultimate electron acceptor $O_2(aq)$. Potential direct sinks for oxygen are the oxidation of pyrite and the oxidation of ferrous iron. Ferrous iron oxidation may also be coupled with the precipitation of ferric-bearing minerals such as ferrihydrite and jarosite. Overall reactions expressed in terms of the ultimate electron acceptor oxygen can be written as:

$$\begin{aligned}
FeS_2(s) + \tfrac{7}{2}O_2(aq) + H_2O &\rightarrow Fe^{2+} + 2SO_4^{2-} + 2H^+ \\
Fe^{2+} + \tfrac{1}{4}O_2(aq) + H^+ &\rightarrow Fe^{3+} + \tfrac{1}{2}H_2O \\
Fe^{2+} + \tfrac{1}{4}O_2(aq) + \tfrac{5}{2}H_2O &\rightarrow Fe(OH)_3(am) + 2H^+ \\
K^+ + 3Fe^{2+} + \tfrac{3}{4}O_2(aq) + 2SO_4^{2-} + \tfrac{9}{2}H_2O &\rightarrow KFe_3(SO_4)_2(OH)_6 + 3H^+
\end{aligned}$$

Figure 6.11a presents the mass balance for oxygen consumption for material A (no calcite) over a time period of 20 years. Pyrite oxidation consumes most of the infiltrating oxygen. Dissolved ferric iron concentrations increase at early times and provide a temporary sink for $O_2(aq)$. Throughout the simulation, jarosite precipitation has only a limited potential to immobilize ferric iron. The total amount of pyrite oxidized within the column amounts to 215 mol during the 20 year time period. A similar picture is obtained for material B (calcite present) (Figure 6.11a). The solubility of ferric iron is lower under pH-buffered conditions, and the precipitation of ferrihydrite is the only notable sink for ferric iron (dissolved oxygen) besides pyrite oxidation. Precipitation of ferrihydrite provides, due to the limited ferric iron solubility, a more pronounced sink than the precipitation of jarosite in the case of material A (no calcite). This results in a slightly decreased pyrite depletion in comparison to material A (no calcite) (205 mol within 20 years). Even in the pH-buffered case, pyrite oxidation has the potential to consume more than 90% of the infiltrating oxygen throughout the simulation.

It is also possible that secondary minerals redissolve, and thus, provide a source for dissolved ferric iron, which may enhance pyrite oxidation rates. Taking into consideration the minor influence of the precipitation of ferric-bearing mineral phases, it can be concluded that their dissolution may also only have a small impact on pyrite oxidation rates. In addition, the alteration of these minerals to sparingly soluble mineral phases such as goethite may inhibit the dissolution of these mineral phases and their potential

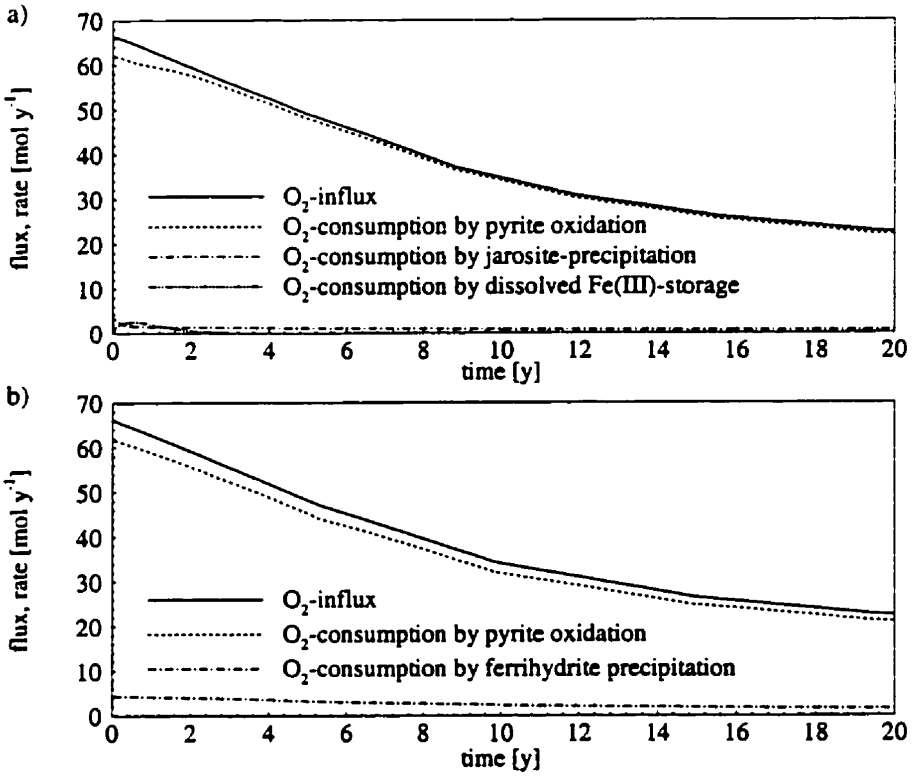

Figure 6.11: Mass balance for oxygen consumption: a) material A (no calcite), b) material B (calcite present)

to influence pyrite oxidation rates [*Bigham et al.*, 1996]. These arguments are supported by the laboratory studies conducted by *Moses et al.* [1987], which showed that the dissolution of ferric-oxyhydroxides does not have a significant influence on the oxidation of pyrite, because the dissolution rates are much slower than pyrite oxidation rates.

It was shown by *Moses et al.* [1987] that pyrite oxidation rates in pH-buffered solutions are much slower than in acidic solutions. A likely cause for this behavior is the limited solubility of ferric iron under circumneutral pH-conditions. Rate expression 6.19 does not account for the dependence of the oxidation rates on the limited solubility of ferric iron and other possible pH-effects. Therefore, the simulations for tailings materials A (no calcite) and B (calcite present) are characterized by similar pyrite oxidation rates. An adequate overall rate expression for pyrite oxidation capable of describing pyrite oxidation under circumneutral and acidic conditions is needed.

Degassing of Carbonic Acid

The contribution of carbon dioxide degassing to pH-buffering in carbonate-buffered tailings (material B, calcite present) is investigated. For this purpose a simulation was conducted, where the exsolution and subsequent diffusive transport of carbon dioxide has been neglected. These model results are compared to simulation results which include carbon dioxide degassing (base case). Figure 6.12a shows that the degassing of carbon dioxide significantly contributes to pH-buffering. If the exsolution of carbon dioxide takes place, the pore water is buffered to pH $\approx$ 6.45. If carbon dioxide degassing is neglected the pH reduces to $\approx$ 5.85. It is instructive to consider the hydrolysis reaction between carbonic acid and bicarbonate:

$$H_2CO_3^{2-} \rightleftharpoons HCO_3^- + H^+ \qquad \log K = 6.35 \tag{6.20}$$

The equilibrium constant of this reaction shows that bicarbonate remains the dominant carbonate species, if carbon dioxide degassing is considered. In this case, carbonic acid concentrations are continually lowered due to the gas exsolution process. On the other hand, the exclusion of carbon dioxide exsolution leads to pH-values for which carbonic acid is the dominant carbonate species. This result is not realistic for semi-open systems such as the unsaturated zone of a mine tailings impoundment, because calcite dissolution rates and partial CO_2-pressures are overpredicted (Figure 6.12b and c). It is anticipated that carbon dioxide degassing, similar to the infiltration of oxygen, is a function of gas saturations of the tailings material. With decreasing gas saturations, rates of gas transport decline and the tailings pile approaches a closed system behavior with respect to pCO_2.

Comparing acid-generation due to pyrite oxidation and the precipitation of secondary minerals with acid-consumption due to CO_2-degassing allows the evaluation of the relative importance of carbon dioxide exsolution as a pH-buffering process. Pyrite oxidation leads subsequently to the precipitation of ferrihydrite, due to the limited solubility of ferric iron in carbonate buffered solutions. The total acid generation due to pyrite oxidation and ferrihydrite precipitation can be calculated based on the reaction stoichiometry:

$$FeS_2 + \tfrac{15}{4}O_2(aq) + \tfrac{5}{2}H_2O \rightarrow Fe(OH)_3(s) + 2SO_4^{2-} + 4H^+ \tag{6.21}$$

The rate of acid generation is therefore equivalent to four times the pyrite oxidation rate. Degassing of carbonic acid is caused by the dissolution of calcite and can be written as

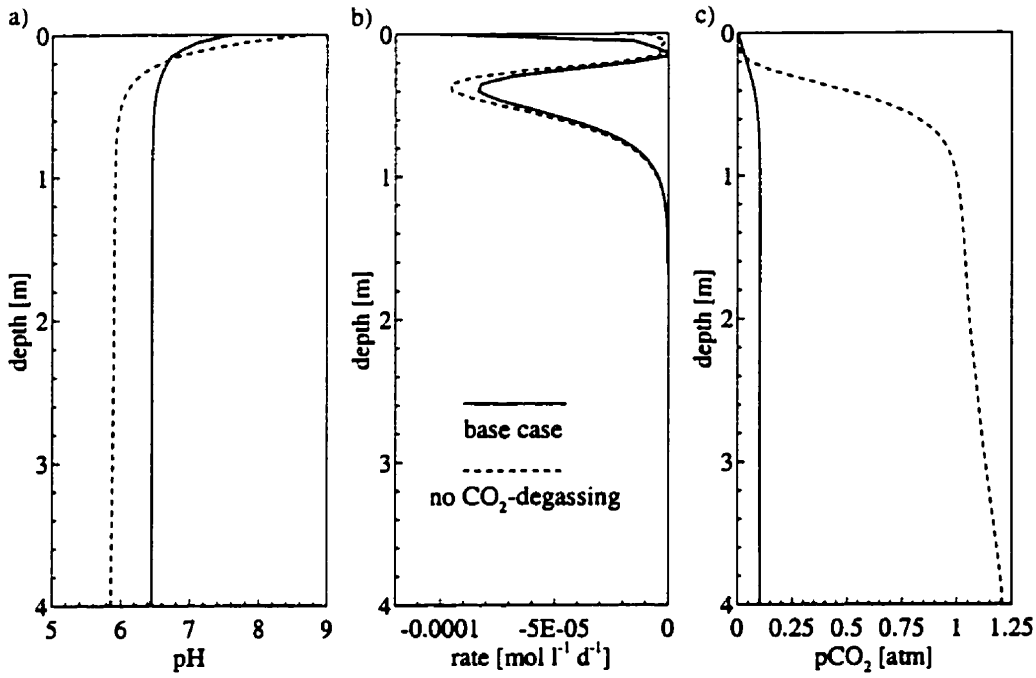

Figure 6.12: Sensitivity with respect to CO_2-degassing, t = 20 years: a) pH, b), calcite dissolution rate, c) partial CO_2-pressures

an overall reaction:

$$CaCO_3(s) + 2H^+ \rightarrow Ca^{2+} + CO_2(g) + H_2O \tag{6.22}$$

Acid consumption due to CO_2-degassing can be calculated as twice the CO_2-flux across the ground surface.

Figure 6.13 shows that CO_2-degassing plays an important role as a pH-buffering process. At early times (t = 1 year), almost 90% of the acidity generated leaves the tailings material by carbon dioxide exsolution and subsequent diffusive transport to the ground surface. This buffering mechanism loses importance, when pyrite oxidation takes place at greater depth, since the diffusion length, and thus, the resistance for CO_2-gas transport increases. After 20 years the fraction of acid-consumption due to CO_2-degassing has decreased from almost 90% to $\approx$ 78% (Figure 6.13). The remaining acidity is consumed

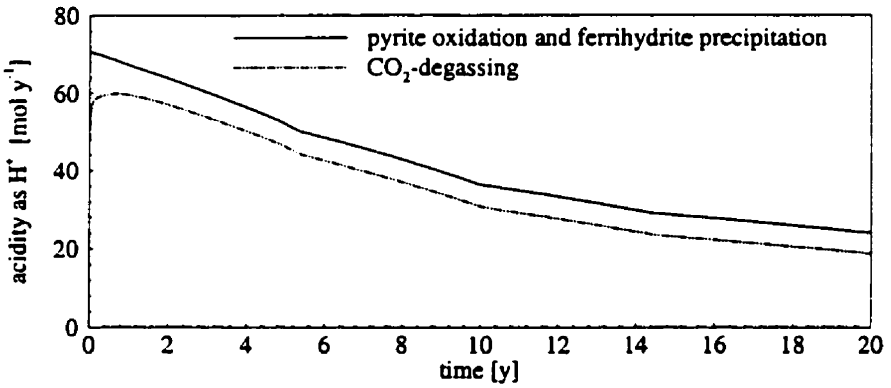

Figure 6.13: Relative importance of CO_2-degassing as an acid-consuming process

by the carbonate and non-carbonate alkalinity of the pore water and enters the saturated zone.

6.3 Conclusions

The example applications have shown that MIN3P can be used to investigate the generation and fate of acid mine drainage. A series of kinetic batch and one-dimensional reactive transport simulations were conducted. The model allows the consideration of complex reaction networks involving parallel and sequential kinetically-controlled reactions. Laboratory-derived rate expressions were used to describe the progress of pyrite oxidation in batch simulations. The simulation results are in agreement with the conceptual model proposed by *Singer and Stumm* [1970] and illustrate that the oxidation of pyrite by ferric iron is an autocatalytic process. Ferrous iron oxidation rates and the precipitation rates of jarosite were varied in a sensitivity analysis. The results can be used to visualize the limiting effect of ferrous iron oxidation and solubility on the autocatalysis of pyrite oxidation.

Reactive transport simulations can be used to illustrate how the rate of pyrite oxidation is affected by the permeability of the tailings material, which has a pronounced influence on gas saturations and therefore on the capability of $O_2(g)$ to penetrate into the tailings. These results are in agreement with previous studies [e.g: *Davis and Ritchie*,

1986]. Effects of the composition of the initial mineralogy on the final composition of the pore water and the tailings material can also be investigated.

Mass balance calculations for oxygen consumption and acid production and consumption were conducted as part of this study. The model can be used to estimate the importance of the various oxygen consuming and pH-buffering processes in tailings as a function of time. For example, the model results can be used to illustrate that pyrite oxidation consumes most of the atmospheric oxygen diffusing into the tailings material in carbonate-buffered and carbonate-free tailings materials. The mass balance for acid generation and consumption illustrates how the dissolution of carbonate minerals leads to an increase in carbonate alkalinity and to pronounced pH-buffering due to CO_2-degassing.

This study has shown that laboratory-derived rate expressions for pyrite oxidation can not be applied directly in a continuum reactive transport model. This is due to the different spatial scales of transport in the bulk porous medium (macro-scale), ferrous iron oxidation (macro-scale - micro-scale) and pyrite oxidation (meso-scale - micro-scale). It can be envisioned that a dual-porosity multicomponent-reactive transport model may be capable of incorporating the various processes at the different spatial scales.

Pyrite oxidation was described as an overall reaction in terms of dissolved oxygen for the reactive transport simulations conducted here. A parallel Fe(III)-dependent reaction rate was included to facilitate an adequate description of the redox conditions below the zone of active oxidation. This approach can be used to match field or laboratory data, and to estimate acid generation due to pyrite oxidation. However, the rate expression does not account for the pH-dependence of pyrite oxidation due to limited Fe(III)-solubility at circumneutral pH. It is also not possible to study reactive transport in conjunction with kinetic limitations due to ferrous iron oxidation. A rate expression, which is expressed in terms of dissolved oxygen, but implicitly accounts for decreasing ferric iron solubility with increasing pH, would be of advantage for the analysis of pyrite oxidation in mine tailings by reactive transport modelling.

MIN3P can be used to conduct sensitivity analysis for tailings materials of varying composition or to evaluate the performance of cover scenarios. The model can also be used in conjunction with the analysis of field data as a tool to improve the understanding of the time-dependent evolution of acid mine drainage generation and pH- and E_H-buffer reactions. The model provides a high degree of versatility and therefore facilitates the investigation of various reaction mechanisms.

Chapter 7

Reactive Transport Through a Reactive Barrier

This chapter demonstrates the applicability of MIN3P for one- and two-dimensional reactive transport simulations involving a large number of components and reactions. The treatment of contaminated groundwater by a an *in-situ* permeable reactive barrier is simulated. The modelling study is based on the conceptual model developed by *Bennett* [1997] for the barrier installation at the U.S. Coast Guard Support Center near Elizabeth City, NC. The reactive barrier was designed to treat the ambient groundwater, which is contaminated with hexavalent chromium and trichloroethylene and its degradation products. The chromium contamination originates from a plating facility located in Hangar 79 (Figure 7.1). The contaminated groundwater is moving north, and is intercepted by the reactive barrier before entering the Pasquotank River. Chromium concentrations upgradient of the reactive barrier exceed 1 mg l^{-1} and reach locally up to 5 mg l^{-1} [*Bennett*, 1997]. A larger plume containing chlorinated organic compounds is also emanating from the vicinity of Hangar 79 and is also treated by the barrier [*Bennett*, 1997]. The barrier is comprised of granular iron and remediates the groundwater by reduction of hexavalent chromium and subsequent precipitation in form of chromium containing hydroxides [*Bennett*, 1997]. Trichloroethylene and its major degradation products cis-1,2 DCE and vinyl-chloride are converted to non-toxic hydrocarbons by reductive elimination and hydrogenolyis [*Bennett*, 1997, *Blowes et al.*, 1997]. An extensive field monitoring program was initiated at the site [*Bennett*, 1997]. Multi-level sampling wells facilitate a detailed

description of the hydrogeology of the aquifer and the geochemical conditions upgradient, within and downgradient of the treatment system along three transects (Figure 7.2).

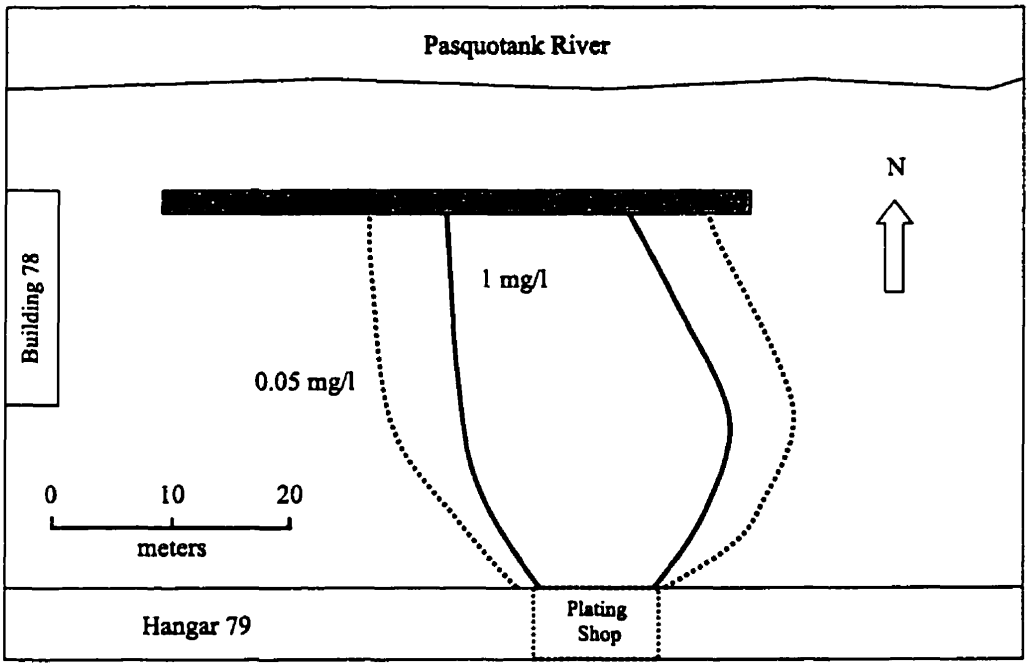

Figure 7.1: Configuration of reactive barrier and approximate location of chromium plume, from *Bennett* [1997]

In the following sections the conceptual model developed by *Bennett* [1997], which describes the controlling transport and reaction processes in the treatment system and which forms the basis for this modelling study, is presented. The reaction network for the numerical analysis is defined based on this conceptual model. One- and two-dimensional reactive transport modelling is conducted to describe the geochemical evolution of groundwater along Transect 2 (Figure 7.2, defined by the multi-level monitoring wells 21-25). Changes of the geochemical composition of the reactive mixture and the aquifer material downgradient of the barrier are also addressed. An investigation of processes potentially affecting the long-term performance of the reactive barrier is carried out. The modelling results are discussed with a focus on the expected efficiency and longevity of the treatment system. The effect of preferential flow on the quality of the treatment for the various contaminants is investigated.

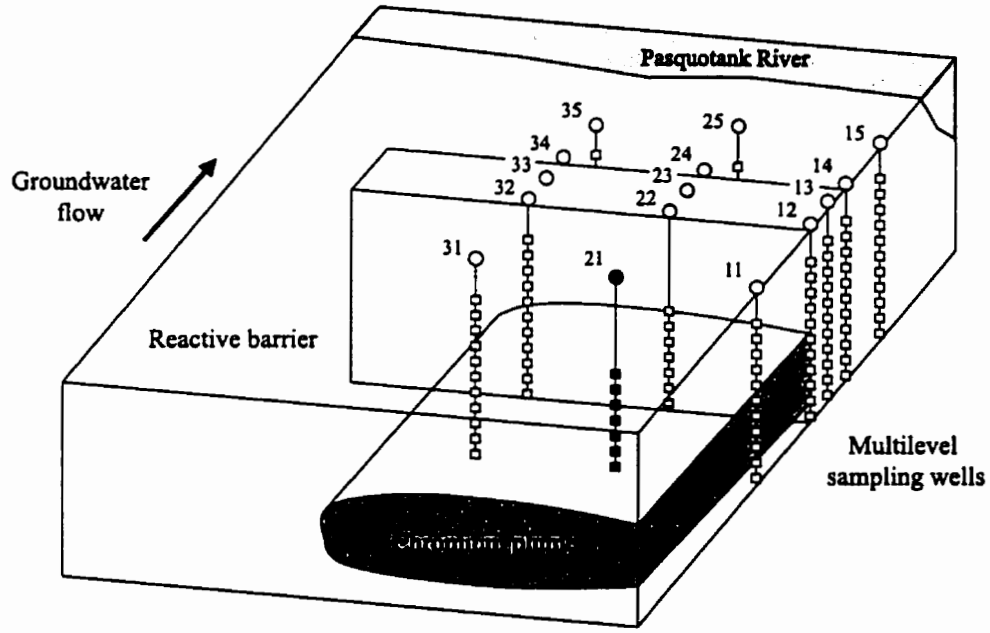

Figure 7.2: Monitoring network, from *Bennett* [1997]

7.1 Conceptual Model

The conceptual model developed by *Bennett* [1997] was subdivided into three zones: upgradient aquifer, the reactive barrier, and the aquifer downgradient of the barrier (Table 7.1). The zone located upgradient of the treatment system was termed the "contaminated zone". The contaminated groundwater in this zone has been in contact with aquifer material for a considerable amount of time, and dissolved species are either in equilibrium with the aquifer material, or reactions are kinetically limited. Dissolved species are transported more or less conservatively through this zone by advective and dispersive transport processes [*Bennett*, 1997].

The second zone is located within the reactive barrier and was termed the "treatment zone". In this zone, the contaminants are transformed by reduction and possibly immobilized by subsequent precipitation [*Bennett*, 1997]. A number of secondary reactions occur simultaneously in the treatment zone. Other oxidized species, such as dissolved oxygen, nitrate, sulfate, dissolved inorganic carbon, dissolved organic carbon and water

Contaminated Zone	Treatment Zone	Buffer Zone
Advective-dispersive transport of contaminants and other dissolved species	Removal of contaminants by reduction and precipitation Reduction of other redox active species Corrosion of zero-valent iron pH-*increase* E_H-*decrease* Precipitation of secondary minerals Exsolution of dissolved gases pH and E_H-buffering	Dissolution of clay minerals Desorption of hydrogen ions pH-*decrease* Reductive dissolution of oxides and oxy-hydroxides Exsolution of dissolved gases E_H-*increase*
upgradient	**reactive barrier**	**downgradient**

Table 7.1: Conceptual model for reactive barriers comprised of zero-valent iron, from *Bennett* [1997]

are reduced either directly by zero-valent iron or by dissolved reduced species, for example, hydrogen gas [*Bennett*, 1997]. These reduction reactions lead to the corrosion of zero-valent iron, which serves as the ultimate electron donor. Major reaction products of these corrosion reactions are ferrous or ferric iron and dissolved gases. The combined effect of the reduction and corrosion reactions leads to a significant increase of pH-values and causes the E_H of the water passing through the barrier to decrease [*Bennett*, 1997]. The high pH-conditions promote the precipitation of a number of secondary minerals throughout the treatment zone. These reactions consume alkalinity and act to buffer further increases in pH [*Bennett*, 1997]. The exsolution of dissolved gases may act to buffer the redox potential of the pore water.

The groundwater leaving the treatment zone is characterized by low dissolved species concentrations and exhibits high pH- and low E_H-conditions [*Bennett*, 1997]. However, pH and E_H are restored to near background values downgradient of the reactive barrier, indicating that reactions with the native aquifer material is buffering the infiltrating high pH, low E_H water. This zone is termed "buffer zone", since interactions with the native aquifer minerals will tend to reestablish a new equilibrium condition. Important

processes for pH-buffering may be the dissolution of aluminosilicate and clay minerals and the sorption of silicic acid combined with the release of protons [*Powell et al.*, 1995]. The desorption of hydrogen ions from oxide and clay mineral surfaces may be an additional pH-buffering process. The reductive dissolution of oxides and oxy-hydroxides and possibly degassing may be responsible for the observed E_H increase.

The conceptual model is applicable for the zones located upgradient and within any zero-valent iron reactive barrier. However, geochemical processes controlling pH and E_H-buffering downgradient of the reactive barrier depend on the site-specific mineralogy and therefore apply only to the Elizabeth City-site.

7.2 Definition of Reaction Network

This section introduces the reaction stoichiometries, rate expressions and equilibrium constants of the reactions considered in this study based on the conceptual model by *Bennett* [1997]. In general, the equilibrium constants were taken from the database of MINTEQA2 [*Allison et al.*, 1991], unless otherwise noted. All reactions considered can be expressed in terms of the following 27 components: Al^{3+}, Ca^{2+}, Cl^-, $CH_4(aq)$, CO_3^{2-}, CrO_4^{2-}, $Cr(OH)_2^+$, DOC, Fe^{2+}, Fe^{3+}, H^+, $H_2(aq)$, H_4SiO_4, HS^-, K^+, Mg^{2+}, Mn^{2+}, Na^+, NH_4^+, NO_3^-, $O_2(aq)$, SO_4^{2-}, TCE, cis-1,2 DCE, VC, ethane and H_2O.

7.2.1 Complexation Reactions

Table 7.2 lists all 79 aqueous complexes considered in this study along with the corresponding equilibrium constants reported as dissociation constants.

7.2.2 Reduction-Corrosion Reactions

The conceptual model considers the reduction of hexavalent chromium, of the chlorinated organic compounds, and of other oxidized species dissolved in the ambient groundwater. Due to its extreme reduction capacity, zero-valent iron ultimately leads to the reduction of all electron acceptors [*Bennett*, 1997] including dissolved oxygen [*MacKenzie et al.*, 1997] Mn(IV), Fe(III), nitrate [*Rahman and Agrawal*, 1997, *Cheng et al.*, 1997], sulfate, DIC, DOC [*Weathers et al.*, 1995, *Orth and Gillham*, 1996] and the solvent water itself [*Reardon*, 1995]. In the present study, it was assumed that dissolved manganese occurs

Reaction			log K_i^x
(1)	OH^-	$= H_2O - H^+$	-13.9980
(2)	$H_3SiO_4^-$	$= H_4SiO_4 - H^+$	-9.8300
(3)	$H_2SiO_4^{2-}$	$= H_4SiO_4 - 2H^+$	-23.0000
(4)	$NH_3(aq)$	$= NH_4^+ - H^+$	-9.2520
(5)	$NH_4SO_4^-$	$= NH_4^+ + SO_4^{2-}$	1.1100
(6)	$MgOH^+$	$= Mg^{2+} + H_2O - H^+$	-11.4400
(7)	$MgCO_3(aq)$	$= Mg^{2+} + CO_3^{2-}$	2.9800
(8)	$MgHCO_3^+$	$= Mg^{2+} + CO_3^{2-} + H^+$	11.4000
(9)	$MgSO_4(aq)$	$= Mg^{2+} + SO_4^{2-}$	2.3700
(10)	$CaOH^+$	$= Ca^{2+} + H_2O - H^+$	-12.7800
(11)	$CaHCO_3^+$	$= Ca^{2+} + CO_3^{2-} + H^+$	11.4400
(12)	$CaCO_3(aq)$	$= Ca^{2+} + CO_3^{2-}$	3.2200
(13)	$CaSO_4(aq)$	$= Ca^{2+} + SO_4^{2-}$	2.3090
(14)	$CaHSO_4^+$	$= Ca^{2+} + SO_4^{2-} + H^+$	3.0680
(15)	$NaCO_3^-$	$= Na^+ + CO_3^{2-}$	1.2680
(16)	$NaHCO_3(aq)$	$= Na^+ + CO_3^{2-} + H^+$	10.0800
(17)	$NaSO_4^-$	$= Na^+ + SO_4^{2-}$	0.7000
(18)	KSO_4^-	$= K^+ + SO_4^{2-}$	0.8500
(19)	$AlOH^{2+}$	$= Al^{3+} + H_2O - H^+$	-4.9900
(20)	$Al(OH)_2^+$	$= Al^{3+} + 2H_2O - 2H^+$	-10.1000
(21)	$Al(OH)_4^-$	$= Al^{3+} + 4H_2O - 4H^+$	-22.7000
(22)	$AlSO_4^+$	$= Al^{3+} + SO_4^{2-}$	3.5000
(23)	$AlHSO_4^{2+}$	$= Al^{3+} + SO_4^{2-} + H^+$	2.4480
(24)	$Al(SO4)_2^-$	$= Al^{3+} + 2SO_4^{2-}$	5.0000
(25)	$Al(OH)_3(aq)$	$= Al^{3+} + 3H_2O - 3H^+$	-16.9000
(26)	$FeOH^+$	$= Fe^{2+} + H_2O - H^+$	-9.5000
(27)	$Fe(OH)_3^-$	$= Fe^{2+} + 3H_2O - 3H^+$	-31.0000
(28)	$FeSO_4(aq)$	$= Fe^{2+} + SO_4^{2-}$	2.2500
(29)	$FeHSO_4^+$	$= Fe^{2+} + SO_4^{2-} + H^+$	3.0680
(30)	$FeHCO_3^+$	$= Fe^{2+} + CO_3^{2-} + H^+$	12.3300
(31)	$FeCO_3(aq)$	$= Fe^{2+} + O_3^{2-}$	4.3800
(32)	$Fe(OH)_2(aq)$	$= Fe^{2+} + 2H_2O - 2H^+$	-20.5700
(33)	$FeOH^{2+}$	$= Fe^{3+} + H_2O - H^+$	-2.1900

Table 7.2: Complexation reactions and equilibrium constants

Reaction			log K_i^x
(34)	$FeSO_4^+$	$\rightleftharpoons Fe^{3+} + SO_4^{2-}$	4.0400
(35)	$FeHSO_4^{2+}$	$\rightleftharpoons Fe^{3+} + SO_4^{2-} + H^+$	4.4780
(36)	$FeCl^{2+}$	$\rightleftharpoons Fe^{3+} + Cl^-$	1.4800
(37)	$FeCl^+$	$\rightleftharpoons Fe^{2+} + Cl^-$	0.1400
(38)	$FeCl_2^+$	$\rightleftharpoons Fe^{3+} + 2Cl^-$	2.1300
(39)	$FeCl_3(aq)$	$\rightleftharpoons Fe^{3+} + 3Cl^-$	1.1300
(40)	$FeOH_2^+$	$\rightleftharpoons Fe^{3+} + 2H_2O - 2H^+$	-5.6700
(41)	$Fe(OH)_3(aq)$	$\rightleftharpoons Fe^{3+} + 3H_2O - 3H^+$	-12.5600
(42)	$Fe(OH)_4^-$	$\rightleftharpoons Fe^{3+} + 4H_2O - 4H^+$	-21.6000
(43)	$Fe(SO_4)_2^-$	$\rightleftharpoons Fe^{3+} + SO_4^{2-}$	5.3800
(44)	$Fe_2(OH)_2^{4+}$	$\rightleftharpoons Fe^{3+} + 2H_2O - 2H^+$	-2.9500
(45)	$Fe_3(OH)_4^{5+}$	$\rightleftharpoons Fe^{3+} + 4H_2O - 4H^+$	-6.3000
(46)	$MnCl^+$	$\rightleftharpoons Mn^{2+} + Cl^-$	0.6070
(47)	$MnCl_2(aq)$	$\rightleftharpoons Mn^{2+} + 2Cl^-$	0.2500
(48)	$MnCl_3^-$	$\rightleftharpoons Mn^{2+} + 3Cl^-$	-.3050
(49)	$MnOH^+$	$\rightleftharpoons Mn^{2+} + H_2O - H^+$	-10.5900
(50)	$Mn(OH)_3^-$	$\rightleftharpoons Mn^{2+} + 3H_2O - 3H^+$	-34.8000
(51)	$MnCO_3(aq)$	$\rightleftharpoons Mn^{2+} + CO_3^{2-}$	4.9000
(52)	$MnSO_4(aq)$	$\rightleftharpoons Mn^{2+} + SO_4^{2-}$	2.2600
(53)	$Mn(NO_3)_2(aq)$	$\rightleftharpoons Mn^{2+} + 2NO_3^-$	0.6000
(54)	$MnHCO_3^+$	$\rightleftharpoons Mn^{2+} + CO_3^{2-} + H^+$	12.2800
(55)	HCO_3^-	$\rightleftharpoons H^+ + CO_3^{2-}$	10.3300
(56)	$H2CO_3(aq)$	$\rightleftharpoons 2H^+ + CO_3^{2-}$	16.6810
(57)	HSO_4^-	$\rightleftharpoons H^+ + SO_4^{2-}$	1.9870
(58)	$H_2S_(aq)$	$\rightleftharpoons HS^- + H^+$	6.9940
(59)	S^{2-}	$\rightleftharpoons HS^- - H^+$	-12.9180
(60)	Cr^{3+}	$\rightleftharpoons Cr(OH)_2^+ + 2H^+ - 2H_2O$	9.6200
(61)	$CrOH^{2+}$	$\rightleftharpoons Cr(OH)_2^+ + H^+ - H_2O$	5.6200
(62)	$Cr(OH)_3(aq)$	$\rightleftharpoons Cr(OH)_2^+ - H^+ + H_2O$	-7.1300
(63)	$Cr(OH)_4^-$	$\rightleftharpoons Cr(OH)_2^+ - 2H^+ + 2H_2O$	-18.1500
(64)	CrO_2^-	$\rightleftharpoons Cr(OH)_2^+ - 2H^+$	-17.7456
(65)	$CrCl^{2+}$	$\rightleftharpoons Cr(OH)_2^+ + Cl^- + 2H^+ - 2H_2O$	9.3683
(66)	$CrCl_2^+$	$\rightleftharpoons Cr(OH)_2^+ + 2Cl^- + 2H^+ - 2H_2O$	8.6580

Table 7.1: Complexation reactions and equilibrium constants - continued

Reaction			log K_i^T
(67)	$CrOHCl_2(aq)$	$\rightleftharpoons Cr(OH)_2^+ + 2Cl^- + H^+ - H_2O$	2.9627
(68)	$CrNO_3^{2+}$	$\rightleftharpoons Cr(OH)_2^+ + NO_3^- + 2H^+ - 2H_2O$	8.2094
(69)	$CrSO_4^+$	$\rightleftharpoons Cr(OH)_2^+ + SO_4^{2-} + 2H^+ - 2H_2O$	10.9654
(70)	$CrOHSO_4(aq)$	$\rightleftharpoons Cr(OH)_2^+ + SO_4^{2-} + H^+ - H_2O$	8.2754
(71)	$Cr_2(OH)_2SO_4^{2+}$	$\rightleftharpoons 2Cr(OH)_2^+ + SO_4^{2-} + 2H^+ - 2H_2O$	16.1550
(72)	$Cr_2(OH)_2(SO_4)_2(aq)$	$\rightleftharpoons 2Cr(OH)_2^+ + 2SO_4^{2-} + 2H^+ - 2H_2O$	17.9288
(73)	$HCrO4^-$	$\rightleftharpoons CrO_4^{2-} + H^+$	6.5089
(74)	$H_2CrO_4(aq)$	$\rightleftharpoons CrO_4^{2-} + 2H^+$	5.6513
(75)	$Cr_2O_7^{2-}$	$\rightleftharpoons 2CrO_4^{2-} + 2H^+ - H_2O$	14.5571
(76)	CrO_3Cl^-	$\rightleftharpoons CrO_4^{2-} + Cl^- + 2H^+ - H_2O$	7.3086
(77)	$CrO_3SO_4^{2-}$	$\rightleftharpoons CrO_4^{2-} + SO_4^{2-} + 2H^+ - H_2O$	8.9937
(78)	$NaCrO_4^-$	$\rightleftharpoons Na^+ + CrO_4^{2-}$	0.6963
(79)	$KCrO_4^-$	$\rightleftharpoons K^+ + CrO_4^{2-}$	0.7990

Table 7.1: Complexation reactions and equilibrium constants - continued

exclusively as Mn(II); the reduction of Mn(IV) was therefore neglected. Furthermore, it was assumed that ferric iron can occur as a reaction product of iron corrosion, if the half reaction for the electron acceptor considered has a higher standard potential than the half reaction for the Fe^{2+}/Fe^{3+} redox couple. For example, *Powell et al.* [1995] reported that the corrosion of zero-valent iron in the presence of oxygen produces ferric iron. Ferric iron reduction was excluded in this study.

The reaction stoichiometries of all reduction-corrosion reactions were normalized with respect to zero-valent iron. The degradation of the organic compounds by reductive elimination and hydrogenolysis was considered. It was assumed that hydrogenolysis leads to the sequential degradation of TCE (C_2HCl_3) to cis-1,2 DCE ($C_2H_2Cl_2$), VC (C_2H_3Cl), and ethane (C_2H_6) *Bennett* [1997]. Laboratory experiments [*O'Hannesin et al.*, 1995] conducted using water from the Elizabeth City site and zero-valent iron indicated that only 7% of TCE were degraded by hydrogenolysis to cis-1,2 DCE. When determining the reaction stoichiometry of TCE-degradation, it was assumed that the remaining 93% are directly degraded to ethane.

All reduction-corrosion reactions are assumed to be irreversible. The reaction rate of hexavalent chromium reduction by zero-valent iron is characterized by a square root de-

pendence on Cr(VI) and H^+ and is proportional to the reactive surface area of zero-valent iron [*Gould*, 1982]. For all other electron acceptors, except water, it was assumed that the reaction rate is first order with respect to the electron acceptor and proportional to iron surface area. Iron corrosion by water was described by a rate expression with a first order dependence on iron surface area [*Reardon*, 1995]. Since this reaction is not dependent on the concentration of the electron acceptor, it was assumed that the reaction rate approaches zero, when equilibrium conditions are approached. An equilibrium constant of log $K_{Fe^0(s)H_2O}$ = -11.78 was calculated based on data from *Reardon* [1995] and *Stumm and Morgan* [1996].

Secondary reactions between reduced reaction products (e.g.: hydrogen gas, hydrogen sulfide, methane or ammonia) and oxidized species (e.g.: hexavalent chromium, dissolved oxygen, nitrate and sulfate) may lead to inhibitive or competitive effects influencing the reaction progress of a particular reduction-corrosion reaction. For example, *Siantar et al.* [1995] observed that the presence of oxygen or nitrite affected the degradation of pesticide by zero-valent iron, indicating that inhibition or competition may play a role. Inhibitive or competitive effects are neglected here and reduction-corrosion reactions are assumed to occur as parallel reactions.

Table 7.3 summarizes the reaction stoichiometries of the reduction-corrosion reactions considered. The total iron corrosion rate can be estimated as the sum of all reduction-corrosion rates.

7.2.3 Formation of Secondary Minerals in Treatment Zone

The conceptual model also accounts for the precipitation of secondary minerals within the treatment system. The reaction stoichiometries of the reduction-corrosion reactions in Table 7.3 imply a net pH-increase creating conditions favorable for the precipitation of carbonate minerals and hydroxide mineral phases [*Bennett*, 1997]. In addition supersaturated conditions were observed locally with respect to iron sulfide minerals [*Bennett*, 1997].

The precipitation of secondary mineral phases A_i^m is described by rate expressions based on transition state theory [*Lasaga*, 1998]:

$$R_i^m = -k_{eff,i}\left(1 - \frac{IAP_i^m}{K_i^m}\right) \tag{7.1}$$

Oxidant	Reaction
Cr(VI)	$Fe^0(s) + CrO_4^{2-} + 6H^+ \rightarrow Fe^{3+} + Cr(OH)_2^+ + 2H_2O$
TCE	$Fe^0(s) + 0.3025\ C_2HCl_3 + 1.2325H^+ \rightarrow$
	$Fe^{2+} + 0.07\ C_2H_2Cl_2 + 0.2325\ C_2H_6 + 0.7675\ Cl^-$
cis-1,2 DCE	$Fe^0(s) + C_2H_2Cl_2 + H^+ \rightarrow Fe^{2+} + C_2H_3Cl + Cl^-$
VC	$Fe^0(s) + \frac{1}{2}C_2H_3Cl + \frac{3}{2}H^+ \rightarrow Fe^{2+} + \frac{1}{2}C_2H_6 + \frac{1}{2}Cl^-$
oxygen	$Fe^0(s) + \frac{1}{4}O_2(aq) + 3H^+ \rightarrow Fe^{3+} + \frac{1}{2}H_2O + H_2(aq)$
nitrate	$Fe^0(s) + \frac{3}{8}NO_3^- + \frac{15}{4}H^+ \rightarrow Fe^{3+} + \frac{3}{8}NH_4^+ + \frac{9}{8}H_2O$
sulfate	$Fe^0(s) + \frac{1}{4}SO_4^{2-} + \frac{9}{4}H^+ \rightarrow Fe^{2+} + \frac{1}{4}HS^- + H_2O$
DOC	$Fe^0(s) + \frac{1}{2}CH_2O + 2H^+ \rightarrow Fe^{2+} + \frac{1}{2}CH_4(aq) + \frac{1}{2}H_2O$
DIC	$Fe^0(s) + \frac{1}{4}CO_3^{2-} + \frac{5}{2}H^+ \rightarrow Fe^{2+} + \frac{1}{4}CH_4(aq) + \frac{3}{4}H_2O$
water	$Fe^0(s) + 2H^+ \rightarrow Fe^{2+} + H_2(aq)$

Table 7.3: Reaction stoichiometries of reduction-corrosion reactions

where $k_{eff,i}$ is an effective rate constant for the dissolution of the mineral phase A_i^m, IAP_i^m is the ion activity product and K_i^m defines the corresponding equilibrium constant. Reactions describing the formation of secondary mineral phases within the treatment zone are summarized in Table 7.4. The equilibrium constant for $Fe(OH)_2(am)$ was taken from the database of EQ3/EQ6 [*Wolery et al.*, 1990].

Reaction		log K
$Fe(OH)_2(am)$	$\rightleftharpoons Fe^{2+} + 2H_2O - 2H^+$	-13.9045
$Fe(OH)_3(am)$	$\rightleftharpoons Fe^{3+} + 3H_2O - 3H^+$	-4.8910
$Cr(OH)_3(am)$	$\rightleftharpoons Cr^{3+} + 3H_2O - 3H^+$	0.7500
$CaCO_3(s)$	$\rightleftharpoons Ca^{2+} + CO_3^{2-}$	8.4750
$CaMg(CO_3)_2(s)$	$\rightleftharpoons Ca^{2+} + Mg^{2+} + 2CO_3^{2-}$	17.0900
$FeCO_3(s)$	$\rightleftharpoons Fe^{2+} + CO_3^{2-}$	10.4500
$MnCO_3(s)$	$\rightleftharpoons Mn^{2+} + CO_3^{2-}$	10.4100
FeS(am)	$\rightleftharpoons Fe^{2+} + HS^- - H^+$	4.6480

Table 7.4: Secondary minerals in reactive barrier and corresponding equilibrium constants

7.2.4 pH- and E_H-buffering Down-Gradient of Barrier

pH-buffering The water exiting the reactive barrier is characterized by alkaline conditions with pH-values ranging from 9 to 11 [*Bennett*, 1997]. This strongly alkaline pore water is likely to interact with the native aquifer material downgradient of the barrier. According to *Puls et al.* [1992], the mineralogy of the aquifer consists primarily of aluminosilicate minerals. The primary minerals present in the aquifer sediments are quartz > albite > sanidine > muscovite and kaolinite [*Puls et al.*, 1992]. *Powell et al.* [1995] reported that the aquifer material from the Elizabeth-City site is capable of buffering the pH towards neutral conditions by the dissolution of aluminosilicate and clay minerals. An additional source of acidity may be the sorption of silicic acid, originating from Si-mineral dissolution, onto iron-oxide/hydroxide surfaces combined with the release of hydrogen ions [*Powell et al.*, 1995].

In preliminary simulations, it was assumed that pH-buffering is due to the dissolution of kaolinite. The pH-dependent rate expression given by *Carroll and Walther* [1990] was used. The field-observed pH-buffering could only be reproduced by disallowing the precipitation of gibbsite and by setting the reactive surface area for kaolinite to values of 10^7 m^2 mineral surface per m^{-3} bulk porous medium. The field data of *Bennett* [1997] is characterized by low dissolved Al-concentrations downgradient of the barrier indicating that aluminosilicate dissolution is not as pronounced or that gibbsite precipitation occurs. The effect of sorption of silicic acid and subsequent release of protons was not investigated here. However, a similar kaolinite reactive surface area would be necessary to reproduce the observed pH-buffering, because sorbing silica is originating from the dissolution of the aluminosilicates. It is likely that other processes also contribute to pH-buffering. Another possible explanation for the observed pH-buffering is the desorption of hydrogen ions from oxide and clay mineral surfaces, which have been in contact with the slightly acidic ambient groundwater prior to installation of the reactive barrier. The desorption of hydrogen ions can be described as [*Stumm and Morgan*, 1996]:

$$S - OH_2^+ + OH^- \rightleftharpoons S - OH + H_2O \tag{7.2}$$

$$S - OH + OH^- \rightleftharpoons S - O^- + H_2O \tag{7.3}$$

A surface complexation model can be used to describe this pH-buffering process. However, such a model is presently not included in MIN3P. This process is therefore approximated as a release of hydrogen ions from a limited reservoir, until the pH reaches circumneutral values.

E_H-buffering The treated pore water exiting from the reactive barrier is extremely reducing due to the presence of reduced gaseous species such as dissolved hydrogen gas, H_2S(aq), ammonia and methane. *Bennett* [1997] observed E_H-values locally lower than -500 mV. Reduced gaseous species may either degas or react with Mn- and Fe-oxides and oxy-hydroxides contained in the aquifer material. Secondary iron oxy-hydroxides are abundant in the native aquifer mineral, while manganese oxides occur at lower concentrations [Puls, personal communication, 1998]. Degassing was observed at the Elizabeth City-site within the reactive barrier, but may not be an important process downgradient of the treatment system. *Appelo and Postma* [1993] and *Stumm and Morgan* [1996] give redox half reactions for the oxidation of the relevant dissolved gas species and the reduction of Mn- and Fe-mineral phases, which can be combined to describe E_H-buffer reactions possibly occurring downgradient of a reactive barrier. The field data of *Bennett* [1997] does not indicate the oxidation of H_2S(aq) and methane, since sulfate concentrations at the monitoring well located 1 m downgradient of the barrier are negligible, and methane concentrations remain high. Data for ammonia was not available. These data indicate that these reactions are not taking place. E_H-buffering reactions involving the consumption of H_2S(aq), ammonia and methane are therefore neglected. However, Fe- and Mn-oxides may undergo reductive dissolution when in contact with dissolved hydrogen gas emanating from the barrier. Assuming that iron and manganese oxides can be represented by goethite and pyrolusite, overall reactions for the oxidation of dissolved hydrogen gas combined with the reductive dissolution of the mineral phases can be written as:

$$\mathrm{FeOOH(s)} + 2\mathrm{H^+} + \tfrac{1}{2}\mathrm{H_2(aq)} \rightleftharpoons \mathrm{Fe^{2+}} + 2\mathrm{H_2O} \tag{7.4}$$

$$\mathrm{MnO_2(s)} + 2\mathrm{H^+} + \mathrm{H_2(aq)} \rightleftharpoons \mathrm{Mn^{2+}} + 2\mathrm{H_2O} \tag{7.5}$$

The equilibrium constant for the reductive dissolution of pyrolusite combined with the oxidation of H_2(aq) (log K = -43.9640) was calculated based on redox half reactions as reported by *Stumm and Morgan* [1996]. The appropriate equilibrium constant for goethite (log K = -13.5940) was obtained from equilibrium constants in the MINTEQA2-database [*Allison et al.*, 1991] and from *Stumm and Morgan* [1996]. These reactions are described by a transition state theory rate expression of the form [*Lasaga*, 1998]:

$$R_i^m = -S_i k_i \left(1 - \frac{IAP_i^m}{K_i^m}\right), \tag{7.6}$$

which includes reactive surface area and permits updating the mineral reactivity with progressing dissolution.

The reductive dissolution of iron and manganese oxides according to equations 7.4 and 7.5 consumes acidity. This additional pH-increase may enhance the depletion of the pH-buffer capacity of the aquifer. The reductive dissolution of oxides and oxy-hydroxides will also lead to an increase in dissolved ferrous iron and manganese concentrations. It is possible that these concentration increases will be controlled by the precipitation of siderite and rhodochrosite, respectively. Hydroxides such as $Fe(OH)_2(am)$ and amorphous pyrocroite ($Mn(OH)_2(am)$) precipitate only in alkaline waters, and are therefore incapable of controlling dissolved iron and manganese concentrations downgradient of the barrier.

7.3 Solution Domain and Model Parameters

One-dimensional and two-dimensional reactive transport analyses were conducted. The two-dimensional solution domain is a vertical cross section through the center of the reactive barrier as illustrated in Figure 7.3 and is aligned along Transect 2 (Figure 7.2).

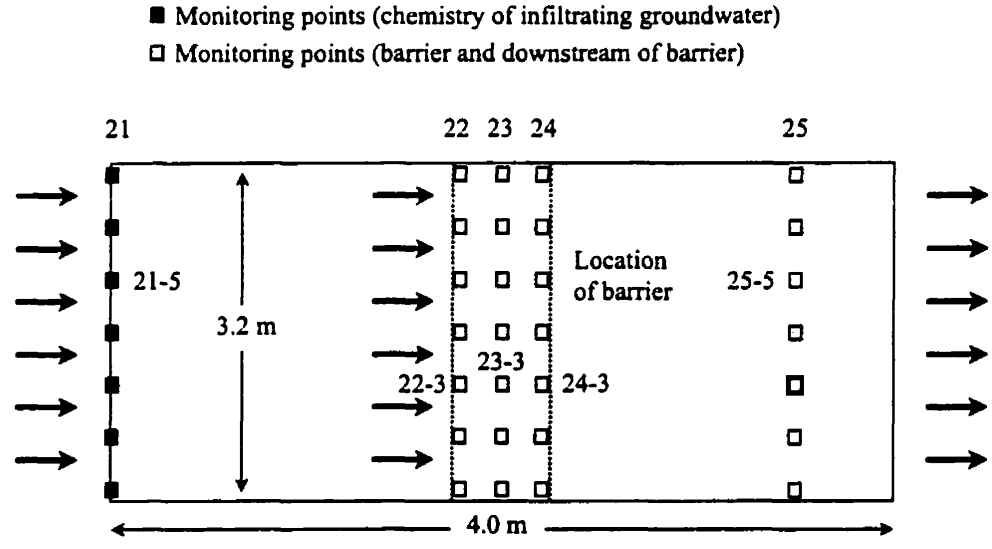

Figure 7.3: Solution domain and including location of barrier and monitoring points along Transect 2

The solution domain extends 4 m in the horizontal direction and 3.2 m in the vertical direction and groundwater flow takes place from the left to the right. The domain contains the multi-level monitoring wells 21-25, which have been installed upgradient, within and downgradient of the reactive barrier (Figure 7.2, Figure 7.3), [*Bennett*, 1997]. Each well contains 7 monitoring points providing a detailed description of the geochemical composition of the groundwater entering the solution domain. The approximate location of the 0.5 m thick reactive barrier is indicated by the dashed vertical lines. One-dimensional simulations were carried out along the flowline carrying the highest chromium concentrations towards the barrier. The field data indicates that this flowline follows a zone of preferential flow and passes through monitoring points 21-5, 22-3, 23-3, 24-3 and 25-5 [*Bennett*, 1997], as indicated in Figure 7.3.

7.3.1 Spatial Discretization

The discretized solution domain for the two-dimensional simulation is shown in Figure 7.4.

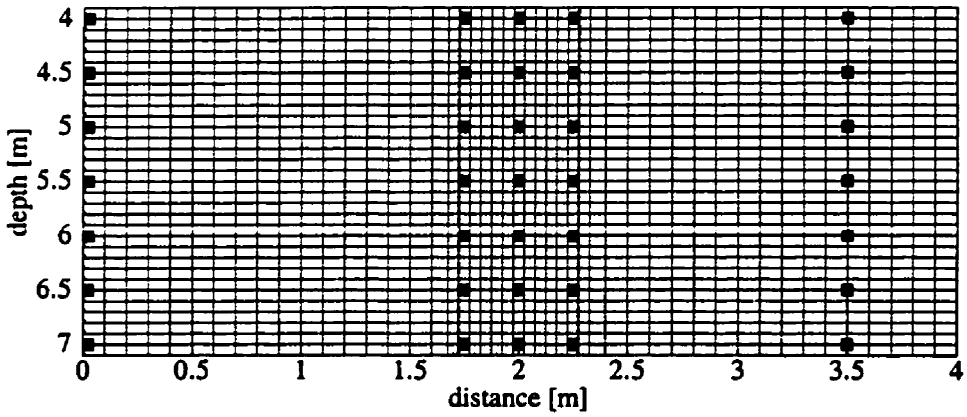

Figure 7.4: Spatial discretization of two-dimensional solution domain

A discretization interval of 10 cm in both vertical and horizontal directions was used. The discretization has been refined to 5 cm in the horizontal direction within and in the direct vicinity of the reactive barrier to facilitate a more accurate representation of rapid geochemical changes within and downgradient of the treatment system. This

discretization leads to 48 grid points in horizontal direction and 33 grid points in the vertical direction (Figure 7.4). For the one-dimensional simulations, a discretization interval of 2.5 cm was used within and in the vicinity of the treatment zone leading to a total number of 62 grid points.

7.3.2 Physical Parameters and Hydraulic Conductivity Distribution

Field measurements indicated a hydraulic gradient varying between 0.0011 and 0.0033 during the sampling intervals [*Bennett*, 1997]. For the modelling study it was assumed that a hydraulic gradient of 0.0022 can be used to represent average flow conditions. The hydraulic head loss along the vertical cross section is negligible and recharge is insignificant, because the ground surface is paved above the treatment system [*Bennett*, 1997]. The flow system is modelled as a fully saturated system with no flow boundaries at the top and the bottom of the domain and first type boundaries at the upgradient and downgradient boundaries. The upper portion of the aquifer was found to be less hydraulically conductive than the underlying layers [*Bennett*, 1997]. The field observations of *Puls et al.* [1995] and *Bennett* [1997] indicate the presence of a highly conductive layer, which is located roughly 4.5 - 6.5 m below ground surface. Significant hydraulic conductivity variations lead to large differences of groundwater flow velocties with depth [*Bennett*, 1997]. The results of slug tests showed hydraulic conductivity values ranging from $1.2 \cdot 10^{-5}$ to $1.9 \cdot 10^{-4}$ m s^{-1} within the aquifer and ranged from to $1.2 \cdot 10^{-7}$ to $2.3 \cdot 10^{-3}$ m s^{-1} within and in the vicinity of the reactive barrier [*Bennett*, 1997]. Hydraulic conductivities have been assigned to the two-dimensional solution domain based on the slug test results and the modelling analysis conducted by *Bennett* [1997] (Figure 7.5 and Table 7.5). Locally isotropic conditions were assumed in this context.

parameter	unit	
hydraulic conductivity (1-D)	[m s^{-1}]	$8.1 \cdot 10^{-5} - 1.2 \cdot 10^{-3}$
hydraulic conductivity (2-D)	[m s^{-1}]	$1.2 \cdot 10^{-6} - 1.2 \cdot 10^{-3}$
hydraulic gradient (average)	[-]	$2.2 \cdot 10^{-3}$
porosity (aquifer)	[-]	0.38
porosity (reactive barrier)	[-]	0.5

Table 7.5: Physical parameters for aquifer and reactive barrier material, from *Bennett, 1997*

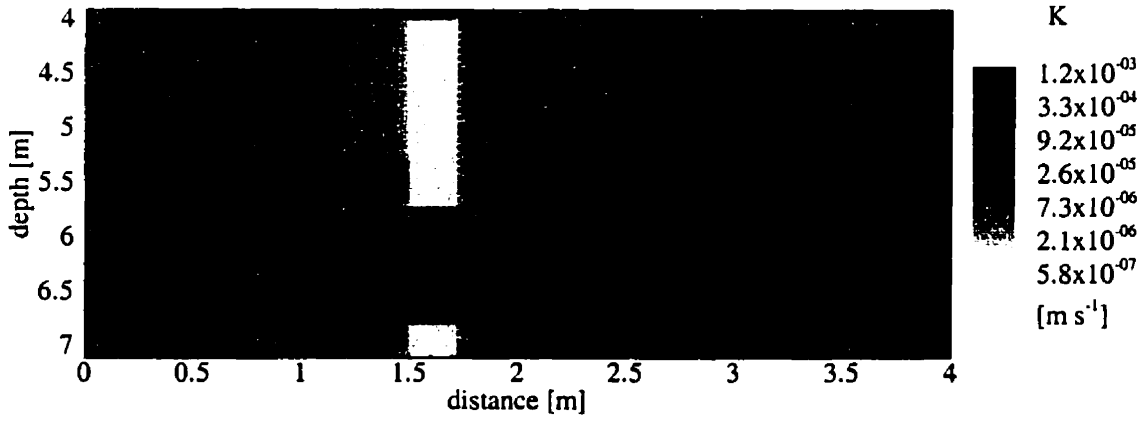

Figure 7.5: Hydraulic conductivity distribution in two-dimensional solution domain, modified from *Bennett* [1997]

For the one-dimensional simulations the hydraulic conductivity in the aquifer was estimated to be K = $8.1 \cdot 10^{-5}$ m s^{-1}, while a hydraulic conductivity of K = $1.2 \cdot 10^{-3}$ m s^{-1} was assigned to the treatment zone. High hydraulic conductivities in the reactive barrier can be explained by a relatively loose packing of the treatment material as a result of the installation procedure [*Bennett*, 1997]. *Bennett* [1997] estimated a porosity within the reactive barrier of approximately 0.43-0.62. It was assumed that the porosity of the barrier is $\phi = 0.5$ within the high hydraulic conductivity zones. A porosity of $\phi = 0.38$ was assumed to be representative for the aquifer and the low hydraulic conductivity zones in the barrier. Dispersive and diffusive transport processes were neglected, since the problem can be characterized as advection-reaction dominated. This simplification eliminates adverse effects of artificial dispersion at the upgradient side of the reactive barrier on the simulation results.

7.3.3 Mineralogical Parameters

The volume fraction for zero-valent iron is $\varphi_{Fe^0(s)} = 0.5$ and $\varphi_{Fe^0(s)} = 0.62$ for porosities of $\phi = 0.5$ and $\phi = 0.38$, respectively. Only qualitative information is available regarding the volume fractions of the minerals contained in the aquifer [*Puls et al.*, 1992]. The bulk of the aquifer material was assumed to be non-reactive. The dissolution of kaolinite

	Mineral	volume fraction	Reference
Reactive barrier	Fe^0(s)	0.5 - 0.62	*Bennett* [1997]
Aquifer	goethite	$1.0 \cdot 10^{-3}$	estimated
	pyrolusite	$1.0 \cdot 10^{-3}$	estimated
	non-reactive	0.698	estimated

Table 7.6: Initial mineral volume fractions in reactive barrier and aquifer

and other aluminosilicate minerals was excluded, because the preliminary simulations showed that these reactions are not likely to be important for controlling pH and the geochemical composition of the pore water. Considered are pyrolusite and goethite which are important for E_H-buffer reactions downgradient of the reactive barrier. The volume fractions of these minerals have been estimated to allow at least a generic description of the specified buffer reactions. The mineral volume fractions are summarized in Table 7.6. There is also no information available regarding the degree of surface protonation in the sediment prior to installation of the reactive barrier. It was assumed that 50 mol H^+ per m^3 bulk porous medium are available for desorption when in contact with the infiltrating high pH-waters.

The largest uncertainty with respect to determining reaction rates can be attributed to reactive surface area estimates. Reactive surface areas for the treatment material used at the field site are presented in Table 7.7 based on data reported by *Bennett* [1997]. It is apparent that the specific reactive surface area (BET-measurement) is more than 500 times larger than the geometric surface area calculated based on the average grain size d_{50}. Differences between geometric and reactive surface areas may be explained by the large intragranular porosity of zero-valent iron. The density of the treatment material can be calculated based on the bulk density from laboratory studies and is $\gamma = 4.77$ g cm^{-3}, which is much lower than average literature values for native iron (γ = 7.3-7.9 g cm^{-3}, *Klein and Hurlbut Jr.*, 1993). This deviation indicates that the treatment material is characterized by a pronounced secondary porosity.

The reactive surface areas of goethite and pyrolusite were estimated, since no site-specific information was available and are summarized in Table 7.8. All other minerals considered in this study are secondary minerals and effective rate constants were used, which implicitly include reactive surface areas. The reactive surface areas of zero-valent iron, goethite and pyrolusite are updated, as the minerals become depleted.

surface area [m^2 mineral m^{-3} mineral]	
geometric surface area (calculated from d_{50} = 0.4 mm)	$7.50 \cdot 10^3$
specific reactive surface area (calculated from laboratory experiment, based on BET-measurement)	$3.88 \cdot 10^6$

Table 7.7: Reactive surface area estimates for zero valent-iron (field installation)

mineral	reactive surface area
goethite	$1.0 \cdot 10^2$
pyrolusite	$1.0 \cdot 10^2$

Table 7.8: Reactive surface area estimates [m^2 mineral m^{-3} bulk] for E_H buffer minerals

7.3.4 Boundary and Initial Chemical Composition of Groundwater

Geochemical data from *Bennett* [1997] was used to define the boundary and initial condition in the solution domain. The chemical composition of water samples from monitoring well 21, which is located upgradient of the reactive barrier (see Figures 7.2 and 7.3), was analyzed on temporal variability. It was found that the general geochemical composition of the groundwater remained constant over time. The data from November 1996 was used to describe the source concentrations upgradient of the treatment system.

pH and E_H were taken from field measurements. The E_H was slightly increased for the sampling points 21-3, 21-5 and 21-7 to allow the determination of ammonia from nitrate based on the assumption of equilibrium for the NO_3^-/NH_4^+ redox couple. Total dissolved carbonate concentrations were obtained from field measured alkalinity [*Bennett*, 1997] using MINTEQA2 [*Allison et al.*, 1991]. Field measured total concentrations were used for Ca^{2+}, Cl^-, K^+, H_4SiO_4, Mg^{2+}, Mn^{2+}, Na^+, NO_3^-, O_2(aq) and SO_4^{2-} [*Bennett*, 1997]. The data for dissolved oxygen was not available for November 1996 and data from June 1997 was used instead. Field measured concentrations from *Bennett* [1997] were also used for the chlorinated organic compounds TCE, cis-1,2 DCE, VC, ethane and methane. The field data for total dissolved organic carbon, expressed in terms of CH_2O [*Bennett*, 1997], was corrected for the chlorinated organic compounds, which are considered separately. Dissolved hydrogen gas concentrations were calculated based on pH and

		21-1	21-2	21-3	21-4
depth	[m]	7.0	6.5	6.0	5.5
pH	[-]	7.36	7.84	7.97	6.40
E_H	[mV]	377	441	356	437
CO_3^{2-}	[mol l^{-1}]	$1.13 \cdot 10^{-03}$	$1.23 \cdot 10^{-03}$	$1.22 \cdot 10^{-03}$	$1.85 \cdot 10^{-03}$
Cl^-	[mol l^{-1}]	$4.23 \cdot 10^{-04}$	$5.87 \cdot 10^{-04}$	$8.44 \cdot 10^{-04}$	$2.33 \cdot 10^{-03}$
SO_4^{2-}	[mol l^{-1}]	$1.91 \cdot 10^{-04}$	$3.28 \cdot 10^{-04}$	$5.30 \cdot 10^{-04}$	$9.38 \cdot 10^{-04}$
HS^-	[mol l^{-1}]	$5.54 \cdot 10^{-88}$	$8.00 \cdot 10^{-100}$	$3.80 \cdot 10^{-90}$	$2.52 \cdot 10^{-86}$
NO_3^-	[mol l^{-1}]	$1.18 \cdot 10^{-05}$	$1.16 \cdot 10^{-05}$	$1.08 \cdot 10^{-05}$	$4.61 \cdot 10^{-05}$
NH_4^+	[mol l^{-1}]	$3.72 \cdot 10^{-11}$	$1.32 \cdot 10^{-24}$	$2.72 \cdot 10^{-14}$	$4.44 \cdot 10^{-09}$
Na^+	[mol l^{-1}]	$8.96 \cdot 10^{-04}$	$1.54 \cdot 10^{-03}$	$2.19 \cdot 10^{-03}$	$3.64 \cdot 10^{-03}$
K^+	[mol l^{-1}]	$2.05 \cdot 10^{-05}$	$4.35 \cdot 10^{-05}$	$2.05 \cdot 10^{-05}$	$4.86 \cdot 10^{-05}$
Ca^{2+}	[mol l^{-1}]	$2.77 \cdot 10^{-04}$	$2.22 \cdot 10^{-04}$	$1.96 \cdot 10^{-04}$	$3.92 \cdot 10^{-04}$
Mg^{2+}	[mol l^{-1}]	$2.69 \cdot 10^{-04}$	$2.06 \cdot 10^{-04}$	$1.81 \cdot 10^{-04}$	$4.20 \cdot 10^{-04}$
Fe^{2+}	[mol l^{-1}]	$1.69 \cdot 10^{-15}$	$5.56 \cdot 10^{-18}$	$6.84 \cdot 10^{-17}$	$1.42 \cdot 10^{-13}$
Fe^{3+}	[mol l^{-1}]	$1.20 \cdot 10^{-12}$	$1.03 \cdot 10^{-12}$	$1.03 \cdot 10^{-12}$	$3.81 \cdot 10^{-12}$
CrO_4^{2-}	[mol l^{-1}]	$5.78 \cdot 10^{-08}$	$1.93 \cdot 10^{-05}$	$3.71 \cdot 10^{-05}$	$4.75 \cdot 10^{-05}$
$Cr(OH)_2^+$	[mol l^{-1}]	$2.16 \cdot 10^{-08}$	$1.60 \cdot 10^{-08}$	$1.53 \cdot 10^{-08}$	$1.11 \cdot 10^{-07}$
Mn^{2+}	[mol l^{-1}]	$1.77 \cdot 10^{-06}$	$1.57 \cdot 10^{-06}$	$2.04 \cdot 10^{-06}$	$5.97 \cdot 10^{-06}$
Al^{3+}	[mol l^{-1}]	$3.88 \cdot 10^{-08}$	$1.15 \cdot 10^{-07}$	$1.55 \cdot 10^{-07}$	$8.07 \cdot 10^{-09}$
H_4SiO_4	[mol l^{-1}]	$9.43 \cdot 10^{-06}$	$9.50 \cdot 10^{-06}$	$9.54 \cdot 10^{-06}$	$9.40 \cdot 10^{-06}$
O_2(aq)	[mol l^{-1}]	$9.13 \cdot 10^{-05}$	$3.72 \cdot 10^{-05}$	$6.25 \cdot 10^{-06}$	$1.56 \cdot 10^{-05}$
H_2(aq)	[mol l^{-1}]	$2.57 \cdot 10^{-31}$	$1.93 \cdot 10^{-34}$	$8.63 \cdot 10^{-32}$	$2.00 \cdot 10^{-31}$
TCE	[mol l^{-1}]	$2.04 \cdot 10^{-05}$	$3.27 \cdot 10^{-06}$	$2.82 \cdot 10^{-07}$	$2.59 \cdot 10^{-07}$
cis-1,2 DCE	[mol l^{-1}]	$5.16 \cdot 10^{-09}$	$5.16 \cdot 10^{-09}$	$5.16 \cdot 10^{-09}$	$9.29 \cdot 10^{-09}$
VC	[mol l^{-1}]	$8.00 \cdot 10^{-09}$	$8.00 \cdot 10^{-09}$	$8.00 \cdot 10^{-09}$	$8.00 \cdot 10^{-09}$
ethane	[mol l^{-1}]	$1.66 \cdot 10^{-07}$	$1.66 \cdot 10^{-07}$	$1.66 \cdot 10^{-07}$	$1.66 \cdot 10^{-07}$
CH_2O	[mol l^{-1}]	$1.37 \cdot 10^{-04}$	$6.99 \cdot 10^{-06}$	$4.84 \cdot 10^{-05}$	$3.55 \cdot 10^{-05}$
CH_4(aq)	[mol l^{-1}]	$4.80 \cdot 10^{-06}$	$1.75 \cdot 10^{-06}$	$3.86 \cdot 10^{-06}$	$3.37 \cdot 10^{-06}$

Table 7.9: Input concentrations at boundary located upgradient of reactive barrier, Transect 2, 21-1 - 21-4, data from November 1996, from *Bennett* [1997]

		21-5	21-6	21-7
depth	[m]	5.0	4.5	4.0
pH	[-]	6.29	6.48	6.94
E_H	[mV]	444	441	385
CO_3^{2-}	[mol l^{-1}]	$1.95 \cdot 10^{-03}$	$2.98 \cdot 10^{-03}$	$2.40 \cdot 10^{-03}$
Cl^-	[mol l^{-1}]	$4.04 \cdot 10^{-03}$	$1.98 \cdot 10^{-03}$	$7.36 \cdot 10^{-04}$
SO_4^{2-}	[mol l^{-1}]	$1.44 \cdot 10^{-03}$	$3.24 \cdot 10^{-04}$	$8.40 \cdot 10^{-05}$
HS^-	[mol l^{-1}]	$5.29 \cdot 10^{-86}$	$4.03 \cdot 10^{-88}$	$1.86 \cdot 10^{-85}$
NO_3^-	[mol l^{-1}]	$8.83 \cdot 10^{-05}$	$2.69 \cdot 10^{-05}$	$3.69 \cdot 10^{-06}$
NH_4^+	[mol l^{-1}]	$1.35 \cdot 10^{-08}$	$1.18 \cdot 10^{-10}$	$1.77 \cdot 10^{-08}$
Na^+	[mol l^{-1}]	$6.01 \cdot 10^{-03}$	$1.78 \cdot 10^{-03}$	$7.92 \cdot 10^{-04}$
K^+	[mol l^{-1}]	$6.65 \cdot 10^{-05}$	$1.25 \cdot 10^{-04}$	$1.48 \cdot 10^{-04}$
Ca^{2+}	[mol l^{-1}]	$5.32 \cdot 10^{-04}$	$6.86 \cdot 10^{-04}$	$5.47 \cdot 10^{-04}$
Mg^{2+}	[mol l^{-1}]	$5.97 \cdot 10^{-04}$	$6.38 \cdot 10^{-04}$	$4.36 \cdot 10^{-04}$
Fe^{2+}	[mol l^{-1}]	$2.53 \cdot 10^{-13}$	$6.91 \cdot 10^{-14}$	$2.48 \cdot 10^{-14}$
Fe^{3+}	[mol l^{-1}]	$4.71 \cdot 10^{-12}$	$3.30 \cdot 10^{-12}$	$1.71 \cdot 10^{-12}$
CrO_4^{2-}	[mol l^{-1}]	$9.84 \cdot 10^{-05}$	$8.93 \cdot 10^{-06}$	$2.89 \cdot 10^{-08}$
$Cr(OH)_2^+$	[mol l^{-1}]	$1.52 \cdot 10^{-07}$	$8.93 \cdot 10^{-08}$	$3.64 \cdot 10^{-08}$
Mn^{2+}	[mol l^{-1}]	$7.88 \cdot 10^{-06}$	$2.13 \cdot 10^{-05}$	$4.37 \cdot 10^{-05}$
Al^{3+}	[mol l^{-1}]	$8.17 \cdot 10^{-09}$	$8.38 \cdot 10^{-09}$	$1.62 \cdot 10^{-08}$
H_4SiO_4	[mol l^{-1}]	$9.40 \cdot 10^{-06}$	$9.40 \cdot 10^{-06}$	$9.40 \cdot 10^{-06}$
O_2(aq)	[mol l^{-1}]	$8.13 \cdot 10^{-06}$	$1.06 \cdot 10^{-05}$	$2.47 \cdot 10^{-05}$
H_2(aq)	[mol l^{-1}]	$1.98 \cdot 10^{-31}$	$1.01 \cdot 10^{-31}$	$9.91 \cdot 10^{-31}$
TCE	[mol l^{-1}]	$1.98 \cdot 10^{-06}$	$2.29 \cdot 10^{-06}$	$4.72 \cdot 10^{-07}$
cis-1,2 DCE	[mol l^{-1}]	$1.37 \cdot 10^{-06}$	$2.95 \cdot 10^{-06}$	$5.73 \cdot 10^{-07}$
VC	[mol l^{-1}]	$1.73 \cdot 10^{-07}$	$1.05 \cdot 10^{-06}$	$1.23 \cdot 10^{-06}$
ethane	[mol l^{-1}]	$2.99 \cdot 10^{-06}$	$1.66 \cdot 10^{-07}$	$1.66 \cdot 10^{-07}$
CH_2O	[mol l^{-1}]	$7.78 \cdot 10^{-05}$	$1.01 \cdot 10^{-04}$	$4.98 \cdot 10^{-05}$
CH_4(aq)	[mol l^{-1}]	$1.37 \cdot 10^{-06}$	$9.29 \cdot 10^{-06}$	$1.35 \cdot 10^{-05}$

Table 7.10: Input concentrations at boundary located upgradient of reactive barrier, Transect 2, 21-5 - 21-7, data from November 1996, from *Bennett* [1997]

E_H. *Puls et al.* [1992] reported that more than 98% of dissolved chromium is present as Cr(VI) in the contaminated groundwater, since the reduction capacity of the aquifer material with respect to hexavalent chromium is low. It therefore was assumed that total dissolved chromium can be used to represent hexavalent chromium. This assumption is consistent with field-measured hexavalent chromium concentrations, which coincide well with analytically determined total chromium concentrations [*Bennett*, 1997]. Trivalent chromium concentrations were determined based on the assumption of equilibrium with amorphous chromium hydroxide. Total ferrous and ferric iron concentrations were close to or below detection in the upgradient portion of the aquifer and were determined based on the assumption of equilibrium with goethite and equilibrium conditions for the Fe^{2+}/Fe^{3+} redox couple. Total NH_4^+ and HS^- concentrations were not analyzed for and were calculated assuming equilibrium for the NO_3^-/NH_4^+ and SO_4^{2-}/HS^- redox couples, respectively. Dissolved aluminum concentrations were determined by equilibrating the groundwater with kaolinite.

The initial condition in the solution domain affects the simulation results only at early time. The chemical composition of the water samples taken from monitoring point 21-7 was therefore used to describe the initial condition in the entire aquifer.

7.4 Calibrated Rate Constants

Some of the reaction rates used in this study were determined in laboratory experiments using groundwater from the field site [*O'Hannesin et al.*, 1995, *Bennett*, 1997]. The rate constants therefore include influences due to the interactions with other dissolved species and can be applied directly in the modelling study, provided that laboratory conditions are representative for conditions encountered in the field. In other cases, laboratory-derived rate constants are based on ideal, single component experiments. It may not be possible to use these rate constants, since they do not account for complex interactions between reduced and oxidized species. Instead, a calibration procedure has to be used to determine effective reaction rates. The calibration of these rate constants was conducted with the objective to reproduce concentrations of dissolved reactant and product species similar to those observed in the field. This approach is justified, because zero-valent iron acts as the ultimate electron donor in the system. However, the application of the method is limited, because calibrated rate constants represent apparent rate constants and may vary significantly depending on the specific geochemical composition of the groundwater

in contact with zero-valent iron. These variations were neglected in the present study.

Preliminary simulations were conducted to approximately calibrate the model with respect to aqueous concentrations observed in the field by *Bennett* [1997]. The calibration was carried out for the one-dimensional solution domain. Effects due to preferential flow or varying water chemistry were therefore not taken into account. The calibrated rate constants were used for the simulations presented in Sections 7.5.1 and 7.5.2.

The simulated data was compared to field observations from February 1997 (240 days after completion of the barrier installation, see Section 7.5.1). The calibration involved adjusting the rate constants for reduction-corrosion reactions, the reactive surface area of zero-valent iron, and effective rate constants for the precipitation of secondary minerals. Table 7.11 shows a list of the components and source and sink terms affecting the component concentrations. This table identifies the interactions between the components and the effect of dissolution-precipitation reactions and serves as a basis for the calibration procedure.

It was assumed that the laboratory-derived rate constants for reductive dechlorination of TCE, cis-1,2 DCE and vinyl chloride [*O'Hannesin et al.*, 1995, *Bennett*, 1997] are representative for the conditions at the site. These rate constants appear to be most reliable, since the experiments were conducted with the treatment material used at the field site and with the Elizabeth City groundwater. To approximately match the field data, it was necessary to decrease the BET-measured reactive surface area for zero-valent iron listed in Table 7.7 by one order of magnitude. This difference may be attributed to scaling from laboratory to field conditions. Possible reasons for this scaling include locally higher flow velocities in the field or mixing of the treatment material with the native aquifer material during installation. The reactive surface area used in the simulations was $3.88 \cdot 10^5$ [m^2 mineral m^{-3} mineral]. The rate constant for hexavalent chromium reduction was taken directly from the laboratory study by *Gould* [1982]. The remaining rate constants were obtained by calibration in an attempt to match the concentrations of the various electron donors and reaction products (Table 7.12). The table also includes laboratory-derived rate constants for nitrate reduction and iron corrosion by water for comparative purposes. Discrepancies between the calibrated and measured reaction rates will be addressed in a later section along with the discussion of the simulation results.

Effective rate constants for the precipitation of secondary mineral phases were adjusted to approximately reproduce dissolved Cr^{3+}, Ca^{2+}, Mg^{2+}, Mn^{2+}, Fe^{2+}, Fe^{3+}, HS^- and CO_3^{2-} concentrations and pH. The resulting rate constants are listed in Table 7.13.

component	sources	sinks
CO_3^{2-}	-	carbonate minerals DIC-reduction
Cl^-	-	-
SO_4^{2-}	-	sulfate reduction
HS^-	sulfate reduction	mackinawite
NO_3^-	-	nitrate reduction
NH_4^+	nitrate reduction	-
Na^+	-	-
K^+	-	-
Ca^{2+}	-	calcite, dolomite
Mg^{2+}	-	dolomite
Fe^{2+}	iron corrosion goethite	siderite, $Fe(OH)_2$, mackinawite
Fe^{3+}	iron corrosion	$Fe(OH)_3$
CrO_4^{2-}	-	Cr(VI)-reduction
$Cr(OH)_2^+$	Cr(VI)-reduction	$Cr(OH)_3$
Mn^{2+}	pyrolusite	rhodocrosite
Al^{3+}	-	-
H_4SiO_4	-	-
O_2(aq)	-	O_2-reduction
H_2(aq)	iron corrosion	-
TCE	-	TCE-reduction
cis-1,2 DCE	TCE-reduction	cis-1,2 DCE-reduction
VC	cis-1,2 DCE-reduction	VC-reduction
ethane	TCE- and VC-reduction	-
CH_2O	-	DOC-reduction
CH_4(aq)	DIC- and DOC-reduction	-
pH	reduction-corrosion reactions secondary mineral formation deprotonation	
E_H	reduction-corrosion reactions secondary mineral formation	

Table 7.11: Reaction processes affecting component concentrations

oxidant	log k calibrated	log k lab data	unit	reference
Cr(VI)	2.895	2.895	[l m^{-2} d^{-1}]	*Gould* [1982]
TCE	-2.207	-2.207	[l m^{-2} d^{-1}]	*O'Hannesin et al.* [1995]
cis-1,2 DCE	-3.179	-3.179	[l m^{-2} d^{-1}]	*O'Hannesin et al.* [1995]
VC	-2.383	-2.383	[l m^{-2} d^{-1}]	*O'Hannesin et al.* [1995]
oxygen	2.5	-	[l m^{-2} d^{-1}]	-
nitrate	-1.589	-2.589	[l m^{-2} d^{-1}]	*Rahman and Agrawal* [1997][1)]
sulfate	-2.5	-	[l m^{-2} d^{-1}]	-
DOC	-3.8	-	[l m^{-2} d^{-1}]	-
DIC	-3.8	-	[l m^{-2} d^{-1}]	-
water	-10.331	-6.331	[mol m^{-2} d^{-1}]	*Reardon* [1995][2)]

1) calculated based on surface area estimated from grain size
2) calculated based on measured surface area

Table 7.12: Rate constants for reduction-corrosion reactions

mineral	log k_{eff} [mol m^{-3} d^{-1}]
$Fe(OH)_2(am)$	-1.000
$Fe(OH)_3(am)$	-1.000
$Cr(OH)_3(am)$	-2.000
$CaCO_3(s)$	-1.200
$CaMg(CO_3)_2(s)$	-2.500
$FeCO_3(s)$	-2.000
$MnCO_3(s)$	-2.500
FeS(am)	-2.000

Table 7.13: Calibrated effective rate constants for secondary mineral formation

Rate constants for the reductive dissolution of goethite and pyrocroite were estimated. Since these minerals are relatively insoluble, comparable slow reaction kinetics have been assumed. The rate constants are summarized in Table 7.14.

mineral	$\log k$ [mol m^{-2} d^{-1}]
FeOOH(s)	-5.000
MnO_2(s)	-5.000

Table 7.14: Estimated rate constants for reductive dissolution reactions

7.5 Results and Discussion

In the following sections, the results of the one- and two-dimensional simulations are presented and discussed. The simulations represent quasi-steady state conditions with respect to the dissolved contaminant concentrations. Quasi-steady state conditions prevail, because the volume fraction of the treatment material is large in comparison with the contaminant and other electron acceptor concentrations entering the treatment system.

7.5.1 One-dimensional Simulations

The simulations presented here are based on a simplified one-dimensional flow field. The effect of the complex flow conditions characteristic for the site can not be reproduced using this approach. On the other hand, two-dimensional simulations enhance the complexity and make an interpretation of the geochemical data more difficult. The results of the one-dimensional simulations conducted here are compared directly to field observations from February 1997 corresponding to 240 days of barrier operation [*Bennett*, 1997].

Removal of Contaminants

Figure 7.6a illustrates the removal of hexavalent chromium by the treatment system. The simulations show very rapid reduction of hexavalent chromium. The results are not sensitive to the chromium reduction rate, since the time scale of chromium removal is much shorter than the time scale of advective transport through the barrier. Trivalent

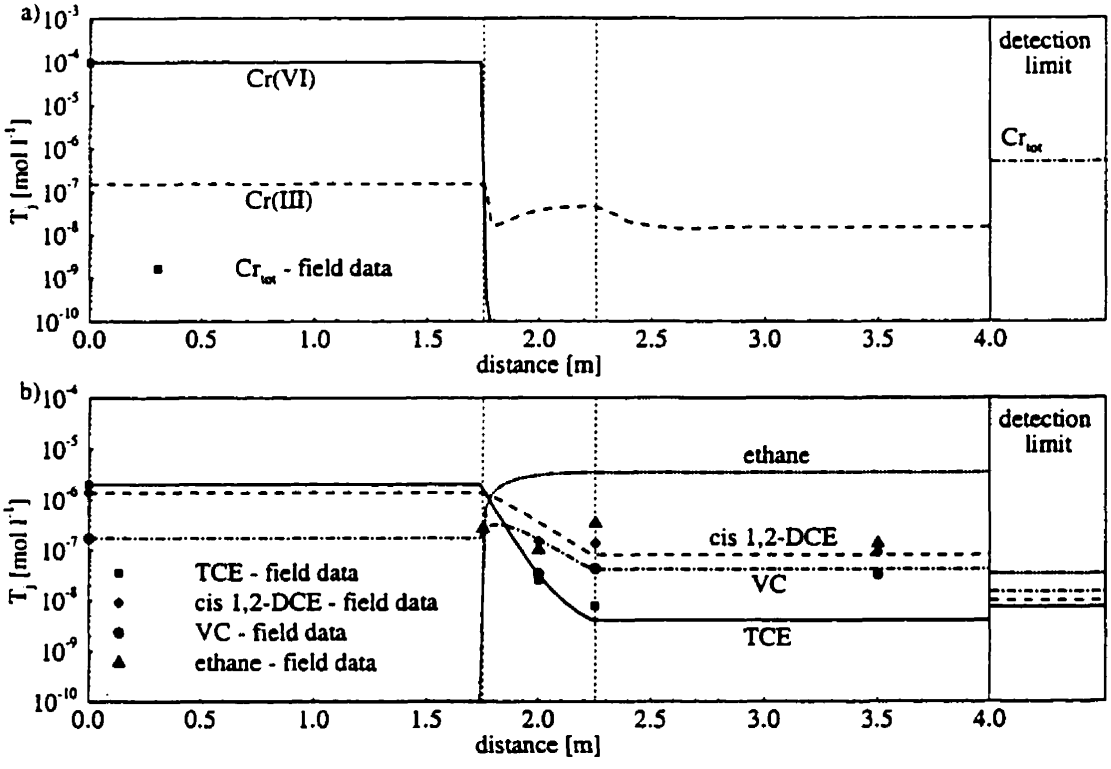

Figure 7.6: Contaminant concentrations after t = 240 days: a) chromium, b) organics - one-dimensional simulation

chromium concentrations never increase significantly, since the conditions in the barrier favor the precipitation of amorphous chromium hydroxide [*Bennett*, 1997]. The combination of the reduction and precipitation reactions leads to low hexavalent and trivalent chromium concentrations within and downgradient of the reactive barrier, and are in agreement with field measured total chromium concentrations, which are below the detection limit of 0.01 mg l^{-1} [*Bennett*, 1997].

The simulated and measured concentrations of the chlorinated organic compounds and ethane are depicted in Figure 7.6b. The model results show that concentrations of TCE, cis-1,2 DCE and VC decline by 1-3 orders of magnitude across the barrier, while ethane concentrations increase to values above detection limit. These results are generally in agreement with the field observations by *Bennett* [1997]. Within the barrier system,

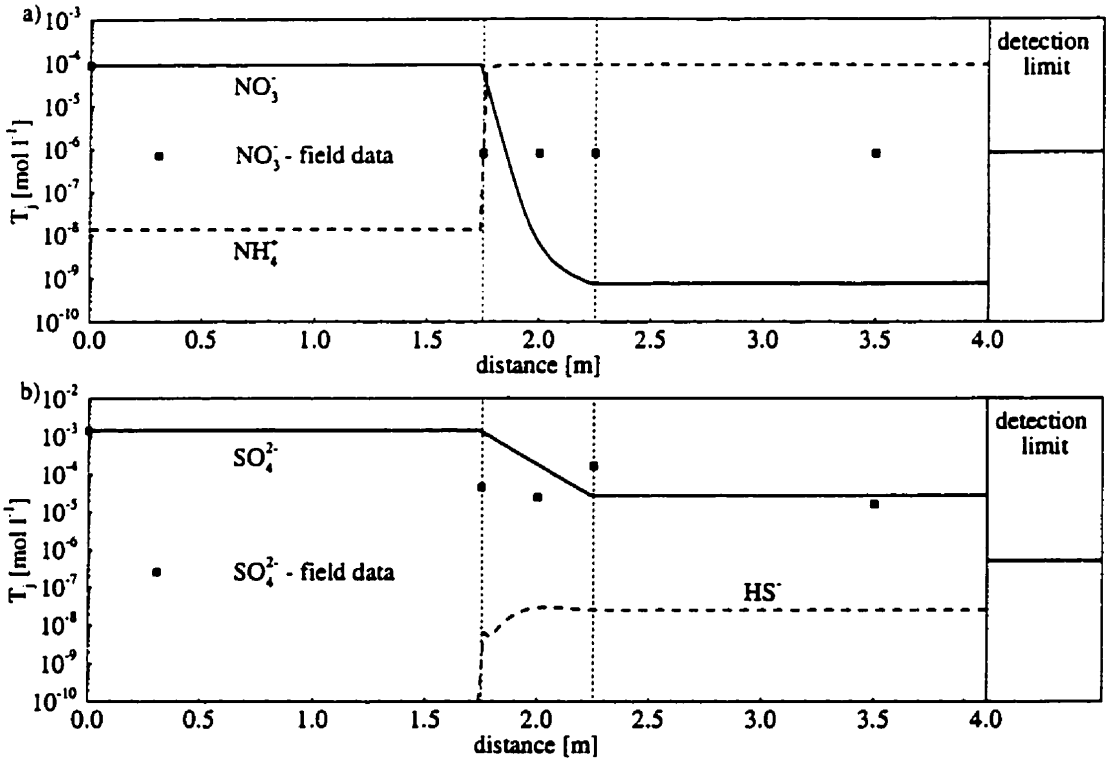

Figure 7.7: Redox couple concentrations after t = 240 days: a) nitrate/ammonia, b) sulfate/sulfide - one-dimensional simulation

TCE is partly reduced to ethane and cis-1,2 DCE. The simulated vinyl chloride concentrations increase temporarily due to the degradation of cis-1,2 DCE. As indicated by the rate constants shown in Table 7.12, the reduction of the chlorinated organic compounds is not as rapid as the reduction of chromium and the transformation remains incomplete. Primarily affected are the degradation products cis-1,2-DCE and VC. The results agree reasonably well with the field data from *Bennett* [1997]. TCE-concentrations downgradient of the barrier are below detection limit, while cis-1,2-DCE and VC persist in low, but measurable concentrations. The simulation significantly overpredicts ethane concentrations, indicating that ethane is either not the degradation product, or that ethane is further degraded, possibly to inorganic carbon.

Reduction of Electron Acceptors

Figure 7.7 compares the computed concentrations for nitrate and sulfate to the field-measured concentrations. The trend of the model results is in agreement with the field data. The concentration of the reaction products sulfide and ammonia are also shown. Nitrate reduction is rapid and field measured concentrations fall below detection limit in the entry portion of the barrier [*Bennett*, 1997]. Field measured ammonia concentrations are not available, a mass balance between nitrate and ammonia is therefore not possible. Sulfate concentrations decrease also by 1-2 orders of magnitude. The reaction product hydrogen sulfide does not reach significant concentrations due to the precipitation of mackinawite (see below).

Selected Cation Concentrations

Figure 7.8 compares computed concentrations for selected cations to analytical concentrations from *Bennett* [1997]. The simulated results are consistent with the field observations, which show declining dissolved cation concentrations while the pore water is flowing through the barrier. The decrease of cation concentrations indicates that secondary minerals precipitate in the treatment system, as was discussed by *Bennett* [1997]. The simulated results for calcium and magnesium compare well with the field data, except for the buffer zone downgradient of the barrier, where magnesium concentrations are overpredicted. The lower field-measured concentrations may be due to surface complexation reactions, involving the desorption of protons as a result of the infiltrating high pH-water in conjunction with the sorption of Mg. The solubility of manganese was assumed to be controlled by rhodochrosite. However, the model results overpredict dissolved manganese concentrations in the treatment zone and downgradient of the barrier. This indicates that Mn does not precipitate as rhodochrosite, but may coprecipitate with other carbonate minerals. The pore water also becomes slightly supersaturated with respect to amorphous pyrocroite ($Mn(OH)_2(am)$, $SI_{max} = 0.5$), which may be an additional sink for dissolved manganese. The model results overpredicted dissolved iron concentrations slightly and underpredicted carbonate concentrations (not shown). It is possible that Mg does not precipitate as a carbonate mineral phase, but rather as brucite ($Mg(OH)_2$, $SI_{max} = 1.2$). The pore water also reached supersaturated conditions with respect to artinite ($Mg_2CO_3(OH)_2$, $SI_{max} = 0.2$). If this is the case, dissolved carbonate becomes less depleted, while the precipitation of siderite may be more extensive. On the other hand,

the precipitation of Ca-hydroxides, such as portlandite ($Ca(OH)_2$), is unlikely (SI_{max} = -5.2), since the pH in the pore water is not sufficiently alkaline.

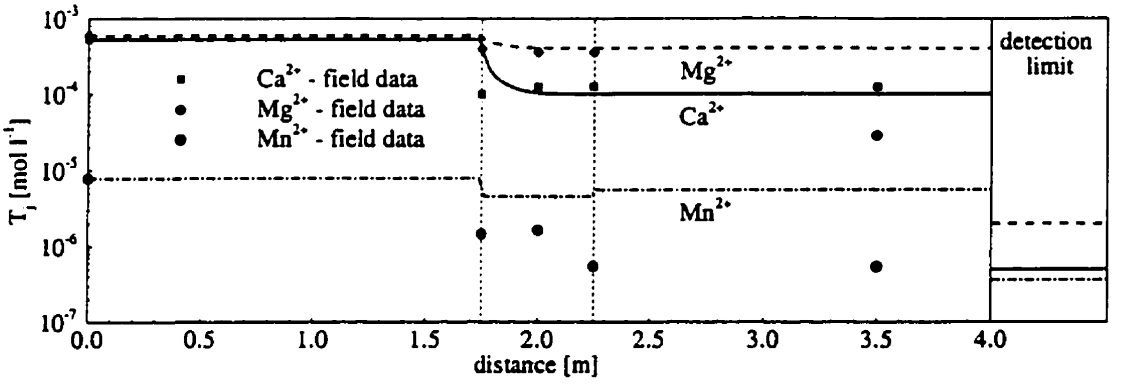

Figure 7.8: Selected cation concentrations after t = 240 days - one-dimensional simulation

pH and E_H

Reduction-corrosion reactions taking place in the treatment zone lead to a pronounced pH-increase and a decrease of the redox-potential of the groundwater passing through the barrier [*Bennett*, 1997]. Figure 7.9 shows the results for pH and E_H for the one-dimensional simulation. The pH of the groundwater upgradient of the reactive barrier is approximately 6.3 and rises in the wall to values up to 9-11. Within the treatment zone, the simulation results agree very well with field-measured pH-values. The field data from *Bennett* [1997] shows that pH-values downgradient of the barrier drop rapidly and approach close-to-background values. It was assumed that pH-buffering is due to deprotonation from mineral surfaces. The observed strong pH-buffering could only be reproduced by specifying a large reservoir of sorbed hydrogen ions (50 mol m^{-3} porous medium). The results give at best a qualitative idea about the processes taking place downgradient of the barrier. Additional mineralogical data is needed to confirm the hypothesized buffer mechanism or to identify additional buffer mechanisms.

It is likely that, if hydrogen gas is present in sufficient quantities, E_H measurements reflect the state of the $H_2(aq)/H^+$ redox couple. Therefore, the redox potential was

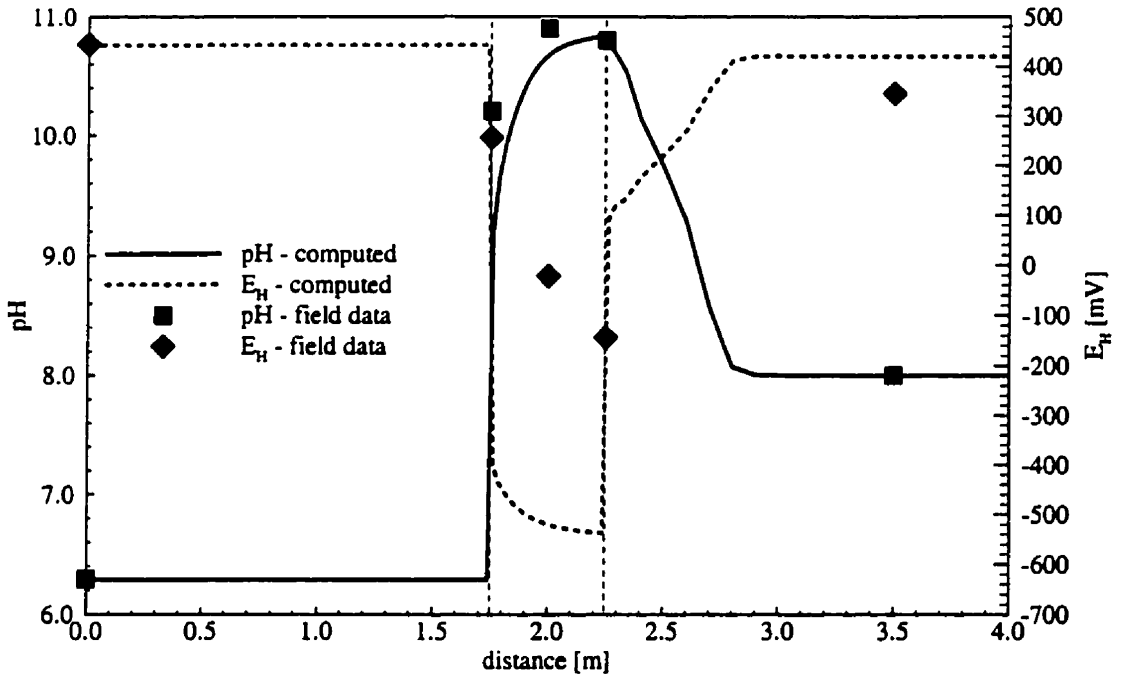

Figure 7.9: pH and E_H after $t = 240$ days - one-dimensional simulation

computed based on dissolved hydrogen gas concentrations. The pore water entering the barrier is characterized by E_H-values of approximately 400-500 mV. The simulation results show a rapid decrease of E_H within the reactive barrier to values below -500 mV. The field-measured E_H does not show such a pronounced decrease [*Bennett*, 1997], which indicates that conditions in the field are less reducing than calculated by the model, or that the field-measured E_H does not correspond to the redox condition defined by the $H_2(aq)/H^+$ redox couple. Assuming that measured E_H-values are representative for conditions in the field, it can be postulated that dissolved hydrogen gas must be consumed by other reduction reactions as an electron donor. At this point it should be mentioned that E_H-values lower than -550 mV have been measured locally in the treatment zone at other locations and sampling times [*Bennett*, 1997]. E_H-values increase up to close to background-values of 200 - 400 mV downgradient of the reactive barrier [*Bennett*, 1997] due to E_H-buffer reactions. The reductive dissolution of goethite and pyrolusite overpredicts E_H-buffering in the downgradient zone indicating that these reactions are

characterized by slow reaction kinetics. Unlike pH-buffering, E_H-buffer reactions do not require a large reservoir of buffer agents. This is due to the comparably low H_2(aq)-concentrations leaving the treatment zone and the persistence of other reduced dissolved gases, such as methane and H_2S(aq)(not shown).

Discussion of Reaction Mechanisms

In order to approximately match the field data, the rate constant for nitrate reduction had to be increased by one order of magnitude, while the iron corrosion rate by water had to be decreased by 4 orders of magnitude in comparison to laboratory-derived rate constants (Table 7.12). Large uncertainties exist with respect to the applicability of the rate constant for nitrate reduction [*Rahman and Agrawal*, 1997] to the reactive barrier at the Elizabeth City-site, since the tested treatment material was different, and the reported rate constant had to be corrected for reactive surface area. The discrepancies with respect to the rate constant for nitrate reduction was therefore considered within the uncertainty of the rate constant derived form the work of *Rahman and Agrawal* [1997].

The differences between the measured rate constant for iron corrosion by water [*Reardon*, 1995] and the corresponding calibrated rate constant is more significant. Modelled E_H-values (based on the H_2(aq)/H^+ redox couple) still fall notably below the field-measured values, despite the decreased rate constant for iron corrosion by water. The laboratory-derived reaction rate from *Reardon* [1995] was normalized with respect to reactive surface area. In this context, it was assumed that the reactive surface area reported by *Reardon* [1995] is representative for the investigated material, which was put into question in the original reference. The differences may be due to problems with the E_H-measurements, which may not represent conditions prevailing at the field-site. It should be pointed out that E_H-values below -550 mV were measured at other sampling locations or sampling times. Such values are more consistent with the modelled data. Hydrogen gas concentrations may also be influenced by the significant rate of sulfate reduction at the field site in Elizabeth City (Figure 7.7). Sulfate reduction at the Elizabeth City-site may be microbially mediated, as proposed by *Bennett* [1997]. In this case, dissolved hydrogen gas may be used as the electron donor. In the present modelling study, sulfate reduction was described as a heterogeneous reaction between sulfate and zero-valent iron. However, the following reaction sequence may better describe the reaction mechanisms

controlling the geochemical conditions at the field-site:

$$\begin{aligned} 4Fe^0(s) + 8H_2O &\rightarrow 4Fe^{2+} + 8OH^- + 4H_2(aq) \\ SO_4^{2-} + 4H_2(aq) &\rightarrow HS^- + OH^- + 3H_2O \\ 4Fe^{2+} + HS^- + 7OH^- &\rightarrow FeS(am) + 3Fe(OH)_2(am) + H_2O \end{aligned}$$

This reaction sequence leads to a net pH-increase, the removal of sulfate and dissolved hydrogen gas, and the immobilization of the reaction products iron and sulfide. Nevertheless, it is also possible that sulfate is simultaneously reduced by the direct interaction with zero-valent iron (Table 7.3). Hydrogen gas may also be consumed as an electron donor in other reduction reactions (nitrate, DIC and DOC, *Lovley and Goodwin*, 1988). Microbially-mediated reduction reactions in porous media composed of zero-valent iron and involving hydrogen gas as the electron donor were previously reported by *Weathers et al.* [1995]. However, sufficient information to uniquely describe the contributions of the various reaction processes is not available to date.

Corrosion of Zero-Valent Iron

The simulation results indicate that iron corrosion is most significant in the entry area of the barrier and decreases along the flow path, when the electron acceptors become depleted. The reaction rates of selected reduction-corrosion reactions are shown in Figure 7.10. It can be seen that nitrate and sulfate are the most important electron acceptors in the system, which is in agreement with the interpretation of *Bennett* [1997]. The reduction of hexavalent chromium also contributes to iron corrosion. The remaining electron acceptors are lumped together, since their contributions are comparably small. Figure 7.10 shows that chromium reduction takes place only in the entry area of the reactive barrier, since the reaction rate is fast in comparison to groundwater velocities. The reduction of nitrate to ammonia is slower, and persists deeper into the barrier. The reduction of sulfate is characterized by even slower reaction kinetics. Reduction rates decrease continuously throughout the barrier, but are still discernable before leaving the treatment system into the downgradient portion of the aquifer. Figure 7.10 illustrates that the major contribution to iron corrosion is ultimately due to the reduction of sulfate. Iron corrosion due to the reduction of the chlorinated organic compounds are not explicitly presented in Figure 7.10, since the rates are negligible on the scale of the graph.

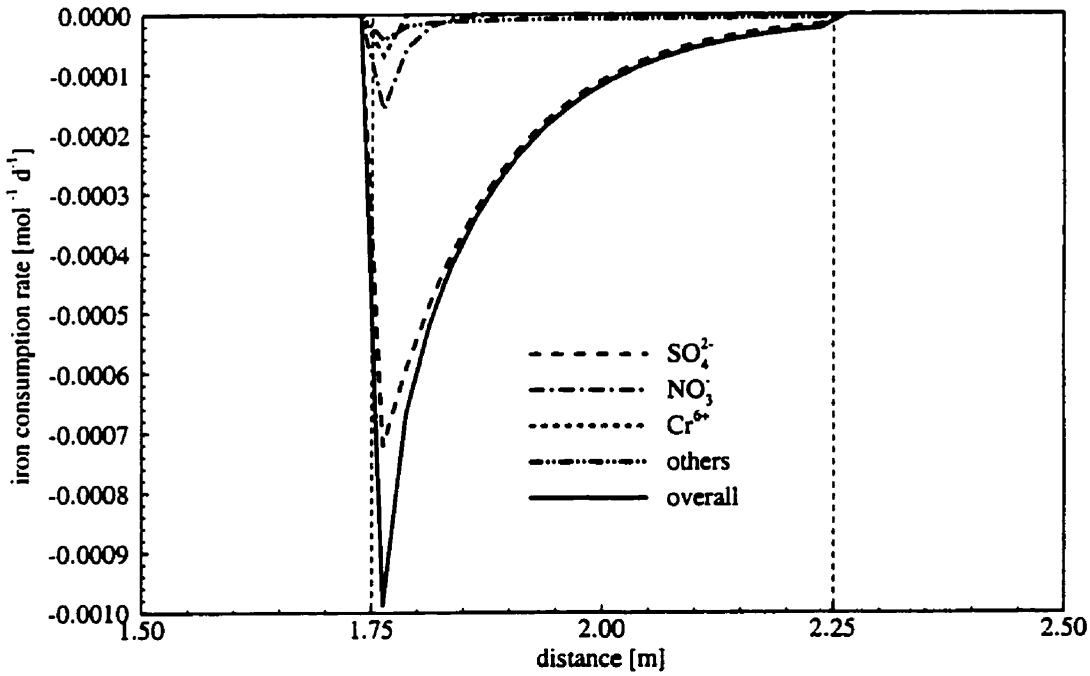

Figure 7.10: Iron corrosion rates in reactive barrier after $t = 240$ days

Precipitation of Secondary Minerals

Figure 7.11 shows that the precipitation of carbonate minerals, such as calcite and siderite, takes place close to the upgradient end of the barrier. Siderite appears to be the dominant carbonate phase, because the corrosion of zero-valent iron sets free comparably large amounts of ferrous iron. Small amounts of rhodocrosite also precipitate in the entry area of the barrier (not shown). Dolomite formation takes place throughout the barrier due to slower reaction kinetics. The real system will likely be characterized by the precipitation of a complex carbonate solid solution containing ferrous iron, calcium, magnesium and manganese rather than by the formation of distinct mineral phases [*Reardon*, 1995]. Ferric iron produced from iron corrosion also precipitates rapidly in the entry zone. On the other hand, minerals such as mackinawite and ferrous hydroxide precipitate throughout the treatment system. The formation of these mineral phases is controlled by the availability

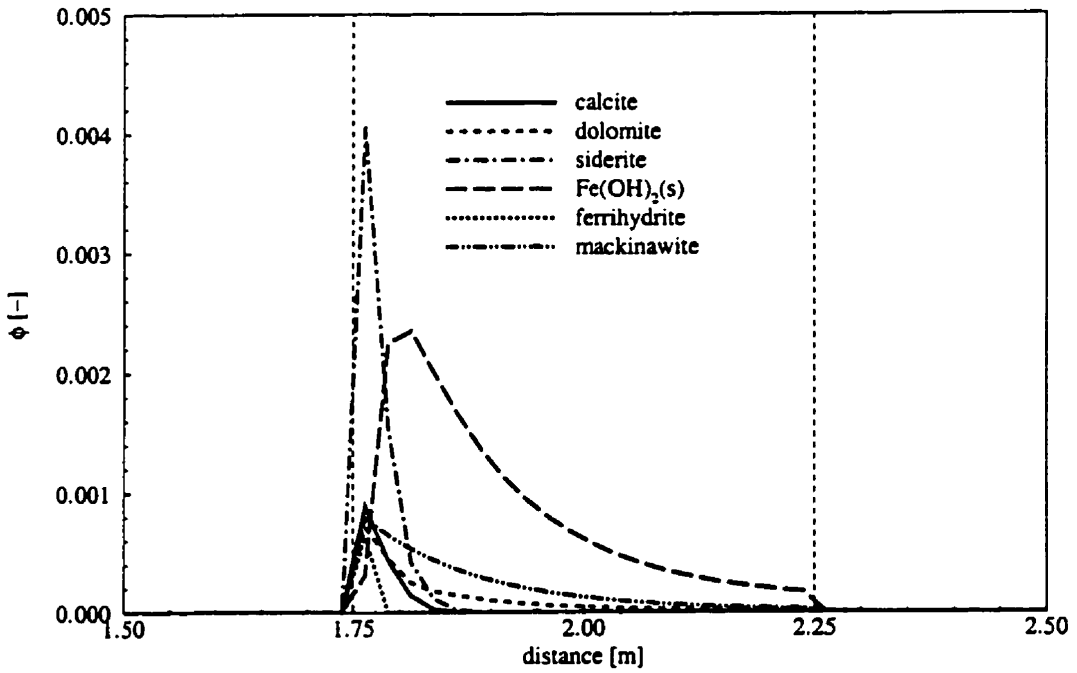

Figure 7.11: Secondary mineral volume fractions in reactive barrier after $t = 240$ days

of the reactants, which are produced by sulfate reduction and iron corrosion by water. These results are consistent with the the field observations and the conceptual model of *Bennett* [1997].

Long Term Efficiency

The tendency to locally precipitate relatively large amounts of secondary minerals may have an impact on the long term efficiency of a reactive barrier [*MacKenzie et al.*, 1997, *Bennett*, 1997]. Significant amounts of the treatment material may also be consumed due to the combined effect of sulfate reduction and iron-corrosion by water. Treatment material depletion in conjunction with secondary mineral formation may also affect the porosity of the treatment zone [*MacKenzie et al.*, 1997, *Bennett*, 1997].

Within the reactive barrier, the bulk porous medium consists at any time of porosity

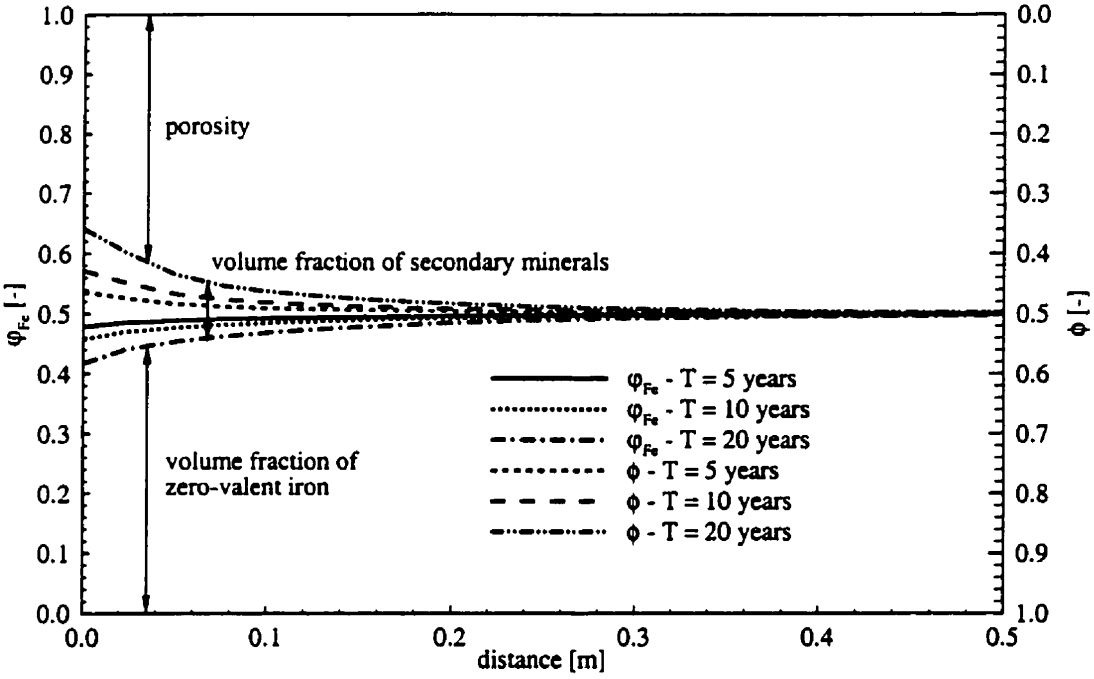

Figure 7.12: Long term effect of iron corrosion and secondary mineral formation

(void space), the volume fraction of the treatment material and the sum of the volume fractions of all secondary mineral phases. Figure 7.12 illustrates the potential for depletion of the treatment material and the precipitation of secondary minerals along the barrier after 5, 10 and 20 years of operation. Secondary minerals are not present initially and the porosity is $\phi = 0.5$ which is equal to the volume fraction of zero-valent iron. After 20 years the volume fraction of zero-valent iron has decreased from 0.5 to approximately 0.42 in the entry zone of the treatment system. However, the zone of significant treatment material depletion is limited to the first 10 cm of the barrier. At the same time, it can be observed that the porosity decreased significantly over the 20 year simulation period from $\phi = 0.5$ to approximately $\phi = 0.36$ in the entry area of the barrier, indicating that a significant amount of secondary minerals has precipitated. The total volume fraction of secondary minerals can be estimated from the decrease of porosity and the depletion of the treatment material and amounts to a maximum value of $\varphi = 0.22$ in the entry

area of the reactive barrier. These results are comparable with porosity loss calculations performed by *Bennett* [1997].

The model results indicate, that over a long period of time porosity may decrease significantly, which will almost certainly affect the hydraulic properties of the treatment system. More importantly, the reactivity of the treatment material may decline over time. In addition to the consumption of Fe^0, the accumulation of secondary mineral phases may significantly compromise the reactivity of the remaining treatment material. It can be hypothesized that the reduction of the reactivity of the treatment material in the entry zone due to the precipitation of secondary minerals will allow the contaminants and other electron acceptors to pass this less reactive zone more or less unaffected. Reduction reactions will still occur in areas located deeper into the barrier, that have been less affected by the precipitation of secondary minerals. However, this process will decrease the effective thickness of the barrier and therefore the contact time of the contaminants with the treatment material. This may lead to the incomplete treatment of contaminants, that require a long residence time. Although the basic concepts of mass loss and secondary mineral formation are not new [e.g.: *MacKenzie et al.*, 1997, *Bennett*, 1997], the simulation results illustrate the distribution of iron-consumption and secondary mineral precipitation in a semi-quantitative way for the first time. In a real system, it can be expected that the depletion of the treatment material and the precipitation of secondary minerals is less concentrated in the inflow area than predicted in Figure 7.12, because decreasing iron reactivity was not accounted for in this study.

7.5.2 Two-dimensional Simulations

Two-dimensional simulations were carried out with input concentrations defined in Tables 7.9 and 7.10. The remaining geochemical parameters were as used in Section 7.5.1. These simulations illustrate the effect of preferential flow on the treatment of the contaminants. All results of the following reactive transport simulation represent conditions after 2 years of barrier operation.

Groundwater Flow

Figure 7.13 shows the streamlines constructed from the steady-state velocity field through the two-dimensional solution domain, which was calculated based on the hydraulic conductivitiy distribution presented in Figure 7.5 and is based on earlier work from *Bennett*

[1997]. The model results indicate a heterogeneous flow field in the aquifer and through the reactive barrier. A zone of preferential flow exists in the reactive barrier at a depth of approximately 6 m below ground surface, which is consistent with the findings of *Puls et al.* [1995] and *Bennett* [1997].

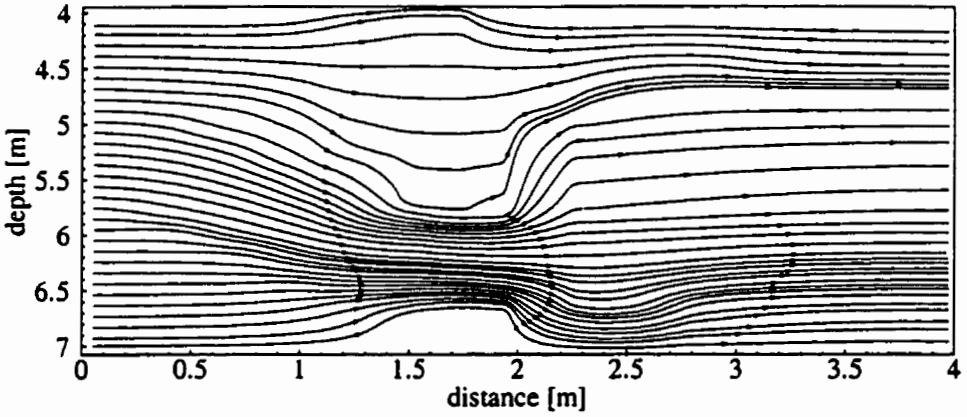

Figure 7.13: Streamlines in two-dimensional solution domain

Removal of Contaminants

The two-dimensional simulation clarifies the effect of the heterogeneous groundwater flow field on the treatment of contaminants. Figure 7.14 illustrates that the remediation of hexavalent chromium appears to be unaffected by the zones of preferential flow within the aquifer and the reactive barrier. The rapid reduction of hexavalent chromium ensures a successful treatment, even in zones of high flow velocities. Amorphous chromium hydroxide precipitates in a narrow fringe in the entry area of the treatment system.

Figure 7.15 shows the concentration distributions of the chlorinated organic compounds for the two-dimensional simulation. The concentration distribution upgradient of the reactive barrier does not coincide well with the concentration distribution of most inorganic compounds (e.g. chromium). This deviation may be due to the infiltration of TCE as a free phase product and subsequent dissolution in the source area [*Bennett*, 1997]. The simulation results indicate that zones of preferential flow may have a significant impact on the treatment of the organic compounds. The removal of the organics in areas

of lower hydraulic conductivity are more pronounced, since a longer contact time of the contaminants with the treatment material is provided. cis-1,2 DCE and VC are treated effectively in the upper portion of the solution domain, while the reductive dechlorination of TCE in the lower portion of the domain leads to the production of these degradation products, which are only incompletely removed. The simulation results for chromium and the chlorinated organics agree reasonably well with field measured concentrations [not shown, see *Bennett*, 1997].

pH and E_H

Figure 7.16 presents the results for pH and E_H. The effect of the heterogeneous flow field on these parameters can be clearly observed. pH-values increase more slowly within the reactive barrier in the zone of preferential flow. The pH-distribution is also affected by chemical heterogeneities. The concentrations of the electron acceptors entering the reactive barrier vary with depth, and higher pH-values can be correlated to high infiltrating electron acceptor concentrations. For example, sulfate concentrations are low in the upper and lower portion of the solution domain (Figure 7.17), resulting in a less pronounced pH-increase. This behavior may be an artifact of the decreased rate constants for iron corrosion by water, which were calibrated for conditions where sulfate is present, but may not be valid for conditions where sulfate is depleted. Elevated pH-values downgradient of the barrier can be observed in areas of high flow velocities, where the pH-buffer capacity of the aquifer is exhausted.

The redox potential decreases rapidly within the reactive barrier. The specified reaction network does not allow a consistent description of E_H-values, since hydrogen gas concentrations are assumed to be independent of the concentrations of electron acceptors such as nitrate and sulfate, which appear to use dissolved hydrogen gas as an electron donor. In areas where these electron acceptors are abundant, dissolved hydrogen gas concentrations may be lower than predicted by the simulations, while conditions may be more reducing in zones where the electron acceptors have been depleted. The E_H increases downgradient of the barrier due to reductive dissolution of goethite and pyrolusite to close-to-background values.

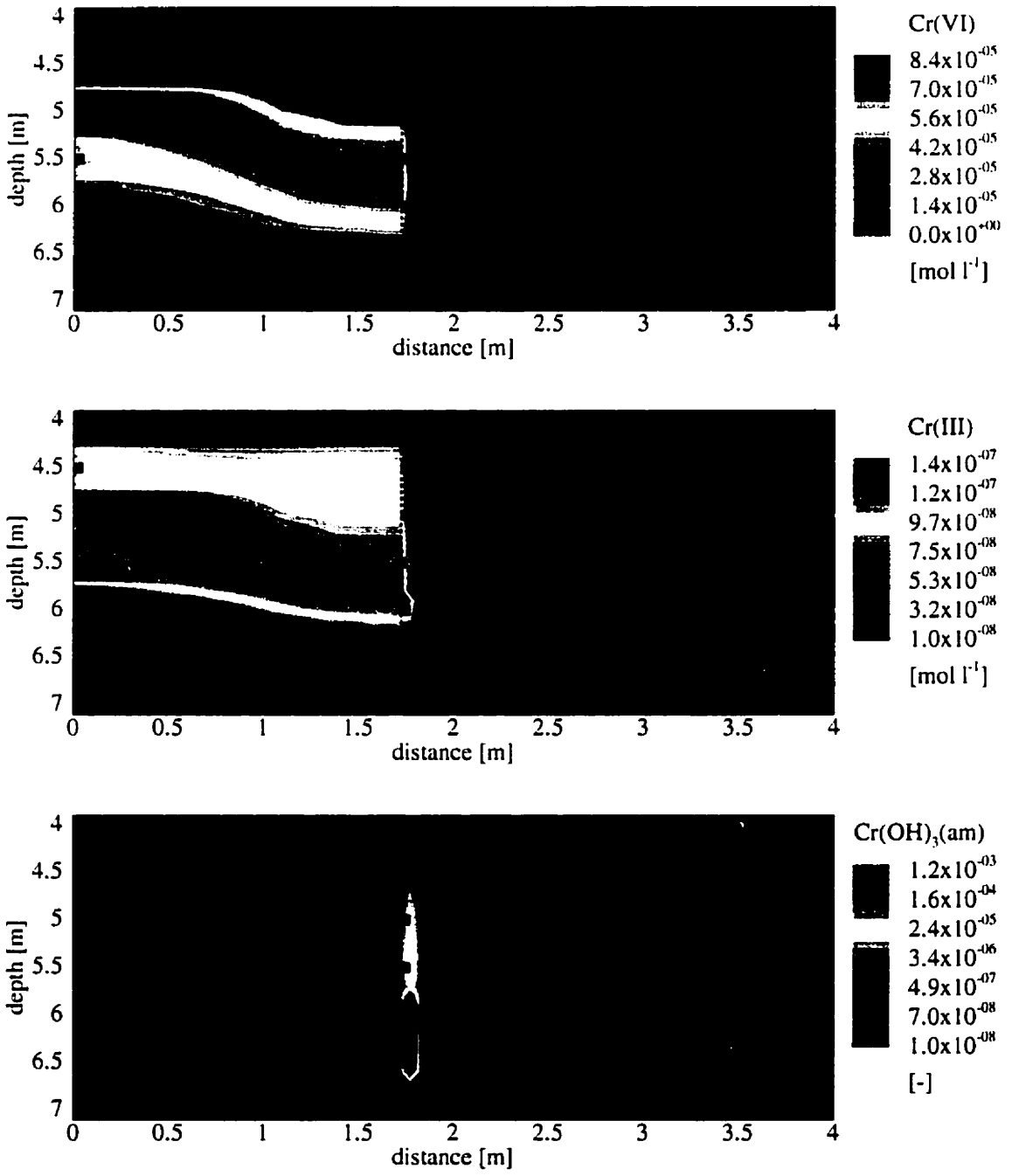

Figure 7.14: Hexavalent and trivalent chromium concentrations and $CrOH_3$(am) volume fractions after $t = 2$ years

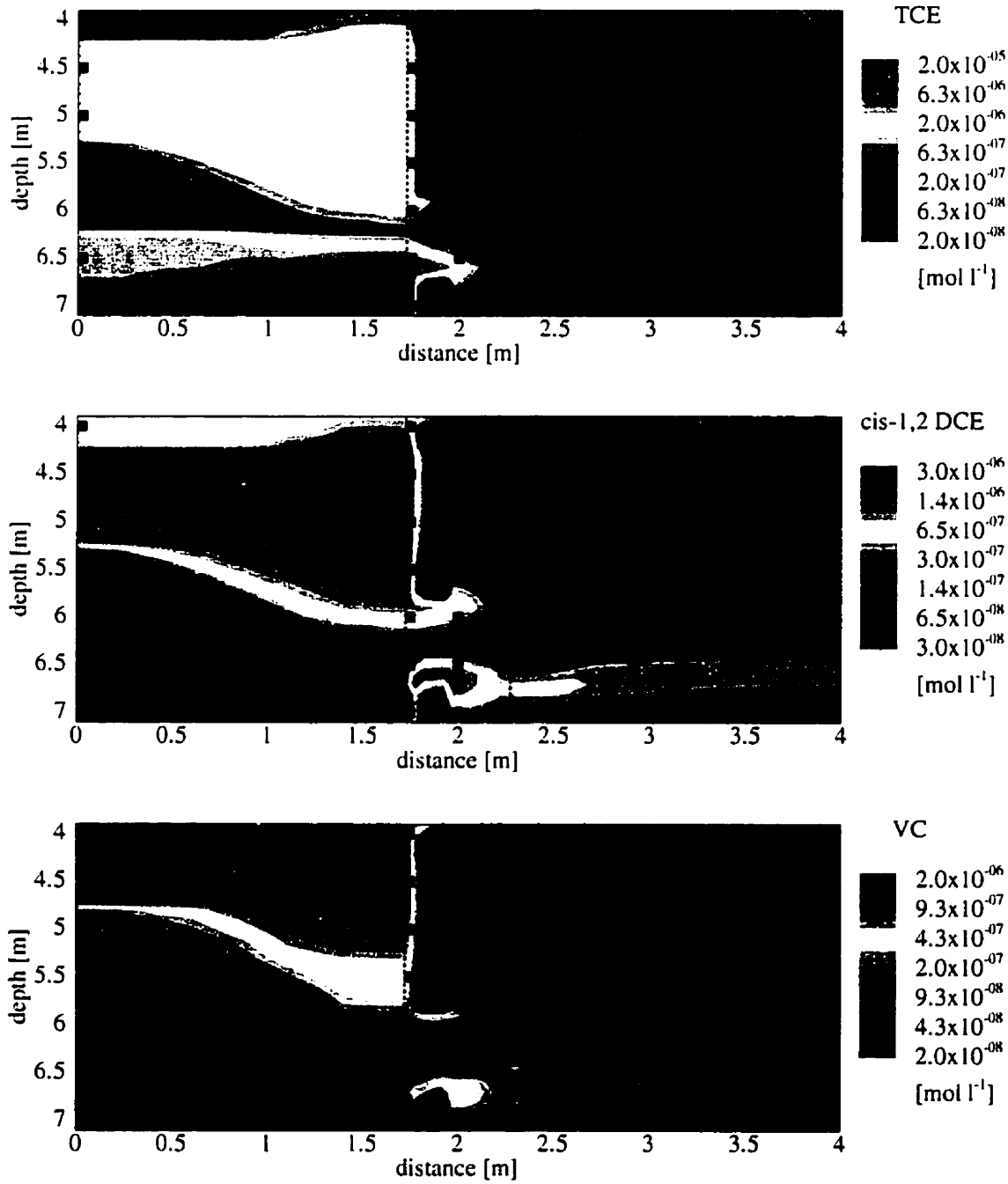

Figure 7.15: TCE, cis-1,2 DCE and VC concentrations after $t = 2$ years

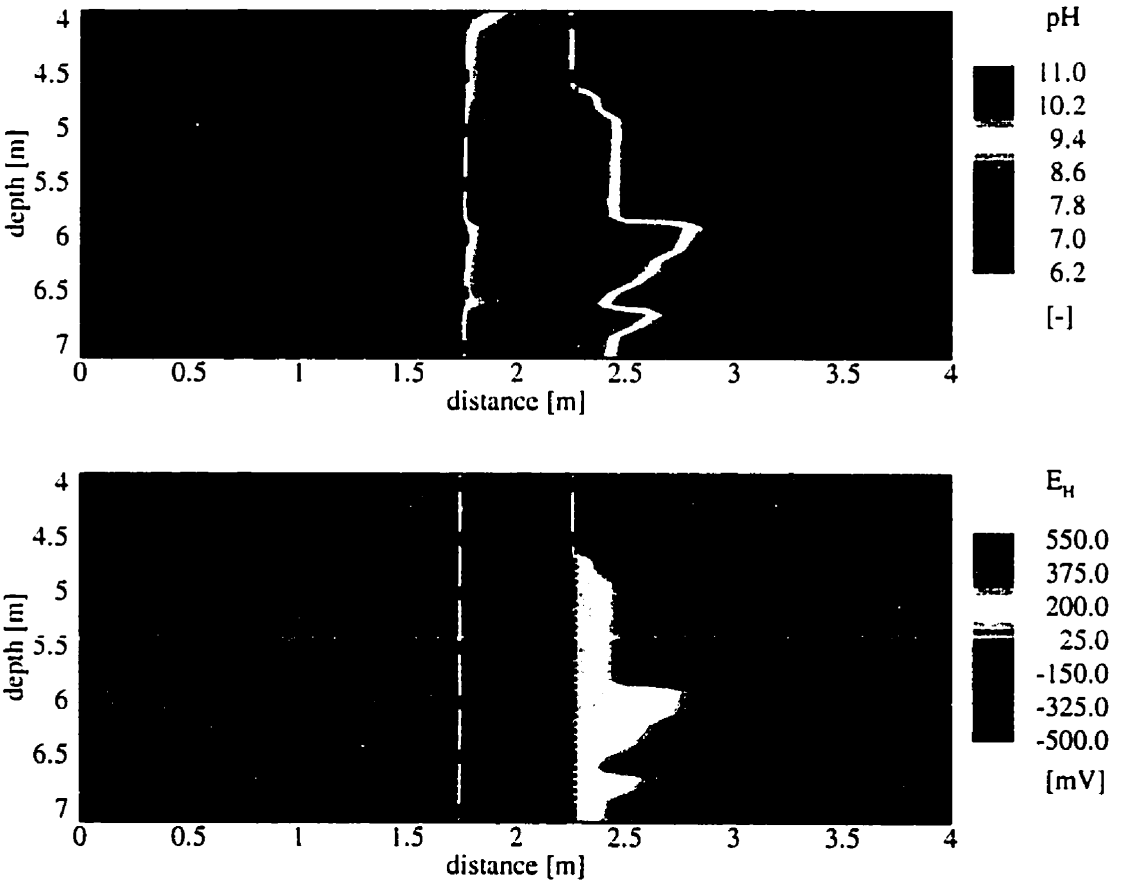

Figure 7.16: pH and E_H distribution after $t = 2$ years

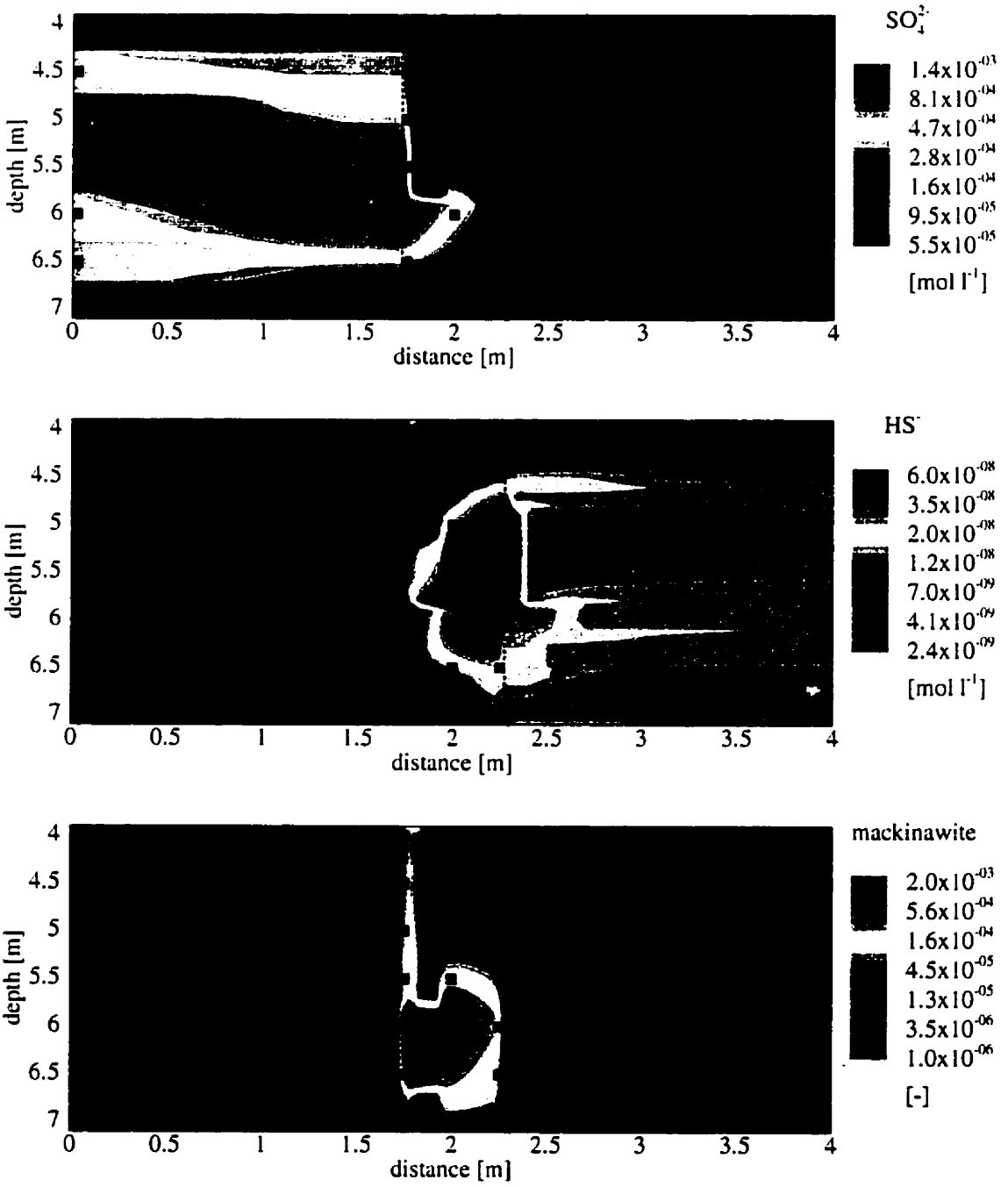

Figure 7.17: Sulfate and sulfide concentrations and mackinawite volume fractions after t = 2 years

Sulfate Reduction

Figure 7.17 illustrates the reduction of sulfate by the treatment system. Sulfate enters the reactive barrier primarily through the area of preferential flow, where it is reduced to dissolved hydrogen sulfide. However, hydrogen sulfide concentrations remain low, because mackinawite controls the solubility of HS^-. Low concentrations of HS^- are observed in selected zones located downgradient of the barrier. The model results indicate that the precipitation of mackinawite is more pronounced in the zone of preferential flow. Secondary mineral precipitation may affect the hydraulic properties of this high permeability zone and may alter the flow distribution in the long term.

7.6 Conclusions

The present study shows the versatility of the model MIN3P with respect to the implementation of complex reaction networks for one- and two-dimensional problems. Reactive transport simulations involving a large number of components, dissolved species and dissolution-precipitation reactions can be conducted with the present model. One-dimensional simulations can be used primarily to assess the chemical complexity, while two-dimensional simulations can be used to identify the importance of the relationship between reaction and transport time scales.

The conceptual model developed by *Bennett* [1997] was implemented into the numerical model MIN3P to describe the interactions between reaction and transport processes taking place at the reactive barrier in Elizabeth City, NC. The simulation results agree reasonably well with the field observations. Processes downgradient of the barrier could only be investigated in a qualitative way, since data was not available and surface complexation is not included in the present model.

The model allows visualization of important processes occurring in a reactive barrier composed of zero-valent iron. Processes such as the corrosion-reduction reactions and secondary mineral precipitation can be evaluated semi-quantitatively. The simulations allow the estimation of iron corrosion rates from the sum of the reduction-corrosion reactions. The total accumulation and distribution of secondary precipitates can be estimated as well. Two-dimensional simulations highlight possibly adverse effects of preferential flow on contaminant treatment.

Discrepancies between the simulated E_H- conditions within the barrier and the field observations by *Bennett* [1997] illustrate that secondary reactions between the reduced reaction products, such as hydrogen gas, and the electron acceptors, which enter the barrier, may be important. The hypothesized reduction of sulfate by hydrogen gas may explain observed relatively low hydrogen gas concentrations. Degassing and the formation of hydrogen gas bubbles, which may affect the permeability and reactivity of the barrier, may be inhibited by this process. It remains unresolved, if sulfate reduction leads to additional iron corrosion, or if iron corrosion by water produces sufficient quantities of hydrogen gas to reduce infiltrating sulfate.

More work is warranted to investigate reactive barriers for groundwater remediation and to study the long term performance of passive treatment systems. Possible model enhancements include the implementation of a more complete reaction network including secondary redox reactions, inhibition effects, surface complexation and effects of secondary mineral precipitation on the permeability and reactivity of the treatment material.

Chapter 8

Summary and Conclusions

The objective of this thesis was to develop a multicomponent reactive transport model for the investigation of transport and reaction processes in variably-saturated groundwater systems involving complex nonlinear reactions. The model was designed to be applicable to a wide variety of reactive transport problems and to be computationally robust. These goals were achieved by implementing the variably-saturated flow equations and the coupled reaction-transport equations into the model MIN3P. A general formulation for kinetically-controlled reactions was developed and included in the formulation to enhance the versatility of the model. Several numerical techniques were incorporated and tested to ensure an efficient and robust solution.

As a foundation for this thesis, important processes and common solution approaches for multicomponent reactive transport in porous media were reviewed. Particular emphasis was placed on coupling methods and formulations for geochemical reactions. Relationships for the time scales of the various transport and reaction processes were summarized. In general it was concluded that the global implicit solution method [*Steefel and Lasaga*, 1994] is best suited for problems characterized by Damköhler numbers < 1 or for systems characterized by quasi-steady state conditions, in agreement with work previously conducted by *Lichtner* [1988] and [1993]. Operator-splitting methods, on the other hand, may be better suited for problems involving rapid local geochemical changes with rapidly moving dissolution-precipitation fronts.

The global implicit solution method [*Steefel and Lasaga*, 1994] was chosen for the present model because it is considered the most rigorous coupling approach and it ensures the simultaneous treatment of transport and reaction processes. The method au-

tomatically provides global and local mass conservation, an important feature for the investigation of reaction-transport problems. This solution approach is also well suited for unsaturated porous media, where rapid diffusive gas transport may lead to short transport time scales.

The model formulation includes advective-diffusive transport in the aqueous phase, diffusive gas transport, and a range of geochemical reactions including aqueous complexation, oxidation-reduction, gas dissolution-exsolution, ion exchange and dissolution-precipitation reactions. The model allows the specification of equilibrium and kinetically-controlled reactions in a database, thus providing a high degree of flexibility with respect to the characterization of the geochemical reaction network. A general formulation for kinetically-controlled reactions is difficult to obtain because there is no standard for kinetic rate expressions as is given by the law of mass action for equilibrium reactions. However, the present model development is a step towards such a generalization, allowing the application of the model to a wide range of reactive transport problems. Kinetically-controlled reactions are implemented for intra-aqueous reactions and mineral dissolution-precipitation reactions. The reaction progress may depend on the activities of any dissolved species or on total aqueous component concentrations. The formulation provides rate expressions for reversible and irreversible reactions and for surface- and diffusion-controlled dissolution-precipitation reactions. The present formulation for intra-aqueous reactions can be used to describe processes such as the kinetically-controlled oxidation of dissolved ferrous iron by oxygen. The pH-dependent dissolution of aluminosilicate minerals, reactions involving several parallel reaction pathways, or sequential reaction steps can be described using the formulation for dissolution-precipitation reactions. The model was primarily designed for inorganic chemicals, however, organic constituents can be considered as well.

Numerical techniques to improve the robustness and to ensure the efficiency of the solution have been implemented in MIN3P and tailored towards applications in reactive transport modelling. Reactive transport problems are often characterized by a highly transient initial behavior with rapid changes caused by transport or reaction processes, followed by a quasi-steady state condition or a series of quasi-steady state conditions [*Lichtner*, 1988] where the concentrations of dissolved species do not change significantly. Such a physico-chemical system requires adaptive methods to obtain an efficient solution. The present model includes an adaptive time stepping and update modifications scheme to ensure that the time step is adjusted to the prevailing conditions. A sensitivity analysis

was conducted to determine the ideal set of parameters controlling the adaptive time stepping scheme. The results indicate that an aggressive time stepping scheme with a large number of Newton iterations per time step and relatively large updates per Newton iteration/time step provides the most efficient solution.

Upstream weighting and a flux-limiter scheme [*van Leer*, 1974, *Unger et al.*, 1996] were included to ensure a monotone and non-oscillatory solution of the reactive transport equations. It was shown that the spatial weighting scheme and the time discretization only have a negligible effect on the accuracy of the solution for species distributions controlled by rapid dissolution-precipitation reactions. This effect can be attributed to the "sharpening" effect of dissolution-precipitation reactions. This also implies, that artificial diffusion, introduced by operator-splitting methods may not lead to significant errors for problems governed by dissolution-precipitation reactions. On the other hand, non-reactive species are greatly affected by the time and spatial discretization parameters, as is commonly known. These results suggest that the simulation of laboratory experiments involving dissolution-precipitation reactions and the passage of several pore volumes may not be affected by the spatial and temporal parameters, and efficient upstream-weighted methods appear to provide a sufficient degree of accuracy.

The model allows the use of three different redox master variables (O_2(aq), H_2(aq) and e^-). The electron can only be used in closed systems (i.e. no gas phase present), while dissolved oxygen and hydrogen gas can be used for saturated or unsaturated problems. A comparison of the approaches using oxygen and hydrogen gas indicated that the efficiency of the solution of reactive transport problems may not only depend on the relative magnitude of the primary variables, but also on the relative concentration change from one time step to the other.

The application of the model to various verification examples involving both field data [*Valocchi et al.*, 1981] and established numerical solutions [*Wunderly et al.*, 1996, *Lichtner*, 1996a] has shown that MIN3P is capable of simulating complex systems involving a large number of reactions between gaseous, dissolved and solid constituents. The verification examples included acid mine drainage generation in unsaturated porous media [*Lichtner*, 1996b, *Lichtner*, 1997a], the simulation of a copper leach operation [*Lichtner*, 1996b, *Lichtner*, 1997b], and reactive transport affected by ion exchange reactions [*Valocchi et al.*, 1981]. Good agreement was obtained for all simulations when the simulation results were compared to the results of established models or to field data. These applications also illustrated the versatility of the model formulation and confirmed that the reaction

network can be adjusted to describe a variety of reactive transport scenarios by simply inserting the required reaction and rate parameters into the model database.

A series of simulations were conducted to demonstrate the model's capabilities for the investigation of the generation and fate of acid mine drainage. These simulations illustrate how the model can be applied to batch and one-dimensional systems involving kinetically-controlled reactions and transport processes. This application shows that the model can be used to conduct sensitivity analyses for the determination of rate-limiting steps in reaction networks involving complex parallel and sequential reaction processes. The usefulness of mass balance calculations was demonstrated by determining the contribution of different reaction processes to the consumption of atmospheric oxygen and by evaluating the importance of CO_2-degassing as a pH-buffering process.

The second application illustrated the capabilities of MIN3P as an analysis tool for the investigation of field data. In this case, one- and two-dimensional simulations were conducted to simulate the remediation of groundwater contaminated by hexavalent chromium and chlorinated organic compounds. These applications demonstrated the applicability of the model to a complex system involving both inorganic and organic contaminants. A reasonable match between observed and simulated concentration distributions was obtained. The existing conceptual model of the field site *Bennett* [1997] could be described in a semi-quantitative way with the help of the model. The model results suggest that the longevity and efficiency of the treatment system may be influenced by secondary mineral formation. The two-dimensional simulations showed the capability of MIN3P to investigate the influence of preferential flow on the treatment efficiency.

It should be pointed out that the usefulness of reactive transport models is often limited by the comprehensiveness of the conceptual model and by the availability of input parameters, some of which are not easy to obtain. Input parameters may include dissolved analytical concentrations in the aqueous phase, mineral volume fractions, mineral reactive surface areas, or the cation exchange capacity of the porous medium. Equilibrium constants, rate constants, and reaction stoichiometries need to be specified to define the reaction network for a specific application.

Important for reactive transport modelling is the characterization of the composition of the infiltrating water and the mineralogical composition of the aquifer. Probably the most difficult aspect of defining the conceptual model is the specification of the mineral phases which contribute significantly to the evolution of the groundwater passing through the porous medium. For primary minerals, an adequate conceptual model depends on

the knowledge of the local geology and lithology as well as on the spatial distribution and quantity of the minerals present. The heterogeneous nature of aquifers requires averaging of measured data and relies on the applicability of the REV-conceptualization.

The interaction of the infiltrating water with the aquifer minerals may lead to a supersaturated solution with respect to mineral phases, which are not part of the initial composition of the aquifer. The incorporation of secondary minerals into the conceptual model is very difficult, yet very important, because these mineral phases may significantly contribute to the buffer capacity of the aquifer. An additional complication arises if ion exchange reactions influence the evolution of the pore water passing through the aquifer. These complications must be carefully considered when attempting to use the model for predictive purposes.

Ideally, MIN3P should be applied to the analysis of laboratory experiments or field data with the goal to quantitatively describe and test the underlying conceptual models. Model applications can focus on either chemical complexity in batch, one- or two-dimensional systems or complex interactions between transport and reaction processes in heterogeneous two- or possibly three-dimensional flow fields. The model can be used for the investigation of processes characterized by a wide range of time scales and can be used to evaluate the importance of various transport and reaction mechanisms on the evolution of groundwater systems.

The model MIN3P is well suited for future extensions and enhancements, because its formulation is based on a modular approach. Future research can be focused in various directions, such as the consideration of irregular domain geometries, additional reaction and transport processes, the consideration of reaction processes in stagnant pore water, mass transfer between stagnant and moving pore water, the implementation of alternative coupling schemes, such as the operator-splitting technique, and the consideration of aquifer heterogeneity.

Reaction processes not considered in the present model include adsorption, surface complexation, isotope fractionation, incongruent mineral dissolution, the dissolution and precipitation of solid solutions, and Monod-kinetics. Any of these processes can be implemented in the existing model by incorporating additional modules/subroutines that specify the reaction parameters and compute the rates (and the corresponding derivatives) of formation or depletion of these species or relate these species concentrations to the components by equilibrium relationships. The model application in Chapter 7 suggests that microbially-mediated reactions (Monod-kinetics) and surface complexation

reactions (for H^+-sorption) should be included in the model to allow a more complete description of reactive transport in porous media.

Theoretical considerations have shown that the existence of a gas phase complicates the solution of reactive transport equations considerably. An inherent coupling exists in this case between reaction and transport processes in the gaseous and aqueous phase. A rigorous formulation that includes advective and diffusive transport processes for both mobile phases must be based on a compositional solution approach [*Corapcioglu and Baehr*, 1987, *Sleep and Sykes*, 1993 *Unger et al.*, 1995]. Such an approach automatically accounts for advective gas transport induced by changes in moisture content or by the production or consumption of gaseous species as a result of geochemical reactions. In this context, it may also be beneficial to enhance the present model to allow for non-isothermal conditions and to account for the influence of mineral dissolution-precipitation reactions on the permeability of the medium.

A model description which takes into account stagnant and mobile water should be developed in future work. This approach is particularly needed in the unsaturated zone. Preliminary simulations in Chapter 6 showed that mass transfer processes between mobile and stagnant water appear to have a significant impact on the oxidation of sulfide minerals and the concentrations of dissolved species. In some cases, the single continuum approach, which assumes complete mixing between stagnant pore water and mobile groundwater, appears to be an insufficient description of processes occurring in nature. This is especially true for heterogeneous reactions involving surface or solid species. Therefore, future research should be directed towards the implementation of a dual-continuum approach which accounts for reaction processes in both immobile and mobile pore water, and diffusion-limited mass transfer between mobile and immobile waters. Such a formulation can be developed from a generalization of the rate expressions for diffusion-controlled dissolution-precipitation reactions or can be based on a dual porosity approach.

Alternative coupling schemes, such as a non-iterative operator-splitting method, could be implemented in the present model. This approach appears to be useful for large scale reactive transport applications in saturated porous media, but it is likely of limited use if a gas phase exists. Extremely short time scales of transport processes in the gas phase may cause the solution of reactive transport equations exclusively by the operator-splitting method to be inefficient. On the other hand, the global implicit method is sometimes affected by severe local chemical changes, which imposes small time steps for the entire solution domain. From a theoretical view point, the most efficient solution method will

therefore incorporate both an operator-splitting and a global implicit solution method. The selection of the optimal solution method should be utilized based on the conditions characterizing the system at a particular instant in time.

Bibliography

Abrams, R. H., K. Loague, and D. B. Kent, Development and testing of a compartmentalized reaction network model for redox zones in contaminated aquifers, *Water Resources Research*, *34*(6), 1531–1541, 1998.

Ahonen, L., and O. H. Tuovinen, Microbiological oxidation of ferrous iron at low temperature, *Applied and Environmental Microbiology*, *55*(2), 312–316, 1989.

Al, T. A., D. W. Blowes, C. J. Martin, L. J. Cabri, and J. L. Jambor, Aqueous geochemistry and analysis of pyrite surfaces in sulfide-rich mine tailings, *Geochimica et Cosmochimica Acta*, *61*(12), 2353–2366, 1997.

Allison, J. D., D. S. Brown, and K. J. Novo-Gradac. *MINTEQA2/PRODEFA2, A geochemical assessment model for environmental systems: Version 3.0 Users's Manual.* Environmental research laboratory, U.S Environmental Protection Agency, EPA/600/3-91/021, 1991.

Appelo, C. A. J., and D. Postma, *Geochemistry, groundwater and pollution*, A. A. Balkema, Rotterdam, Netherlands, 1993.

Bahr, J. M., and J. Rubin, Direct comparison of kinetic and local equilibrium formulations for solute transport affected by surface reactions, *Water Resources Research*, *23*(3), 438–452, 1987.

Ball, J. W., and D. K. Nordstrom. *User's Manual for WATEQ4F, with revised thermodynamic database and test cases for calculating speciation of major, trace and redox elements in natural waters.* US Geological Survey, Open-File Report 91-183, 189 pp., plus diskette, 1991.

Baron, D. Iron-chromate precipitates in Cr(VI)-contaminated soils: identification, solubility, and solid solution/aqueous solution reactions. Ph.D. thesis, Oregon Graduate Institute of Science & Technology, Oregon, 1996.

Barry, D. A., C. T. Miller, and P. J. Culligan-Hensley, Temporal discretisation errors in non-iterative split-operator approaches solving chemical reaction/groundwater transport models, *Journal of Contaminant Hydrology*, *22*(1-2), 1–17, 1996.

Bear, J., *Dynamics of fluids in porous media*, Elsevier Science, New York, 1972.

Bennett, T. A., An *in-situ* reactive barrier for the treatment of hexavalent chromium and trichloroethylene in grondwater, M.Sc. thesis, University of Waterloo, Waterloo, Ontario, Canada, 1997.

Benson, D., *Mechanisms of Inorganic Reactions in Solution*, McGraw Hill, New York, 1968.

Berner, R. A., Rate control of mineral dissolution under earth surface conditions, *American Journal of Science*, *278*, 1235–1252, 1978.

Bethke, C. M., *Geochemical Reaction Modeling*, Oxford University Press, New York, 1996.

Bigham, J. M., U. Schwertmann, S. J. Traina, R. L. Winland, and M. Wolf, Schwertmannite and the chemical modelling of iron in acid sulfate waters, *Geochimica et Cosmochimica Acta*, *60*(12), 2111–2121, 1996.

Blowes, D. W., T. A. Al, L. Lortie, W. D. Gould, and J. L. Jambor, Microbiological, chemical and mineralogical characterization of the Kidd Creek mine tailings impoundment, Timmins area, Ontario, *Geomicrobiology Journal*, *13*, 13–31, 1995.

Blowes, D. W., J. A. Cherry, and E. J. Reardon, The hydogeochemistry of four inactive tailings impoundments: Perspectives on tailings pore water evolution, in National Symposium on Mining, Hydrology, Sedimentology and Reclamation, Lexington, Kentucky, University of Kentucky, 1987, December 7-11).

Blowes, D. W., and J. L. Jambor, The pore water geochemistry and mineralogy of the vadose zone of sulfide tailings, Waite Amulet, Quebec, Canada, *Applied Geochemistry*, *5*, 327-346, 1990.

Blowes, D. W., J. L. Jambor, E. C. Appleyard, E. J. Reardon, and J. A. Cherry, Temporal observations of the geochemistry and mineralogy of a sulfide-rich mine-tailings impoundment, Heath Steeles Mines, New Brunswick, *Explor. Mining Geol.*, *1*(3), 251–264, 1992.

Blowes, D. W., and C. J. Ptacek, Acid-neutralization mechanisms in inactive mine tailings, in The environmental geochemistry of sulfide mine-wastes, Short course

handbook 22, edited by D. W. Blowes, and J. L. Jambor, Chapter 10, 271–292. Mineralogical Association of Canada, 1994.

Blowes, D. W., C. J. Ptacek, and J. L. Jambor, *In-Situ* remediation of Cr(VI)-contaminated groundwater using permeable reactive walls: Laboratory studies, *Environmental Science & Technology*, *31*(12), 3348–3357, 1997.

Blowes, D. W., E. J. Reardon, J. L. Jambor, and J. A. Cherry, The formation and potential importance of cemented layers in inactive sulfide mine tailings, *Geochimica et Cosmochimica Acta*, *55*, 965–978, 1991.

Blum, A. E., and A. C. Lasaga, Role of surface speciation in the low temperature dissolution of minerals, *Nature*, *33*, 431–433, 1988.

Blum, A. E., and A. C. Lasaga, The role of surface speciation in the dissolution of albite, *Geochimica et Cosmochimica Acta*, *55*, 2193–2201, 1991.

Blum, A. E., and L. L. Stillings, Feldspar dissolution kinetics, in Chemical Weathering Rates of Silicate Minerals, edited by A. F. White, and S. L. Brantley, *31* of *Reviews in Mineralogy*, Mineralogical Society of America, Washington, DC, 1995.

Bodo, C., and D. G. Lundgren, Iron oxidation by cell envelopes of Thiobacillus ferroxidans, *Canadian Journal of Microbiology*, *20*, 1647–1652, 1974.

Brand, T., C. König, and G. Schmid, Hydrogeochemical transport model, Paper presented at the *Tenth International Conference on Computational Methods in Water Resources, Heidelberg, Germany*, (unpublished), 1994.

Bryant, S. L., R. S. Schechter, and L. W. Lake, Interactions of precipitation/dissolution waves and ion exchange in flow through permeable porous media, *AIChE Journal*, *32*(5), 751–764, 1986.

Burnett, R. D., and E. O. Frind, Simulation of contaminant transport in three dimensions 2. Dimensionality effects, *Water Resources Research*, *23*(4), 695–705, 1987.

Carroll, S. A., and J. V. Walther, Kaolinite dissolution at 25°, 60°, and 80°, *American Journal of Science*, *290*, 797–810, 1990.

Cathles, L. M., Predictive capabilities of a finite difference model of copper leaching in low grade industrial sulfide waste dumps, *Mathematical Geology*, *11*(2), 175–191, 1979.

Cederberg, G. A., R. L. Street, and J. O. Leckie, A groundwater mass transport and

equilibrium chemistry model for multicomponent systems, *Water Resources Research*, *21*(8), 1095–1104, 1985.

Cheng, I. F., R. Muftikian, Q. Fernando, and N. Korte, Reduction of nitrate to ammonia by zero-valent iron, in Proc. 213th ACS National Meeting, Vol. 37, No. 1, 165–166, San Francisco, CA, American Chemical Society, Division of Environmental Chemistry, 1997.

Chou, L., R. M. Garrels, and R. Wollast, Comparative study of the kinetics and mechanisms of dissolution of carbonate minerals, *Chemical Geology*, *78*, 269–282, 1989.

Chou, L., and R. Wollast, Steady-state kinetics and dissolution mechanisms of albite, *American Journal of Science*, *285*, 963–993, 1985.

Cirpka, O. Numerische Methoden zur Simulation des reaktiven Mehrkomponententransports im Grundwasser. Ph.D. thesis, Universität Stuttgart, Institut für Wasserbau, Germany, 1997.

Claesson, A. N., and K. Andersson, PHRQKIN - A program simulating dissolution and precipitation kinetics in groundwater solutions, *Computers & Geosciences*, *22*(5), 559–567, 1996.

Cleary, R. W., and M. J. Ungs, Analytical models for groundwater pollution and hydrology, Report No. 78-WR-15, Water Resources Program, Princeton University, N. J., 1978.

Clement, T. P., W. R. Wise, and F. J. Molz, A physically based, two-dimensional, finite-difference algorithm for modeling variably saturated flow, *Journal of Hydrology*, *161*, 71–90, 1994.

Cooley, R. L., Some new procedures for numerical solution of variably saturated flow problems, *Water Resources Research*, *19*(5), 1271–1285, 1983.

Corapcioglu, M. Y., and A. L. Baehr, A compositional multiphase model for groundwater contamination by petroleum products 1. Theoretical considerations, *Water Resources Research*, *23*(1), 191–200, 1987.

Crerar, D. A., A method for computing multicomponent chemical equilibria based on equilibrium constants, *Geochimica et Cosmochimica Acta*, *39*, 1375–1384, 1975.

Damköhler, G., Einflüsse der Strömung, Diffusion und des Wärmeübergangs auf die Leistung von Reaktionsöfen, *Ztschr. Elektrochem.*, *42*(12), 846–862, 1936.

Daus, A. D., E. O. Frind, and E. A. Sudicky, Comparative error analysis in finite element formulations of the advection-dispersion equation, *Advances in Water Resources*, *8*, 86–95, 1985.

Davis, G. B., and A. I. M. Ritchie, A model of oxidation in pyritic mine wastes: Part 1: Equations and approximate solution, *Applied Mathematical Modelling*, *10*, 314–322, 1986.

Davis, L., and S. P. Neuman. *Documentation and User's Guide: UNSAT2 - Variably saturated flow model.* U.S. Nuclear Regulatory Commission Report, NUREG/CR-3390, Washington, D.C., 1983.

Dove, P. M., Kinetic and thermodynamic controls on silica reactivity in weathering environments, in Chemical Weathering Rates of Silicate Minerals, edited by A. F. White, and S. L. Brantley, *31* of *Reviews in Mineralogy*, Mineralogical Society of America, Washington, DC, 1995.

Dubrovsky, N. M. Geochemical evolution of inactive pyritic tailings in the Elliot Lake uranium district. Ph.D. thesis, University of Waterloo, University of Waterloo, Waterloo, Ontario, Canada, 1986.

Dubrovsky, N. M., J. A. Cherry, E. J. Reardon, and A. J. Vivyurka, Geochemical evolution of inactive pyritic tailings in the Elliot Lake uranium district: 1. The groundwater zone, *Canadian Geotechnical Journal*, *22*(1), 110–128, 1984.

Dubrovsky, N. M., K. A. Morin, J. A. Cherry, and D. J. A. Smyth, Uranium tailings acidification and subsurface contaminant migration in a sand aquifer, *Water Poll. Res. J. Canada*, *19*(2), 55–89, 1984.

Eary, L. E., and J. A. Schramke, Rates of inorganic oxidation reactions involving dissolved oxygen, in Chemical Modeling of Aqueous Systems II, edited by D. C. Melchior, and R. L. Bassett, Chapter 30, 379–396. Washington, D.C., USA, American Chemical Society, 1990.

Engesgaard, P., and T. H. Christensen, A review of chemical solute transport models, *Nordic Hydrology*, *19*, 183–216, 1988.

Engesgaard, P., and K. L. Kipp, A geochemical transport model for redox-controlled movement of mineral fronts in groundwater systems: A case of nitrate removal by oxidation of pyrite, *Water Resources Research*, *28*(10), 2829–2843, 1992.

Fletcher, R., *Practical Methods of Optimization* (2nd ed.)., John Wiley & Sons, Chichester, New York, 1987.

Förster, R., A multicomponent transport model, *Geoderma*, *38*, 261–278, 1986.

Forsyth, P. A., Comparison of the single-phase and two-phase numerical model formulation for saturated-unsaturated groundwater flow, *Computer Methods in Applied Mechanics and Engineering*, *69*, 243–259, 1988.

Forsyth, P. A., and P. H. Sammon, Practical considerations for adaptive implicit methods in reservoir simulation, *Journal of Computational Physics*, *62*, 265–281, 1986.

Forsyth, P. A., and B. Y. Shao, Numerical simulation of gas venting for NAPL site remediation, *Advances in Water Resources*, *14*(6), 354–367, 1991.

Forsyth, P. A., and R. B. Simpson, A two-phase, two-component model for natural convection in a porous medium, *International Journal for Numerical Methods in Fluids*, *12*, 655–682, 1991.

Forsyth, P. A., A. J. A. Unger, and E. A. Sudicky, Nonlinear iteration methods for nonequilibrium multiphase subsurface flow, *Advances in Water Resources*, *21*, 433–449, 1998.

Forsyth, P. A., Y. S. Wu, and K. Pruess, Robust numerical methods for saturated-unsaturated flow with dry initial conditions in heterogeneous media, *Advances in Water Resources*, *18*, 25–38, 1995.

Friedly, J. C., and J. Rubin, Solute transport with multiple equilibrium-controlled or kinetically controlled reactions, *Water Resources Research*, *28*(6), 1935–1953, 1992.

Garrels, R. M., and M. E. Thompson, Oxidation of pyrite by iron sulfate solutions, *American Journal of Science*, *258-A*, 57–67, 1960.

Gerke, H. H., J. W. Molson, and E. O. Frind, Modelling the effect of chemical heterogeneity on acidification and solute leaching in overburden mine spoils, *Journal of Hydrology*, *209*, 166–185, 1998.

Glinski, J., and W. Stepniewski, *Soil aeration and its role for plants*, CRC Press, Boca Raton, Florida, 1985.

Gould, J. P., The kinetics of hexavalent chromium reduction by metallic iron, *Water Research*, *16*, 871–877, 1982.

Greenberg, J., and M. Tomson, Precipitation and dissolution kinetics and equilibria of aqueous ferrous carbonate vs temperature, *Applied Geochemistry*, *7*, 185–190, 1992.

Hall, C. A., and T. A. Porsching, *Numerical Analysis for Partial Differential Equations*, Englewood Cliffs, New Jersey, 1990.

Helgeson, H. C., T. H. Brown, A. Nigrini, and T. A. Jones, Calculation of mass transfer in geochemical processes involving aqueous solutions, *Geochimica et Cosmochimica Acta*, *34*, 569–592, 1970.

Helgeson, H. C., W. M. Murphy, and P. Aagaard, Thermodynamics and kinetic constraints on reaction rates among minerals and aqueous solutions. II. Rate constants, effective surface area and the hydrolysis of feldspar, *Geochimica et Cosmochimica Acta*, *48*, 2405–2432, 1984.

Herzer, J., and W. Kinzelbach, Coupling of transport and chemical processes in numerical transport models, *Geoderma*, *44*, 115–127, 1989.

Hindmarsh, A. C., and L. R. Petzold, Algorithms and software for ordinary differential equations and differential/algebraic equations, Part I: Euler methods and error estimation, *Computers in Physics*, *9*(1), 34–41, 1995a.

Hindmarsh, A. C., and L. R. Petzold, Algorithms and software for ordinary differential equations and differential/algebraic equations, Part II: Higher-order methods and software packages, *Computers in Physics*, *9*(2), 148–155, 1995b.

Hiskey, J. B., and W. J. Schlitt, Aqueous oxidation of pyrite, in Interfacing Technologies in Solution Mining, 55–74, AIME, Proc. 2nd SME-SPE Int'l Solution Mining Symp., 1982.

Holm, T. R., Comment on "Computing the equilibrium composition of aqueous systems: An iterative solution at each step in Newton-Raphson", *Environ. Sci. Technol.*, *23*(12), 1531–1532, 1989.

Hundsdorfer, W., and J. G. Verwer, A note on splitting errors for advection-reaction equations, Technical Report NM-R9424, CWI, Amsterdam, The Netherlands, 1991.

Hunter, K. S., Y. Wang, and P. VanCappellen, Kinetic modeling of microbially-driven redox chemistry of subsurface environments: coupling transport, microbial metabolism and geochemistry, *Journal of Hydrology*, *209*, 53–80, 1998.

Huyakorn, P. S., S. D. Thomas, and B. M. Thompson, Techniques for making finite elements competitive in modeling flow in variably saturated media, *Water Resources Research*, *20*(8), 1099–1115, 1984.

I, T.-P., and G. H. Nancollas, EQUIL - A general computational method for the calculation of solution equilibria, *Analytical Chemistry*, *44*(12), 1940–1950, 1972.

Jambor, J. L., Nature, origin and evolution of ferrihydrite, Unpublished report, Department of Public Works and Government Services Canada for Natural Resources Canada, Contract. Nr. 23440-5-1323/01-SQ, 1996.

Jaynes, D. B., A. S. S. Rogowski, and H. B. Pionke, Acid mine drainage from reclaimed coal strip mines. 1. Model description, *Water Resources Research*, *20*(2), 233–242, 1984a.

Jaynes, D. B., H. B. Pionke, and A. S. Rogowski, Acid mine drainage from reclaimed coal strip mines. 2. Simulation results of model, *Water Resources Research*, *20*(2), 243–250, 1984b.

Jennings, A. A., D. J. Kirkner, and T. L. Theis, Multicomponent equilibrium chemistry in groundwater quality models, *Water Resources Research*, *18*(4), 1089–1096, 1982.

Johnson, R. H., The physical and chemical hydrogeology of the Nickel Rim Mine Tailings, Sudbury, Ontario, M.Sc. thesis, University of Waterloo, Waterloo, Ontario, Canada, 1993.

Kaluarachichi, J. J., and J. Morshed, Critical assessment of the operator-splitting technique in solving the advection-dispersion-reaction equation: 1. First-order reaction, *Advances in Water Resources*, *18*(2), 89–100, 1995.

Kinzelbach, W., and W. Schäfer, Coupling of chemistry and transport, in Groundwater Management: Quantity and Quality, edited by A. Sahuquillo, J. Andreu, and T. O'Donell, 237–259. International Association of Hydrogeological Sciences, 1989.

Kirkner, D. J., and H. Reeves, Multicomponent mass transport with homogeneous and heterogeneous chemical reactions: Effect of the chemistry on the choice of the numerical algorithm 1. Theory, *Water Resources Research*, *24*(10), 1719–1729, 1988.

Klein, C., and C. S. Hurlbut Jr., *Manual of Mineralogy* (21 ed.)., John Wiley & Sons, Inc., New York, 1993.

Knapp, R. B., Spatial and temporal scales of local equilibrium in dynamic fluid-rock systems, *Geochimica et Cosmochimica Acta*, *53*, 1955–1964, 1989.

Lasaga, A. C., Rate laws of chemical reactions, in Kinetics of geochemical processes, edited by A. C. Lasaga, and R. J. Kirkpatrick, Chapter 1, 1–68. Washington, D.C.,

USA, Mineralogical Society of America, 1981.

Lasaga, A. C., Chemical kinetics of water-rock interactions, *Journal of Geophysical Research*, *89*(B6), 4009–4025, 1984.

Lasaga, A. C., *Kinetic Theory in the Earth Sciences*, Princeton University Press, Princeton, New Jersey, 1998.

Lasaga, A. C., J. M. Soler, J. Ganor, T. E. Burch, and K. L. Nagy, Chemical weathering rate laws and global geochemical cycles, *Geochimica et Cosmochmica Acta*, *58*(10), 2361–2386, 1994.

Leeming, G. J. S., K. U. Mayer, and R. B. Simpson, Effects of chemical reactions on iterative methods for implicit time stepping, *Advances in Water Resources*, *22*, 333–347, 1998.

Levenspiel, O., *Chemical Reaction Engineering*, J. Wiley and Sons, New York, 1972.

Lewis, G. N., and M. Randall, *Thermodynamics*, 2nd. ed. revised by: *K.S. Pitzer* and *L. Brewer*, McGraw Hill, New York, 1961.

Lichtner, P. C., Continuum model for simultaneous chemical reactions and mass transport in hydrothermal systems, *Geochimica et Cosmochimica Acta*, *49*, 779–800, 1985.

Lichtner, P. C., The quasi stationary state approximation to coupled mass transport and fluid-rock interaction in a porous medium, *Geochimica et Cosmochimica Acta*, *52*, 143–165, 1988.

Lichtner, P. C., Time-space continuum description of fluid/rock interaction in permeable media, *Water Resources Research*, *28*(12), 3135–3155, 1992.

Lichtner, P. C., Scaling properties of time-space kinetic mass transport equations and the local equilibrium limit, *American Journal of Science*, *293*, 257–296, 1993.

Lichtner, P. C., Continuum formulation of multicomponent-multiphase reactive transport, in Reactive Transport in Porous Media, edited by P. C. Lichtner, C. I. Steefel, and E. H. Oelkers, *34* of *Reviews in Mineralogy*, Mineralogical Society of America, Washington, DC, 1996a.

Lichtner, P. C., Modeling of reactive flow and transport in natural systems, in Proceedings of the Rome Seminar on Environmental Geochemistry, 5–72, Castelnuovo di Porto, 1996b, May 22-26).

Lichtner, P. C. Benchmark problem: Acid mine drainage. Workshop on Subsurface Reactive Transport Modeling, Pacific Northwest National Laboratory, Richland, WA, 1997a, Oct 29 - Nov 1).

Lichtner, P. C. Benchmark problem: Copper leaching from a five spot well pattern. Workshop on Subsurface Reactive Transport Modeling, Pacific Northwest National Laboratory, Richland, WA, 1997b, Oct 29 - Nov 1).

Lichtner, P. C., and M. S. Seth, Multiphase-multicomponent nonisothermal reactive transport in partially saturated porous media: Application to the proposed Yucca Mountain HLW Repository, in Proceedings International Conference on Deep Geologic Disposal of Radioactive Waste, 3–133–3–142, Winnipeg, Manitoba, Canada, Canadian Nuclear Society, 1996, September 16-19).

Liu, C. W., and T. N. Narasimhan, Redox controlled multiple-species reactive chemical transport: 1. Model development, *Water Resources Research*, *25*(5), 869–882, 1989a.

Liu, C. W., and T. N. Narasimhan, Redox controlled multiple-species reactive chemical transport: 2. Verification and application, *Water Resources Research*, *25*(5), 883–910, 1989b.

Lovley, D. R., and S. Goodwin, Hydrogen concentrations as an indicator of the predominant terminal electron-accepting reactions in aquatic sediments, *Geochimica et Cosmochmica Acta*, *52*, 2993–3003, 1988.

Lowson, R. T., Aqueous oxidation of pyrite by molecular oxygen, *Chemical Reviews*, *82*(5), 461–497, 1982.

Luckner, L., and W. M. Schestakow, *Migration Processes in the Soil and Groundwater Zone*, Lewis Publishers, Inc., Chelsea, Michigan, 1991.

MacKenzie, P. D., T. M. Sivavec, and D. P. Horney, Mineral precipitation and porosity losses in iron treatment zones, in Proc. 213th ACS National Meeting, Vol. 37, No. 1, 154–157, San Francisco, CA, American Chemical Society, Division of Environmental Chemistry, 1997.

MacQuarrie, K. T. B. Multicomponent simulation of wastewater-derived nitrogen and carbon in shallow unconfined aquifers. Ph.D. thesis, University of Waterloo, Waterloo, Ontario, Canada, 1997.

MacQuarrie, K. T. B., E. A. Sudicky, and E. O. Frind, Simulation of biodegradable

organic contaminants in groundwater 1. Numerical formulation in principal directions, *Water Resources Research*, *26*(2), 207–222, 1990.

Mangold, D. C., and C.-F. Tsang, A summary of subsurface hydrological and hydrochemical models, *Review of Geohysics*, *29*(1), 51–79, 1991.

Marzal, P., A. Seco, J. Ferrer, and C. Gabaldón, Modeling multiple reactive solute transport with adsorption under equilibrium and nonequilibrium conditions, *Advances in Water Resources*, *17*, 363–374, 1994.

Massmann, J., and D. F. Farrier, Effects of atmospheric pressures on gas transport in the vadose zone, *Water Resources Research*, *28*(3), 777–791, 1992.

McKibben, M. A., and H. L. Barnes, Oxidation of pyrite in low temperature acidic solutions: Rate laws and surface textures, *Geochimica et Cosmochimica Acta*, *50*, 1509–1520, 1986.

McNab Jr., W. W., and T. N. Narasimhan, Modeling reactive transport of organic compounds in groundwater using a partial redox disequilibrium approach, *Water Resources Research*, *30*(9), 2619–2635, 1994.

Miller, C. T., and A. J. Rabideau, Development of split-operator, Petrov-Galerkin methods to simulate transport and diffusion problems, *Water Resources Research*, *29*(7), 2227–2240, 1993.

Miller, C. W., and L. V. Benson, Simulation of solute transport in a chemically reactive heterogeneous system: Model development and application, *Water Resources Research*, *19*(2), 381–391, 1983.

Millero, F. J., The effect of ionic interactions on the oxidation of metals in natural waters, *Geochimica et Cosmochimica Acta*, *49*, 547–553, 1985.

Millington, R. J., Gas diffusion in porous media, *Science*, *130*, 100–102, 1959.

Morin, K. A., and J. A. Cherry, Migration of acidic groundwater seepage from uranium-tailings impoundment, 3. Simulation of the conceptual model with application to seepage area A, *Journal of Contaminant Hydrology*, *2*(4), 323–342, 1988.

Morin, K. A., J. A. Cherry, K. D. Nand, T. P. Lim, and A. J. Vivyurka, Migration of acidic groundwater seepage from uranium-tailings impoundment, 1. Field study and conceptual hydrogeochemical model, *Journal of Contaminant Hydrology*, *2*(4), 271–303, 1988.

Morshed, J., and J. J. Kaluarachichi, Critical assessment of the operator-splitting technique in solving the advection-dispersion-reaction equation: 2. Monod kinetics and coupled transport, *Advances in Water Resources*, *18*(2), 101–110, 1995.

Moses, C. O., and J. S. Herman, Pyrite oxidation at circumneutral pH, *Geochimica et Cosmochimica Acta*, *55*, 471–482, 1991.

Moses, C. O., D. K. Nordstrom, J. S. Herman, and A. L. Mills, Aqueous pyrite oxidation by dissolved oxygen and by ferric iron, *Geochimica et Cosmochimica Acta*, *51*, 1561–1571, 1987.

Murphy, W. M., E. H. Oelkers, and P. C. Lichtner, Surface reaction versus diffusion control of mineral dissolution and growth rates in geochemical processes, *Chemical Geology*, *78*, 357–380, 1989.

Nagy, K. L., Dissolution and precipitation kinetics of sheet silicates, in Chemical Weathering Rates of Silicate Minerals, edited by A. F. White, and S. L. Brantley, *31* of *Reviews in Mineralogy*, Mineralogical Society of America, Washington, DC, 1995.

Narasimhan, T. N., A. F. White, and T. Tokunaga, Groundwater contamination from an inactive uranium mill tailings pile. 2. Application of a dynamic mixing model, *Water Resources Research*, *22*(13), 1820–1834, 1986.

Neuman, S. P., Saturated-unsaturated seepage by finite elements, *ASCE - Journal of the Hydraulics Division*, *99*(HY12), 2233–2250, 1973.

Nguyen, V. V., W. G. Gray, G. F. Pinder, J. F. Botha, and D. A. Crerar, A theoretical investigation on the transport of chemicals in reactive porous media, *Water Resources Research*, *18*(4), 1149–1156, 1982.

Nicholson, R. V., Iron-sulfide oxidation mechanisms,: Laboratory studies, in The environmental geochemistry of sulfide mine-wastes, Short course handbook 22, edited by D. W. Blowes, and J. L. Jambor, Chapter 6, 163–183. Mineralogical Association of Canada, 1994.

Nicholson, R. V., R. W. Gillham, and E. J. Reardon, Pyrite oxidation in carbonate-buffered solution: 1. Experimental kinetics, *Geochimica et Cosmochimica Acta*, *52*, 1077–1085, 1988.

Nicholson, R. V., R. W. Gillham, and E. J. Reardon, Pyrite oxidation in carbonate-buffered solution: 2. Rate control by oxide coatings, *Geochimica et Cosmochimica Acta*, *54*, 395–402, 1990.

Nordstrom, D. K., and C. N. Alpers, Geochemistry of acid mine waters, part A - Processes, techniques and health, in Environmental Geochemistry of Mineral Deposits, Rev. Econ. Geol., edited by G. Plumlee, and M. Logsdon, *6a*, Chapter 6. Soc. Econ. Geol., in preparation, 1998.

Nordstrom, D. K., and G. Southam, Geomicrobiology of sulfide mineral oxidation, in Geomicrobiology: Interactions between microbes and minerals, edited by J. F. Banfield, and K. H. Nealson, *35* of *Reviews in Mineralogy*, Mineralogical Society of America, Washington, DC, 1997.

Ogata, A., and R. B. Banks, A solution of the differential equation of longitudinal dispersion in porous media, Prof. Paper 411-A, USGS, 1961.

O'Hannesin, S. F., C. J. Hanton-Fong, D. W. Blowes, R. W. Gillham, and C. J. Ptacek. Remediation of groundwater contaminated with chromium and TCE using reactive barriers: Laboratory batch and column testing. Progress Report II for EPA - R.S. Kerr Environmental Research Lab, Waterloo Centre for Groundwater Research, University of Waterloo, Waterloo, Ontario, 1995, June).

Orth, W. S., and R. W. Gillham, Dechlorination of trichloroethene in aqueous solution using Fe^0, *Environmental Science & Technology*, *30*(1), 66–71, 1996.

Ortoleva, P., E. Merino, C. Moore, and J. Chadam, Geochemical self-organization I: Reaction-transport feedbacks and modeling approach, *American Journal of Science*, *287*, 979–1007, 1987a.

Ortoleva, P., J. Chadam, E. Merino, and A. Sen, Geochemical self-organization II: The reactive infiltration instability, *American Journal of Science*, *287*, 1008–1040, 1987b.

Panday, S., P. S. Huyakorn, R. Therrien, and R. L. Nichols, Improved three-dimesional finite-element techniques for field simulation of variably saturated flow and transport, *Journal of Contaminant Hydrology*, *12*, 3–33, 1993.

Paniconi, C., and M. Putti, A comparison of Picard and Newton iteration in the numerical solution of multidimensional variably saturated flow problems, *Water Resources Research*, *30*(12), 3357–3374, 1994.

Pantelis, G., and A. I. M. Ritchie, Macroscopic transport mechanisms as a rate-limiting factor in dump leaching of pyritic ores, *Applied Mathematical Modeling*, *15*(3), 136–143, 1991.

Parkhurst, D. L., D. C. Thorstensen, and N. L. Plummer. *PHREEQE - A computer program for geochemical calculations.* U.S. Geological Survey, Reston, VA, USGS/WRI-80-96, 1980.

Perkins, E. H., Y. K. Kharaka, W. D. Gunter, and J. D. De Braal, Geochemical modeling of water-rock interactions using SOLMINEQ.88, in Chemical Modeling of Aqueous Systems II, edited by D. C. Melchior, and R. L. Bassett, Chapter 9, 117–127. Washington, D.C., American Chemical Society, 1990.

Powell, R. M., R. W. Puls, S. K. Hightower, and D. A. Sabatini, Coupled iron corrosion and chromate reduction: Mechanisms for subsurface remediation, *Environmental Science & Technology*, *29*, 1913–1922, 1995.

Prein, A. Sauerstoffzufuhr als limitierender Faktor für die Pyritverwitterung in Abraumkippen von Braunkohletagebauen. Ph.D. thesis, Universität Hannover, Hannover, Germany, 1994.

Puls, R. W., D. Clark, C. J. Paul, and J. Vardy, Characterization of chromium contaminated soils and ground water in the vicinity of a chrome plating operation, in Subsurface Restoration Conference. Third International Conference on Ground Water Quality Research, 180–182, Dallas, Texas, 1992.

Puls, R. W., R. M. Powell, and C. J. Paul, In situ remediation of ground water contaminated with chromate and chlorinated solvents using zero-valent iron: A field study, in Proc. 209th ACS National Meeting, Vol. 35, No. 1, 788–791, Anaheim, CA, American Chemical Society, Division of Environmental Chemistry, 1995.

Puls, R. W., T. F. Rees, P. M. Lindley, and C. J. Paul, Surface analysis of chromium contaminated soils using scanning electron microscopy with energy dispersive X-ray (SEM-EDS) and secondary ion mass spectroscopy (SIMS), in Subsurface Restoration Conference. Third International Conference on Ground Water Quality Research, 125–127, Dallas, Texas, 1992.

Rahman, A., and A. Agrawal, Reduction of nitrate and nitrite by iron meatl: Implications for groundwater remediation, in Proc. 213th ACS National Meeting, Vol. 37, No. 1, 157–159, San Francisco, CA, American Chemical Society, Division of Environmental Chemistry, 1997.

Reardon, E. J., Anaerobic corrosion of granular iron: Measurement and interpretation of hydrogen evolution rates, *Environmental Science & Technology*, *29*(12), 2936–2945, 1995.

Reardon, E. J., and P. M. Moddle, Gas diffusion coefficient measurements on uranium mill tailings: Implications to cover layer design, *Uranium*, *2*, 111–131, 1985.

Reeves, H., and D. J. Kirkner, Multicomponent mass transport with homogeneous and heterogeneous chemical reactions: Effect of the chemistry on the choice of the numerical algorithm 2. Numerical results, *Water Resources Research*, *24*(10), 1730–1739, 1988.

Ritchie, A. I. M., Oxygen transport, in The environmental geochemistry of sulfide mine-wastes, Short course handbook 22, edited by D. W. Blowes, and J. L. Jambor, Chapter 8, 201–245. Mineralogical Association of Canada, 1994.

Rubin, J., Transport of reacting solutes in porous media: Relation between mathematical nature of problem formulation and chemical nature of reactions, *Water Resources Research*, *19*(5), 1231–1252, 1983.

Rubin, J., Solute transport with multisegement, equilibrium controlled, classical reactions: Problem solvability and feed forward method's applicability for complex segments of at most binary participants, *Water Resources Research*, *28*(6), 1681–1702, 1992.

Schnoor, J. L., Kinetics of chemical weathering: A comparison of laboratory and field weathering rates, in Aquatic Chemical Kinetics, Reaction rates of processes in natural waters, edited by W. Stumm, John Wiley & Sons, Inc., New York, 1990.

Schulz, J. *Aufbau von Säulenversuchen zur Untersuchung der Pyritoxidation in Braunkohlentagebausedimenten.* Diplomarbeit, Ruhr-Universität Bochum, Bochum, Germany, 1995.

Sevougian, S. D., R. S. Schechter, and L. W. Lake, Effect of partial local equilibrium on the propagation of precipitation/dissolution waves, *Ind.Eng.Chem.Res.*, *32*, 2281–2304, 1993.

Shen, H., and N. P. Nikolaidis, A direct substitution method for multicomponent solute transport in ground water, *Ground Water*, *35*(1), 67–78, 1997.

Siantar, D. P., C. G. Schreier, and M. Reinhard, Transformation of the pesticide 1,2-dibromo-3-chloropropane (DBCP) and nitrate by iron powder and by $H_2/Pd/Al_2O_3$, in Proc. 209th ACS National Meeting, Vol. 35, No. 1, 745–748, Anaheim, CA, American Chemical Society, Division of Environmental Chemistry, 1995.

Šimůnek, J., and D. L. Suarez, Two-dimensional transport model for variably saturated porous media with major ion chemistry, *Water Resources Research*, *30*(4), 1115–1133, 1994.

Singer, P. C., and W. Stumm, Acid mine drainage: The rate determining step, *Science*, *167*, 1121–1123, 1970.

Sleep, B. E., and J. F. Sykes, Compositional simulation of groundwater contamination by organic compounds 1. Model development and verification, *Water Resources Research*, *29*(6), 1697–1708, 1993.

Smyth, D. J. A., Hydrogeological and geochemical studies above the watertable in an inactive uranium tailings impoundment near Elliot Lake, Ontario, M.Sc. thesis, University of Waterloo, Waterloo, Ontario, Canada, 1981.

Southam, G., and T. J. Beveridge, Enumeration of Thiobacilli within *p*H-neutral and acidic mine tailings and their role in the development of secondary mineral soil, *Applied and Environmental Microbiology*, *58*(6), 1904–1912, 1992.

Sparks, D. L., *Kinetics of soil chemical processes*, Academic Press Inc., San Diego, CA, USA, 1989.

Sposito, G., *Chemical Equilibria and Kinetics in Soils*, Oxford University Press, Inc., New York, 1994.

Steefel, C. I., and A. C. Lasaga, A coupled model for transport of multiple chemical species and kinetic precipitation/dissolution reactions with application to reactive flow in single phase hydrothermal systems, *American Journal of Science*, *294*, 529–592, 1994.

Steefel, C. I., and P. C. Lichtner, Multicomponent reactive transport in discrete fractures: II. Infiltration of hyperalkaline groundwater at Maqarin, Jordan, a natural analogue site, *Journal of Hydrology*, *209*, 200–224, 1998.

Steefel, C. I., and K. T. B. MacQuarrie, Approaches to modeling of reactive transport in porous media, in Reactive Transport in Porous Media, edited by P. C. Lichtner, C. I. Steefel, and E. H. Oelkers, *34* of *Reviews in Mineralogy*. Washington, DC, Mineralogical Society of America, 1996.

Stone, A. T., and J. J. Morgan, Kinetics of chemical transformations in the environment, in Aquatic Chemical Kinetics, Reaction rates of processes in natural waters, edited by W. Stumm, John Wiley & Sons, Inc., New York, 1990.

Stumm, W., and J. J. Morgan, *Aquatic chemistry*, Wiley & Sons, INC., New York, 1996.

Stumm, W., and R. Wollast, Coordination chemistry of weathering, *Reviews of Geophysics*, *28*(1), 53–69, 1990.

Suarez, D. L., and J. Šimůnek, Modeling of carbon dioxide transport and production in soil 2. Parameter selection, sensitivity analysis, and comparison of model predictions to field data, *Water Resources Research*, *29*(2), 499–513, 1993.

Sung, W., and J. J. Morgan, Kinetics and product of ferrous iron oxygenation in aqueous systems, *Environmental Science & Technology*, *14*(5), 561–568, 1980.

Therrien, R., and E. A. Sudicky, Three-dimensional analysis of variably-saturated flow and transport in discretely-fractured porous media, *Journal of Contaminant Hydrology*, *23*, 1–44, 1996.

Thorstenson, D. C., and D. W. Pollock, Gas transport in unsaturated porous media: The adequacy of Fick's law, *Reviews of Geophysics*, *27*(1), 61–78, 1989.

Tibble, P. A., and R. V. Nicholson, Oxygen consumption on sulphide tailings and tailings covers: Measured rates and applications, in Fourth International Conference on Acid Rock Drainage, Volume II, 647–661, Vancouver, B.C., 1997.

Unger, A. J. A., P. A. Forsyth, and E. A. Sudicky, Variable spatial and temporal weighting schemes for use in multi-phase compositional problems, *Advances in Water Resources*, *19*(1), 1–27, 1996.

Unger, A. J. A., E. A. Sudicky, and P. A. Forsyth, Mechanisms controlling vacuum extraction coupled with air sparging for remediation of heterogeneous formations contaminated by dense non-aqueous phase liquids, *Water Resources Research*, *31*(8), 1913–1925, 1995.

Valocchi, A. J., and M. Malmsted, Accuracy of operator splitting for advection-dispersion-reaction problems, *Water Resources Research*, *28*(5), 1471–1476, 1992.

Valocchi, A. J., R. L. Street, and P. V. Roberts, Transport of ion-exchanging solutes in groundwater: Chromatographic theory and field simulation, *Water Resources Research*, *17*(5), 1517–1527, 1981.

van Breukelen, B. M., C. A. J. Appelo, and T. N. Olsthoorn, Hydrogeochemical transport modeling of 24 years of Rhine water infiltration in the dunes of the Amsterdam Water Supply, *Journal of Hydrology*, *209*, 281–296, 1998.

van der Vorst, H. A., BI-CGSTAB: A fast and smoothly converging variant of BI-CG for the solution of nonsymmetric linear systems, *SIAM J. Sci. Stat. Comput.*, *13*(2), 631–644, 1992.

van Leer, B., Towards the ultimate conservative scheme. II Monotonicity and conservation combined in a second order scheme, *J. Comp. Phys.*, *14*, 361–370, 1974.

van Zeggeren, F., and S. H. Storey, *The Computation of Chemical Equilibria*, Cambridge University Press, London, England, 1970.

VanderKwaak, J. E., P. A. Forsyth, K. T. B. MacQuarrie, and E. A. Sudicky. *WatSolv - Sparse Matrix Iterative Solver, User's Guide for Version 2.16.* University of Waterloo, Waterloo, ON, 1997.

Vauclin, M., D. Khanji, and G. Vachaud, Experimental and numerical study of a transient, two-dimensional unsaturated-saturated water table recharge problem, *Water Resources Research*, *15*(5), 1089–1101, 1979.

Viswanathan, H. S., B. A. Robinson, A. J. Valocchi, and I. R. Triay, A reactive tranport model of neptunium migration from the potential repository at Yucca Mountain, *Journal of Hydrology*, *209*, 251–280, 1998.

Walsh, M. P., S. L. Bryant, R. S. Schechter, and L. W. Lake, Precipitation and dissolution of solids attending flow through porous media, *AIChE Journal*, *30*(2), 317–328, 1984.

Walter, A. L., E. O. Frind, D. W. Blowes, C. J. Ptacek, and J. W. Molson, Modelling of multicomponent reactive transport in groundwater, 1. Model development and evaluation, *Water Resources Research*, *30*(11), 3137–3148, 1994a.

Walter, A. L., E. O. Frind, D. W. Blowes, C. J. Ptacek, and J. W. Molson, Modelling of multicomponent reactive transport in groundwater, 2. Metal mobility in aquifers impacted by acidic mine tailings discharge, *Water Resources Research*, *30*(11), 3149–3158, 1994b.

Weathers, L. J., G. F. Parkin, P. J. Nivak, and P. J. J. Alvarez, Methanogens couple anaerobic Fe(0) oxidation and $CHCl_3$ reduction, in Proc. 209th ACS National Meeting, Vol. 35, No. 1, 829–831, Anaheim, CA, American Chemical Society, Division of Environmental Chemistry, 1995.

Wheeler, M. F., and C. N. Dawson, An operator-splitting method for advection-diffusion-reaction problem, Technical Report 87-9, Rice University, Department of Mathematical Sciences, 1987.

White, A. F., and M. L. Peterson, Role of reactive-surface-area characterization in geochemical kinetic models, in Chemical Modeling of Aqueous Systems II, edited by D. C. Melchior, and R. L. Bassett, Chapter 35, 461–475. Washington, D.C., American Chemical Society, 1990.

Wieland, E., B. Wehrli, and W. Stumm, The coordination chemistry of weathering: III. A generalization on the dissolution rates of minerals, *Geochimica et Cosmochimica Acta*, *52*, 1969–1981, 1988.

Williamson, M. A., and J. D. Rimstidt, The kinetics and electrochemical rate-determining step of aqueous pyrite oxidation, *Geochimica et Cosmochimica Acta*, *58*(24), 5443–5454, 1994.

Willis, C., and J. Rubin, Transport of reacting solutes subject to a moving dissolution boundary: Numerical methods and solutions, *Water Resources Research*, *23*(8), 1561–1574, 1987.

Wolery, T. J., K. J. Jackson, W. L. Bourcier, C. J. Bruton, B. E. Viani, K. G. Knauss, and J. M. Delany, Current status of the EQ3/6 software package for geochemical modelling, in Chemical Modeling of Aqueous Systems II, edited by D. Melchior, and R. Bassett, Chapter 8, 105–116. Washington, D.C., USA, American Chemical Society, 1990.

Wösten, J. H. M., and M. T. van Genuchten, Using texture and other soil properties to predict the unsaturated soil hydraulic functions, *Soil Sci. Soc. Am. J.*, *52*, 1762–1770, 1988.

Wunderly, M. D., D. W. Blowes, E. O. Frind, and C. J. Ptacek, Sulfide mineral oxidation and subsequent reactive transport of oxidation products in mine tailings impoundments: A numerical model, *Water Resources Research*, *32*(10), 3173–3187, 1996.

Yeh, G. T., and V. S. Tripathi, A critical evaluation of recent developments in hydrogeochemical transport models of reactive multichemical components, *Water Resources Research*, *25*(1), 93–108, 1989.

Yeh, G. T., and V. S. Tripathi, A model for simulating transport of reactive multispecies components: Model development and demonstration, *Water Resources Research*, *27*(12), 3075–3094, 1991.

Zysset, A. Modellierung des chemischen Zustandes in Grundwasser-Infiltrations-Systemen. Ph.D. thesis, Eidgenössische Technische Hochschule Zürich, Zürich,

Switzerland, 1993.

Zysset, A., F. Stauffer, and T. Dracos, Modelling of chemically reactive groundwater transport, *Water Resources Research*, *30*(7), 2217–2228, 1994.

Appendix A

Model Performance

Run	$\Delta \log C^c_{ant}$	$\Delta \log C^c_{max}$	N^{max}_{it}	N^{tot}_{t}	N^{tot}_{ft}	N^{tot}_{it}	CPU [h:m:s]
(1)	0.5	2.0	20	1097	29	6977	1:35:02
(2)			40	1026	5	6383	1:26:45
(3)			60	1002	2	6311	1:25:53
(4)			80	1002	2	6331	1:26:25
(5)		3.0	20		DNC		
(6)			40	1021	9	6408	1:27:35
(7)			60	1030	8	6502	1:28:22
(8)			80	1030	7	6543	1:28:54
(9)		4.0	20		DNC		
(10)			40	1031	12	6535	1:30:12
(11)			60	1055	7	6796	1:33:42
(12)			80	1055	7	6856	1:34:10
(13)		5.0	20		DNC		
(14)			40	1020	5	6378	1:26:47
(15)			60	1045	6	6693	1:30:54
(16)			80	1030	6	6611	1:33:37
(17)	1.0	2.0	20	447	92	5067	1:11:53
(18)			40	318	11	3190	0:42:48
(19)			60	301	3	2982	0:40:00
(20)			80	301	2	3022	0:40:45
(21)		3.0	20	378	69	4074	0:54:39
(22)			40	310	11	3049	0:40:58
(23)			60	309	14	3331	0:44:35
(24)			80	308	12	3375	0:45:09
(25)		4.0	20		DNC		
(26)			40	318	29	3601	0:48:27
(27)			60	317	9	3353	0:44:56
(28)			80	319	16	3416	0:46:07
(29)		5.0	20		DNC		
(30)			40	320	19	3385	0:45:27
(31)			60	309	13	3394	0:45:34
(32)			80	309	13	3474	0:46:37

Table A.1: Model performance as a function of adaptive time stepping parameters, t = 4 years - determination of time increment based on anticipated update, part A, DNC = did not converge

Run	$\Delta \log C^c_{\text{ant}}$	$\Delta \log C^c_{\max}$	$N^{\max}_{it}$	N^{tot}_{t}	N^{tot}_{ft}	N^{tot}_{it}	CPU [h:m:s]
(33)	2.0	2.0	20	279	113	4786	1:04:38
(34)			40	187	23	3026	0:40:46
(35)			60	166	11	2818	0:37:45
(36)			80	164	10	2944	0:39:17
(37)		3.0	20	268	133	4839	1:04:47
(38)			40	176	19	2772	0:36:56
(39)			60	163	7	2358	0:31:30
(40)			80	170	11	2806	0:37:28
(41)		4.0	20	260	138	4837	1:05:08
(42)			40	182	35	3289	0:44:03
(43)			60	181	27	3612	0:48:43
(44)			80	175	19	3290	0:47:13
(45)		5.0	20	271	151	5187	1:09:21
(46)			40	180	28	3154	0:42:07
(47)			60	171	22	3151	0:42:15
(48)			80	172	19	3036	0:40:37
(49)	3.0	3.0	20	231	171	5328	1:11:10
(50)			40	133	17	2421	0:32:22
(51)			60	131	14	2406	0:32:10
(52)			80	129	12	2577	0:34:18
(53)		4.0	20	245	190	5661	1:16:08
(54)			40	144	33	3093	0:41:35
(55)			60	135	22	2815	0:38:03
(56)			80	129	18	2626	0:35:13
(57)		5.0	20	250	214	6312	1:24:22
(58)			40	161	49	3722	0:49:37
(59)			60	136	19	2767	0:36:57
(60)			80	136	19	2887	0:38:31

Table A.2: Model performance as a function of adaptive time stepping parameters, $t = 4$ years - determination of time increment based on anticipated update, part B

Run	N_{it}^{ant}	$\Delta \log C_{max}^{c}$	N_{it}^{max}	N_{t}^{tot}	N_{ft}^{tot}	N_{it}^{tot}	CPU [h:m:s]
(1)	10	2.0	20	460	156	6426	1:26:29
(2)			40	219	3	2504	0:33:31
(3)			60	224	3	2640	0:35:20
(4)			80	222	2	2558	0:34:13
(5)		3.0	20	359	104	4655	1:02:34
(6)			40	247	15	2933	0:39:21
(7)			60	227	7	2692	0:36:01
(8)			80	227	7	2752	0:36:48
(9)		4.0	20	289	68	3525	0:47:19
(10)			40	236	16	3058	0:40:55
(11)			60	248	12	3191	0:42:40
(12)			80	248	12	3271	0:43:41
(13)		5.0	20	331	95	4361	0:58:34
(14)			40	245	16	3157	0:42:10
(15)			60	233	7	3061	0:44:43
(16)			80	233	6	3141	0:41:57
(17)	20	2.0	40	128	13	2505	0:33:15
(18)			60	127	10	2515	0:33:25
(19)			80	126	8	2646	0:35:06
(20)		3.0	40	143	15	2673	0:35:39
(21)			60	138	13	2736	0:36:28
(22)			80	138	13	2896	0:38:33
(23)		4.0	40	144	23	2799	0:37:26
(24)			60	139	13	2750	0:36:35
(25)			80	139	13	2810	0:37:22
(26)		5.0	40	140	14	2832	0:37:39
(27)			60	139	16	2947	0:39:16
(28)			80	139	16	3087	0:41:05

Table A.3: Model performance as a function of adaptive time stepping parameters, $t = 4$ years - determination of time increment based on anticipated number of iterations, part A

Run	N_{it}^{ant}	$\Delta \log C_{max}^{c}$	N_{it}^{max}	N_{t}^{tot}	N_{ft}^{tot}	N_{it}^{tot}	CPU [h:m:s]
(29)	30	2.0	40	100	28	2649	0:35:12
(30)			60	89	10	2284	0:30:19
(31)			80	92	10	2711	0:35:51
(32)		3.0	40	104	20	2229	0:29:56
(33)			60	111	22	2647	0:35:27
(34)			80	111	22	2747	0:36:45
(35)		4.0	40	118	36	2897	0:38:50
(36)			60	108	20	2846	0:37:30
(37)			80	106	16	2866	0:38:01
(38)		5.0	40	115	27	2895	0:38:29
(39)			60	117	21	2970	0:39:53
(40)			80	116	20	3345	0:44:34
(41)	40	2.0	60	86	20	2653	0:35:08
(42)			80	81	15	2624	0:34:45
(43)		3.0	60	93	34	2937	0:39:01
(44)			80	90	25	3010	0:39:50
(45)		4.0	60	88	19	2324	0:30:59
(46)			80	91	25	2953	0:39:16
(47)		5.0	60	98	29	2712	0:36:19
(48)			80	89	21	2747	0:36:39

Table A.4: Model performance as a function of adaptive time stepping parameters, $t = 4$ years - determination of time increment based on anticipated number of iterations, part B